UNIVERSITÄT
BERN

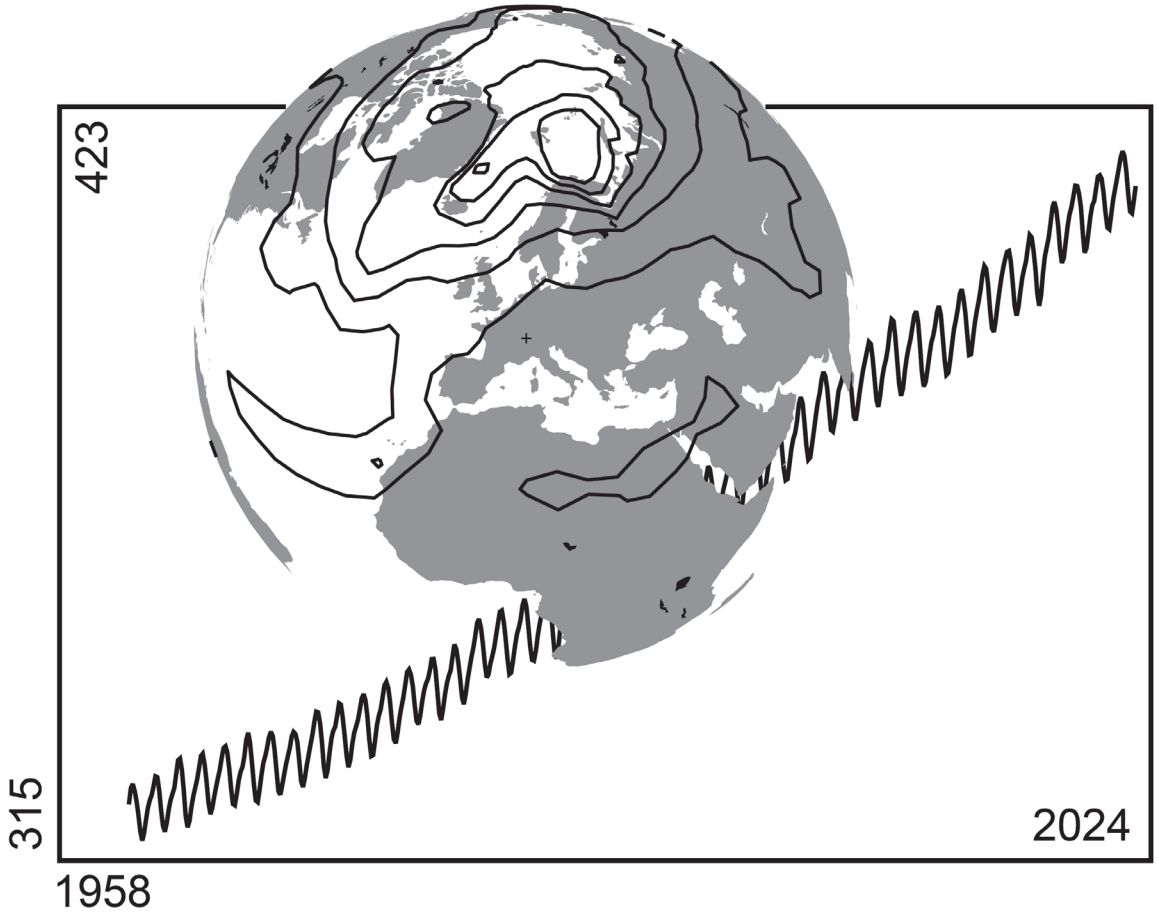

Introduction to Climate Modelling

Prof. Thomas Stocker
Climate and Environmental Physics
Physics Institute
University of Bern

Spring Semester 2024

Version October 15, 2024

Contents

1 Introduction

These lecture notes form the basis of a one-semester course taught at the Physics Institute and the Oeschger Centre of Climate Change Research of the University of Bern. The present version bases the original short textbook (Stocker, 2011) and has been extended over the years and updated.

1.1 Goals of these lecture notes

The *main goals* of these notes are:

1. To introduce the students to the physical basis and the mathematical description of the different *components of the climate system*;
2. to provide the students with a first approach to the *numerical solution* of ordinary and partial differential equations using examples from climate modelling;
3. to use and apply *python* as a mathematical-numerical tool.

A course of two hours per week plus computer lab is too short to reach these goals. A modest additional literature study, www included, and the application of the knowledge gained in the computer lab shall enable the student to proceed further in the education, e.g., in the framework of an MSc or a PhD thesis.

The course should enable the students, who are increasingly becoming users of climate models and are missing the direct contact and developmental involvement with climate models, to gain an insight into the construction of climate model components, the nature of parameterisations and some of the potential pitfalls of numerical computation in the context of climate modelling. The present lecture notes aim to achieve this by presenting and illustrating a few simple and basic examples of how different components of the Earth system are simulated, including the processes governing their dynamics and their relevance for past and future climate change.

Numerical climate models enable a physically based estimate of the range of future climate change. These models, which rest on the fundamental laws of physics and chemistry (conservation of energy, mass, momentum, etc.), are invaluable in providing scientific information towards political and societal decision making. When the effects of a doubling of the atmospheric CO_2 concentration, as it is expected around the year 2050, and other changes in the atmospheric composition have to be evaluated, only numerical climate models can generate a well-founded quantitative answer.

Climate models bring together findings of many disciplines in natural sciences. The understanding of dynamical processes in the atmosphere and the ocean is crucial for its modelling. Fluid dynamics in a rotating frame of reference (geophysical fluid dynamics) plays a major role. The resulting partial differential equations need to be solved with calculation schemes: a problem for numerical mathematics. As in each

model representation of natural systems, there are processes that cannot be simulated because they are insufficiently understood or because they occur on temporal or spatial scales which the model cannot capture. Therefore, parameterisations are formulated, some of which will be presented in these lecture notes.

Here is a selection of some helpful textbooks on the topic of climate and climate modelling:

- Peixoto J.P., Oort, A.H., 1992, *Physics of Climate*, 2nd ed., American Institute of Physics, 520 pp.

  Very clear and detailed introduction into the physical basis of the climate system and its different components (Atmosphere, Ocean, Ice). Good presentation of the climatology of important quantities. The aspect of climate models, however, is treated only briefly. The textbook is based on an earlier review article by these authors which is available at https://journals.aps.org/rmp/pdf/10.1103/RevModPhys.56.365

- *Ocean Circulation and Climate, 2nd Edition. A 21st Century Perspective*, 2013, G. Siedler, S.M. Griffies, J. Gould, J.A. Church (Eds.), International Geophysics Series 103, Academic Press, 904 pp.,

  Very good overview of research in oceanography on a global scale. Excellent figures. The introductory overview article *The ocean as a component of the climate system* is available at https://climatehomes.unibe.ch/~stocker/papers/stocker13ocean.pdf

- G.K. Vallis, 2017, *Atmospheric and Oceanic Fluid Dynamics, 2nd Edition*, Cambridge, 946 pp.

  Oustanding and very accessible graduate-level textbook on geophysical fluid dynamics in the atmosphere and ocean. Succinct derivations of the dynamics. Excellent figures.

- McGuffie K., A. Henderson-Sellers, 2005, *A Climate Modelling Primer*, 3rd ed., John Wiley, 296 pp.

  Introduction into the hierarchy of models and formulations including examples and programs.

- Washington W.M., C.L. Parkinson, 2005, *An Introduction to Three-Dimensional Climate Modeling*, University Science Books, 354 pp.

  Clear presentation of the physics of the different system components, not as detailed as Peixoto & Oort (1992), but targeted at modelling the Earth System. Many parameterisations are described. An update of the classic first edition of 1986.

- Houghton J., 2002, *The Physics of Atmospheres*, 3rd ed., Cambridge University Press, 320 pp.

  Basic and comprehensive presentation of the physics of the atmosphere (radiation, clouds, circulation), with an overview of climate change, climate models and predictability.

- Hartmann D.L., 2016, *Global Physical Climatology, 2nd Edition*, Elsevier, 498 pp.

  Very clear and rigorous introduction to the physics of ocean and atmosphere and a physically-based discussion on climate variability and climate change.

- *Climate Change 2013: The Physical Science Basis. Contribution of Working Group I to the Fifth Assessment Report of the Intergovernmental Panel on Climate Change*, T.F. Stocker (eds.).

  Comprehensive assessment of the scientific knowledge on natural and anthropogenic climate change as of 2013. See https://www.ipcc.ch/report/ar5/wg1.

- *Climate Change 2021: The Physical Science Basis. Contribution of Working Group I to the Sixth Assessment Report of the Intergovernmental Panel on Climate Change*, V. Masson-Delmotte, (eds.).

  Comprehensive assessment of the latest knowledge about climate change, including and interactive Atlas based on the Climate Modelling Intercomparison Project CMIP6. See https://www.ipcc.ch/report/sixth-assessment-report-working-group-i.

- Houghton J., 2009, *Global Warming: The Complete Briefing*, 4th ed., Cambridge, 456 pp.

  Excellent overview of the science knowledge regarding global warming and consequences. Sir John Houghton was Co-Chair of IPCC for the Second and Third Assessment Reports of the Intergovernmental Panel on Climate Change published in 1995 and 2001, respectively.

Some books on the basics of numerical solutions of problems in mathematical physics:

- Schwarz, H.R., N. Köckler, 2011, *Numerische Mathematik, 8. Auflage*, Springer, 595 pp.

  German. Complete introduction into the different numerical methods, interpolation, integration and solution of partial differential equations. Numerous examples.

- Press W.H., S.A. Teukolsky, W.T. Vetterling, B.P. Flannery, 1992, *Numerical Recipes in Fortran (Volumes 1 and 2)*, Cambridge, 963 pp. (Volume 2 for Fortran 90, 1996).

  Large collection of numerical schemes in different programming languages. Schemes are explained briefly and succinctly. Their good and bad properties are discussed. Must be part of the library of every modeler. The newest edition (third edition, 2007) is written in C++.

- Krishnamurti T.N., L. Bounoua 1996, *An Introduction to Numerical Weather Prediction Techniques*. CRC Press, 304 pp.

  Comprehensive explanation of different solving schemes and parameterisations which are used in atmospheric circulation models.

- Griffies S.M. 2005, *Fundamentals in Ocean Climate Models*. Princeton, 528 pp.

  Excellent graduate level textbook on ocean modelling, including the implementation of complex ocean dynamics into a numerical model.

- Haltiner, G.J., R.T. Williams, 1980, *Numerical Prediction and Dynamic Meteorology*. Wiley, 477 pp.

  Advanced text with many derivations of numerical techniques. Comprehensive and far beyond the scope of these lecture notes.

- For programming with *python* we recommend the web page: `www.python.org`.

1.2 The climate system

1.2.1 Components of the climate system

The climate system can be divided into five components (Fig. 1.1) which are introduced below. The overview mentions some important processes as examples:

1. *Atmosphere*: Gaseous part above the Earth's surface including traces amounts of other gaseous, liquid and solid substances. Weather, radiation balance, formation of clouds and precipitation, atmospheric flow, reservoir of natural and anthropogenic trace gases, transport of heat, water vapour, tracers, dust and aerosols.
2. *Hydrosphere*: All forms of water above and below the Earth's surface. This includes the whole ocean and the global water cycle after precipitation has reached the Earth's surface. Global distribution and changes of the inflow into the different ocean basins, transport of ocean water masses, transport of heat and tracers in the ocean, exchange of water vapour and other gases between ocean and atmosphere, most important reservoir of carbon with fast turnover.
3. *Cryosphere*: All forms of ice in the climate system, including inland ice masses, ice shelves, sea ice, glaciers and permafrost. Long-term water reserves, changes of the radiation balance of the Earth surface, influence on the salinity in critical regions of the ocean.
4. *Land Surface*: Solid Earth. Position of the continents as a determining factor of the climatic zones and the ocean currents, changes in sea level, transformation of short-wave to long-wave radiation, reflectivity of the Earth's surface (sand different from rock, or other forms), reservoir of dust, transfer of momentum and energy.
5. *Biosphere*: Organic cover of the land masses (vegetation, soil) and marine organisms. Determines the exchange of carbon between the different reservoirs, and hence the concentration of CO_2 in the atmosphere, as well as the balances of many other gases, and therefore also the radiation budget. Influences the reflectivity of the surface, hence the radiation balance (e.g., tundra different from grassland), regulates the water vapour transfer soil-atmosphere, and via its roughness, the momentum exchange between the atmosphere and the ground.

A sixth component, which is particularly relevant for the assessment of future changes, is often treated as a distinct part of the climate system: the *anthroposphere* ($\alpha\nu\theta\rho\sigma\pi\sigma\sigma$ = human), consisting of the processes which are caused or altered by humans. The most important ones are the emission of substances which alter the radiation balance, and land use change (deforestation, desertification, degradation and transformation into constructed areas).

Most of the climate models treat processes and fluxes of the anthroposphere as an external forcing, i.e., the models are run by prescribing atmospheric concentrations and emissions of CO_2, other greenhouse gases and aerosols from anthropogenic sources. Prescribed are also dust and sulphate emissions from volcanoes: for the

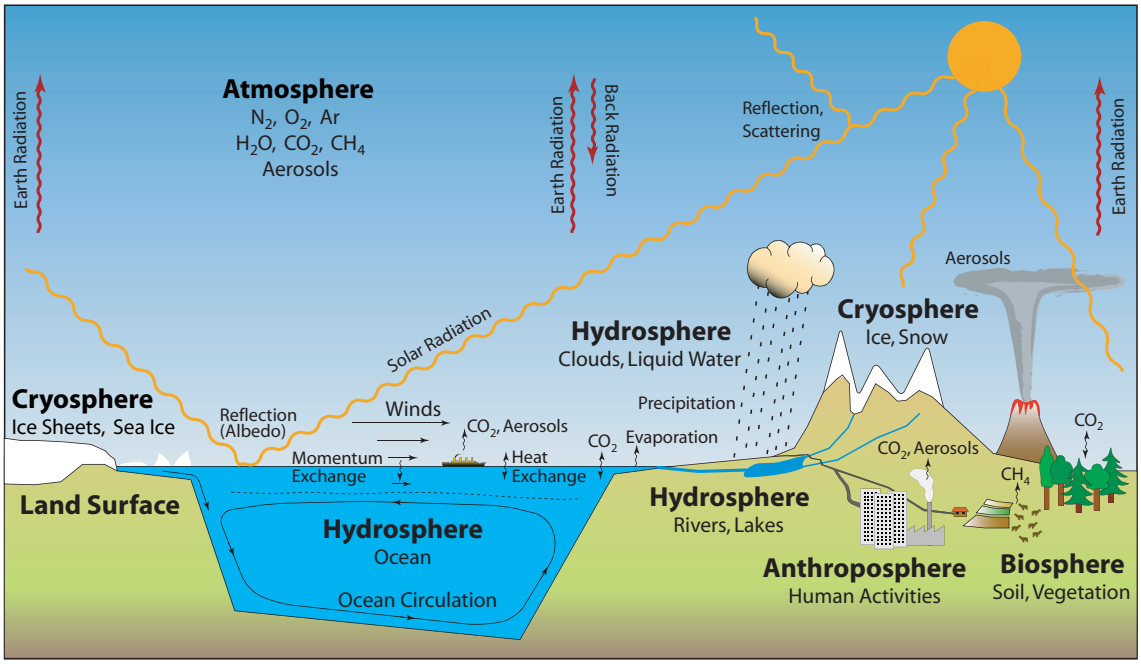

Figure 1.1: The most important components and associated processes of the climate system on a global scale.

past based on documented data and paleoclimatic information of volcanic eruptions, for the future they may be based on a random event generator informed by observed space-time statistics of volcanic events.

A complete climate model contains physical descriptions of all five components mentioned above and takes into consideration their coupling. Some components may be described in a simplified form or even be prescribed.

Not all questions in climate sciences require a model comprising all components. It is part of the scientific work to select an appropriate model combination and complexity, so that *robust results* are produced for a specific science question.

Each climate system component operates on a range of characteristic temporal and spatial scales. The knowledge of these scales is necessary for a correct formulation of climate models. Table 1.1 summarizes some of relevant scales. Usually, the definition of processes to be represented in the model restricts the temporal and spatial resolution of the model's grid.

1.2.2 Global radiation balance of the climate system

The Sun is the only relevant energy source for the climate system on a temporal scale of less than about 10^6 years. Regionally, the geothermal heat flux may be of importance, e.g. to correctly simulate the Antarctic ice sheet in the presence of basal heat sources. The different global-scale energy fluxes in the atmosphere are shown in Fig. 1.2. Coming from the Sun, on average 340 W/m^2 reach the top of the atmosphere (this corresponds to about a quarter of the solar energy flux density, Solar Constant $S_0 = 1361$ W/m^2), while barely half of this is available for heating of the Earth's surface. Major parts of the short-wave radiation are reflected by clouds or reflected directly on the Earth's surface itself and are absorbed by the

Component of the Climate System	Process	Characteristic Time Scale	Characteristic Spatial Scale
Atmosphere	collision of droplets during cloud formation	10^{-6} – 10^{-3} s	10^{-6} m
	formation of convection cells	10^{4} – 10^{5} s	10^{2} – 10^{4} m
	development of large-scale weather systems	10^{4} – 10^{5} s	10^{6} – 10^{7} m
	persistence of pressure distributions	10^{6} s	10^{6} – 10^{7} m
	Southern Oscillation	10^{7} s	10^{7} m
	troposphere-stratosphere exchange	10^{7} – 10^{8} s	global
Hydrosphere	gas exchange atmosphere-ocean	10^{-3} – 10^{6} s	10^{-6} – 10^{3} m
	deep water formation	10^{4} – 10^{6} s	10^{4} – 10^{5} m
	meso-scale oceanic gyres	10^{6} – 10^{7} s	10^{4} – 10^{5} m
	propagation of Rossby waves	10^{7} s	10^{7} m
	El Niño	10^{7} – 10^{8} s	10^{7} m
	turnover of deep water	10^{9} – 10^{10} s	global
Cryosphere	formation of permafrost	10^{7} – 10^{9} s	1 – 10^{6} m
	formation of sea ice	10^{7} – 10^{8} s	1 – 10^{6} m
	formation of land ice masses	10^{8} – 10^{11} s	10^{2} – 10^{7} m
Land Surface	changes in reflectivity	10^{7} – 10^{8} s	10^{2} m – global
	isostatic equilibration of the crust by covering ice masses	10^{8} – 10^{11} s	10^{6} m – global
Biosphere	exchange of carbon with the atmosphere	10^{4} – 10^{8} s	10^{-3} m – global
	transformation of vegetation zones	10^{9} – 10^{10} s	10^{2} – 10^{7} m

Table 1.1: Some examples of processes determining the climate with their characteristic time and spatial scales.

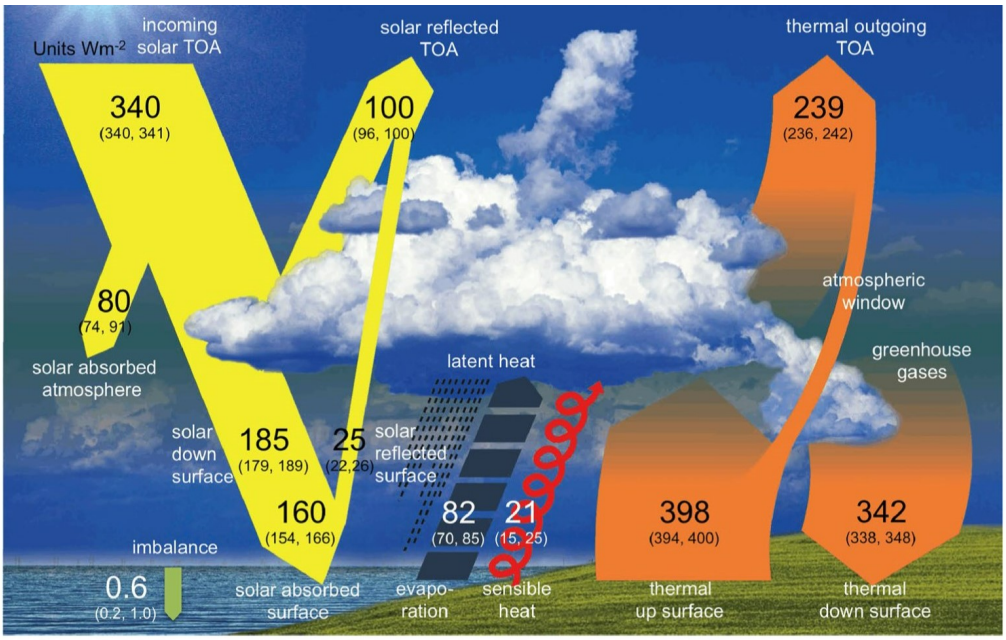

Figure 1.2: Global energy fluxes from different sources which determine the radiation balance of the Earth. Figure from Wild et al. (2015).

atmosphere. Incoming short-wave radiation contrasts with outgoing surface long-wave radiation of around 398 W/m^2. Through convection and evaporation, the surface loses another 103 W/m^2, which would—if other important processes were absent—result in a negative energy balance of the surface.

The natural *greenhouse effect*, caused by greenhouse gases such as H_2O, CO_2, CH_4, N_2O and further trace gases, is responsible for the infrared back-radiation of around 342 W/m^2. This results in an energy balance with a global mean surface temperature of about 14°C.

1.3 Purpose and limitations of climate modelling

Until around the early 20$^{\text{th}}$ century, climate sciences were primarily concerned with the study of past climatic states. This was done by observation of the environment using mostly geological, geographical and botanical methods. By the end of the 1950ies, important physical measurement methods were developed. The measurement of weak radioactivity of various isotopes was the basis for the dating of organic material using the naturally occuring ^{14}C isotope. An entire palette of additional radioisotopes covering a range of decay times enabled the determination of flux rates in different environmental systems (see Lecture Notes *Introduction to Climate and Envrionmental Physics*).

The measurement of the stable isotopes in precipitation ($H_2{}^{16}O$, $H_2{}^{18}O$) revealed a conspicuous temperature dependence owing to different phase change rates caused by the mass difference between the two isotopes. By analysing stable isotope ratios in permanently deposited water (i.e., polar ice) a natural "paleo-thermometer" was realised. Furthermore, the determination of the concentration of trace gases and other tracers in ice cores from Antarctica and Greenland made it possible, for the

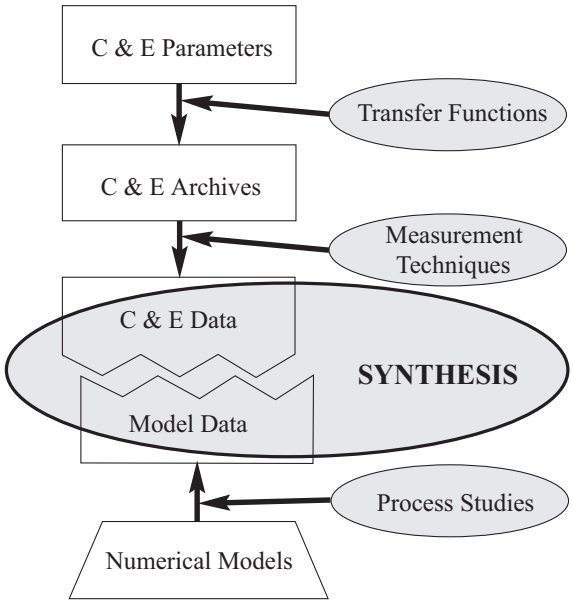

Figure 1.3: The role of climate modelling in climate science. C & E stands for *climate and environmental*.

first time, to produce an accurate reconstruction of the chemical composition of the atmosphere. By exploring different *paleoclimatic archives*, which may be described as environmental systems that record and conserve physical quantities varying with time, an important step towards a quantitative science was taken. Such archives include ice cores from Greenland and Antarctica, ocean and lake sediments, tree rings, speleothems, and many more. This enabled the transition of climate science from the purely descriptive to a quantitative science providing numbers with units.

To understand the increasingly detailed paleo-data hypotheses are required regarding the mechanisms responsible for climate change. Such hypotheses need to be tested quantitatively and within a consistent physical framework. This is where *climate modelling* comes in. Its goal is the understanding of the physical and chemical information and data retrieved from, among others, paleo-data. Such models permit a quantitative formulation and testing of hypotheses about the causes and mechanisms of past, and the magnitude and impact of future climate change.

Figure 1.3 visualizes the role of modelling in paleoclimate science in a schematic way. Climate change alters certain climate and environmental (C & E) parameters which then can be "read" using appropriate transfer functions. Even in this case, model formulation and application play a central role, but the term *climate modelling* is not applicable. Climate archives can only be made accessible to research by reliable measurement techniques. An experimental physicist produces climate data (e.g., the reconstruction of the atmospheric CO_2 concentration over the past 800,000 years). The modeler works on the development and application of models that yield model results within the framework process studies. The goal is the synthesis of model results and climate data, which is achieved when the underlying mechanisms and hypotheses are in quantitative agreement. Hence, the model yields *a quantitative interpretation of the evolution of climate*, based on the laws of physics and chemistry.

The evolution of the annual mean surface temperature averaged over the northern hemisphere over the course of the last 1,150 years is part of some of the most important climatic information in the debate on current climate change (Fig. 1.4). A central question, that has to be resolved by models, is whether the reconstructed

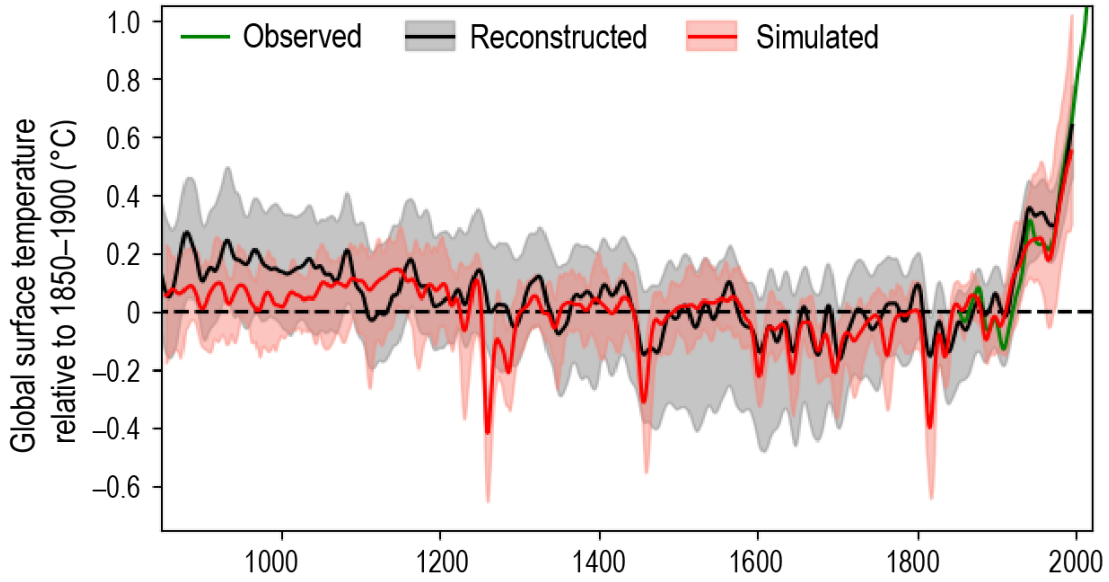

Figure 1.4: Comparison of climate model simulations and reconstructions of global surface temperature over the last 1150 years that are based on information from various paleoclimatic archives (tree rings, lake sediments, borehole temperatures, ice cores). The multi-model mean and 5-95% range are shown as the red curve and red band, respectively. Reconstructed temperature shown in black with the estimated 5-95% uncertainty range in grey. Observations available from 1850 onwards are in green showing the unprecedented increase of temperature. Figure from IPCC (2021), Box TS.2 Fig. 2

warming—and what fraction of it—can be explained by the increase in atmospheric CO_2 and the resulting changes in the radiation budget. The modelling of the last 1200 years of climate evolution necessitates an accurate knowledge of the different forcings to the radiation budget and a credible representation of natural variations by climate models. The most important forcings are the variations in solar radiation, changes in atmospheric composition, e.g. greenhouse gases, aerosols and dust, the location, magnitude and duration of volcanic eruptions, and changes in land cover by deforestation and other land use changes. Besides sophisticated statistical approaches, only climate models are able to answer these questions in a quantitative way and in within a consistent physical framework. Figure 1.4 compares the most recent reconstructions of northern hemispheric temperature with those simulated by an ensemble of climate models run over the past millennium and forced by various levels of prescribed solar variations and volcanic eruptions. The model simulations exhibit variations well within the range of reconstructed temperatures over the past 1,150 years and reproduce the significant increase in northern hemispheric temperature during the 20^{th} century. Some paleoclimate reconstructions suggest warm temperatures around the year 1000 CE, but climate models do not show such anomalies during that period. Multi-annual coolings caused by volcanic eruptions are well simulated.

The estimation of *climate sensitivity*, that is the increase in the global mean temperature with a doubling of the atmospheric CO_2 concentration above the pre-industrial level (from 280 ppm to 560 ppm), provides important information about the coupled climate system. Models, that are employed to address this question, must be capable of simulating the natural climate variability as well as past climate changes

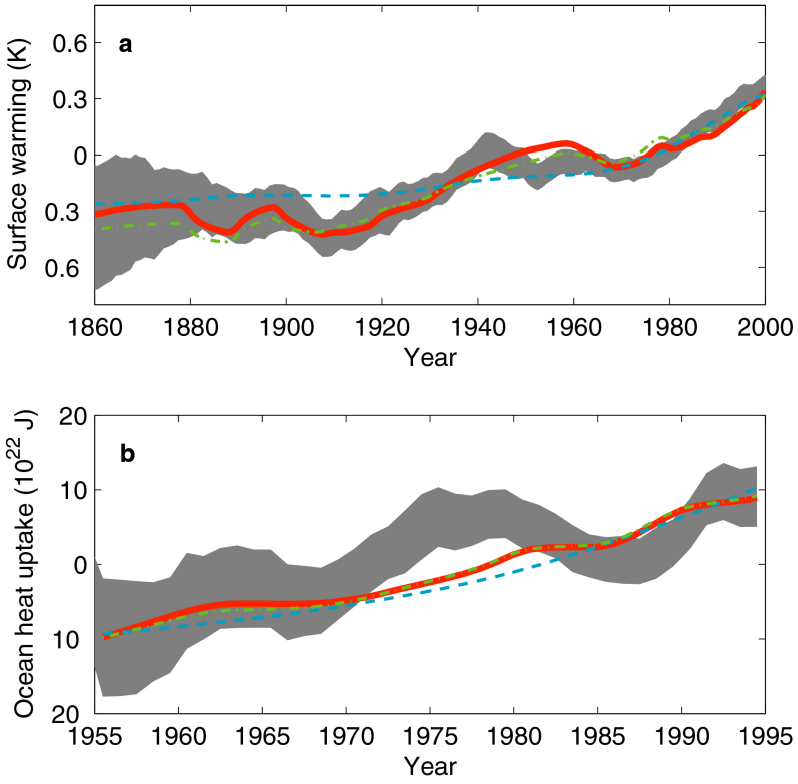

Figure 1.5: Changes in global mean temperature since 1860 **a)**, and heat uptake in the ocean since 1955 **b)**. *Grey bands* for observations, a forward model simulation *solid line*, and two members of an ensemble of emulator simulatios trained by a neural network *dashed lines*. Figure from Knutti et al. (2003).

in a quantitatively correct manner.

An example is shown in Fig. 1.5. Here, the Bern2.5d model, a simplified climate model that describes the large-scale processes in the ocean and atmosphere, was used (Stocker et al., 1992; Knutti et al., 2002). The globally averaged warming, which is observed between 1860 and 2000 (grey band) can roughly be reproduced with different model simulations. While the long-term trend is modeled in an acceptable way, single variations on a time scale of less than 10 years can only partly be captured. The uptake of heat by the ocean is only simulated in broad terms. The important deviations between 1970 and 1990 in ocean heat uptake may well be captured by particular simulations but, until today, have not been explained by climate models in a satisfactory way. However, this is a rare, but interesting example of a case in which a recent correction of the *observational* database has brought an improvement of the correspondence between experimental and computed data (Domingues et al., 2008).

As any mathematical model of natural systems, a climate model is a *simplification*. The degree of accepted simplification determines the complexity of the model and restricts the applicability of a specific model to certain questions. Determining these limitations requires considerable experience since no objective rules or guidelines exist. Especially for the development of climate models, particular care and a natural scepticism are needed: It is not desirable to implement and parameterize all processes without careful consideration of overall model consistency. The quality of a climate model is not judged by the mere number of processes considered, but rather

Figure 1.6: Vilhelm Bjerknes (1862–1951), founder of dynamical meteorology.

by the quality of how chosen processes and their couplings are reproduced.

Of course, it is the ambition of research and development to continuously increase the resolution and realism of climate models, and this is happening at a fast pace. However, this rather quickly and notoriously reaches the limits of existing computing resources, particularly if long-term simulations (e.g., over 10^5 years or more), or massive ensembles are desired. For this reason, intelligent simplifications and models of reduced complexity are required. This becomes manifest in the way how a *hierarchy of models* is used in current climate research. This will be discussed in Chapter 2.

1.4 Historical development

Climate models emerged from models that were developed for weather prediction since around 1940. Modelling atmospheric processes and circulation is the cradle of climate model development. *Vilhelm Bjerknes* (1862–1951, Fig. 1.6) was the first to realize that weather prediction was a problem of mathematics and physics. Thus, conservation equations for mass, momentum and energy need to be formulated in order to calculate the dynamics of the atmospheric circulation. They are combined with an equation of state for an ideal gas. This results in a complex dynamical system that describes the evolution of atmosphere based on physical laws.

Bjerknes assumed that a sufficiently accurate knowledge of the basic laws and the initial conditions were necessary and sufficient for a prediction. He therefore adopted from *Pierre-Simon Laplace* (1749–1827) the classical notion of predictability of nature, or determinism. Only later it will become apparent, most notably through the work of *Edward Lorenz* (1917–2008) in 1963 (see Section 7.2), that the predictability of the evolution of a non-linear system, in this case the atmospheric circulation, is naturally limited. Bjerknes founded the "Bergen School" of meteorology and has produced ground-breaking contributions to the knowledge of cyclogenesis.

Lewis Fry Richardson (1881–1953, Fig. 1.7) was the first to formulate a numerically-based weather forecast. The calculations, which he conducted in 1917, were based on observational data from 12 vertical profiles of pressure and temperature at different stations across Europe, which—incidentally—were established by Bjerknes. These data served as initial conditions for the calculation. Richardson defined a calculation grid with a resolution of $3° \times 1.8°$ and five vertical layers across Europe. It consisted of 150 grid points, on which the pressure trends were calculated. Richardson made use of the so-called primitive equations: the horizontal momentum conservation

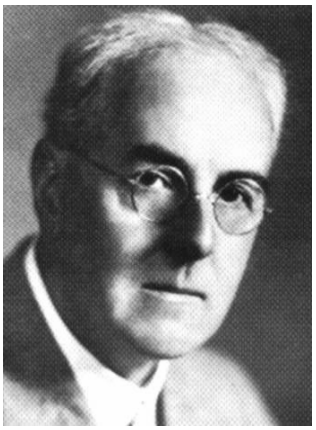

Figure 1.7: Lewis Fry Richardson (1881–1953) computed the first weather forecast.

equations, the continuity equation prescribing conservation of mass, and the ideal gas equation. The workload for the calculation of a 24-hour forecast was enormous: It took three months. Only after the first computers were available in the 1940ies, weather forecasts were feasible and were deployed as a tactical means by the end of the World War II. Richardson's first computations were a significant achievement of principle value but did not provide reliable predictions. The prediction for the change in surface pressure over six hours yielded a value of 145 hPa. Not even in the center of a low-pressure system such a fast drop in pressure can be observed. Nevertheless, Richardson published his result in the famous book *Weather Prediction by Numerical Process* (Richardson, 2007). The problem was that the initial conditions, in this case the data for the surface pressure, contained small errors that multiplied during the numerical procedure and led to strong trends in pressure. A calculation based on the same data but filtered at the beginning by adjusting unnaturally strong pressure gradients, led to a plausible prediction with Richardson's algorithms (3.2 hPa/6 h).

This points to the fact that initial conditions, or the *initialization* of weather and climate models, is a central problem of which the modeler must always be aware. Not only the initial conditions, but also the formulation of conservation equations is crucial. Even the most accurate initial data would have rapidly led to instability using the equations of Richardson, because they contained physical processes (gravity waves), which destabilize the solution and make a long-term prediction impossible.

Carl-Gustav Rossby (1898–1957) achieved a break-through by realizing that the conservation of *vorticity* was a more robust constraint than that of momentum. This approach is suitable for the system of the rotating Earth, because the Coriolis effect can be implemented in a natural way. Planetary waves (Rossby waves) appear in rotating fluids (Fig. 1.8) and are prominent features of the circulation in the atmosphere and the ocean (see Section 6.4.4). Atmosphere and ocean respond to disturbances (temperature anomalies, onset of deep water formation, etc.) with the propagation of Rossby waves that cause currents which then are able to modify the background state. Rossby waves are fundamental for the understanding of weather systems in the atmosphere and the large-scale circulation in the ocean. Interesting further information is provided at http://www.ocean.washington.edu/research/gfd including many descriptions of table-top experiments in geophysical fluid dynamics.

In the 1940ies and 50ies the first computer (ENIAC, Electronic Numerical Integrator and Computer) was deployed in Princeton for the US Army. The first project was the

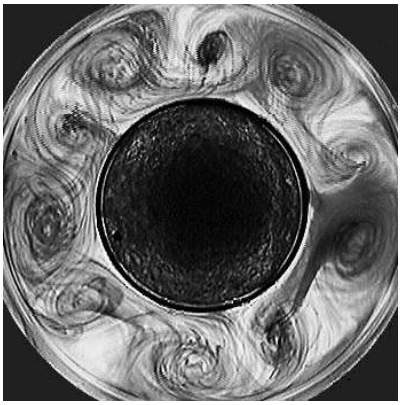

Figure 1.8: Stationary Rossby waves in a rotating tank (http://www.ocean.washington.edu/research/gfd).

Figure 1.9: Edward Lorenz (1917–2008), the discoverer of chaos in deterministic dynamical systems.

prediction of a storm surge at the American East Coast. In 1955, the first long-term integrations of a simplified atmospheric circulation model were realized by *Norman Phillips* (Phillips, 1956). This marked the beginning of *general circulation models* which would solve the complete equations of atmospheric flow.

Besides the numerically complex problems, theoretical studies on the fundamentals of the dynamic behaviour of the atmosphere and the ocean were advanced. The conservation of momentum and vorticity in a rotating fluid implies non-linear terms in the equation system. They result from advection of momentum in a flow (terms of the form $u\,\partial u/\partial x$, etc.). In addition, in a rotating frame such as the Earth, the Coriolis force causes a coupling of the components of the horizontal movements. Non-linearities are responsible for the finite predictability of such flow as Edward Lorenz (Fig. 1.9) has found in 1963. In his landmark paper *Deterministic non-periodic flow* (Lorenz, 1963) he describes how the patterns of large-scale flow can lead to chaotic behaviour (see Section 7.2).

This pioneering paper set the basis for a entirely new scientific domain: *Chaos Theory*. Although, the evolution of a classical system can be calculated in a deterministic way at all times (by solving partial differential equations), the system loses its predictability after a finite time. Smallest differences in the initial conditions may result in totally different states already after a short time. A scaling of the final state as a function of the initial states is no longer possible after a while. This finding is well known as the "butterfly effect". An excellent book with many reminiscences and mathematical examples is *The Essence of Chaos* by Edward Lorenz (Lorenz, 1996).

Figure 1.10: *Syukuro Manabe* (at a reception in Tokyo in 2004), and *Klaus Hasselmann*, pioneers of coupled climate modelling, won the Nobel Prize in Physics in 2021 for *groundbreaking contributions to our understanding of complex physical systems, in particular for the physical modelling of Earth's climate, quantifying variability and reliably predicting global warming.*

In the mid 1960ies, almost 20 years after the development of the first models for the circulation in the atmosphere, three-dimensional ocean models were formulated (Bryan and Cox, 1967; Bryan, 1969).

The 2021 Nobel Prize in Physics was awarded to *Giorgio Parisi*, *Syukuro Manabe*, and *Klaus Hasselmann*, for their groundbreaking contributions to our understanding of complex physical systems. Giorgio Parisi developed methods for generalized predictions of complex systems, on scales from molecular to galactic. Here, however, we focus on the work by Manabe and Hasselmann (Fig. 1.10).

Syukuro Manabe was a pioneer in developing the first coupled climate models. With the advent of large computers, so-called mainframes, such an endeavour became feasible. In a collaboration with *Kirk Bryan*, both at the Geophyscial Fluid Dynamics Laboratory in Princeton, they presented the first coupled climate model that simulated the general circulations of both atmosphere and ocean (Manabe and Bryan, 1969). It was formulated in spherical coordinates and consisted of a very simplified domain: 120° in longitude with half of the zonal domain a land mass, the resolution in the atmosphere was 500 km and 9 vertical levels. This configuration captured the essential elements of the global climate system while still computationally feasible in the mid 1960ies. The salient features in the atmosphere, such as the vertical temperature structure in the atmosphere, the equator-to-pole temperature distribution, the jet stream, and the key elements in the ocean, such as the vertical temperature distribution, the gyre circulations with their western boundary currents, and the thermohaline circulation, were simulated. The work was more than a proof-of-concept, since it marked the beginning of climate modelling using comprehensive models. Building on this early success, Suki Manabe and colleagues pushed the coupled modelling forward, by improving the model and, at the same time, cleverly applying it to emerging problems both in the area of paleoclimate questions regarding the mechanism of abrupt climate change as seen in the Greenland ice core (Manabe and Stouffer, 1988), and global warming and the response of the thermohaline circulation to warming (Manabe and Stouffer, 1994).

Klaus Hasselmann initially approached the challenge from a more theoretical angle by simulating and analysing the climate system using a combination of models and new statistical methods. His basic insight was that climate variability could be understood as the interplay of stochastic weather forcing of a slow-responding

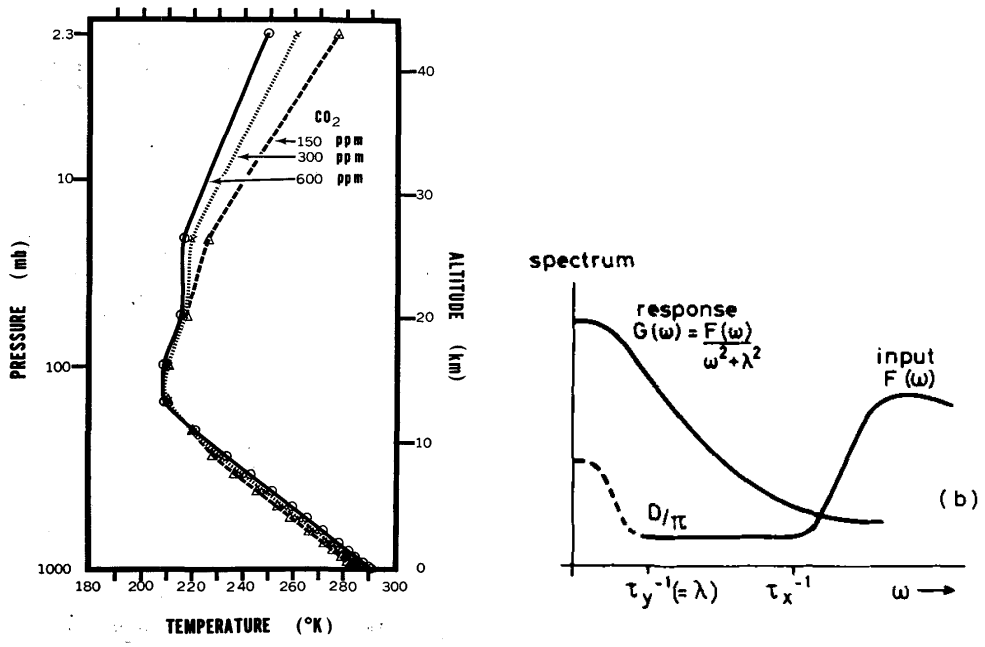

Figure 1.11: Two early key contributions of the Nobel laureates *Syukuro Manabe* and *Klaus Hasselmann*. **Left:** Radiative-convective model showing the temperature response through the atmospheric column when increasing or decreasing the CO_2 concentration (Manabe and Wetherald, 1967). **Right** Schematic illustration of the spectra of the fast and slow responding components, the atmosphere and ocean, respectively (Hasselmann, 1976).

ocean-cryosphere component (Hasselmann, 1976). Klaus Hasselmann and colleagues then developed new statistical techniques to detect and attribute observed climate change to human activity. The approach uses pattern analysis (empirical orthogonal functions) from climate models and observations and combines them to quantify the amount of warming of the 20$^{\text{th}}$ century that is caused by the increase in CO_2 concentrations. This fingerprinting method permitted, for the first time, to individually estimate the contributions of greenhouse gases, aerosols and solar variations to the observed global mean surface warming (Hegerl et al., 1997). Today, detection and attribution has evolved into a new field in climate research and provides attribution information of many quantities in the climate system (e.g. changes in sea ice, ocean temperature and salinity, heat waves, floodings). Most recently, single extreme events have been attributed to human influence. This *event attribution* (Otto, 2017) has serious legal implications regarding liability for loss and damage caused by climate change and climate extreme events. Klaus Hasselmann also laid out a plan for an efficient ocean model (Hasselmann, 1982) which was then used for the first simulations of the carbon cycle in the world ocean (Maier-Reimer and Hasselmann, 1987). With this approach, physical climate modelling has extended to other disciplines. Today coupled modelling includes also modules of chemistry (e.g., in the tropo- and stratosphere), biogeochemistry (e.g., in the ocean) and biology (e.g., in land vegetation), as illustrated on the time axis in Fig. 1.12.

Finally, we show two key figures of the early contributions by the two Nobel laureates (Fig. 1.11). Manabe and Wetherald (1967) developed a one-dimensional radiative-convective model, the first model that simulated the vertical thermal structure of the atmosphere in which the temperature decreases with altitude to about -56°C up to the tropopause at around 10 km, remains nearly constant until 20 km, and then

increases again to about −3°C up to the stratopause at 50 km altitude. This vertical distribution is the effect of adiabatic cooling and the presence of H_2O, CO_2, and O_3 in the atmosphere. With this model they calculated the changes in temperature upon a doubling of the CO_2 concentration (Fig. 1.11, left). They concluded, that the surface warming would be 2°C, a value that is still consistent with the latest assessment of the IPCC (see Section 2.4). More remarkable is their prediction that the entire troposphere will be warming while the stratosphere will be cooling. More than 50 years later, this conspicuous vertical temperature fingerprint is now robustly observed (IPCC, 2021).

Hasselmann (1976) presented a radically reduced description of the climate system by focussing on the time variability of an observed quantity and recognizing that there is a significant gap of time scales between the atmosphere and the ocean, cryosphere and land. The fast responding component represents the atmosphere which through weather, an essentially stochastic variability, acts upon the ocean, the slow responding component. The spectra of the two components are sketched in Fig. 1.11 (right), as red and blue noise, respectively. He found that the time evolution of the probability of the slow component can be described by a Fokker-Planck equation. This also allowed basic inferences regarding predictability under stochastic forcing. Hasselmann's study opened up a new avenue to utilize methods of theoretical physics, classically applied to problems such as Brownian motion, turbulence and plasma fluid dynamics, and thereby rooted climate science firmly in Physics.

Already theoretically addressed by Hasselmann (1976), a particular challenge in the implementation of climate models remained were the widely disparate time scales for the atmosphere and the ocean (see Table 1.1). In consequence, for each time step in the ocean, 100 time steps in the atmosphere were calculated. This *asynchronous coupling* is still employed today, in particular in the recent efforts to couple polar ice sheets, an even slower component, to climate models. A notorious problem was that the required heat and water fluxes from the atmosphere and the ocean, which yield surface climatologies of these models that are coherent with observations, were not compatible across the two model components. This necessitated the introduction of a non-physical *flux corrections* or *anomaly coupling*, which was used in most models for over 30 years. This topic will be discussed in Chapter 8.7. The problem could only be resolved in the early 2000s thanks to a higher resolution of the models – generally a resolution of at least $2° \times 2°$ is required –, as well as with improved parameterisations of not explicitly resolved processes.

Since the early 1990ies, significant improvements were also achieved by incorporating further climate system components (Fig. 1.12). Climate models are progressively becoming more complete. The carbon cycle, dynamical formulations of vegetation types, the chemistry of the atmosphere and ice sheets, belong to components that are currently implemented into existing physical circulation models. In consequence, climate modelling has become an *interdisciplinary* science.

Besides ever more detailed models, also simplified climate models are being developed. They permit the study of basic problems of climate sciences in an efficient way. The development and application of climate models of reduced complexity (often called EMICs, *Earth System Models of Intermediate Complexity*) have made important contributions to the understanding of the climate system, in particu-

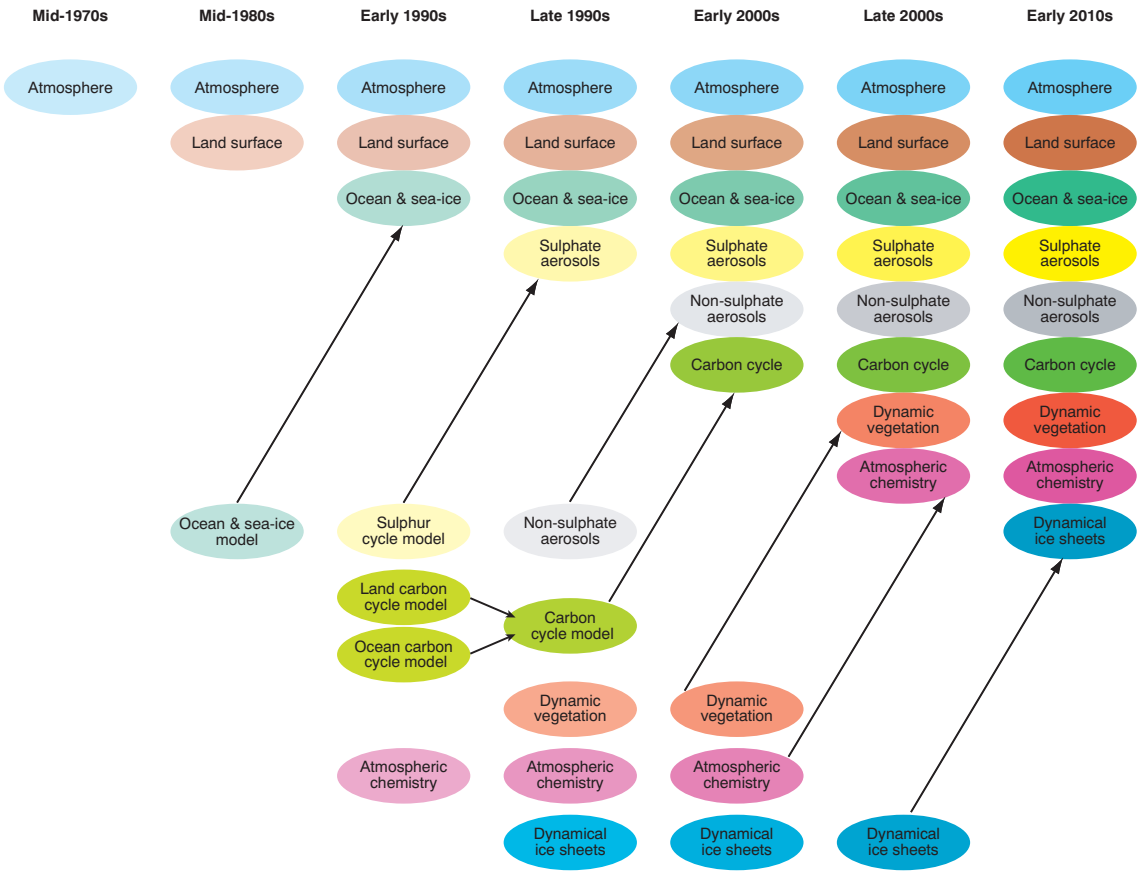

Figure 1.12: Chronology of climate model development. The implementation of new components (carbon cycle, vegetation and atmospheric chemistry) leads to an increased complexity as well as to an increase in required computational resources. Yet it is a necessary development when the interaction of the different processes needs to be simulated quantitatively. Figure modified from IPCC (2001), Technical Summary (Box 3, Figure 1, p. 48).

lar in the quantitative interpretation of paleoclimatic reconstructions and ensemble simulations of future climate change.

1.5 Some current examples in climate modelling

1.5.1 Detection and attribution of anthropogenic climate change

Given that the most important driving factors of the radiation balance are known, the effect of increasing CO_2 concentrations on the annual mean atmospheric temperature and other variables can be estimated. Figure 1.13 presents the results of simulations with climate models carried out within CMIP5, the Coupled Model Intercomparison Project Phase 5, to inform the 5th Assessment Report of the Intergovernmental Panel on Climate Change (IPCC). The averaged temperatures, ocean heat content, and sea ice extent of the model runs are compared with observations during the 20^{th} century (bold lines). If the models consider all driving factors: change in the solar irradiance, volcanic eruptions, atmosphere-ocean interactions, changes in the concentration of CO_2, other greenhouse gases as well as sulphate aerosols, an agreement of the simulations with the observational records is found (red bands). In case the anthropogenic driving factors are not included, a system-

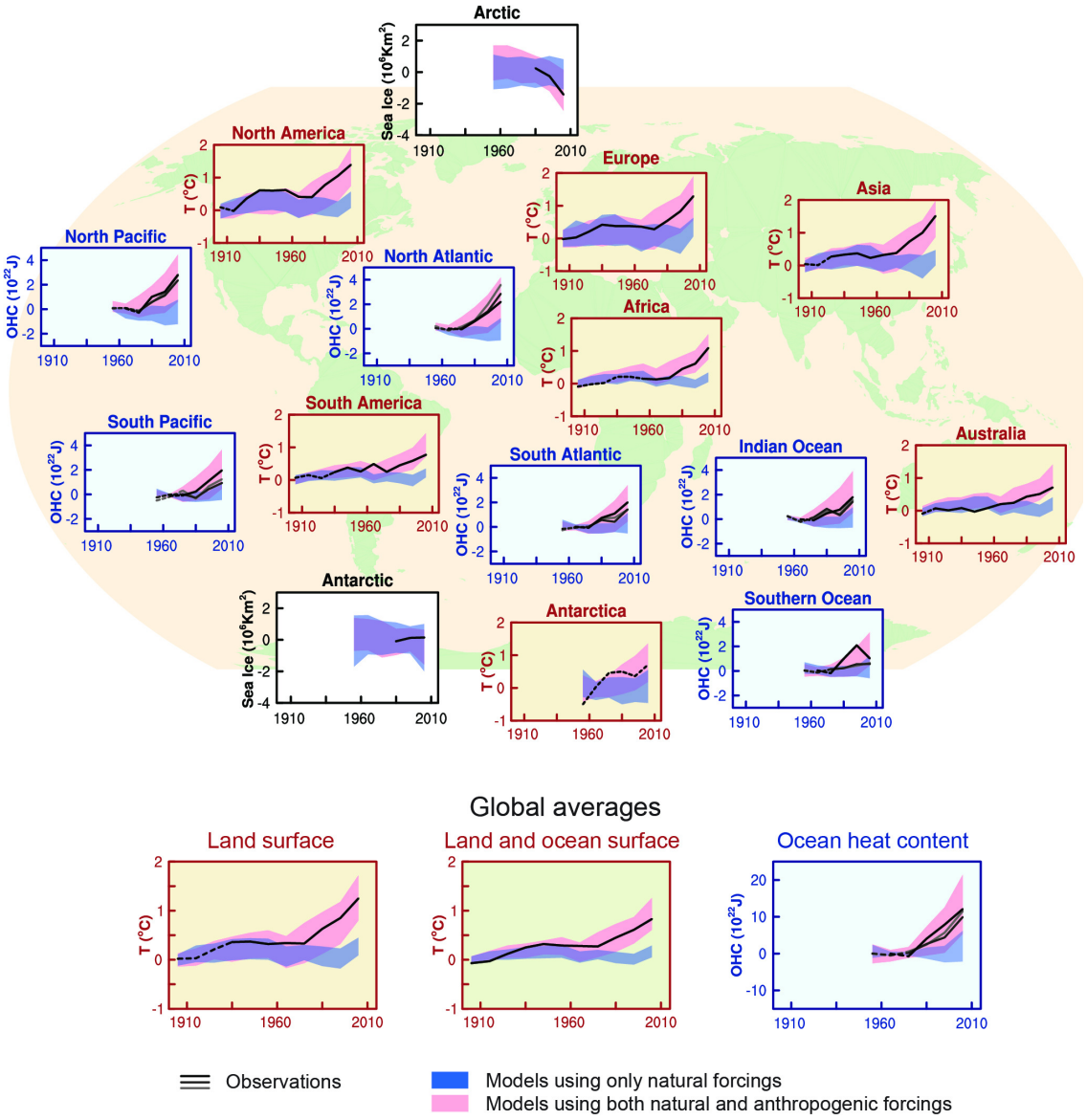

Figure 1.13: Evolution of continental land surface air temperature along with Arctic and Antarctic September sea ice extent and upper ocean heat content in the major ocean basins, based on measurements (*bold line*) and ensemble simulations with coupled climate models (*bands*). Only simulations with a complete forcing which includes changes in greenhouse gases, aerosols, observed volcanic eruptions and variable solar radiation, show reasonable agreement with the observations over the entire 20$^{\text{th}}$ century (*red bands*). In case the effect of anthropogenic forcings (greenhouse gases, aerosols) on the radiative balance is not taken into account, the global and continental-scale increase in temperature cannot be simulated (*blue bands*). Figure from IPCC (2013), Summary for Policymakers (Figure SPM.6).

atic deviation of all model simulations from the observations appears from about 1970 onwards (blue bands). This finding is valid globally, as well as averaged over continental scales, both on land and in the ocean basins.

This leads to a clear statement in 2013:

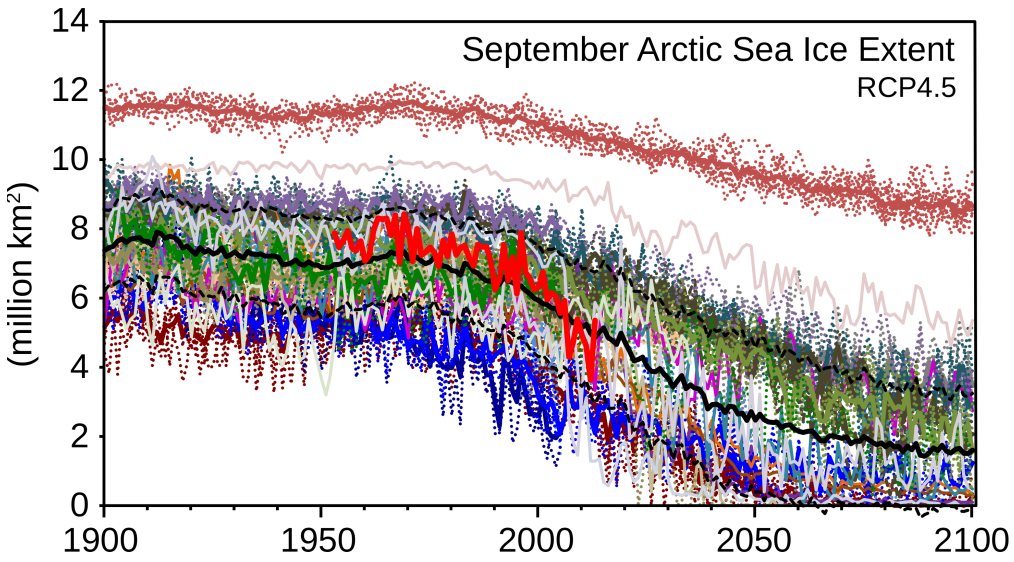

Figure 1.14: Changes in sea ice cover in the Arctic from 1900 to 2100. Shown are time-series of the Arctic sea ice extent, firstly experimental data from satellite observations (*red solid line*), and secondly ensembles of numerical simulations computed from 20 climate models, where each *dotted colored line* signifies an ensemble member and each *solid colored line* an ensemble mean. The numerical simulations are based on the representative concentration pathway 4.5 (RCP4.5) which leads to a stabilization of the radiative forcing in the year 2100 at 4.5 $\mathrm{W\,m^{-2}}$. This Figure is discussed in Stroeve et al. (2012); observations are updated with recent data (figure supplied by Julienne Stroeve and modified).

IPCC 2013, WGI Summary for Policymakers:
Human influence has been detected in warming of the atmosphere and the ocean, in changes in the global water cycle, in reductions in snow and ice, in global mean sea level rise, and in changes in some climate extremes. This evidence for human influence has grown since AR4. It is *extremely likely* that human influence has been the dominant cause of the observed warming since the mid-20$^{\mathrm{th}}$ century.

which was made in the Fifth Assessment Report of the Intergovernmental Panel on Climate Change (IPCC, 2013). Eight years later, in 2021 this attribution statement could be strengthened (IPCC, 2021):

IPCC 2021, WGI Summary for Policymakers:
Human-induced climate change is already affecting many weather and climate extremes in every region across the globe. Evidence of observed changes in extremes such as heatwaves, heavy precipitation, droughts, and tropical cyclones, and, in particular, their attribution to human influence, has strengthened since AR5.

1.5.2 Decrease in Arctic sea ice cover since around 1970

The decrease in the Arctic ice cover is documented by direct observations as well as by remote sensing. Since around 1970, the decrease in total area has accelerated (Fig. 1.14). Evidence from submarine missions also points to a drastic decrease in the

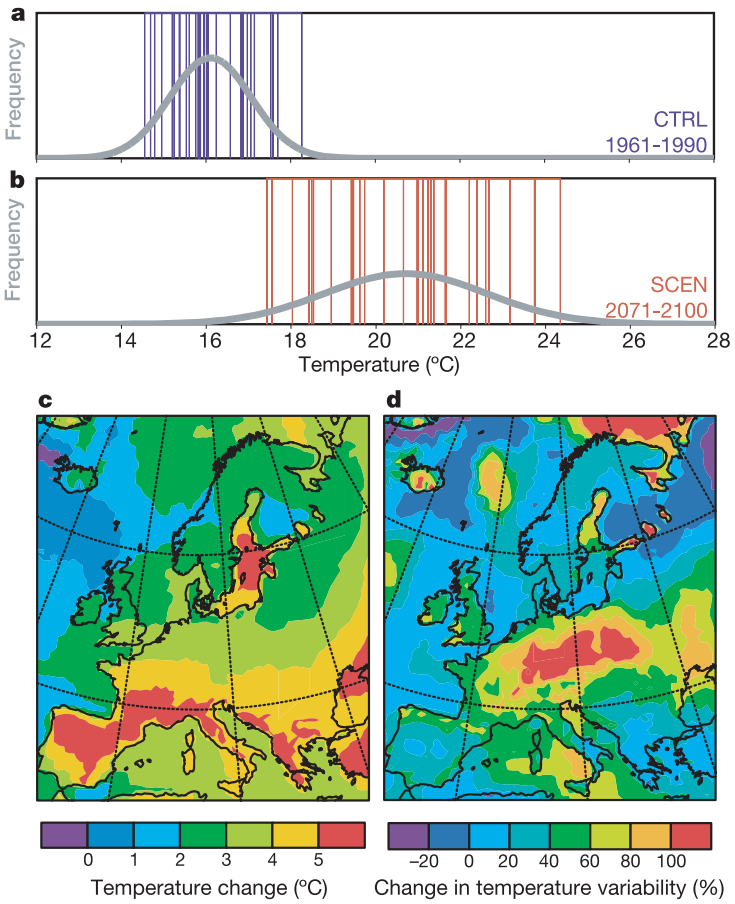

Figure 1.15: Distribution and estimate of the changes in summer temperatures over Europe in the years 2070–2100, calculated with a regional climate model (Schär et al., 2004). Panels **a)** and **b)**: Distribution of summer temperatures for 30 years in the 20th century (CTRL) and 30 years at the end of the 21st century (SCEN). Panels **c)** and **d)**: Temperature change and change in temperature variability between CTRL and SCEN.

thickness of sea ice. A similar development is visible in all coupled climate models which were used for the Fifth Assessment Report of the IPCC (IPCC, 2013). The models indicate an accelerated decrease in the extent of Arctic sea ice since around 1970. The simulations are based on the representative concentration pathway 4.5 (RCP4.5) assuming a stabilization of the actually increasing radiative forcing in the year 2100 at 4.5 W m^{-2} (Moss et al., 2010). Observations and model simulations agree with negative trends of Arctic sea ice cover. This issues a stark warning regarding the development of this important variable in the next few decades. In fact, a sea ice-free Arctic in late summer before mid-century is *likely* for a business-as-usual emission scenario (RCP8.5, see IPCC, 2013).

1.5.3 European summer temperatures by year 2100

The question how an increase in global mean temperatures will affect the climate in Europe can still only roughly be answered by a few climate models with regional resolution (Fig. 1.15). The high resolution (56 km) requires enormous computational resources and only so-called *time slices* can be calculated. The simulation with a regional climate model shows a significant increase in summer temperatures in Europe between 2071–2100 (Schär et al., 2004). The warming is accentuated at high altitudes due to the positive snow-albedo feedback and in the Mediterranean area due to the positive feedback of soil drying. Besides a strong warming by the end of the 21st century, every second or third summer then will be equally hot or

hotter than the extreme summer of 2003, an extreme event which had not occurred in the last 500 years.

A single simulation, however, is not yet a reliable description of the expected warming. Therefore, ensemble simulations with individual models and the aggregation of such into multi-model ensembles have become the standard. Uncertain quantities such as the climate sensitivity or the influence of clouds must be examined systematically. Future climate projections will be associated with estimates of probability which can be derived from *ensemble simulations*. This approach has already been used for the Fourth Assessment Report of the Intergovernmental Panel on Climate Change IPCC (2007).

1.5.4 Allowable emissions for CO_2 concentration pathways

A cornerstone of the Paris Agreement (UNFCCC, 2015) is Article 4:

> **Paris Agreement, Article 4:**
> 1. In order to achieve the long-term temperature goal set out in Article 2, Parties aim to reach global peaking of greenhouse gas emissions as soon as possible, recognizing that peaking will take longer for developing country Parties, and to undertake rapid reductions thereafter in accordance with best available science, so as to achieve a balance between anthropogenic emissions by sources and removals by sinks of greenhouse gases in the second half of this century, on the basis of equity, and in the context of sustainable development and efforts to eradicate poverty.

How much greenhouse gases, for example CO_2, may be emitted each year without exceeding the tolerated concentrations of these gases, and the consequent warming? The answer to this question can only be given on the basis of climate model simulations that include representations of biogeochemical cycles, in particular the carbon cycle. The exchange of carbon between atmosphere and ocean and the role of the terrestrial and marine biosphere have to be considered with suitable sub-models and parameterisations.

Figure 1.16 shows an example of the application of an EMIC. The long-term stabilisation of CO_2 concentrations can only be achieved by strongly reduced and ultimately vanishing emissions of CO_2. This would require a complete replacement of fossil fuels. In 1998, the emissions of all fossil energy sources (cement production included) was around 6.6 GtC/yr (1 GtC/yr = 1 gigaton carbon per year = 10^{12} kg C/yr); 10 years later it was exceeding 8 GtC/yr. The computations show that after a permitted maximum in 2030, the emissions need to decrease drastically (globally around 1% per year). Such model simulations are of crucial significance to global political decisions related to international treaties such as the Kyoto-Protocol and the Paris Agreement of 2015. In fact, our calculations in 2008 were part of the scientific foundation of Article 4 of the Paris Agreement of 2015.

1.5.5 Predicting El Niño: The example of the 2015/16 ENSO

The irregular warming of waters in the tropical Eastern Pacific, known as the *El Niño-Southern Oscillation* (ENSO) phenomenon, strongly affects the tropical cli-

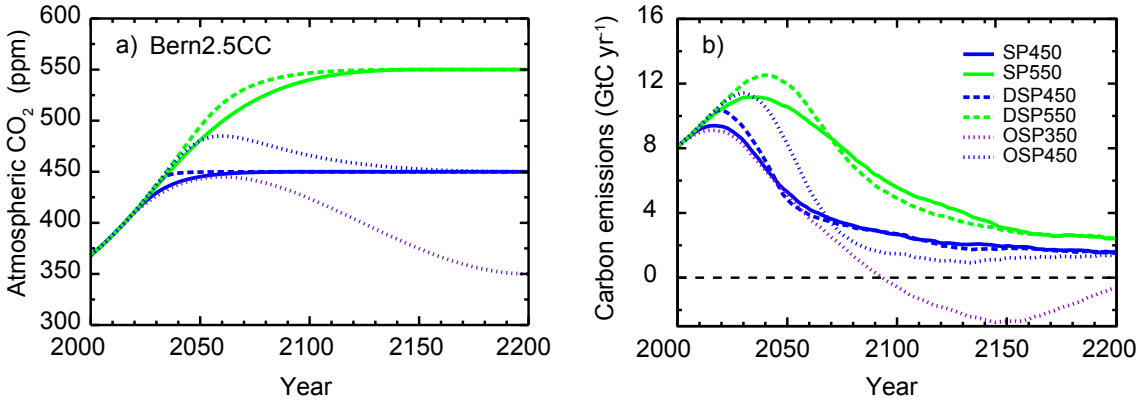

Figure 1.16: Projected allowable carbon emissions leading to stabilization of atmospheric CO_2 at given stabilization levels for the Bern2.5CC EMIC for different pathways leading to stabilization. **a)** Assumed trajectories of CO_2 concentrations in the SP, OSP, and DSP profiles. **b)** Implied carbon emissions as projected with the Bern2.5CC EMIC. Profiles with the delayed turning point in the atmospheric CO_2 increase (DSP) or atmospheric CO_2 overshoot (OSP) are compared to the standard SP profile. 31-yr running averages are applied to the results. Figure from Plattner et al. (2008).

mate and in particular the water cycle. The formation of atmospheric pressure and temperature anomalies also causes deviations from the usual climate around the globe (*teleconnections*). In the eastern equatorial Pacific the warming is due to a cessation of the upwelling of cold, nutrient-rich waters, as the trade wind system weakens. This affects the fisheries in this regions fundamentally. The changes which may last some months up to around 1.5 years, cause severe economic damage.

Due to the various teleconnections, some regions may exist which are affected by El Niño in a positive way (e.g., by increased precipitation in vegetation regions, where water is normally the limiting factor). However, the strong El Niño of 1997–1998 is estimated to have caused net economic damage (gains and losses, depending on the region) in the USA of around 25 billion US$. Therefore, a reliable prediction of El Niño is of highest economic and societal significance.

For the first time, the ENSO event of 1997–1998 could be predicted already 6 months in advance. This time span allowed the affected regions to take precautions and to adapt to the expected climatic consequences (droughts, floods, poor harvest, increased prevalence of Malaria by unusually high temperatures, etc.). This success was enabled by the set-up of a dense observation net in the tropical Pacific (in situ and via remote sensing) since the early 1980ies (TOGA Program, 1985–1994, McPhaden et al. (1998)), the intensive research in the theory of the coupling between ocean and atmosphere in the tropics, and statistical and dynamical model development.

Figure 1.17 shows the prediction of the evolving ENSO 2015/2016 based on dynamical and statistical models for two initialization periods. By then, such predictions with several months of lead time have become routine and many countries and businesses depended on them. The 2015/16 ENSO came as a complete surprise to the prediction centres and demonstrated still unsolved issues in the ENSO forecast systems. Initialization of the models in mid January 2015 showed non-anomalous temperature conditions persisting into late fall 2015. However, in the course of the year, sea surface temperature in the eastern equatorial Pacific started to rise and

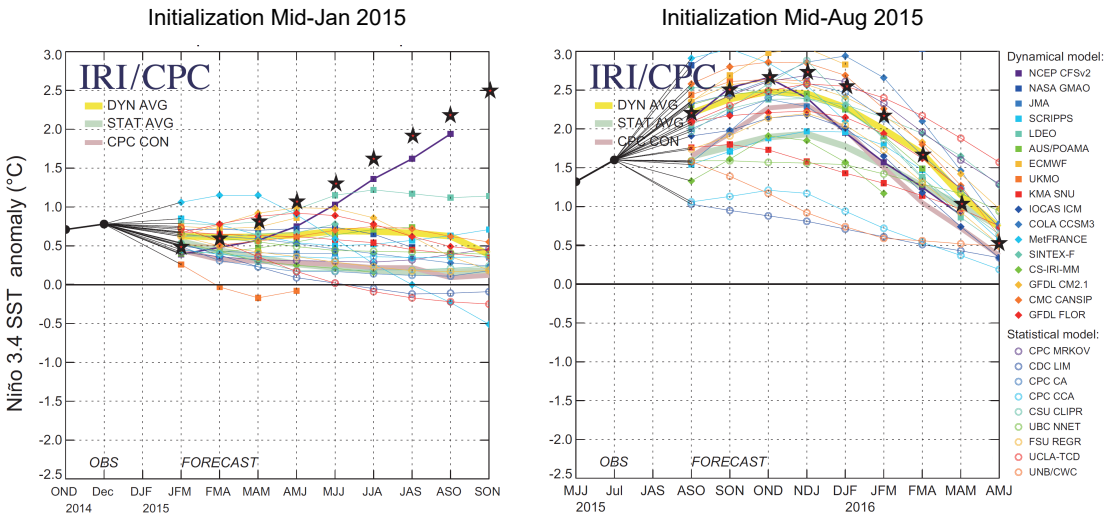

Figure 1.17: Sea surface temperature evolution in the tropical Eastern Pacific (Niño 3.4 region) simulated with several dynamical and statistical models. **Left**: Initialization in mid January shows generally insufficient skill beyond 2 months lead time: the prediction of the onset of the 2015/16 ENSO failed. **Right**: When the same models are initialized in mid August predictability is high with lead times of up to 8 months. The demise of ENSO is correctly predicted. Figure from Tang et al. (2018), collected from http://iri.columbia.edu/our-expertise/climate/forecasts/enso.

a full-blown ENSO developed by December 2015. Comparison with observations shows that the models initialized in January 2015 had almost no skill, with the exception of one model that captured the onset of the 2015/16 ENSO correctly. This was a complete surprise, as usually only initializations from April to June show very low predictability. This is referred to as the *spring predictability barrier* of ENSO. Initializations in mid August show remarkable skills by most models. They correctly predict the demise of the 2015/16 ENSO, with lead times of up to 8 months. It is important to note that the single models differ in their quantitative prediction, with the dynamical models being generally superior to the statistical models.

1.6 Conclusions

Climate models are simplified descriptions of complex processes within the climate system. They are used for the quantitative testing of hypotheses regarding the mechanisms of climate change, as well as for the interpretation of instrumental data from paleo-data from various archives. Climate models are also essential for the operational prediction of the economically important ENSO-phenomenon and other climate modes. A further important motivation for the development and application of climate models remains the aim to assess future climate change and inform policymakers and the public about the consequences of climate policies.

Research developing and using climate models has become interdisciplinary and comprises domains of physics (thermodynamics, fluid dynamics, atmospheric physics, oceanography), chemistry (organic, inorganic and surface chemistry, reaction kinetics, geochemistry, cycles of carbon, nitrogen, etc.) and biology (vegetation dynamics, ecology), and even economics (cost of climate impacts, loss and damage).

By the end of the 1960ies, simple climate models (energy balance models) were

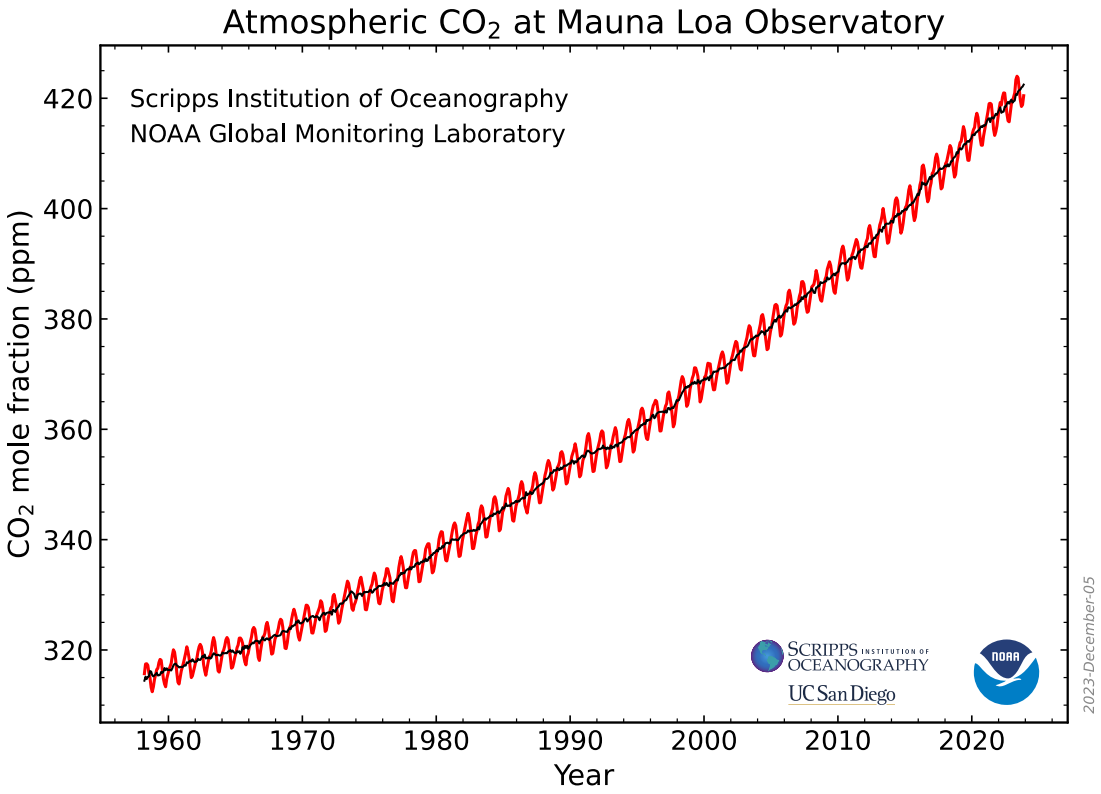

Figure 1.18: Increase in CO_2 concentration, measured since 1958 on Mauna Loa (Hawai'i). CO_2-data from https://gml.noaa.gov/ccgg/trends/.

developed in order to examine planned climate modifications (Budyko, 1969). The idea was to strongly reduce the snow cover by a large-scale distribution of ash and therefore cause a warming of Siberia in order to access new agricultural lands ("*geoengineering*"). In the meantime, we have become aware that humans alter the climate inadvertently by continuous emissions of CO_2 and other greenhouse gases. The increase in atmospheric CO_2 concentrations (Fig. 1.18) testifies to this fact with great precision. This time series has become a cornerstone in global change research.

Figure 1.18 also provides evidence of life on planet Earth and shows its global signature. The seasonal fluctuations in CO_2 are the result of the "breathing" of the biosphere (vegetation and soils). During spring in the Northern Hemisphere, carbon is taken up and is released in winter through respiration. Additionally, the interannual variability of CO_2 is visible, which is caused by the warming and cooling of large parts of the ocean, for example during ENSO events or volcanic eruptions.

Today, CO_2 concentrations are 35% higher than ever before in the last 800,000 years (Lüthi et al., 2008). This important fact has been derived from several decades of research on ice cores from Greenland and Antarctica. Ice contains bubbles in which air is enclosed. The enclosure process occurs at the firn-ice transition in a depth of about 80 to 120 meters on the two polar ice sheets of Greenland and Antarctica. Ice cores are therefore natural archives which preserve information on the content and composition of the atmosphere in the past.

Figure 1.19 shows a compilation of such measurements of CO_2 and an estimate of local temperature based on the concentrations of the stable isotopes in ice. At the

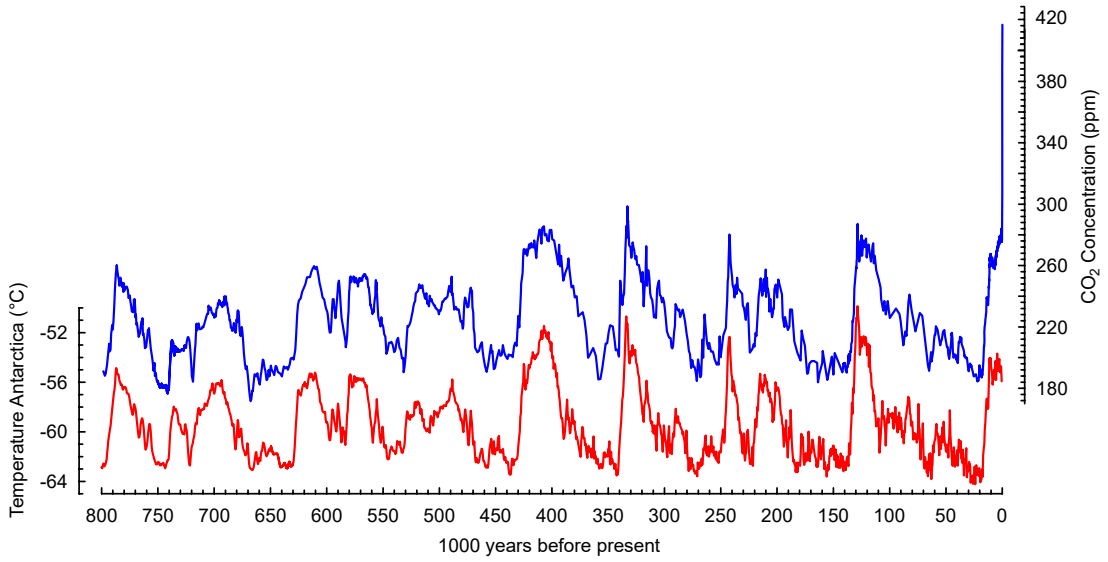

Figure 1.19: Evolution of the atmospheric CO_2 concentration (*blue*) and Antarctic temperature (*red*) over the past 800,000 years from measurements on several ice cores from Antarctica (Petit et al., 1999; Siegenthaler et al., 2005; Jouzel et al., 2007; Lüthi et al., 2008). Direct measurements of CO_2 in the atmosphere since 1958 are added.

far right side the anthropogenic increase in CO_2 during the last 250 years is added to the graph. The CO_2 measurements in the older half of this time series were performed at the University of Bern (Siegenthaler et al., 2005; Lüthi et al., 2008). This demonstrates not only the unprecedented concentrations of CO_2 today over the last 800,000 years, but also the rate of increase of CO_2 during the last 250 years, which is estimated to be about one hundred times faster than ever during the last 20,000 years.

Recognizing the increasing greenhouse gas concentrations, and the climate change induced by them, the global community has defined a remarkable goal in Article 2 of the UN Framework Convention on Climate Change (UNFCCC, 1992):

> **UNFCCC, Article 2:**
> The ultimate objective of this Convention and any related legal instruments that the Conference of the Parties may adopt is to achieve, in accordance with the relevant provisions of the Convention, stabilization of greenhouse gas concentrations in the atmosphere at a level that would prevent dangerous anthropogenic interference with the climate system. Such a level should be achieved within a time-frame sufficient to allow ecosystems to adapt naturally to climate change, to ensure that food production is not threatened and to enable economic development to proceed in a sustainable manner.

Climate research, has informed policymakers about the consequences of anthropogenic climate change since 1990 when the first assessment report of the IPCC was approved. The quantification of future climate change and its regional impact was enabled by climate modelling. In the past 30 years it has become clear that we cannot afford unabated climate change and that global heating beyond a certain level does become dangerous. The danger lies not only in the shift of the mean climate, the rising sea level and the ocean acidification, but also in the risk posed

by climate extrem events whose intensity and frequency increase rapidly with the warming. The limits of warming have been negotiated for many years at the annual Conferences of the Parties (CoPs) of the UN Framework Convention on Climate Change. Finally in 2015, at CoP21 in Paris, the Paris Agreement was approved (UNFCCC, 2015). The key statements in this legally binding treaty read:

Paris Agreement, Article 2:
1. This Agreement, in enhancing the implementation of the Convention, including its objective, aims to strengthen the global response to the threat of climate change, in the context of sustainable development and efforts to eradicate poverty, including by:

(a) Holding the increase in the global average temperature to well below 2°C above pre-industrial levels and to pursue efforts to limit the temperature increase to 1.5°C above pre-industrial levels, recognizing that this would significantly reduce the risks and impacts of climate change;

(b) Increasing the ability to adapt to the adverse impacts of climate change and foster climate resilience and low greenhouse gas emissions development, in a manner that does not threaten food production;

(c) Making finance flows consistent with a pathway towards low greenhouse gas emissions and climate-resilient development.

2. This Agreement will be implemented to reflect equity and the principle of common but differentiated responsibilities and respective capabilities, in the light of different national circumstances.

In the light of limiting global warming and the difficulty (and reluctance of certain stakeholders) to eliminate fossil fuels, geoengineering has experienced a recent revival. Of particular interest is solar radiation management, or anthropogenic solar dimming (Robock et al., 2008; Tilmes et al., 2020; NAS, 2021). This is achieved by injecting substances into the lower stratosphere to reduce the shortwave radiation reaching the Earth's surface. Here, climate models are indispensable to quantify the impact of such interventions.

However, no proposal so far has convincingly shown that geoengineering is able to reduce global warming without other, undesired side-effects particularly associated with the water cycle and changes in regional water availability. Also, the consequence of a constant loading of the lower stratosphere with substances on stratospheric cloud processes and chemistry remain poorly known. Furthermore, ocean acidification, caused directly by the rising atmospheric levels of CO_2 is not addressed at all. Therefore, many physical reasons can be brought forward, not least moral, intergenerational responsibility ones, to reject the option of geoengineering (Robock, 2008). In fact, geoengineering is likely to constitute *dangerous anthropogenic interference with the climate system*, which according to Article 2 of the UNFCCC, must be prevented.

2 Model hierarchy and simplified climate models

2.1 Hierarchy of physical climate models

There is no *best* climate model! Different models have different advantages which may be due to their complexity or the form of their implemented parameterisations (used in climate models). Table 2.1 gives an (incomplete) overview of the hierarchy of models used for climate simulations. They are ordered according to their spatial dimensions. Only model types are listed but each type may be formulated in different ways. For instance, different resolutions are used, different grid structures, parameters and parameterisations are chosen in a different way, etc. There are, for example, more than a dozen different ocean circulation models, all of which essentially solve the same conservation equations. For model development and progress the various *Modelling Intercomparison Projects* provide important insight: AMIP (*Atmospheric Modelling Intercomparison Project*), OMIP (*Ocean* ...), OCMIP (*Ocean Carbon-cycle* ...), CMIP (*Coupled* ...), PMIP (*Paleo* ...), C^4MIP (*Coupled Climate-Carbon Cycle Modelling Intercomparison Project*), etc.

In order to tackle problems across the board in climate dynamics, a model hierarchy is required. An example is the investigation of the climate at the time of the *Last Glacial Maximum* some 21,000 years ago. Simplified models of the type shown in the bold framed area of Table 2.1 permit a systematic examination of the parameter space: which driving factors (solar radiation, greenhouse gases, aerosol, volcanic forcing) are important for simulating, for example, the water mass distribution in the ocean, which parameters and processes produce a significant cooling of the tropics, etc.

Models of spatial dimension 0 or 1 help us illustrate some fundamental concepts in climate dynamics. Clever formulations of these 0-dimensional models are, under given circumstances, very useful for scenario or ensemble calculations. An EBM will be presented in Section 2.2.

So called *Saltzman Models* are globally averaged models which simulate some time dependent, large-scale variables that are coupled via heuristic relationships (e.g., global mean temperature, ice volume, atmospheric CO_2 concentrations, etc.) and form a non-linear, dynamical system. These models can be derived from the basic equations in a rigorous way (Saltzman, 2001). They are a radical alternative to the classic approach in climate modelling, but they often provide very valuable insight into Earth System processes and their interactions. For example, the question regarding the origin of the transition from a 40,000- to a 100,000-year periodicity of the glacial cycles about 10^6 years ago, The Mid-Pleistocene Transition, can be addressed with such conceptual models (Paillard, 1998; Tziperman and Gildor, 2003).

Pulse response models are efficient substitute models for particular quantities which are simulated in a more comprehensive and expensive way by three-dimensional models. They require a linear behaviour of the simulated processes which at first

Dim		Ocean			
		0	**1**	**2**	**3**
Atmosphere	**0**	EBM point model **2.2** bipolar seesaw **9.2** Lorenz model **7.2** pulse reponse model neural networks **Fig. 1.5**	Ekman model global mixing (z) Munk model (z)	wind-driven Stommel model (lat,lon) **6.7** deep ocean Stommel model (lat,lon) **6.8** thermohaline Stommel model (lat,z) **9.4**	OGCM
	1	EBM (lat) **4.3, (6.38)** radiative-convective model (z) **Fig. 1.11**		2.5D ocean (lat,z) + EBM (lat) **Bern2.5D model (Figs. 1.5, 2.1, 9.10)**	
	2	EBM (lat,lon)	stat.-dyn. atm. (lat,z) + diffusive ocean (z)	ocean (lat,z) + stat.-dyn. atmosphere (lat,lon)	OGCM + EBM (lat,lon) **Bern3D model (Fig. 2.1)** OGCM + QG atm. model
	3	AGCM + SST **Fig. 2.3**	AGCM + mixed layer	AGCM + slab ocean	AOGCM **8.7, 9.5** Earth System Model **Figs. 1.12, 2.4, 2.5**

Table 2.1: Hierarchy of coupled models for the ocean and the atmosphere with some examples, ordered according to the number of spatial dimensions considered. The direction of dimensions is specified in brackets (lat = latitude, lon = longitude, z = vertical); 2.5D corresponds to several two-dimensional ocean basins linked in the Southern Ocean; EBM stands for *energy balance model*; QG is the abbreviation for quasi-geostrophic, AGCM (*atmospheric general circulation model*), OGCM (*ocean general circulation model*), SST (*sea surface temperature*). The bold framed cells indicate climate models of reduced complexity, also called *Earth System Models of Intermediate Complexity* (EMICs), which permit integrations over very long periods (several 10^3 to 10^6 years) or massive ensemble simulations. Sections, figures, or equations, where these models are presented, are given in small bold. The table is not completely filled because some combinations are not meaningful.

has to be verified by a more complex model. The response of a complex model to any disturbance (for example the warming caused by an increase in atmospheric CO_2 can be regarded as a temporal integral of elementary responses of a complex model to a pulse-like perturbation (δ-function). These models are, e.g., successfully applied to the calculation of CO_2 uptake by the ocean or for the global warming as an input for vegetation models. Thanks to their simplicity, they permit extended scenario calculations (Siegenthaler and Joos, 1992; Joos et al., 2013).

A not yet common but promising method is the application of *neural networks* with which substitutes for complex climate models can be built. In contrast to *pulse response models* processes that are non-linear or include several equilibria can be substituted. A limiting factor is the fact that neural networks need to be trained with simulations of the model to be substituted. Since such "training sets" require information, a certain amount of computational effort is necessary. Once the network is trained, the calculation of ensembles can be realized very efficiently. This method was employed using a simplified model (Knutti et al., 2003).

Energy balance models (EBM) belong to the earliest simplified climate models that

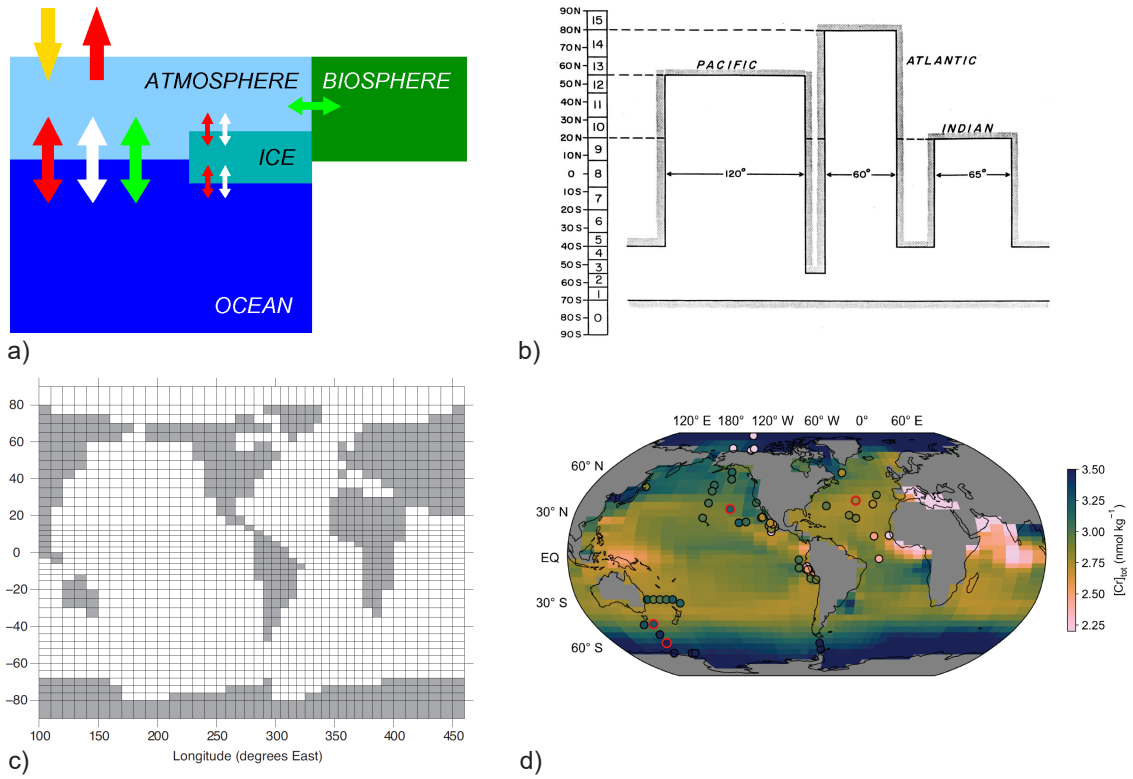

Figure 2.1: Two generations of EMICs developed and used at Climate and Environmental Physics. **(a, b)** Components and geometry of the first generation Bern2.5D model, one of the first climate models of reduced complexity (Stocker et al., 1992). Ocean currents are averaged zonally and are simulated in three basins, connected in the south (category 1/2). **c, d** Second generation Bern3D model grid and application simulating the global distribution of chromium in the ocean, a novel paleoceanographic tracer (Pöppelmeier et al., 2021). These EMICs are computationally very efficient and permit simulations spanning over 10^5 to 10^6 years.

were used for the quantitative assessment of climate change. An example shall be discussed later in Sects. 2.2 and 4.3.

Advection-diffusion models describe, e.g., the vertical mixing in the ocean on a global scale in a summarized form. They provide insight into some aspects of the carbon cycle (e.g. Siegenthaler and Joos, 1992); they are applied for questions concerning past changes in atmospheric CO_2 (last 10,000 years) as well as for the assessment of emission scenarios for future climate change.

Models of the category (0/2) are theoretical models of physical oceanography, but some of them are used as ocean components in simplified climate models. The class of climate models of reduced complexity (*Earth System Models of Intermediate Complexity, EMIC* is framed in bold in Table 2.1. Long-term simulations, particularly important for paleoclimate dynamics, are based on such models.

The Division of Climate and Environmental Physics at the University of Bern, Switzerland, has developed and applied such models since 1993. The concept and the geometries of two successive generations of EMICS, the Bern2.5D and the Bern3D models, are shown in Fig. 2.1. Although only very few atmospheric and oceanic processes are considered, and the number of parameterisations is kept at a minimum, these models are fairly consistent with observations on large spatial scales ($> 10^6$ m). For example, the meridional distribution of air temperature or the distribution of

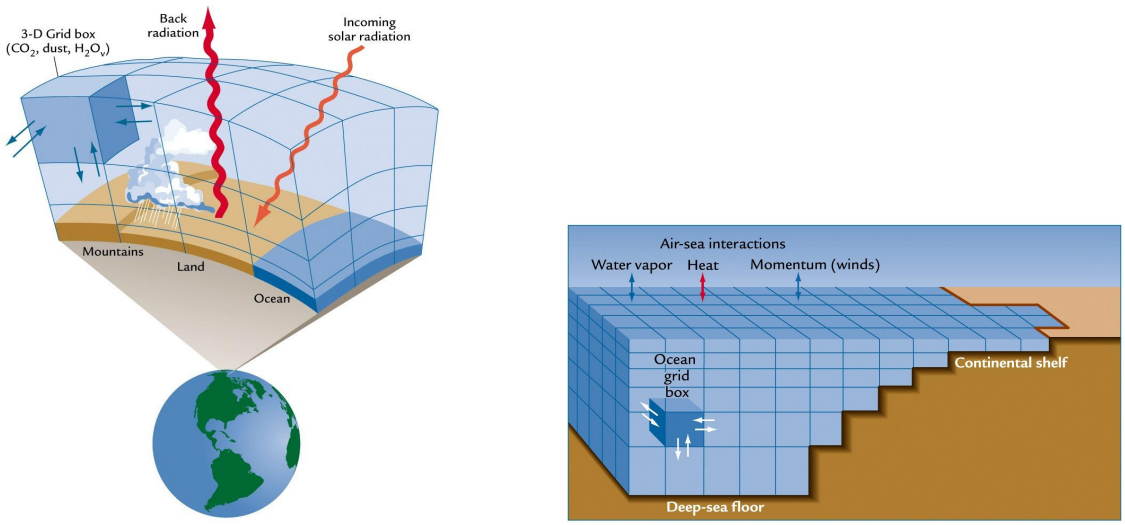

Figure 2.2: Schematic illustration of model grids in three-dimensional AGCMs and OGCMs. The resolution of a coupled climate model is typically set at $4° \times 4°$ to $2° \times 2°$ and 20 to 40 vertical layers. Today, for single components, resolutions of up to $0.1°$ are applied. In this case, the calculation is restricted to either limited regions or an extremely short time of integration, hence not yet applicable for global climate studies. Figures from Ruddiman (2007).

water masses in the three ocean basins compare well with observational estimates. These models were successfully employed in various ways in order to simulate quantitatively past climate change as, for example, found in Greenland ice cores. Even some basic aspects of biogeochemical cycles were implemented which permitted the direct comparison of model results with ice core measurements of CO_2 and other greenhouse gases (Marchal et al., 1999).

These models were also used to assess the stability of the oceanic circulation in the Atlantic under a global warming scenario. The models showed that the stability of the circulation not only depends on the absolute amount of warming, but also on the rate of warming (Stocker and Schmittner, 1997). Later, this fundamental finding was confirmed by three-dimensional AOGCMs (*Atmosphere/Ocean General Circulation Models*). This is a good example for how new and relevant climate mechanisms are found and explored with models of reduced complexity. Of course, such results then need to be verified or falsified by more comprehensive models. The implementation of suitable biogeochemical components permits the examination of the interaction of the carbon cycle with the ocean over the course of the next 1000 years (Joos et al., 1999; Plattner et al., 2008, see also Fig. 1.16). This is of significance for the question of a possible *run-away greenhouse effect* as a result of an anthropogenic increase in atmospheric CO_2. In the future, such models (e.g., the MIT model in category 2/1) may be coupled to macro-economic models, which assess the economic effects of climate change and mitigation options.

The latest developments at the Division of Climate and Environmental Physics, University of Bern, are devoted to models of category 3/2, where the ocean is three-dimensional as in Fig. 2.2 (right), but coarsely resolved. Still considered an EMIC, this model has been combined with biogeochemical modules representing the marine carbon cycle and a dynamical vegetation. Furthermore, the model now includes a palette of paleoceanographic tracers that allow direct simulations and comparison with marine sediment records. This represents an important novel instrument in pa-

leoclimate research (Müller et al., 2006; Ritz et al., 2008, 2011; Rempfer et al., 2011; Pöppelmeier et al., 2021), including a dynamical ice sheet model of the northern hemisphere (Pöppelmeier et al., 2023).

Comprehensive climate models consist of a three-dimensional formulation for the atmosphere (AGCM, *Atmospheric General Circulation Model*) as well as for the ocean (OGCM, *Ocean General Circulation Model*). The grid structures are shown schematically in Fig. 2.2. The coupling of the two, often given in differently formulated grids, is dynamic, meaning that ideally, at each time step, momentum, heat and water, and other tracers, are exchanged. For sufficiently good models, this is possible in a physically consistent way. Otherwise *flux corrections* have to be implemented in order to stabilize the simulated climate. AGCMs are classified in the highest levels of the model hierarchy shown in Table 2.1. They are extremely demanding with regard to their development, maintenance, computer time and storage and, finally, the analysis of results. Although such models are already run on personal computers or clusters, for their integration period quite strong limitations exist. A simulation of a hundred years is already a large project! These models contain a large number of parameterisations. They are being developed at various centers globally (Hadley Centre, UK; MPI Hamburg, DE; NCAR, USA; NASA-GISS, USA and many others).

The agreement of the current highest-resolution atmospheric general circulation models with observations is remarkable. This is illustrated for the visible cloud cover shown in Fig. 2.3). The model has a resolution of 9 km and 1.4 km, respectively. The atmosphere consists of a rich structure of regions that are very dry (between 20° and 45° in latitude) and regions that have a wide-spread cloud cover (50° to 65° in latitude). The effects of simulated eddies and large-scale circualtion features, as well as tropical convection are evidenced in the characteristic cloud cover over the different regions. At the km-scale resolution, atmospheric and oceanic models achieve a remarkable degree of realism (Schär et al., 2020).

Simulations carried out under CMIP5 show that climate models are reproducing the mean of surface air temperature remarkably well (Fig. 2.4). Given the large spread of mean surface air temperature over the globe (about 50°C), deviations of ±5°C must be considered as relatively moderate (Fig. 2.4 left). Over the poles, simulated temperatures are generally too cold. The seasonal cycle of surface temperature is also assessed in CMIP5 (Fig. 2.4 right). Over continents the amplitude of the seasonal cycle tends to be overestimated, while over the ocean it is smaller than climatology.

Precipitation is much more difficult to simulate because it strongly depends on surface characteristics (e.g., soil moisture, vegetation cover) and topography which are still poorly resolved in current coupled models. Hence, deviations between the simulated data of individual climate models on the one hand and between the simulated and observed data on the other hand can be large for all variables of the water cycle. Figure 2.5 (left) shows the deviation of the multi-model mean of the annual mean precipitation rate. The deviation is large in regions with high precipitation such as in the tropics. The relative deviation (Fig. 2.5 right) is large close to mountain ranges in North America and Central Asia and in the equatorial Atlantic and Pacific Oceans where the models have largely overestimated the precipitation rate. In spite of considerable progress in the reliability and realism of the simulation of the

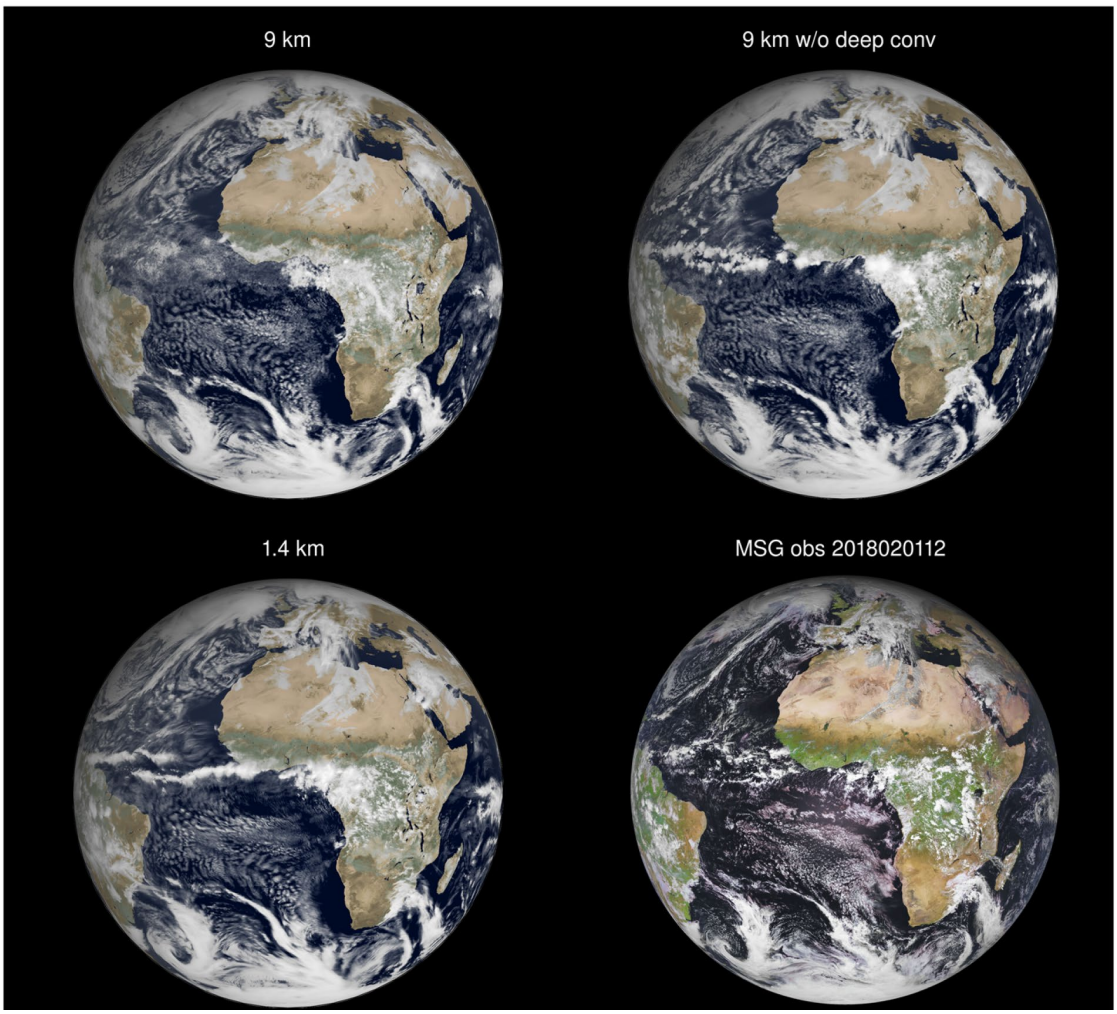

Figure 2.3: Atmosphere-general circulation model at kilometer-scale resolution compared to a visible satellite image (lower right). Deep convection in the atmosphere is explicitly resolved at 9 km and 1.4 km grid resolution (left column), and parameterized in the lower resolution version (top right). The model is capable of simulating a realistic cloud distribution at the 1.4 km scale, but the tropical cloud cover, e.g., over central Africa is still too dense. Figure from Wedi et al. (2020).

global water cycle, deviations on regional scales can be still of the same order as the observed signal. For this reason, climate projections regarding regional rainfall changes and changes in the statistics of associated extreme events are still uncertain, although robust patterns can be identified. In short, such projections show that wet regions become wetter and dry regions become drier (IPCC, 2013).

Another important quantity is the distribution of cloud cover because it strongly affects the radiative balance of the Earth. A model intercomparison of the zonally averaged cloud cover and the annual mean net radiative effects by clouds is shown in Fig. 2.6. The overall latitudinal structure of the representation of cloud cover and its radiative effect is well reproduced with larger coverage and cooling in the mid-latitudes and less coverage and cooling in the subtropics. Deviations and model spread are large in the tropics where many models have difficulties in simulating the regional structure of the Intertropical Convergence Zone (Section 7.1).

A recent overview and assessment of climate models and their performance in com-

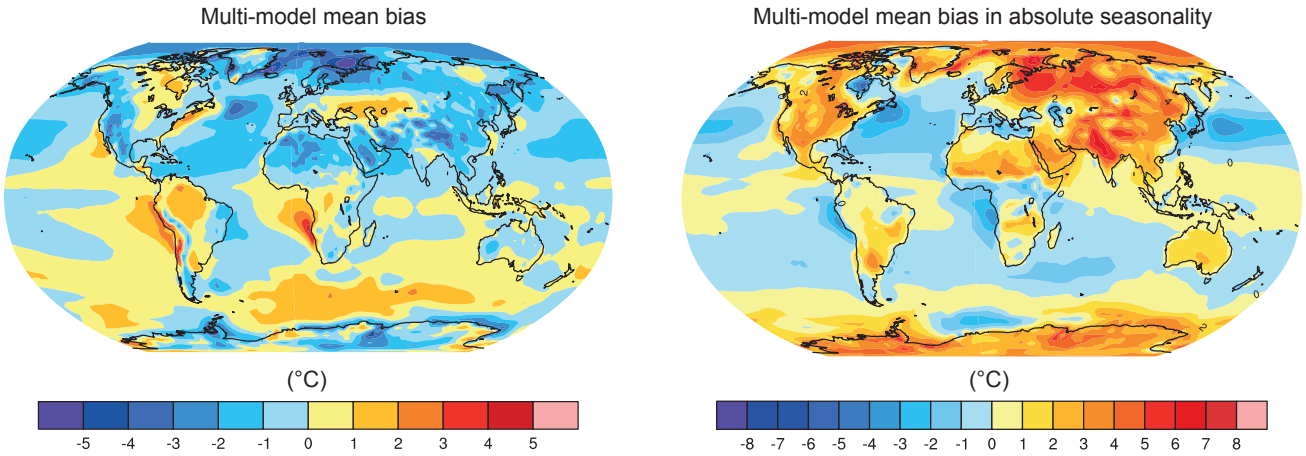

Figure 2.4: Left panel: Difference between surface air temperature (2 metre) simulated by CMIP5 models (multi-model mean) and the climatology from the ECMWF climatology for the period 1980 to 2005. **Right panel**: Difference between the absolute seasonality, defined as abs(DJF−JJA), as simulated by CMIP5 models and climatology. Positive values signify that the models overestimate the seasonal temperature amplitude. Figure from IPCC (2013), Fig. 9.2b and 9.3d.

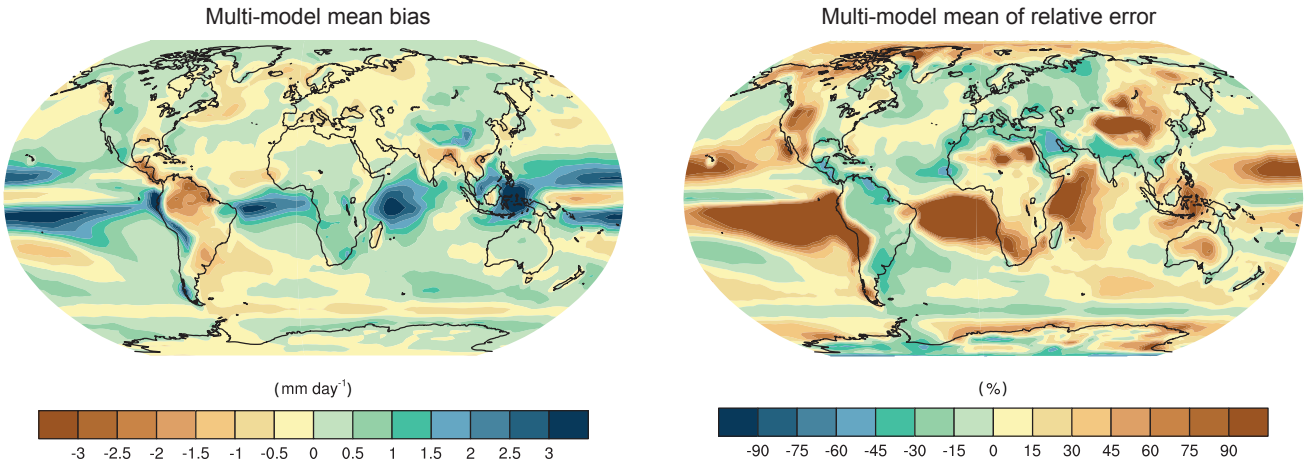

Figure 2.5: Left panel: Difference between annual mean precipitation rate (mm/day) simulated by CMIP5 models (multi-model mean) and precipitation analyses from the Global Precipitation Climatology Project for the period 1980 to 2005. **Right panel**: Difference relative to the multi-model mean precipitation rate. Figure from IPCC (2013), Fig. 9.4b and 9.4d.

parison with observations is given in Chapter 9 of IPCC (2013).

Model development has made significant progress in the past decade. Particularly the consistent coupling of dynamical representations of the atmosphere and the ocean now permits more realistic simulations of atmosphere-ocean interactions. This is central for example when quantifying the uptake of heat and carbon into the world ocean, assessing the importance of natural variability such as the El Niño-Southern Oscillation, or projecting future changes in monsoon systems. As an example of coupled model performance Figure 2.7 shows the differences of temperature and salinity, zonally averaged over all ocean basins based on the CMIP5 multi-model means. Generally, temperature deviations are less than 10% but there are systematic patterns such as a too warm intermediate ocean and the deep ocean tends to be too cold. Salinity deviations are relatively larger and this is not surprising as their distribution results from the balance of evaporation and precipitation at the ocean

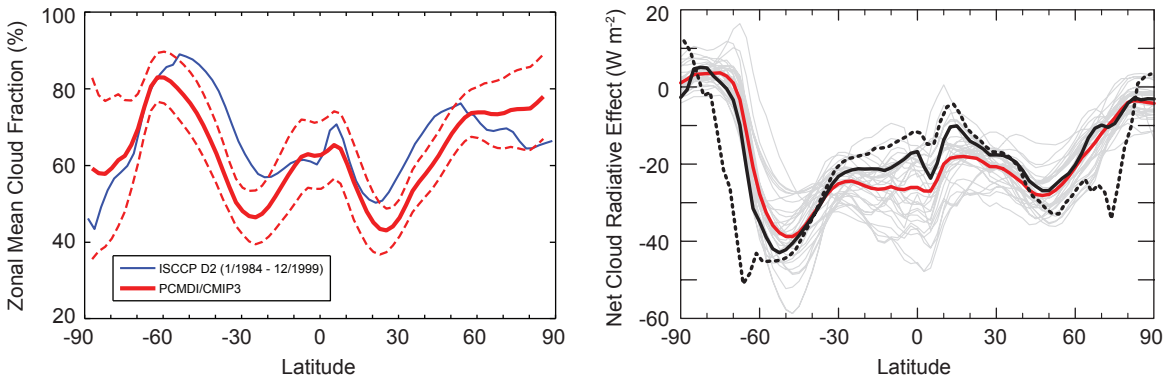

Figure 2.6: Left panel: Zonal mean cloud fraction from CMIP3 models and compared to observations (International Satellite Cloud Climatology Project, ISCCP). **Right panel**: Annual and zonal mean of the net radiative effect of clouds compared to two different analyses based on observations from the Clouds and the Earth's Radiant Energy System (*black solid* and *dashed*). The multi-model mean (*red*) is in close agreement with one of the observation-based analysis at most latitudes, except for the tropics. Individual model simulations are shown as *thin grey lines*. Figures modified from Probst et al. (2012) and IPCC (2013), Fig. 9.5f.

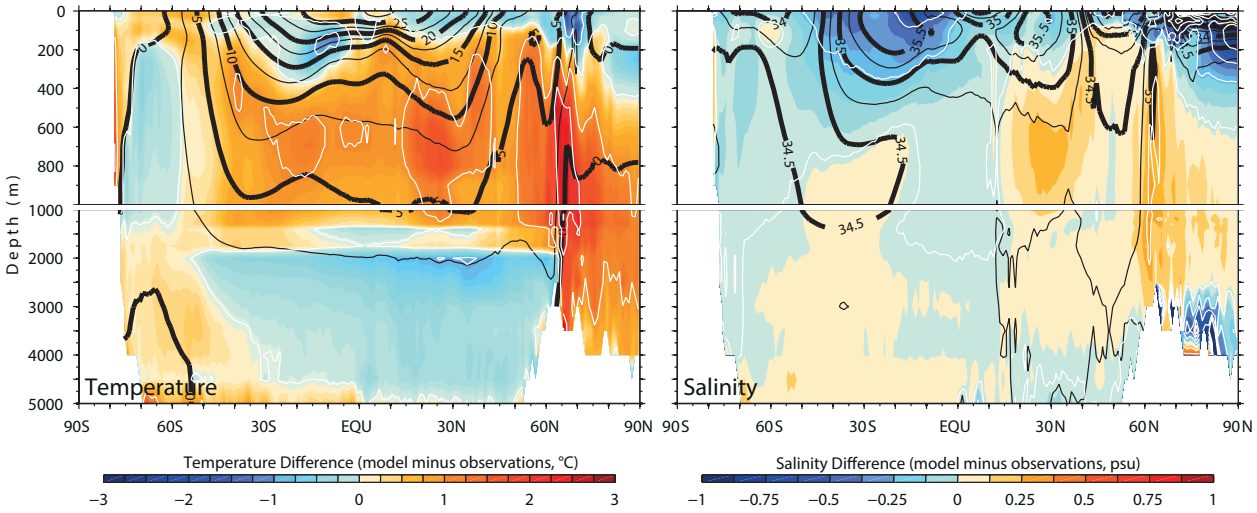

Figure 2.7: Comparison of simulated temperature and salinity in the world ocean with observations. *Black contours* show climatological values from observations from the World Ocean Atlas 2009, temperature and salinity differences are given in *colors*, and *white contours* mark positive or negative differences of 1, 2, 3°C (left) and 0.25, 0.5, 0.75, 1 psu (right), respectively. Figure from IPCC (2013), Fig. 9.13.

surface and the circulation patterns in the ocean. Large differences of precipitation between observations and simulations are propagated to the salinity distribution at the ocean surface.

In preparation of the IPCC Assessment Reports the World Climate Research Program WCRP coordinates various Coupled Climate Modelling Intercomparison Projects (CMIP). These are multi-year efforts of the international climate modelling centers to provide simulations over the historical period and scenario simulations for the 21st century. CMIP5 informed the IPCC's Fifth Assessment Report (IPCC, 2013); the current CMIP6 has provided the climate projections, including an interactive Atlas for regional climate change information, for AR6 (IPCC, 2021). These simulations represent a collective effort. CMIP data is being used extensively for

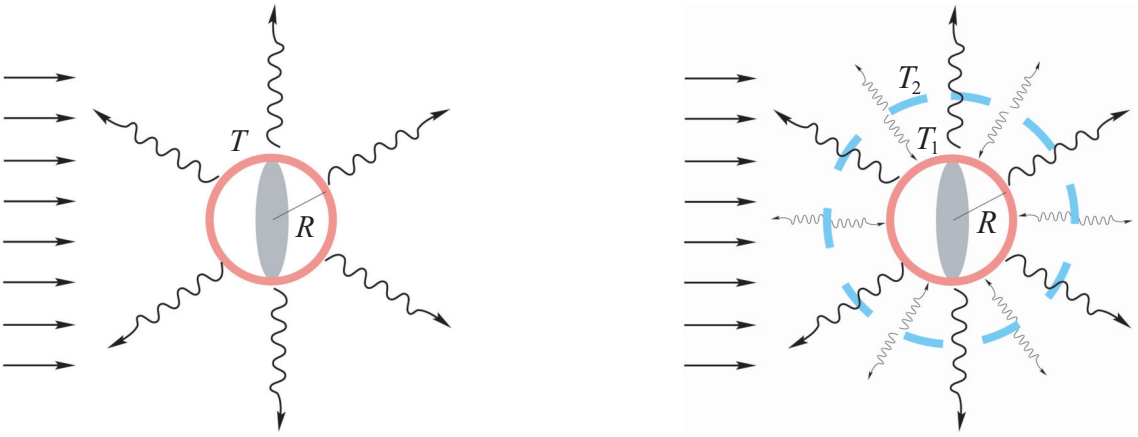

Figure 2.8: Schematic depiction of the simple global energy balance models (**left**), and a two-layer layer varian (**right**). The short-wave radiation coming from the Sun is drawn with straight arrows; the long-wave radiation from the Earth and from higher layers of the atmosphere is shown as wiggly arrows.

model comparison, detailed investigation of climate processes, and the estimate of the climate system's response to increasing greenhouse gases.

2.2 Point model of the radiation balance

For illustrative purposes and to introduce numerical schemes for time integration we consider first the simplest of all possible climate models with 0 dimensions. A single conservation equation for the globally integrated heat content is formulated (see Table 2.1, 0/0). Even though the model is not of great importance, it is instructive in various aspects. Using this simple example we will show how solutions of climate models fundamentally depend on the exact choice of parameterisations.

We assume a geometry as shown in Fig. 2.8 (left). The conservation of the energy of a thin spherical surface air layer (as a model for the atmosphere) is given approximately as:

$$4\,\pi\,R^2\,h\,\rho\,c\,\frac{\mathrm{d}T}{\mathrm{d}t} = \pi\,R^2\,(1-\alpha)\,S_0 - 4\,\pi\,R^2\,\varepsilon\,\sigma\,T^4\ , \tag{2.1}$$

where the following quantities are used:

$R = 6371$ km	radius of the Earth
$h = 8.3$ km	vertical extent of the air layer
$\rho = 1.2$ kg m^{-3}	density of air
$c = 1000$ J kg^{-1} K^{-1}	specific heat of air
T	globally averaged surface temperature
$\alpha = 0.3$	planetary albedo (reflectivity)
$S_0 = 1361$ W m^{-2}	solar constant (solar energy flux density)
$\varepsilon = 0.6$	planetary emissivity
$\sigma = 5.67 \cdot 10^{-8}$ W m^{-2} K^{-4}	Stefan-Boltzmann constant

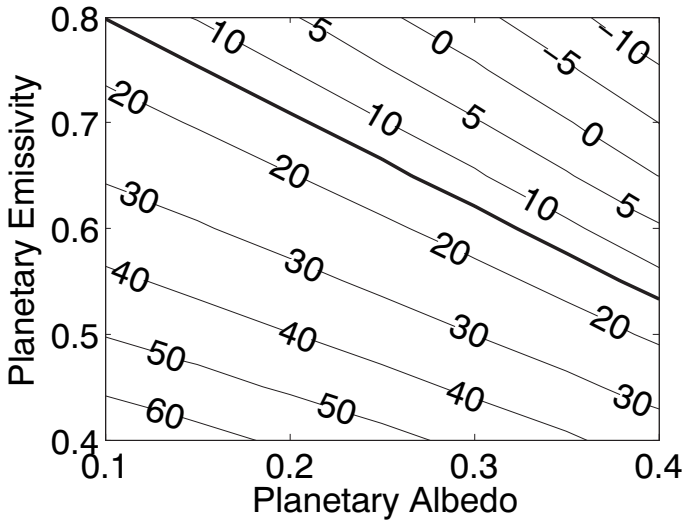

Figure 2.9: Contour lines of equilibrium temperature according to equation (2.2) as a function of planetary albedo (α) and planetary emissivity (ε). The global mean surface temperature derived from measurements is equal to 14°C (*bold line*).

Equation (2.1) states that the heat content of the global atmosphere (left) can be changed due to two processes (right). The equation is a statement on the conservation of energy. This model is therefore referred to as an energy balance model (EBM). The first term on the right-hand side is the energy flux coming from the Sun, reaching the Earth through a circular disk, reduced by the reflected part. The second term describes the (mainly long-wave) irradiance emitted from the complete Earth surface. This term is a *parameterisation* of complex processes in the atmosphere not further described in this model. The parameterisation assumes that the long-wave radiation can be quantified by the classical grey body radiation with parameter ε (emissivity). We will illustrate the role of this parameter by an example.

Equation (2.1) is an ordinary, non-linear differential equation of 1st order for an unknown time-dependent variable $T(t)$, the globally averaged surface temperature. For simple cases, (2.1) can be solved analytically.

The equilibrium temperature can be found easily by setting the left-hand side equal to 0:

$$T = \left(\frac{(1-\alpha)\, S_0}{4\, \varepsilon\, \sigma} \right)^{1/4} . \tag{2.2}$$

It is independent of the size of the Earth and the thermal characteristics of air. Figure 2.9 shows T in °C for different values of α and ε. The bold line highlights 14°C, approximately the mean surface temperature of the Earth. It is obvious that various, but not any, combinations of the model parameters α and ε can yield 'realistic' solutions. The process of choosing model parameters in such a way that model results agree with nature, is called *tuning*. When tuning was applied, agreement of the model with observations is not a measure for the quality of the model unless further independent information about the values of *tunable parameters* is used.

In this case, estimates for α and ε based on remote sensing data (ERBE, *Earth Radiation Balance Experiment*) could be used to determine the components of the radiation balance. Results based on remote sensing yield a planetary albedo of $\alpha = 0.3$. In order to obtain a mean temperature of 14°C in this EBM, the planetary

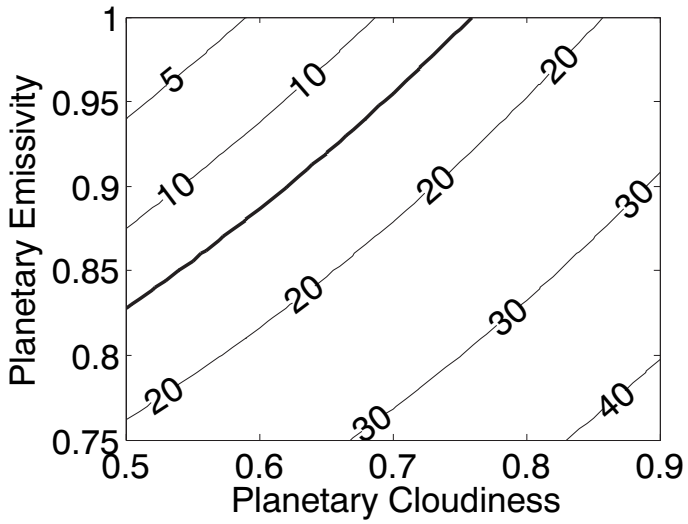

Figure 2.10: Contour lines of equilibrium temperature according to equation (2.4a). The global mean surface temperature derived from measurements is 14°C (*bold line*).

emissivity has to be set to $\varepsilon = 0.6206$. This is a value significantly lower than the emissivity of natural surface areas which is around $\varepsilon \approx 0.8 \ldots 0.99$. Hence, this model parameter is unrealistic for an average Earth surface and does not give any information about the processes leading to this radiative equilibrium.

Assuming the Earth were a perfect black body, hence $\varepsilon = 1$, the temperature would be -18.6°C. Thanks to the natural greenhouse effect, mainly caused by water vapour and CO_2, we find a difference of approximately 32.6°C.

This will be illustrated with a second, slightly more complex EBM (Fig. 2.8, right). We assume, that irradiance occurs at the Earth surface at a temperature T_1, as well as from a higher level („cirrus clouds“, which are supposed not to affect the short wave radiation and hence the albedo) at temperature T_2. The high-altitude cloud cover is not complete, but extends over a fraction c of the total area. The stationary energy balance for both levels is given by:

$$\pi R^2 (1-\alpha) S_0 + c\, 4\pi R^2 \sigma T_2^4 = 4\pi R^2 \varepsilon \sigma T_1^4 \tag{2.3a}$$

$$c\, 4\pi R^2 \varepsilon \sigma T_1^4 = 2\, c\, 4\pi R^2 \sigma T_2^4 \,, \tag{2.3b}$$

(2.3b) where we have assumed that the Earth's surface is a „grey“ body with emissivity ε, the cloud cover is assumed to be a black body. The solution is now given as follows:

$$T_1 = \left(\frac{(1-\alpha) S_0}{4 \varepsilon \sigma \left(1 - \frac{c}{2}\right)} \right)^{1/4} \,, \tag{2.4a}$$

$$T_2 = \left(\frac{(1-\alpha) S_0}{4 \sigma \, (2-c)} \right)^{1/4} \,. \tag{2.4b}$$

Here we have a slightly more detailed description of the „Earth's climate“ (two temperatures). This comes at the expense of having more parameters (α, ε, c) for which reasonable values have to be chosen.

Figure 2.10 shows that in this model more realistic values of the surface emissivity can be applied. From Fig. 2.6 we derive a global-mean cloud cover of around 0.6. Tuning the model we choose $\varepsilon \approx 0.882$ and obtain an equilibrium temperature of 14°C. This yields $T_2 = -38.8$°C the temperature that is approximately measured at a height of 8.2 km. An important information emerging from this model is that the Earth emits infrared radiation not only from the surface, but also from higher, much colder levels of the atmosphere, as was already evident from Fig. 1.2.

The natural greenhouse effect is caused by the fact that a higher irradiance occurs at a lower temperature and that these levels also radiate downwards (downward radiation). Hence, the surface is heated by a combination of direct short-wave solar radiation and long-wave back radiation. Fig. 2.10 is only valid for high altitude clouds which do not affect α significantly. In general, clouds affect α and ε, and the net effect on a global scale is a cooling one (see Section 2.4.3).

In reality, the atmosphere has to be regarded as a continuum because radiative fluxes occur at all levels. These considerations lead to *radiative-convective models*. The first 1-dimensional radiative convective model was formulated by Manabe and Wetherald (1967). This type of model (category 1/0 in Table 2.1) layed the ground how to implement vertical atmospheric processes in AGCMs.

2.3 Numerical solution of an Ordinary Differential Equation of 1st order

2.3.1 Discretization of the energy balance model

We consider again the climate model given by equation (2.1), but now we examine its time-dependence. For this we will use a numerical algorithm.

Before we derive it, we look at the temporal behaviour of the energy balance model (EBM) near the equilibrium and write the temperature $T(t)$ as follows:

$$T(t) = \overline{T} + \tilde{T}(t) \; ,$$

where $\overline{T}$ is the constant equilibrium temperature given in (2.2) and $\tilde{T}$ is a small time-dependent temperature perturbation ($|\tilde{T}| \ll \overline{T}$). Hence, (2.1) can be written as

$$h\,\rho\,c\,\frac{\mathrm{d}\tilde{T}}{\mathrm{d}t} = \frac{1-\alpha}{4}\,S_0 - \varepsilon\,\sigma\left(\overline{T}+\tilde{T}\right)^4 \; . \tag{2.5}$$

Now we write $\left(\overline{T}+\tilde{T}\right)^4 = \overline{T}^4\left(1+\tilde{T}/\overline{T}\right)^4$ and use the Taylor series expansion

$$(1+x)^n = 1 + n\,x + \frac{n\,(n-1)}{2}\,x^2 + \ldots$$

with $x = \tilde{T}/\overline{T}$ and $n = 4$. Neglecting the higher-order terms in this expansion with regard to $|\tilde{T}| \ll \overline{T}$ we obtain from (2.5), using (2.2)

$$\frac{\mathrm{d}\tilde{T}}{\mathrm{d}t} = -\left(\frac{4\,\varepsilon\,\sigma\,\overline{T}^3}{h\,\rho\,c}\right)\tilde{T} \; . \tag{2.6}$$

This is a linear, homogenous differential equation of 1st order for the temperature perturbation $\tilde{T}$, of which the solution is known:

$$\tilde{T}(t) = a\,\mathrm{e}^{-t/\tau}, \qquad \tau = \frac{h\,\rho\,c}{4\,\varepsilon\,\sigma\,\overline{T}^3}\ , \tag{2.7}$$

where a is constant depending on the initial conditions ($a = \tilde{T}(0)$). Solution (2.7) states that a temperature disturbance in the EBM approximately decays on a characteristic time scale of $\tau \approx 35$ days, and the radiation equilibrium is attained at temperature $T(t) = \overline{T}$. Hence, the temporal behaviour is determined by the thermal properties of the atmosphere and responds rather rapidly. Above considerations also show that $\overline{T}$ is a stable state, because the perturbation $\tilde{T}(t)$ approaches 0 for $t \to \infty$, as evident from (2.7).

In the following we will discuss the procedure to solve (2.1) numerically. First, the question arises of how to compute the derivatives in this equation. We assume that it is sufficient to know them only at certain points in time chosen a priori. Therefore, the problem can be discretized in time. The times are chosen according to the rule

$$t = n\,\Delta t\ , \qquad n = 0,\ 1,\ 2,\ \ldots \tag{2.8}$$

Δt is the *time step*. (2.8) can also be interpreted as grid points on the time axis.

Let us assume we know the solution at time t. Therefore, the function $T(t)$ can be expanded in a Taylor series:

$$T(t+\Delta t) = T(t) + \left.\frac{\mathrm{d}T}{\mathrm{d}t}\right|_t \Delta t + \frac{1}{2!}\left.\frac{\mathrm{d}^2T}{\mathrm{d}t^2}\right|_t \Delta t^2 + \frac{1}{3!}\left.\frac{\mathrm{d}^3T}{\mathrm{d}t^3}\right|_t \Delta t^3 + \ldots\ . \tag{2.9}$$

We can solve (2.9) for the first derivative evaluated at time t:

$$\left.\frac{\mathrm{d}T}{\mathrm{d}t}\right|_t = \frac{T(t+\Delta t) - T(t)}{\Delta t} \underbrace{- \frac{1}{2!}\left.\frac{\mathrm{d}^2T}{\mathrm{d}t^2}\right|_t \Delta t - \frac{1}{3!}\left.\frac{\mathrm{d}^3T}{\mathrm{d}t^3}\right|_t \Delta t^2 - \ldots}_{\text{terms of order } \Delta t \text{ and higher}}\ . \tag{2.10}$$

By neglecting the terms of order Δt and higher we obtain the so-called *Euler scheme*, a finite difference scheme of 1st order. This means that the corrections of this scheme scale with Δt. Whether the scheme is correct can be directly determined by considering the limit $\Delta t \to 0$. It is the simplest but at the same time the most inaccurate way of numerically representing first derivatives.

Adding to (2.10) the corresponding equation with Δt replaced by $-\Delta t$, a new equation results which yields an alternative scheme for the first derivative:

$$\left.\frac{\mathrm{d}T}{\mathrm{d}t}\right|_t = \frac{T(t+\Delta t) - T(t-\Delta t)}{2\,\Delta t} \underbrace{- \frac{1}{3!}\left.\frac{\mathrm{d}^3T}{\mathrm{d}t^3}\right|_t \Delta t^2 - \frac{1}{5!}\left.\frac{\mathrm{d}^5T}{\mathrm{d}t^5}\right|_t \Delta t^4 - \ldots}_{\text{terms of order } \Delta t^2 \text{ and higher}}\ . \tag{2.11}$$

This is the scheme of *central differences*. The name refers to the position on the time grid, where derivatives at one point are calculated by taking differences of values from two neighbouring points. The corrections of this scheme scale with Δt^2 and

Continuous	Finite differences	Error	Name
$f'(x)$	$\dfrac{f(x+\Delta x)-f(x)}{\Delta x}$	$\mathrm{O}(\Delta x)$	Euler forward
$f'(x)$	$\dfrac{f(x)-f(x-\Delta x)}{\Delta x}$	$\mathrm{O}(\Delta x)$	Euler backward
$f'(x)$	$\dfrac{f(x+\Delta x)-f(x-\Delta x)}{2\,\Delta x}$	$\mathrm{O}(\Delta x^2)$	central difference
$f''(x)$	$\dfrac{f(x+\Delta x)-2\,f(x)+f(x-\Delta x)}{\Delta x^2}$	$\mathrm{O}(\Delta x^2)$	central difference

Table 2.2: Overview of the simplest schemes for the calculation of 1st and 2nd derivatives of the function f.

for small Δt, they converge to 0 faster than in (2.10). These simple schemes are summarized in Table 2.2.

The formulations assume an equidistant discretization; adjustments are necessary if the grid's resolution is spatially dependent (e.g., on a spherical spatial grid).

2.3.2 Time stepping: Euler forward scheme

We consider the first-order ordinary differential equation (2.6) which is written in a more compact form as

$$\frac{\mathrm{d}T}{\mathrm{d}t} = -A\,T\ , \tag{2.12}$$

with the unknown function $T(t)$. The exact solution is obviously $T(t) = T_0 \cdot \mathrm{e}^{-A\,t}$. By now evaluating T only at time points $n \cdot \Delta t$ we distrectize (2.12). For the time discretization we have several choices, some are listed in Tab. 2.2. Using as a first example the Euler forward scheme, the discretized form of (2.12) reads

$$\frac{T_{n+1}-T_n}{\Delta t} = -A\,T_n\ , \tag{2.13}$$

where we have used the notation $T_n \equiv T(n\,\Delta t)$. Stepping forward in time we obtain

$$T_{n+1} = (1-A\,\Delta t)T_n = (1-A\,\Delta t)^2 T_{n-1} = \ldots = (1-A\,\Delta t)^{n+1} T_0\ . \tag{2.14}$$

We need to show that for the limit of $\Delta t \to 0$, the numerical solution converges to the analytical one. Therefore, we apply the transformation $s = -1/\,(A\,\Delta t)$:

$$T(n\,\Delta t) = T_n = T_0(1-A\,\Delta t)^n = T_0(1+\frac{1}{s})^{-s\,A\,t}\ , \tag{2.15}$$

and then take the limit $\Delta t \to 0$, i.e., $s \to \infty$:

$$T(t) = T_0 \lim_{s\to\infty} \left(\left(1+\frac{1}{s}\right)^s \right)^{-A\,t} = T_0\,\mathrm{e}^{-A\,t}\ .$$

Therefore, the numerical solution converges to the exact solution for $\Delta t \to 0$. However, there are some cases where the scheme fails. From (2.14) it is evident that the numerical solution only remains bounded for $|1 - A\Delta t| < 1$. In particular, we require the *stability criterion*

$$0 < \Delta t < 1/A \tag{2.16}$$

for a monotonously converging solution. For $1/A < \Delta t < 2/A$ the numerical solution is still bounded but exhibits a sign change at every time step. This is a *computational mode in time* which is a numerical artifact. We also note that for some special values, e.g. $\Delta t = 1/A$ the scheme yields $T_n = 0$, whereas for $\Delta t = 2/A$ we have $T_n = (-1)^n T_0$; both results do not make sense.

2.3.3 Time stepping: Central difference

Central differences are second-order accurate (see Tab. 2.2) and should therefore be preferred. However, as we will see, this poses new challenges. We first assume that the decay term $-A\,T$ of (2.12) is evaluated at $n\Delta t$, therefore

$$\frac{T_{n+1} - T_{n-1}}{2\Delta t} = -A\,T_n \ . \tag{2.17}$$

The time stepping is using information from two previous times:

$$T_{n+1} = T_{n-1} - 2\alpha\,T_n \ , \tag{2.18}$$

where we set $\alpha = A\ \Delta t$ for shorthand. The stability condition for (2.17) can be determined by defining a vector $\underline{\mathrm{T}}_n = (T_n, T_{n-1})$ and writing (2.18) as

$$\underline{\mathrm{T}}_{n+1} = \mathbf{A}\ \underline{\mathrm{T}}_n = \mathbf{A}^2\ \underline{\mathrm{T}}_{n-1} = \ldots = \mathbf{A}^n\ \underline{\mathrm{T}}_1 \ , \text{ with } \mathbf{A} = \begin{pmatrix} -2\alpha & 1 \\ 1 & 0 \end{pmatrix} . \tag{2.19}$$

For this scheme to remain stable, the eigenvalues $\lambda_\pm$ of the propagator matrix $\mathbf{A}$ need to satisfy $|\lambda_\pm| < 1$. We find $\lambda_\pm = -\alpha \pm \sqrt{1+\alpha^2}$, for which $\lambda_- < -1$, and therefore discretization (2.17) is *unconditionally unstable*.

A small, but important modification resolves this problem. Instead of evaluating the decay term at time level n, as the consistent application of the central-in-time scheme suggests, we take the time average between levels n and $n-1$. This yields

$$\frac{T_{n+1} - T_{n-1}}{2\Delta t} = -A\,\frac{T_n + T_{n-1}}{2} \ . \tag{2.20}$$

The propagator matrix now reads

$$\mathbf{A} = \begin{pmatrix} -\alpha & 1-\alpha \\ 1 & 0 \end{pmatrix} \ , \text{ with eigenvalues } \lambda_\pm = -1, 1-\alpha \ . \tag{2.21}$$

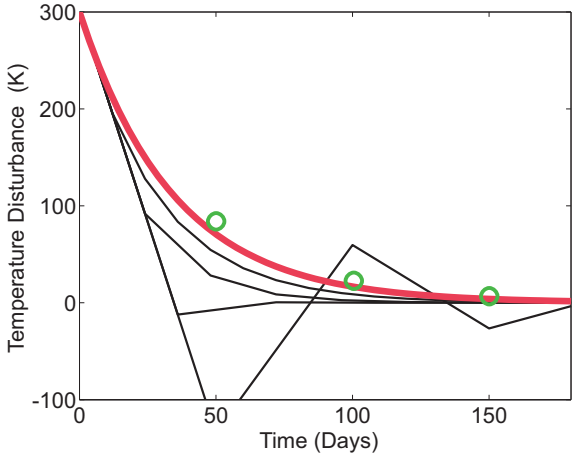

Figure 2.11: Various numerical solutions of equation (2.6), with $1/A = 34.6$ days and the initial condition $\tilde{T}(0) = 300$ K, computed with the Euler scheme and $\Delta t =$ 12, 24, 36, 50 days. The exact solution of (2.6) is in red, the results from the classical Runge-Kutta scheme with $\Delta t = 50$ days are indicated by green circles.

The stability criterion for this choice is therefore $\alpha < 2$. Note that for $1 < \alpha < 2$ a computational mode arises in which T_n changes sign every time step. As this is a numerical artifact, we require $\alpha < 1$. This is identical with the stability criterion for the Euler forward scheme (2.16).

2.3.4 Runge-Kutta scheme

The Euler scheme is the simplest, but also the most inaccurate one-step scheme. Generally, it solves

$$\frac{\mathrm{d}y}{\mathrm{d}x} = f\Big(x, y(x)\Big) \ , \tag{2.22}$$

with an initial condition $y(x_0) = y_0$. For the EBM given by equation (2.1) the following correspondences hold: $y = T$, $x = t$ and $f(x, y) = (1 - \alpha)\, S_0 / (4\, h\, \rho\, c) - \varepsilon\, \sigma\, y^4 / (h\, \rho\, c)$. The Euler scheme evaluates derivatives only at the points x and $x + \Delta x$ which corresponds to the linearisation that was used in (2.10).

By the evaluation of $f(x, y)$ at further locations in the interval $[x,\ x + \Delta x]$ and their suitable linear combination, the error can be reduced from $\mathrm{O}(\Delta x)$ to $\mathrm{O}(\Delta x^k)$. This leads to schemes of the type *Runge-Kutta of order k*. For $k = 4$ we obtain the classical Runge-Kutta scheme for which the rule is as follows:

$$\begin{aligned}
y_{n+1} &= y_n + \Delta x\, F(x_n, y_n) \\
F(x_n, y_n) &= \tfrac{1}{6}\,(K_1 + 2\,K_2 + 2\,K_3 + K_4) \\
K_1 &= f(x_n,\ y_n) \\
K_2 &= f\left(x_n + \tfrac{1}{2}\,\Delta x,\ y_n + \tfrac{1}{2}\,\Delta x\ K_1\right) \\
K_3 &= f\left(x_n + \tfrac{1}{2}\,\Delta x,\ y_n + \tfrac{1}{2}\,\Delta x\ K_2\right) \\
K_4 &= f\left(x_n + \Delta x,\ y_n + \Delta x\ K_3\right) \quad .
\end{aligned} \tag{2.23}$$

Figure 2.11 compares the different schemes with the exact solution (2.7) of the linearized system (*red line*). The Euler scheme was applied with time steps of $\Delta t = 12,\ 24,\ 36,\ 50$ days. Schemes, for which the time step is larger than their characteristic time scale τ, see (2.7), do converge to the exact solution but show a completely wrong transient behaviour. Only time steps smaller than the char-

acteristic time scale of 35 days approximately yield the transient behaviour of the exact solution when using the Euler forward scheme. For the Runge-Kutta scheme (circles) $\Delta t = 50$ days was chosen. The agreement with the exact solution is already significantly better than with the Euler scheme with $\Delta t = 12$ days, in spite of the large time step. A time step larger than τ is permissible for this scheme because according to (2.23) f is evaluated at intermediate locations on the time axis.

The use of the Runge-Kutta scheme requires that the function f in equation (2.22) can be evaluated at any point (x, y). In most of the climate models this important prerequisite is not fulfilled and the Runge-Kutta scheme can therefore not be applied for the time integration.

2.4 Climate sensitivity and feedbacks

An important quantity in climate dynamics is the *equilibrium climate sensitivity*, defined as the global mean temperature change resulting from a doubling of the atmospheric CO_2 concentration after the climate system has re-established a new equilibrium. This quantity, often referred to as $\Delta T_{2\times}$, is a fundamental characteristic of the climate system and at the same time a useful metric for climate models. It serves to compare models of different categories or of successive generations. Over the last three decades $\Delta T_{2\times}$ was estimated at 1.5 to 4.5°C, without any information about a possible distribution within this range. In (IPCC, 2013), more quantitative statements about the climate sensitivity could be made:

- likely range ($> 66\%$): 1.5 to 4.5°C;
- extremely unlikely ($< 5\%$): smaller than 1°C;
- very unlikely ($< 10\%$): greater than 6°C.

The latest IPCC report (IPCC, 2021) had available more information from models, theoretical understanding and observations so that these ranges could be tightened and a best estimate could be given:

- very likely range ($> 90\%$): 2 to 5°C;
- best estimate: 3°C;
- likely ($> 66\%$): 2.5 to 4 6°C.

The basis for this assessment is the detailed review by Sherwood et al. (2020). The *equilibrium climate sensitivity* is evaluated when the climate model has established a new equilibrium under an altered radiation balance. In computationally expensive coupled climate models, it usually has to be determined by a temporal extrapolation.

The temperature increase with a doubling of the atmospheric CO_2 concentration is the result of complex processes and interactions in the atmosphere that affect the radiation balance. The contributions of the single processes as a response to the disturbance of the radiation balance (e.g., by an increase in greenhouse gas concentrations or a volcanic eruption) can be quantified by the strength of the feedback. Therefore, the term *feedback parameter*, given as λ ($\mathrm{W\,m^{-2}\,K^{-1}}$), is introduced. It quantifies the change in the radiation balance per change of the global mean temperature. The estimation of λ for various processes is a central task of climate research.

The concept of *feedback parameters* can be illustrated using the linearised EBM. We write the energy balance as

$$h\ \rho\ c\ \frac{\partial T}{\partial t} = A(T) + B(T) + C(T) + \Delta Q\ , \tag{2.24}$$

where h, ρ, and c are the height of the atmosphere, ρ air density and c the heat capacity of air (values given after eq. 2.1), A, B, and C describe energy fluxes in Wm^{-2} caused by climate system processes that change the Earth's energy balance. Specifically, A is the short-wave radiation (which may be temperature-dependent via albedo), B is the long-wave back-radiation, C is an additional term of the radiation balance (e.g., water vapour, effects of clouds, greenhouse gases, such as H_2O, CO_2, ..., and aerosols) and ΔQ is a disturbance (often called *forcing*) of the balance which causes a change in temperatures.

Assuming now that we can express the Earth's globally averaged temperature $T(t)$ as the sum of an equilibrium temperature $\overline{T}$, and a time-dependent perturbation temperature $\tilde{T}(t)$, namely

$$T(t) = \overline{T} + \tilde{T}(t) \tag{2.25}$$

with $\tilde{T} \ll \overline{T}$, we obtain upon linearizing 2.24, and rearranging of the terms

$$h\ \rho\ c\ \frac{\partial \tilde{T}}{\partial t} = \left(\frac{\partial A}{\partial T} + \frac{\partial B}{\partial T} + \frac{\partial C}{\partial T}\right) \cdot \tilde{T} + \Delta Q\ , \tag{2.26}$$

where we used the fact that at the equilibrium temperature $\overline{T}$ we have energy balance: $A(\overline{T}) + B(\overline{T}) + C(\overline{T}) = 0$.

We now define a *feedback parameter* for each of the Earth System processes as

$$\lambda_A = \frac{\partial A}{\partial T},\ \ \lambda_B = \frac{\partial B}{\partial T},\ \ \lambda_C = \frac{\partial C}{\partial T}\ , \tag{2.27}$$

and a total feedback parameter λ according to

$$\lambda = \lambda_A + \lambda_B + \lambda_C\ . \tag{2.28}$$

With this, the perturbed energy balance equation can be written compactly as

$$h\ \rho\ c\ \frac{\partial \tilde{T}}{\partial t} = \lambda\ \tilde{T} + \Delta Q\ . \tag{2.29}$$

The general solution is given by

$$\tilde{T}(t) = \tilde{T}(0) \cdot \mathrm{e}^{\lambda/(h\rho c)\cdot t} - \frac{1}{\lambda}\ \Delta Q\ , \tag{2.30}$$

and therefore

$$T(t) = \overline{T} + \tilde{T}(0) \cdot \mathrm{e}^{\lambda/(h\rho c)\cdot t} - \frac{1}{\lambda}\ \Delta Q\ . \tag{2.31}$$

Equation (2.31) highlights the two key roles that the feedback parameter λ plays in characterizing both the transient and equilibrium response of the climate system to perturbations. First, the time scale on which an initial perturbation $\tilde{T}(0)$ decays or grows is proportional to λ^{-1}. Second, λ determines the equilibrium response of the

effect of a permanent radiative forcing ΔQ on the global mean temperature. The sign of the feedback parameter λ indicates the stability of the climate system: For $\lambda > 0$ an initial temperature perturbation $\tilde{T}(0)$ grows exponentially, i.e., the climate system is **unstable**. Climate stability therefore requires $\lambda < 0$.

Alternatively, a useful parameter for the quantification of the climate system response to a perturbation is the *sensitivity parameter* defined as

$$s = -\frac{1}{\lambda}$$

in units $\mathrm{K}/(\mathrm{W\,m^{-2}})$. The smaller λ, the larger is the temperature change due to a perturbation ΔQ. The total feedback is the sum of the single feedbacks; the total sensitivity is equal to the inverse of the sum of the inverse sensitivities:

$$\lambda = \lambda_A + \lambda_B + \lambda_C \;, \qquad \frac{1}{s} = \frac{1}{s_A} + \frac{1}{s_B} + \frac{1}{s_C} \;. \tag{2.32}$$

In the following this framework will be applied to the „two-layer“-EBM presented in eqs. (2.3). The radiation budget for the surface temperature is given by

$$0 = A(T) + B(T) + C(T) = \frac{1-\alpha}{4}\, S_0 - \varepsilon\,\sigma\, T^4 + \frac{c}{2}\,\varepsilon\,\sigma\, T^4 \;,$$

where C describes the effects of high clouds. Cirrus clouds make a positive contribution to the radiation balance, hence a warming.

The derivatives of the individual radiation terms yield the individual *feedback parameters*:

$$\left.\begin{aligned} \lambda_A &= -\frac{S_0}{4}\,\frac{\mathrm{d}\alpha}{\mathrm{d}T} \\ \lambda_B &= -4\,\varepsilon\,\sigma\, T^3 \\ \lambda_C &= 2\,c\,\varepsilon\,\sigma\, T^3 + \frac{1}{2}\,\varepsilon\,\sigma\, T^4\,\frac{\mathrm{d}c}{\mathrm{d}T} + \frac{c}{2}\,\sigma\, T^4\,\frac{\mathrm{d}\varepsilon}{\mathrm{d}T} \end{aligned}\right\} \tag{2.33}$$

Eqs. 2.33 illustrate how different feedback processes operate in concert. Temperature-dependent changes in albedo and longwave radiation back to space are fundamental climate system processes. The response of „clouds“ in our simplified framework already indicates new complexities: Apart from the longwave contribution, there are two more terms that quantify how temperature changes affect the fractional cloud cover and the radiation properties of the clouds via emissivity which is influenced by the cloud structure and the size of the ice crystals.

Assuming that the albedo is not temperature-dependent, and the effect of high clouds is irrelevant, and no additional forcing exists, we obtain:

$$\begin{aligned} \lambda = \lambda_B &= -4 \cdot 0.6206 \cdot 5.67 \cdot 10^{-8} \cdot (287.15)^3\,\mathrm{W\,m^{-2}\,K^{-1}} \\ &= -3.3\,\mathrm{W\,m^{-2}\,K^{-1}} \;. \end{aligned} \tag{2.34}$$

This is the feedback parameter of long-wave radiation without other feedbacks, in particular without the water vapour. This is referred to as the *Planck feedback*, also denoted λ_{P}. The feedback is negative, implying that an increase in temperature

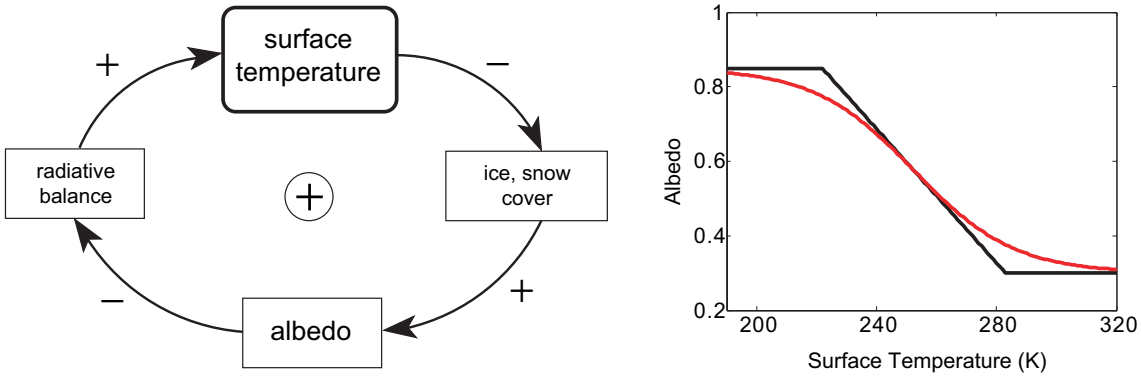

Figure 2.12: Ice-albedo feedback (**left**) and two plausible parameterisations for an EBM (**right**). The signs next to the arrows denote the correlation between changes in the quantities in the boxes at the beginning and at the end of the arrow. The resulting correlation is given in the centre of the *feedback loop*. A self-enhancing process has a positive sign and can therefore lead to instabilities in the climate system. A negative sign corresponds to a damped process. For the parameterisation shown in the graph at the right, it is assumed that for low temperatures a complete snow-/ice cover exists and the albedo is $\alpha \approx 0.85$. For high temperatures a planetary albedo of 0.3 is assumed.

leads to an increased long-wave irradiance and hence to a cooling. λ_P is a key **stabilizing feedback** in the climate system. Latest estimates from the CMIP5 climate models yield $\lambda_P = -(3.2 \pm 0.1)\ \mathrm{W\,m^{-2}\,K^{-1}}$ (IPCC, 2013, Tab. 9.5).

Especially the strong temperature dependence of the water vapour content in the atmosphere (via the Clausius-Clapeyron equation)—the most important greenhouse gas—as well as the temperature-dependent change in albedo and cloud cover, strongly affect the overall feedback. We would like to assess this with the snow-ice-albedo feedback, the water vapour- and the cloud feedback. In addition, we also consider the various soil moisture feedbacks which are very important on the regional scale but have a minor effect globally.

2.4.1 Snow-ice-albedo feedback

A globally and locally important feedback mechanism arises from the temporal and spatial change in the extent of the snow- and ice cover with changing temperatures. If the extent of the snow and ice cover is large—this is generally the case at low temperatures—more solar radiation is reflected. Snow and ice have a high reflectivity, i.e., albedo ($\alpha \approx 0.85$). This implies a positive feedback, as one can see in Fig. 2.12 (left). Under a global warming scenario the extent of the snow and ice cover is expected to shrink; also, the seasonal snow and ice cover begins later and ends earlier. This leads to a shortening of the seasonal cover and hence to a positive contribution to the seasonal radiation balance.

This temperature-dependence of the albedo shall now be parametrised. This problem was studied by Sellers in 1969 (Sellers, 1969), who based it on the parameterisation given in Fig. 2.12 (right). It is obvious that in a global point model the evolution of the snow and ice cover cannot be simulated. For this reason, *plausible* assumptions are made, which may be based on the correlation of snow cover and regional temperatures. Sellers proposed:

$$\alpha(T) = 0.3 - 0.009\,(T - 283\ \mathrm{K})\,/\mathrm{K}\ , \qquad 222\ \mathrm{K} \leq T \leq 283\ \mathrm{K}\ , \tag{2.35}$$

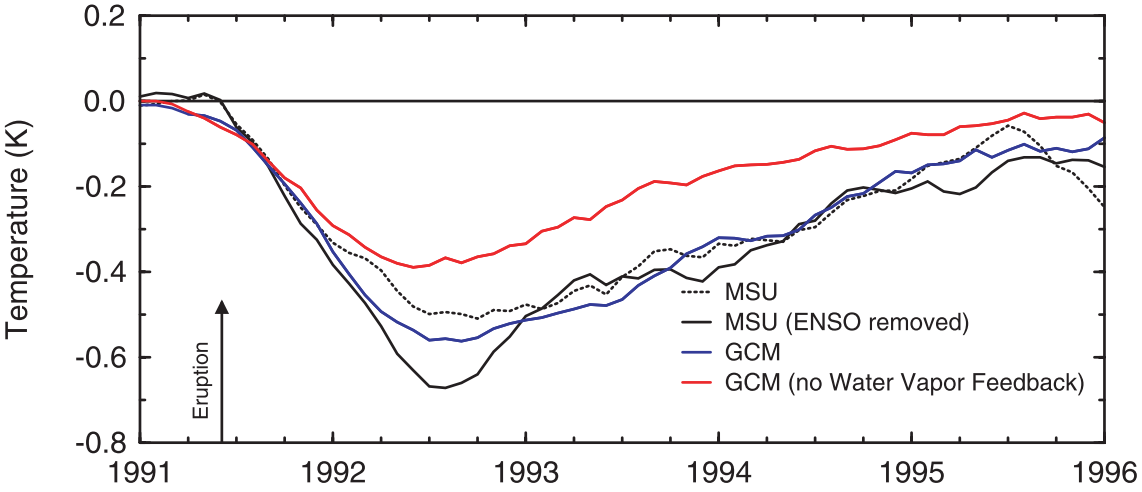

Figure 2.13: Global mean temperature anomaly in the mid-troposphere after the eruption of Mount Pinatubo in 1991. A global cooling of 0.7°C was observed with remotely sensed radiation measurements (microwave sounding unit, MSU) after a warming effect of the 1992/93 ENSO was subtracted. A climate model in which the water vapour feedback was turned off shows a smaller cooling inconsistent with the observations. Figure from Soden et al. (2002).

with constant values beyond the upper and lower bounds of the temperature range. A mathematically differentiable function may be preferable (Fig. 2.12, right; see also eq. 9.6).

From (2.35) we derive

$$\lambda_A = -\frac{S_0}{4}\frac{\mathrm{d}\alpha}{\mathrm{d}T} = \frac{1361 \cdot 0.009}{4}\ \mathrm{W\,m^{-2}\,K^{-1}} = 3.1\ \mathrm{W\,m^{-2}\,K^{-1}}\ , \tag{2.36}$$

hence, a positive feedback. Therefore, the total feedback is

$$\lambda = \lambda_B + \lambda_A = (-3.3 + 3.1)\ \mathrm{W\,m^{-2}\,K^{-1}} = -0.2\ \mathrm{W\,m^{-2}\,K^{-1}}\ . \tag{2.37}$$

Compared with (2.34) this results in a large reduction of the absolute value of the feedback parameter which causes a strong enhancement of the sensitivity. The derivation of (2.36) is unrealistic because not the whole planet but only polar and snow-covered regions are influenced by the snow-ice-albedo feedback. The planetary albedo feedback is essentially caused by the snow and sea ice cover of the Northern Hemisphere, assuming the albedo of Greenland remains constant. A rough estimate of the surface from 40°N to 90°N, with about 210° longitude covered by land, would give about 10% of the entire Earth's surface. With this scaling we would obtain $\lambda_A = 0.3\ \mathrm{W\,m^{-2}\,K^{-1}}$. Latest estimates based on CMIP5 climate models yield $\lambda_A = (0.3 \pm 0.1)\ \mathrm{W\,m^{-2}\,K^{-1}}$ (IPCC, 2013, Tab. 9.5).

2.4.2 Water vapour feedback

The water vapour feedback is the most important **destabilizing feedback** in the climate system because water vapour is the primary natural greenhouse gas. A warm atmosphere can hold more water vapour than a cold atmosphere. These additional water molecules in the warm atmosphere cause an enhancement of the natural greenhouse effect by increased absorption of long-wave radiation. Latest

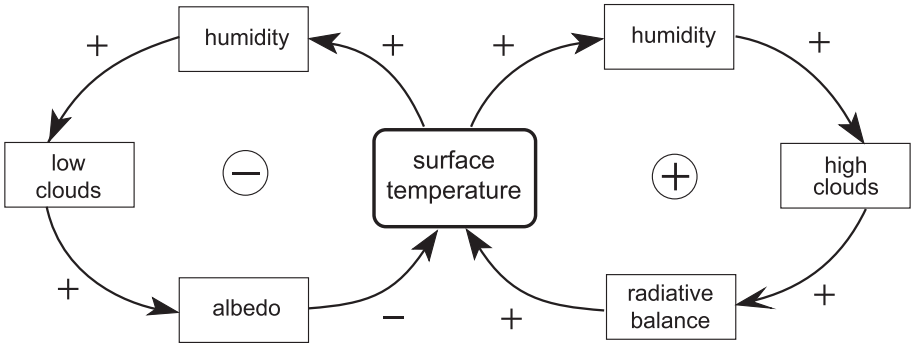

Figure 2.14: Cloud feedback loops. The sign depends on the location and the quality of clouds. Low clouds affect short-wave radiation via albedo as opposed to high clouds affecting long-wave irradiance.

estimates from various climate models yield $\lambda_{\mathrm{WV}} = (1.6 \pm 0.3)\ \mathrm{W\,m^{-2}\,K^{-1}}$ (IPCC, 2013, Tab. 9.5).

With this we find

$$\lambda = \lambda_B + \lambda_{\mathrm{WV}} = (-3.3 + 1.6)\ \mathrm{W\,m^{-2}\,K^{-1}} = -1.7\ \mathrm{W\,m^{-2}\,K^{-1}}\,, \tag{2.38}$$

hence, again a significant reduction of the absolute value of λ which amounts to an increased sensitivity $1/\lambda$ by a factor of about 2 compared to (2.34). ***The presence of water vapour in the atmosphere doubles the climate sensitivity.***

It is difficult to directly observe the water vapour feedback, but various independent approaches have resulted in a much better quantification of this feedback in the last few years. The agreement of the spatial structure of the water vapour distribution, as it was shown in Fig. 2.3, does not yet guarantee that climate models compute the climate sensitivity in a reasonable way.

However, based on observations of the change in temperature after the large volcanic eruption of Pinatubo in 1991, it has been shown that current climate models simulate the water vapour feedback reasonably well. A climate model with water vapour feedback is capable of simulating the global cooling of the mid-troposphere by 0.7°C following the eruption (Fig. 2.13). A model, in which the water vapour content was fixed, shows a significantly smaller cooling. Such a model therefore has a smaller sensitivity as expected from (2.38). Fig. 2.13 also points to the fact that current climate models simulate this effect rather well.

2.4.3 Cloud feedback

Modelling the cloud cover still belongs to one of the greatest challenges in climate modelling and in the assessment of future climate change. A fundamental aspect of the problem is apparent in Fig. 2.14. It illustrates, in a very simplified form, two possible feedback mechanisms: They can be positive or negative because clouds affect both short-wave radiation (via albedo) and long-wave radiation.

A global estimate for the effect of clouds is given in Table 2.3. The averaged effect of the global cloud cover results in a *cooling* which suggests the albedo effect dominates. The estimates in Table 2.3 yields a value for the *forcing* with respect to the change

	Mean	Without clouds	With clouds
Long-wave radiation	−234	−266	+31
Absorbed short-wave radiation	239	288	−48
Net radiation	**+5**	**+22**	**−17**
Albedo	30%	15%	+15%

Table 2.3: Estimate for the change in radiation in $\mathrm{W\,m^{-2}}$ due to the global cloud cover (from Hartmann, 2016).

in cloud cover, under the assumption of a mean cloud cover of 60%, of about

$$\frac{\Delta W}{\Delta \text{clouds}} \approx -\frac{17\ \mathrm{W\,m^{-2}}}{60\%} \approx -0.3\ \mathrm{W\,m^{-2}/\%}\ . \tag{2.39}$$

An increase in cloud cover by about 13% would constitute a forcing of $\Delta W \approx -3.7\ \mathrm{W\,m^{-2}}$. This negative forcing (cooling) would compensate the positive forcing expected from a doubling of the atmospheric CO_2 concentration, see (2.44) below.

To illustrate the concept, consider the two-layer EBM given by (2.3) as a model for a very simplified representation of the effect of clouds and assume—as a first step—that ε and c do not depend on temperature and that $c \approx 0.6$ (Fig. 2.6). Hence, (2.34) becomes

$$\lambda = \lambda_B + \lambda_C = (-3.3 + 1.0)\ \mathrm{W\,m^{-2}\,K^{-1}} = -2.3\ \mathrm{W\,m^{-2}\,K^{-1}} \tag{2.40}$$

which suggests a reduction of the absolute value of λ, corresponding to an increase in the sensitivity ($\approx 50\%$) compared to (2.34).

Of course, the two-layer EBM is not a realistic model to quantify the cloud feedback correctly. To this end, atmosphere models are necessary that resolve the formation of clouds in all their forms. Latest estimates from several climate models yield $\lambda_C = (0.3 \pm 0.7)\ \mathrm{W\,m^{-2}\,K^{-1}}$ (IPCC, 2013, Tab. 9.5); see Fig. 2.17.

Within the last few years model consistency with regard to the cloud feedback has increased considerably. Multiple lines of evidence indicate that the total feedback is *positive*. A warming by 1°C leads to a total additional forcing and height of clouds) of about $0.7\ \mathrm{W\,m^{-2}}$.

2.4.4 Lapse rate feedback

All air masses of the atmosphere emit continuously long-wave radiation to space. The rate of the resulting heat loss of any vertical air column depends on its vertical temperature profile: Air masses at high altitudes lose heat more easily than air masses of the same temperature at low altitudes, just because they are closer to space. The so called *lapse rate feedback* on Earth's surface temperature results from the fact that a warming at Earth's surface modifies the temperature profile in the air column above and thus, in general, also the rate of heat loss of this air column and the temperature of its bottom layer adjacent to the Earth's surface.

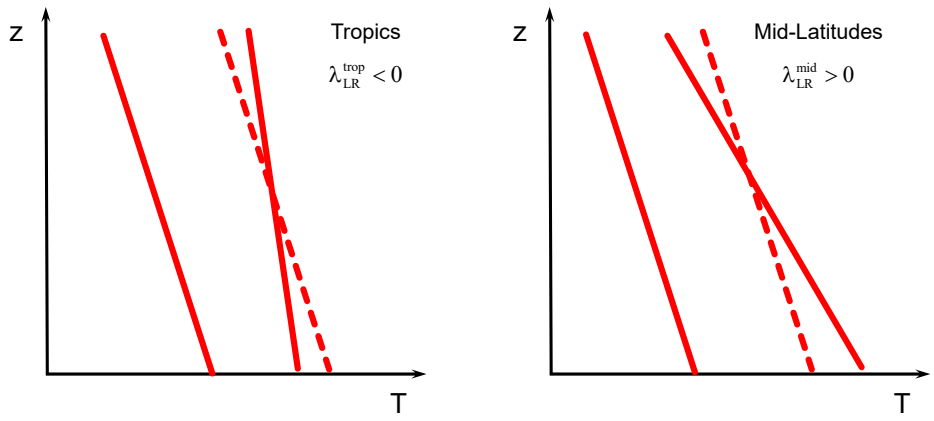

Figure 2.15: Schematic illustration of changes in the vertical temperature structure in the tropics and in the mid-latitudes. Due to increased convection, the lapse rate decreases in the tropics. In the mid-latitudes the horizontal flow limits the warming to the surface and the lower atmosphere which causes the lapse rate to increase. Compared to the mean warming, a reduced warming of the surface occurs in the tropics (therefore a negative feedback), while it is enhanced in the mid-latitudes (positive feedback).

The lapse rate (of the atmospheric air temperature) is defined as the rate of decrease of the atmospheric air temperature T with increase in altitude z, corresponding to the negative differential quotient of the temperature profile $T(z)$,

$$\gamma = -\frac{\mathrm{d}T}{\mathrm{d}z} \,.$$

Well mixed dry and humid air masses of the troposphere have lapse rates of about 10°C/km and 6°C/km, respectively.

The change of the lapse rate due to warming at the surface strongly depends on the location. In the tropics, a warming leads to an increased convective activity: water vapour rises and condensates at high altitudes. This transport of latent heat results in a stronger warming in the high layers of the atmosphere which is supported by the additional greenhouse effect due to the increased concentration of water vapour there. In consequence, the lapse rate decreases (Fig. 2.15, left panel). In the mid-latitudes, where horizontal circulation associated with high- and low-pressure systems dominates, and hence, the vertical movement is less pronounced compared to the tropics, the warming is limited to layers close to the surface. In consequence, the lapse rate increases (Fig. 2.15, right panel).

A decreasing lapse rate (as in the tropics) reflects a warming of the upper troposphere relative to the lower troposphere. This leads to a stronger long-wave radiation to space, causing a stronger cooling and therefore a negative feedback to the warming at the surface. In contrast, an increasing lapse rate (as in the mid-latitudes) reflects a cooling of the upper troposphere relative to the lower troposphere and leads analogously to a positive feedback. For the global average the tropics dominate due to their larger spatial extent. The resulting feedback is therefore negative but with rather large uncertainties. Latest estimates from several climate models yield $\lambda_{\mathrm{LR}} = (-0.6 \pm 0.4)\ \mathrm{W\,m^{-2}\,K^{-1}}$ (IPCC, 2013, Tab. 9.5).

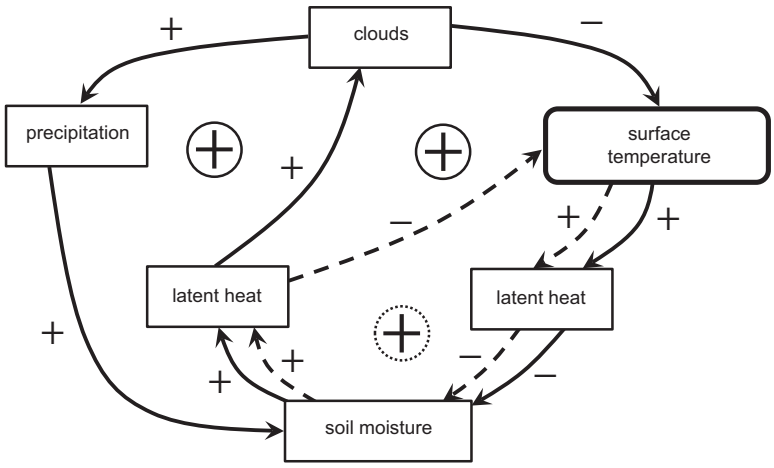

Figure 2.16: Three soil moisture feedback loops are generally positive and amplify local and regional climate perturbations. Figure modified from Vogel et al. (2018).

2.4.5 Soil moisture feedbacks

On a local and regional basis, the soil moisture feedback is very important as its related processes amplify the temperature response to warming (Fig. 2.16). For instance, the 2003 summer heat wave in Europe owes its extraordinary amplitude to the soil moisture feedback which produced very dry conditions in spring and so primed the soil for very efficient heating. While an estimate of the global soil-moisture feedback yields about $\lambda_S = 0.1$ $\mathrm{Wm^{-2}K^{-1}}$, regionally extreme temperatures can be amplified substantially. The temperature of the hottest day in a year, projected by the end of the 21$^{\mathrm{st}}$ century, would be 50% higher than without the soil moisture feedback (Vogel et al., 2017).

2.4.6 Summary and conclusion regarding feedbacks

Figure 2.17 summarizes the various feedbacks discussed above. Different model studies and the inclusion of remote sensing data, as well as direct measurements permit a quantification of the single feedbacks. The strongest positive feedback is the water vapour feedback, which—in spite of the overall negative lapse rate feedback—remains positive in total. Although the cloud feedback is assessed to be *likely* positive in total, it is still associated with the largest uncertainties (IPCC, 2013).

The best estimate for the *Planck-feedback* is $\lambda_{\mathrm{P}} = -3.2\ \mathrm{W\,m^{-2}\,K^{-1}}$ and for all other feedbacks, $\lambda_{\mathrm{all}} = +1.6\ \mathrm{W\,m^{-2}\,K^{-1}}$ (see Fig. 2.17, and IPCC, 2013, Tab. 9.5). Therefore, the total feedback becomes:

$$\lambda = \lambda_{\mathrm{P}} + \lambda_{\mathrm{all}} = (-3.2 + 1.6)\ \mathrm{W\,m^{-2}\,K^{-1}} = -1.6\ \mathrm{W\,m^{-2}\,K^{-1}}\ . \tag{2.41}$$

With this, the equilibrium climate sensitivity ECS, $\Delta T_{2\times}$, can be estimated. ECS is a key climate system metric to estimate the global mean temperature change at equilibrium for a doubling of the CO_2 concentration in the atmosphere. The increase of the greenhouse gas concentration constitutes a *radiative forcing*, expressed as ΔQ,

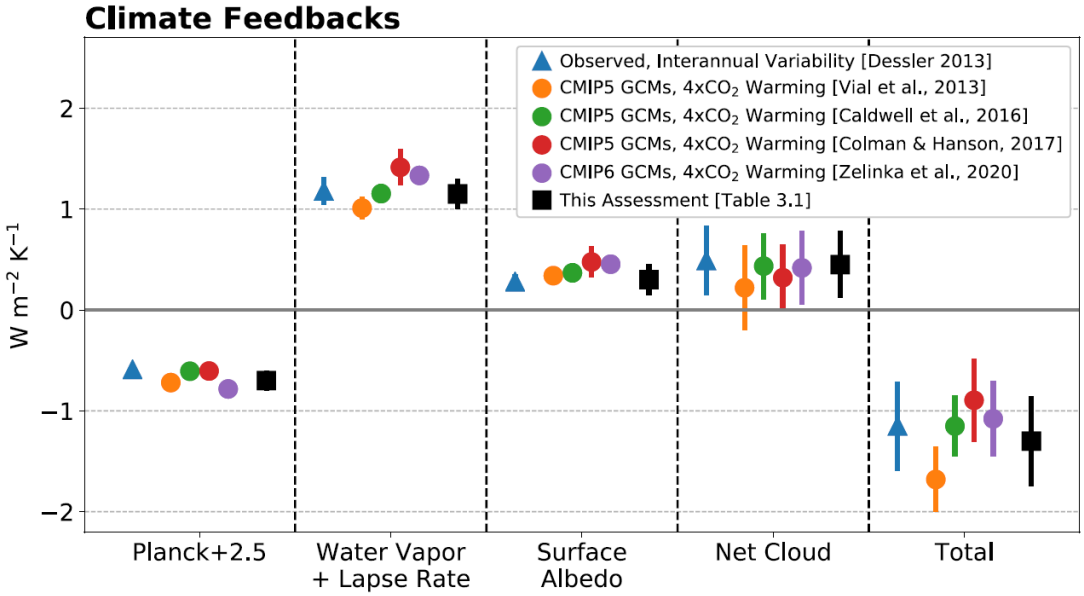

Figure 2.17: Overview of the most important global-scalev feedbacks in the atmosphere from observations and various model simulations. Note that the Planck feedback parameter is shifted by 2.5 $\mathrm{Wm^{-2}K^{-1}}$. Results from the present model generation (CMIP6) can be compared to the previous generation (CMIP5). The feedback of the three processes (water vapour+lapse rate, surface albedo, clouds) is overall positive. The total feedback remains, owing to the strongly negative Planck feedback, negative, indicating an overall stable climate system. Figure from Sherwood et al. (2020).

specifically for a doubling of the atmospheric CO_2 concentration $\Delta Q_{2\times}$. We use (2.31), define $\Delta T_{2\times} = T(\infty) - \overline{T}$, and obtain

$$\Delta T_{2\times} = -\frac{1}{\lambda}\,\Delta Q_{2\times}\ . \tag{2.42}$$

The radiative forcing associated with changes in the atmospheric concentration of CO_2 is given by Myhre et al. (1998):

$$\Delta Q(\mathrm{CO_2}) = 5.35\ \mathrm{W\,m^{-2}}\ \ln\frac{[\mathrm{CO_2}]}{280\ \mathrm{ppm}}\ , \tag{2.43}$$

hence

$$\Delta Q_{2\times} = 5.35\ \mathrm{W\,m^{-2}}\ \ln\frac{560\ \mathrm{ppm}}{280\ \mathrm{ppm}} = 3.7\ \mathrm{W\,m^{-2}}\ . \tag{2.44}$$

From (2.42) it follows, that

$$\Delta T_{2\times} = -\frac{1}{\lambda}\,\Delta Q_{2\times} = 2.3\ \mathrm{K}\ . \tag{2.45}$$

This is consistent with the *likely* range of 1.5°C to 4.5°C, as given in the latest IPCC assessment (IPCC, 2013).

The combined effect of different feedbacks can be illustrated by a latitudinal and altitudinal cross-section of the warming of the atmosphere with an increase in CO_2 concentrations. Figure 2.18 shows the zonal mean temperature change in the years

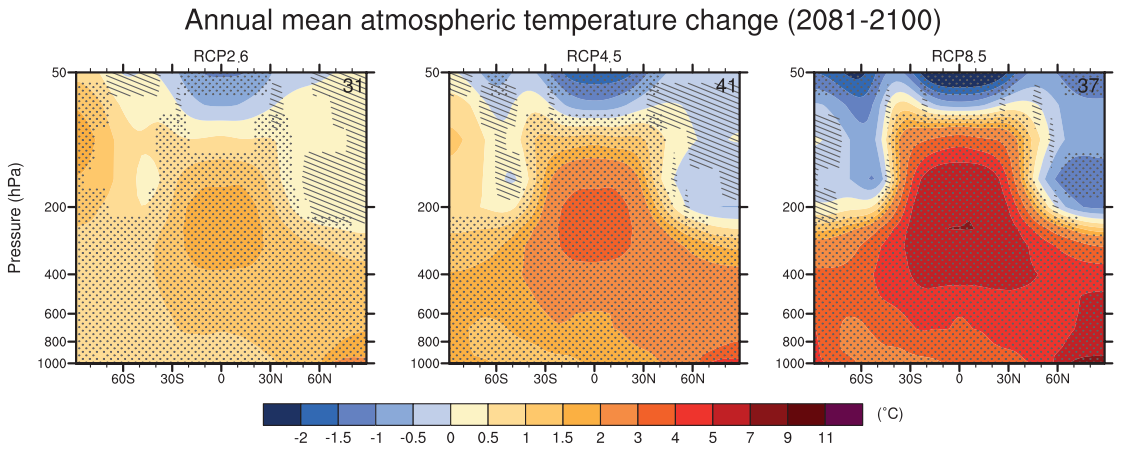

Figure 2.18: Projected changes (1986–2005 to 2081–2100) in annual mean zonal mean atmospheric temperature for three emission scenarios. Multi-model means are calculated from the available CMIP5 ensembles. The number of CMIP5 models used is indicated in the upper right corner. *Hatching* indicates regions where the multi-model mean change is less than one standard deviation of internal variability. *Stippling* indicates regions where the multi-model mean change is greater than two standard deviations of internal variability and where at least 90% of the models agree on the sign of change. The warming is stronger at high latitudes of the northern hemisphere towards the surface. This increase is caused by the *ice-albedo feedback*, which is mainly effective in the northern hemisphere, where the seasonal snow cover undergoes fast changes. Cooling is simulated in the stratosphere as is expected from the effect of increasing greenhouse gas concentrations. Figure modified from IPCC (2013), Fig. 12.12.

2080–2099 in a multi-model ensemble for three emission scenarios (strong reduction in emission RCP2.6, stabilisation RCP4.5, and business-as-usual RCP8.5). The warming is stronger at high latitudes of the northern hemisphere towards the surface. This increase is caused by the *ice-albedo feedback*, which is mainly effective in the northern hemisphere, where the seasonal snow cover undergoes fast changes.

A clear enhancement of the warming also occurs in latitudes between 30°S and 30°N at an altitude between 7 and 12 km. This is due to the lapse rate feedback. The strong convection there transports water vapour (the most important greenhouse gas) as well as condensation heat to the upper troposphere.

An important *fingerprint* of global warming is expected to take place in the stratosphere, where a cooling will occur at all latitudes. This cooling is actually observed (IPCC, 2013, Fig. 2.24 and 2.26). It is due to the rise of the irradiance altitude for long-wave radiation with an increase in CO_2 concentrations. At these higher altitudes, the temperatures are lower (in equilibrium at $T \approx 255$ K, hence at 5.1 km). This causes a disequilibrium, which the warming of the whole atmosphere compensates for. This warming leads to a rise of the irradiance altitude (level of equivalent black body radiation). Hence, a bigger part of the atmosphere now lies underneath the irradiance altitude, meaning that the optical path up to the radiation altitude has increased. Underneath this altitude a larger part of the long-wave irradiance is absorbed and the stratosphere experiences a corresponding deficit, which leads to a cooling. This was already predicted by Manabe and Wetherald (1967) using a one-dimensional radiative-convective model (Fig. 1.11).

Thanks to a significantly improved knowledge of the individual feedback mechanisms in the atmosphere, the equilibrium climate sensitivity $\Delta T_{2\times}$ is now better quantified. Climate models of different categories of the hierarchy (Table 2.1) are used to

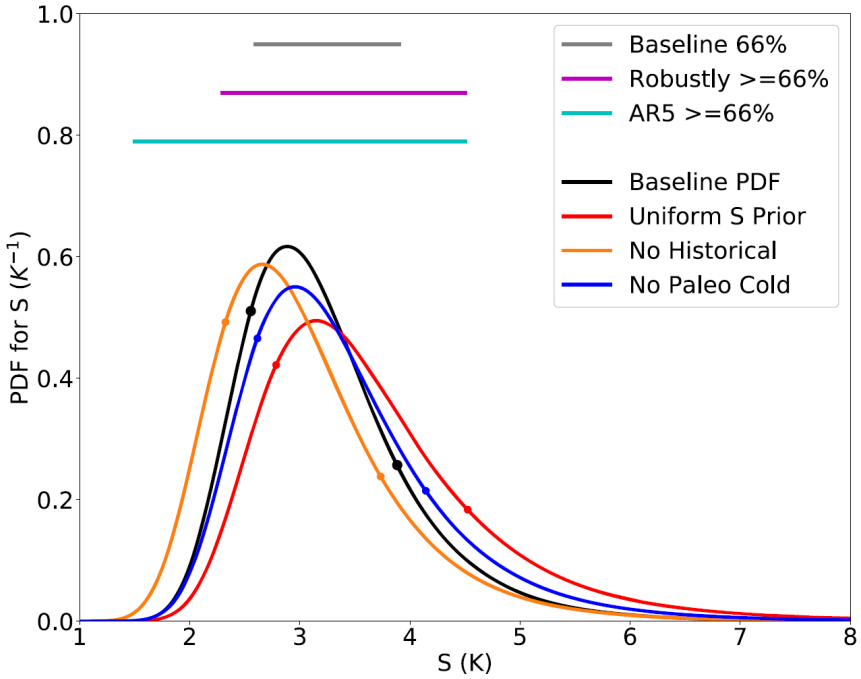

Figure 2.19: Probability density functions for equilibrium climate sensitivity (ECS, here denoted as S). Different assumptions regarding priors yield slightly different distributions. Ranges for AR5, and the most recent ranges adopted by AR6 are shown as horizontal lines. Dots indicate the 17th and 83rd precentile values. Including the historical information leads to higher ECS values. From Sherwood et al. (2020).

simulate the temperature change over the last 150 to 1000 years. The agreement of the model simulations with observations and paleo-reconstructions is computed which provides constraints for the range of various tuning parameters in the models, or eliminates certain simulations.

In summary, this yields estimates of the probability distribution of the equilibrium climate sensitivity based on various independent lines of evidence (Fig. 2.19).

Note that in order to estimate temperature increases in the near-term (e.g., by 2050 or the end of the 21st century), a more suitable metric is the Transient Climate Response (TCR). TCR is defined as the change in global mean temperature at the time when the atmospheric CO_2 concentration has doubled in a scenario of concentration increasing at 1% per year. The TCR is *likely* in the range of 1.0°C to 2.5°C with *high confidence* and *extremely unlikely* greater than 3°C.

3 Describing transports of energy and matter

In nature the transport of energy and matter in fluids is determined by diffusion and advection. These processes induce fluxes of energy and matter, of which the mathematical description is derived by continuum mechanics. Diffusion is a random process taking place at all times and leading to a net transport only under certain conditions. Advection is caused by an ambient flow which transports energy and matter.

All processes in the climate system are fundamentally influenced by the advective and diffusive transport of mass, energy, momentum in a rotating environment. For example, the temperatures at a particular latitude are determined by the balance of heat at that location which consists of the local radiation fluxes and the horizontal and vertical transports of heat in the atmosphere, including the transport of moisture. Another example concerns the transport of salt in the ocean through advective and diffusive processes. These change the density and are thus exerting a strong influence on the large-scale circulation in the ocean. Hence, the mathematical description of these transport processes in models is fundamental to climate science.

3.1 Diffusion

Diffusive processes are caused by the thermal motion of molecules (Brownian motion)and can be described only in a statistical way. It is instructive to consider first the one-dimensional case and divide the x-axis into cells of width Δx and cross-section area A in which molecules reside (Fig. 3.1). Due to a positive thermodynamic temperature $T > 0$ the molecules are in thermal motion. The particle density (particles per volume) at coordinate x is denoted by $n(x)$. We describe the random motion by a probability p that a particle jumps from one cell to the neighboring cell. We further assume, that diffusion is an isotropic process (this is not always the case in nature). Therefore, the probability p is uniform and independent of the direction of the particle movement.

We determine the particle flux density at the cell boundary $i/i+1$ for a time interval Δt. From cell i, a number of $p\, n(x_i)\, A\, \Delta x$ particles jump to the right, while from cell

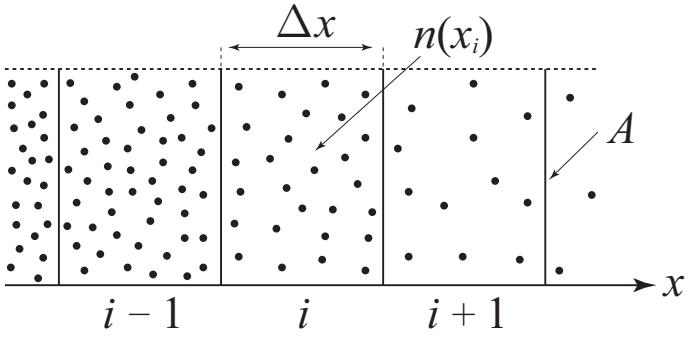

Figure 3.1: Model of one-dimensional diffusion. The particle density in cell i is given by $n(x_i)$.

$i+1$ a number $p\,n(x_i+\Delta x)\,A\,\Delta x$ jump to the left. Hence, the net diffusive particle flux density (number of particles per area A and time Δt) at the cell boundary $i/i+1$ is given by

$$F = \frac{p\,n(x_i)\,A\,\Delta x - p\,n(x_i+\Delta x)\,A\,\Delta x}{A\,\Delta t} = -\frac{p\,\Delta x^2}{\Delta t}\,\frac{n(x_i+\Delta x)-n(x_i)}{\Delta x}\;.$$

In the limit of $\Delta x \to 0$ and $\Delta t \to 0$, provided $\Delta x^2/\Delta t$ = constant, we get *Fick's first law* of one-dimensional diffusion

$$F = -\left(\frac{p\,\Delta x^2}{\Delta t}\right)\frac{\partial n}{\partial x} = -D\,\frac{\partial n}{\partial x}\;. \tag{3.1}$$

The quantity D is the *diffusion constant*, also referred to as *diffusion coefficient* or *diffusivity*, with the unit $\mathrm{m^2\,s^{-1}}$; it depends on the physical properties of both the diffusing particles and the medium containing these particles (the medium can be vacuum, a gas, a liquid or a solid). This derivation shows that the diffusion constant parametrises processes that evolve on a molecular scale.

From (3.1) it follows that net diffusive fluxes only occur when concentration gradients, in the case of (3.1) particle density gradients, are present. Due to the random motion, gross-fluxes of particles always exist.

The generalization of (3.1) to a three-dimensional isotropic space and a concentration $C = C(x,y,z)$ of an arbitrary physical quantity (e.g., particles, mass, energy, salt, momentum, tracer, etc.) yields Fick's first law of three-dimensional diffusion

$$\vec{F} = -D\,\vec{\nabla}C\;. \tag{3.2}$$

$\vec{\nabla}$ is the gradient operator and D an isotropic diffusion constant (scalar). The gradient operator is given by

$$\vec{\nabla} = \left(\frac{\partial}{\partial x},\,\frac{\partial}{\partial y},\,\frac{\partial}{\partial z}\right)$$

and converts any scalar $\Phi(x,y,z)$, for example the concentration $C = C(x,y,z)$ from (3.2), into the gradient of $\Phi(x,y,z)$, the vector

$$\begin{aligned}\vec{\nabla}\Phi(x,y,z) &= \left(\frac{\partial}{\partial x},\,\frac{\partial}{\partial y},\,\frac{\partial}{\partial z}\right)\Phi(x,y,z)\\ &= \left(\frac{\partial\Phi(x,y,z)}{\partial x},\,\frac{\partial\Phi(x,y,z)}{\partial y},\,\frac{\partial\Phi(x,y,z)}{\partial z}\right)\;,\end{aligned}$$

which points in the direction of the highest increase of $\Phi(x,y,z)$. The negative sign in (3.2) ensures, that the diffusive flux density $\vec{F}$ is in the opposite direction of the gradient, namely in the direction of the highest decrease of C. The diffusive flux densities in Table 3.1 serve as examples.

transported quantity	formulation
mass	$\vec{F} = -D\,\vec{\nabla}\rho$
heat	$\vec{F} = -D\,\rho\,c\,\vec{\nabla}T = -\lambda\,\vec{\nabla}T$
salt	$\vec{F} = -D\,\vec{\nabla}\,\rho_\mathrm{s}$
y-momentum	$\vec{F} = -D\,\vec{\nabla}\,(\rho\,u_y)$

Table 3.1: Examples of diffusive flux densities, ρ denotes a mass density and ρ_s the particle or the mass density of salt.

3.2 Advection

For the derivation of a formulation of advective flux densities of physical quantities in the climate system, we again consider the one-dimensional case which is illustrated in Fig. 3.2. We assume a flow $u(x,t)$ which transports the quantity to be considered. The fluid (gas, air, water) moves across a fixed control area A. The transported physical quantity (e.g., particles, mass, energy, salt, momentum, tracer, etc.) is given as a concentration $C(x,t)$, hence, the quantity is referred to a volume. In a short time interval Δt a volume $A\,\Delta x$ of length $\Delta x = u\,\Delta t$ passes through a cross section of area A and transports the quantity $A\,\Delta x\,C$ through here. The advective flux density is given by

$$F = \frac{A\,\Delta x\,C}{A\,\Delta t} = \frac{\Delta x}{\Delta t}\,C = u\,C\ .$$

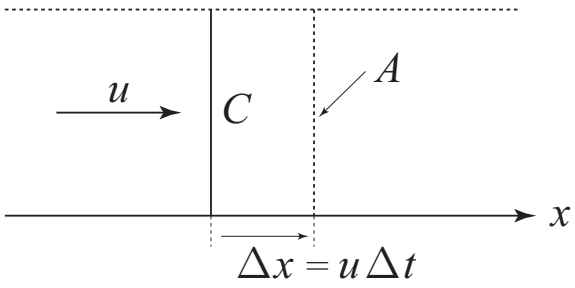

Figure 3.2: Flow along the x-axis.

In three dimensions, the advective flux density of a scalar quantity C in a three-dimensional flow $\vec{u}(\vec{x},t)$ is

$$\vec{F} = \vec{u}\,C\ . \tag{3.3}$$

The advective flux density is a vector aligned parallel to the flow. The advective flux densities in Table 3.2 serve as examples.

transported quantity	formulation
mass	$\vec{F} = \vec{u}\,\rho$
heat	$\vec{F} = \vec{u}\,\rho\,c\,T$
salt	$\vec{F} = \vec{u}\,\rho_\mathrm{s}$
y-momentum	$\vec{F} = \vec{u}\,\rho\,u_y$

Table 3.2: Examples of advective flux densities, ρ denotes a mass density and ρ_s the particle or the mass density of salt.

3.3 Advection-diffusion equation and continuity equation

In the following discussion we will describe the connection between fluxes of physical quantities and time rates of changes of these quantities. It is established by formulating balance statements for those physical quantities which satisfy conservation laws. An example was presented in Section 2.2, where we have discussed a point model of the radiation balance.

We will set up a conservation equation for a physical quantity (e.g., particles, mass, energy, salt, momentum, tracer, etc.) with density C and start with one single dimension x (Fig. 3.3).

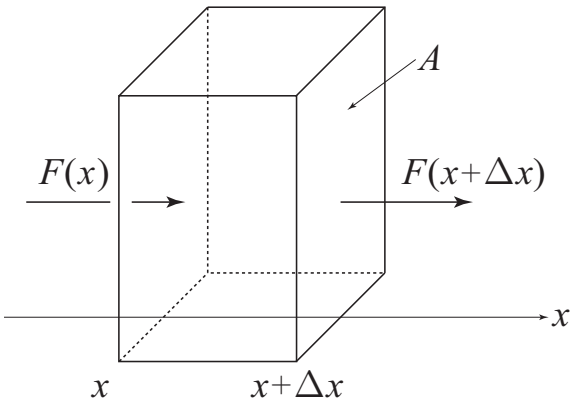

Figure 3.3: Spatially dependent flux in one dimension.

We consider a small fixed control volume $\Delta V = A\,\Delta x$. The (mean) density C inside the control volume changes in time due to fluxes into the control volume (taken positive), fluxes out of the control volume (taken negative), and sources and sinks operating inside the control volume. Thus, we have

$$\frac{\partial}{\partial t}(C\,\Delta V) = F(x)\,A - F(x+\Delta x)\,A + P\,\Delta V\ , \tag{3.4}$$

where F is the flux density (advective + diffusive) of quantity C and P is the *net source density* (sources minus sinks per unit volume) of this quantity. Inserting (3.2) and (3.3) into (3.4) and division by ΔV yields

$$\frac{\partial C}{\partial t} = -\frac{u(x+\Delta x)\,C(x+\Delta x) - u(x)\,C(x)}{\Delta x} + \frac{D\,\frac{\partial C}{\partial x}\Big|_{x+\Delta x} - D\,\frac{\partial C}{\partial x}\Big|_{x}}{\Delta x} + P$$

and taking the limit $\Delta x \to 0$, we obtain

$$\frac{\partial C}{\partial t} = -\frac{\partial\,(u\,C)}{\partial x} + \frac{\partial}{\partial\,x}\left(D\,\frac{\partial C}{\partial x}\right) + P\ . \tag{3.5}$$

Generalizing to three dimensions leads to the *advection-diffusion equation*:

$$\frac{\partial C}{\partial t} = -\vec{\nabla}\cdot(\vec{u}\,C) + \vec{\nabla}\cdot\left(D\,\vec{\nabla}C\right) + P\ , \tag{3.6}$$

where $\vec{\nabla}\cdot$ is the divergence operator. It acts on vectors and yields the "scalar prod-

uct" of $\vec{\nabla}$ and the vector:

$$\vec{\nabla} \cdot \vec{u} = \left(\frac{\partial}{\partial x}, \frac{\partial}{\partial y}, \frac{\partial}{\partial z} \right) \cdot \begin{pmatrix} u_x \\ u_y \\ u_z \end{pmatrix} = \frac{\partial u_x}{\partial x} + \frac{\partial u_y}{\partial y} + \frac{\partial u_z}{\partial z} \ .$$

When C is the mass density ρ and diffusion as well as sources or sinks vanish, then a special case arises from (3.6):

$$\frac{\partial \rho}{\partial t} = -\vec{\nabla} \cdot (\vec{u}\,\rho) \ . \tag{3.7}$$

This is the *mass balance equation*, namely the general form of the continuity equation. Physically, (3.7) describes the conservation of mass: the total mass is conserved, mass is neither produced nor destroyed ($P = 0$), local mass density changes are always due to divergences of the mass flux (apart from molecular fluctuations due to diffusion). The equations (3.6) and (3.7) are balances representing the basis for the mathematical description of processes in the climate system. Their solution is the task of climate modelling.

For an incompressible fluid (e.g., ocean water in a thin interior layer) the density is constant, and (3.7) simplifies to the continuity equation for incompressible fluids:

$$\vec{\nabla} \cdot \vec{u} = 0 \ . \tag{3.8}$$

3.4 Describing small- and large-scale motions

The motions of air in the atmosphere and of water in the oceans occurs on a wide range of space and time scales 1.1. They are described using methods of geophysical fluid dynamics. The way this is achieved strongly depends on the spatial scale and the time scale of the motion that needs to be resolved. A useful concept is the statistical description of fluid flow.

Figure 3.4 a) shows an illustrative time series of wind velocity measurements, which could have been taken at a fixed position in the free atmosphere during a time of, for example, a few minutes, or a few days, or a few weeks. It illustrates the well-known consequences of the complexity just mentioned, namely a typically slowly varying mean air velocity (denoted by the thick line in this Figure) and a mostly rapidly varying deviation from the mean of the instantaneous air velocity. The cause for such a local time dependence of the air velocity are specific movements of numerous *eddies* of various sizes. These eddies are parts of the large air stream moving with the mean air velocity, mostly parts of larger eddies themselves, and move through the air surrounding them, after being generated by irregular disturbances. In so doing they cause collectively so called *eddy fluctuations* of the air velocity at a point, i.e. local time varying deviations from the mean of the air velocity, and furthermore—as they transport advectively measurable air properties (e.g., water, CO_2, ...)—eddy fluctuations of the physical quantities C of these properties (Fig. 3.4 b). Climate research is mainly interested in processes on large spatial scales (global or continental) and long time scales (several days or longer). So the question arises whether the small and fast movements of the eddies within the large air stream

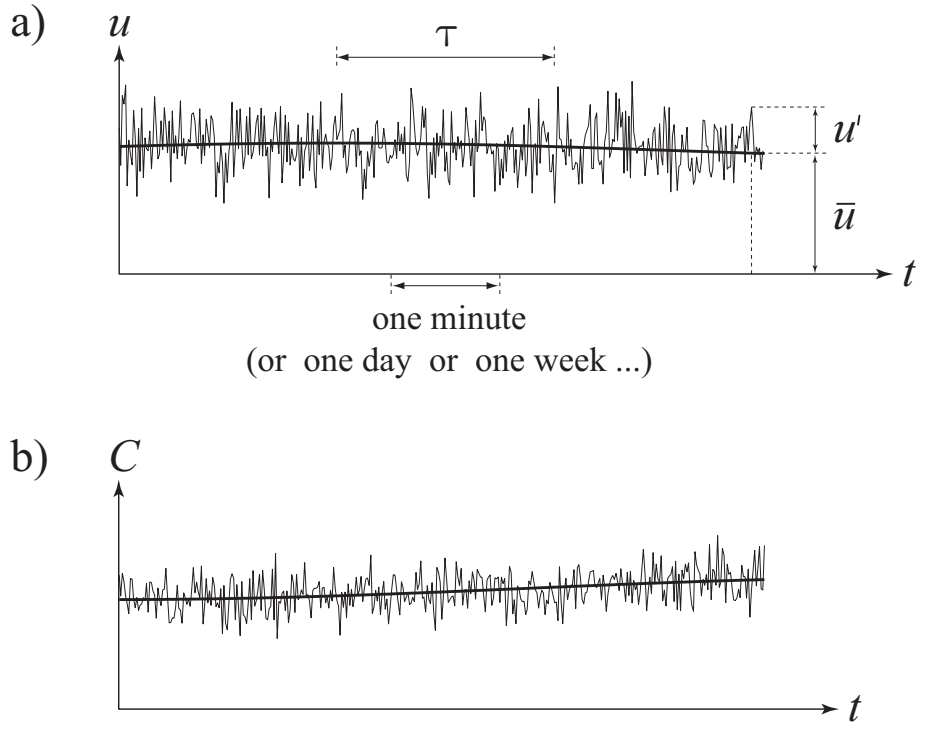

Figure 3.4: Illustration of eddy fluctuations of **a)** air velocity u and **b)** another physical quantity C, for example particle density or humidity. *Bold lines* designate mean values ($\overline{u}$ and $\overline{C}$), τ is the averaging time. Fluctuations around the mean are denoted by primes, e.g. u'

.

have any relevance for the long-term trend of the physical quantity C satisfying the advection-diffusion equation (3.5). In the following we show that they do have an influence and cannot be neglected in general.

Consider the one-dimensional advection-diffusion equation (3.5) and separate the air velocity u, the physical quantity C and the source P in a temporal mean taken over successive time intervals $\tau = t_2 - t_1$ (which should be significantly shorter than the characteristic time scale of the processes to be considered) and an instantaneous deviation from this temporal mean, respectively,

$$u = \overline{u} + u' \,, \qquad \overline{u} = \frac{1}{\tau} \int_{t_1}^{t_2} u(t)\,\mathrm{d}t \qquad\qquad (\tau = t_2 - t_1)$$

$$C = \overline{C} + C' \,, \qquad \overline{C} = \frac{1}{\tau} \int_{t_1}^{t_2} C(t)\,\mathrm{d}t$$

$$P = \overline{P} + P' \,, \qquad \overline{P} = \frac{1}{\tau} \int_{t_1}^{t_2} P(t)\,\mathrm{d}t \,,$$

where u', C' and P' denote instantaneous deviations from the time means $\overline{u}$, $\overline{C}$ and $\overline{P}$, just eddy fluctuations. The time means of the eddy fluctuations vanish, for

example the time mean of the eddy fluctuation u':

$$\overline{u'} = \frac{1}{\tau}\int_{t_1}^{t_2} u'(t)\,\mathrm{d}t = \frac{1}{\tau}\int_{t_1}^{t_2} (u(t)-\overline{u})\,\mathrm{d}t = \overline{u}-\overline{u} = 0\ . \tag{3.9}$$

With this (3.5) becomes

$$\frac{\partial\left(\overline{C}+C'\right)}{\partial t} = -\frac{\partial\left((\overline{u}+u')\left(\overline{C}+C'\right)\right)}{\partial x} + \frac{\partial}{\partial x}\left(D\,\frac{\partial\left(\overline{C}+C'\right)}{\partial x}\right) + \overline{P}+P'\ .$$

Multiplying out the first term on the right side of the equation and using the sum rule of differentiation we obtain

$$\begin{aligned}\frac{\partial\overline{C}}{\partial t}+\frac{\partial C'}{\partial t} = &-\frac{\partial\left(\overline{u}\,\overline{C}\right)}{\partial x} - \frac{\partial\left(u'\,\overline{C}\right)}{\partial x} - \frac{\partial\left(\overline{u}\,C'\right)}{\partial x} - \frac{\partial\left(u'\,C'\right)}{\partial x}\\ &+\frac{\partial}{\partial x}\left(D\,\frac{\partial\overline{C}}{\partial x}\right)+\frac{\partial}{\partial x}\left(D\,\frac{\partial C'}{\partial x}\right)+\overline{P}+P'\ .\end{aligned}$$

This equation describes the processes at any moment exactly. But now we take the average with respect to time over the time interval (averaging time) τ, taking into account relation (3.9) and its consequences, namely

$$\begin{aligned}&\overline{\frac{\partial\overline{C}}{\partial t}} = \frac{\partial\overline{\overline{C}}}{\partial t} = \frac{\partial\overline{C}}{\partial t}\ ,\quad \overline{\frac{\partial\left(\overline{u}\,\overline{C}\right)}{\partial x}} = \frac{\partial\left(\overline{u}\,\overline{C}\right)}{\partial x}\ ,\quad \overline{\frac{\partial}{\partial x}\left(D\,\frac{\partial\overline{C}}{\partial x}\right)} = \frac{\partial}{\partial x}\left(D\,\frac{\partial\overline{C}}{\partial x}\right)\ ,\\ &\overline{\overline{P}} = \overline{P}\ ,\\ &\overline{\frac{\partial C'}{\partial t}} = \frac{\partial\overline{C'}}{\partial t} = 0\ ,\quad \overline{\frac{\partial\left(u'\,\overline{C}\right)}{\partial x}} = \overline{\frac{\partial\left(\overline{u}\,C'\right)}{\partial x}} = 0\ ,\quad \overline{\frac{\partial}{\partial x}\left(D\,\frac{\partial C'}{\partial x}\right)} = 0\ ,\\ &\overline{P'} = 0\ ,\end{aligned}$$

and obtain for the variation in time of the temporal mean of the physical quantity C:

$$\frac{\partial\overline{C}}{\partial t} = -\frac{\partial\left(\overline{u}\,\overline{C}\right)}{\partial x} - \frac{\partial\left(\overline{u'\,C'}\right)}{\partial x} + \frac{\partial}{\partial x}\left(D\,\frac{\partial\overline{C}}{\partial x}\right)+\overline{P}\ . \tag{3.10}$$

We see from this that the variation in time of $\overline{C}$ indeed depends on the eddy fluctuations u' and C'; the nonlinearity of the term $u\,C$ (advection flux) prevents the eddy fluctuations from being cancelled out by time averaging. From the statistical viewpoint, the quantity $\overline{u'\,C'} = \overline{(u-\overline{u})\left(C-\overline{C}\right)}$ corresponds to the *covariance* between the quantities u and C. It vanishes if u and C are uncorrelated. From the physical viewpoint, it describes the influence of the eddy fluctuations on the temporal change of $\overline{C}$ and denotes an *eddy flux density*,

$$F = \overline{u'\,C'}\ ,$$

which is, unlike the molecular fluxes explained in Section 3.1 and described by the second term on the right-hand side of (3.5), a part of the advective flux $u\,C$. If, for example, u and C are significantly positively correlated, then a positive deviation

u' goes in hand probably with a positive deviation C' and a negative deviation u' probably with a negative deviation C', whereby in both cases a transport of the quantity C in the positive direction of the x-coordinate axis results. Instead, if u and C are uncorrelated, the eddy flux density vanishes.

The motions of the eddies are seemingly stochastic, quite similar to the thermal motion of molecules. With regard to this fact we are talking about *eddy diffusion*, in contrast to the *molecular diffusion* presented in Section 3.1, and describe the eddy (diffusive) fluxes similar to the (molecular) diffusive fluxes. A widely used simple parameterisation (used in climate models) assumes the eddy flux density of the physical quantity C to be proportional to the gradient of the temporal mean of C, formally identical to Fick's first law (3.1),

$$F = \overline{u'\,C'} = -K\,\frac{\partial \overline{C}}{\partial x}\;, \tag{3.11}$$

where K denotes the *eddy diffusion constant* (also called *eddy diffusion coefficient* or *eddy diffusivity*) with the unit $\mathrm{m^2\,s^{-1}}$. The latter depends, like the molecular diffusion constant D, on the physical properties of both the transporting fluid and the transported physical quantity C, but, unlike the molecular diffusion constant, furthermore, among other physical properties (for example the stability of stratification), on the air velocity field $u(x,t)$ and finally on the averaging time τ. This parameterisation takes care of the problem that the smallest eddy motions cannot be resolved by the temporal and spatial resolution of the actual climate models. In a three-dimensional isotropic space, the eddy flux density of a scalar quantity C in a flow $\vec{u}(\vec{x},t)$ is

$$\vec{F} = \overline{\vec{u}'\,C'} = -K\,\vec{\nabla}\overline{C}\;, \tag{3.12}$$

in analogy to (3.2). Table 3.3 shows examples of eddy flux densities.

Table 3.3: Examples of eddy flux densities, ρ denotes a mass density and ρ_s the particle or the mass density of salt.

transported quantity	formulation
mass	$\vec{F} = \overline{\vec{u}'\,\rho'} = -K\,\vec{\nabla}\overline{\rho}$
heat	$\vec{F} = \rho\,c\,\overline{\vec{u}'\,T'} = -K\,\rho\,c\,\vec{\nabla}\overline{T}$
salt	$\vec{F} = \overline{\vec{u}'\,\rho_\mathrm{s}'} = -K\,\vec{\nabla}\overline{\rho}_\mathrm{s}$
y-momentum	$\vec{F} = \rho\,\overline{\vec{u}'\,u_y'} = -\rho\,K\,\vec{\nabla}\overline{u}_y$

With this we obtain for the averaged one-dimensional advection-diffusion equation (3.10)

$$\frac{\partial \overline{C}}{\partial t} = -\frac{\partial\left(\overline{u}\,\overline{C}\right)}{\partial x} + \frac{\partial}{\partial x}\left(K\,\frac{\partial \overline{C}}{\partial x}\right) + \frac{\partial}{\partial x}\left(D\,\frac{\partial \overline{C}}{\partial x}\right) + \overline{P} \tag{3.13}$$

and analogously for the averaged three-dimensional advection-diffusion equation

$$\frac{\partial \overline{C}}{\partial t} = -\vec{\nabla}\left(\overline{\vec{u}}\,\overline{C}\right) + \vec{\nabla}\cdot\left(K\,\vec{\nabla}\overline{C}\right) + \vec{\nabla}\cdot\left(D\,\vec{\nabla}\overline{C}\right) + \overline{P}\;. \tag{3.14}$$

These general relations apply for the ocean, too. In the case of large-scale motions in the free atmosphere or the free ocean the molecular flux densities are mostly very

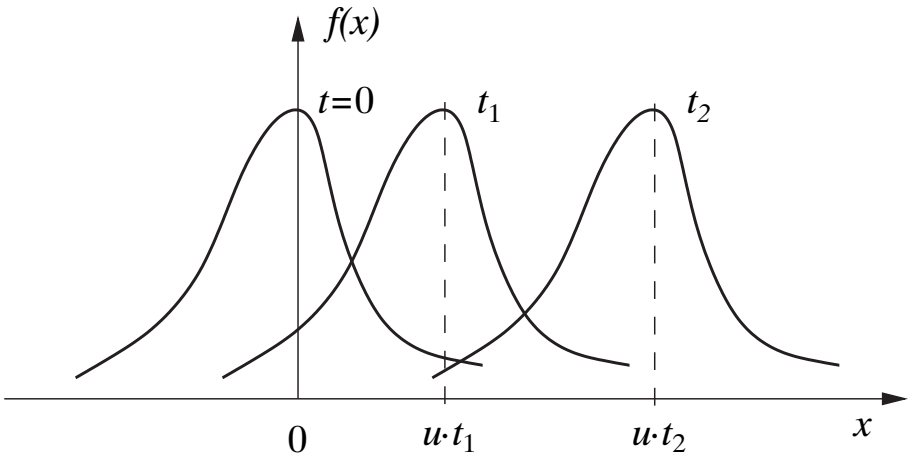

Figure 3.5: Transport of function $f(x)$ along the positive x-axis in a constant flow velocity $u > 0$ under the preservation of its form.

small and in many cases even negligibly small compared to the eddy flux densities.

3.5 Solution of the advection equation

In order to explore some fundamental characteristics of the numerical solution of the advection equation we consider the simplest case of (3.13). We assume a constant flow velocity u and ignore diffusion, sources or sinks. This leads to the one-dimensional advection equation

$$\frac{\partial C}{\partial t} + u \frac{\partial C}{\partial x} = 0 \ , \tag{3.15}$$

which is a partial differential equation (PDE) of particularly simple form.

3.5.1 Analytical solution

The general solution of this equation can be written as

$$C(x,t) = f(x - u\,t) \ , \tag{3.16}$$

where f is an arbitrary differentiable function. As a PDE of first order in time, (3.15) requires one initial condition for $t = 0$, which is given by $f(x)$.

Equation (3.16) describes a constant movement of a concentration distribution without any changes in shape f along the positive x-axis, as illustrated in Fig. 3.5. It represents a dispersion-free propagation of a disturbance along the x-axis at constant speed u and is reminiscent of a wave. Although (3.15) is not the classical wave equation, it can be shown that it is indeed part of the classical wave equation.

We note that a disturbance moving to the left is given by the following PDE:

$$\frac{\partial C}{\partial t} - u \frac{\partial C}{\partial x} = 0 \ ,$$

with $u > 0$. We now seek a PDE for which the solution propagates at a constant velocity along the positive *as well as* along the negative x-axis. The following PDE has the required characteristic:

$$\left(\frac{\partial}{\partial t} - u\,\frac{\partial}{\partial x}\right)\left(\frac{\partial}{\partial t} + u\,\frac{\partial}{\partial x}\right) C = 0\ .$$

The order of the operators inside the brackets may be interchanged. Eliminating the brackets and setting $u =$ constant leads to

$$\frac{\partial^2 C}{\partial t^2} - u^2\,\frac{\partial^2 C}{\partial x^2} = 0\ . \tag{3.17}$$

This is the *classical wave equation* with a constant phase velocity u. It has the general solution

$$C(x,t) = f(x - u\,t) + g(x + u\,t)\ . \tag{3.18}$$

A particular choice for f and g is the harmonic functions sin and cos. According to the famous identity found by *Leonhard Euler* (1707–1783), $\mathrm{e}^{\mathrm{i}\,x} = \sin x + \mathrm{i}\cos x$, we can write the solution of (3.17) in compact form:

$$C(x,t) = A\,\mathrm{e}^{\mathrm{i}\,k\,(x-u\,t)} + B\,\mathrm{e}^{\mathrm{i}\,k\,(x+u\,t)}\ . \tag{3.19}$$

The solution of the advection equation (3.15), subject to the initial condition

$$C(x,0) = A\,\mathrm{e}^{\mathrm{i}\,k\,x}\ , \tag{3.20}$$

is given by

$$C(x,t) = A\,\mathrm{e}^{\mathrm{i}\,k\,(x-u\,t)}\ . \tag{3.21}$$

(3.21) represents a plane wave of amplitude A propagating into positive x-direction. The quantities shown in Table 3.4 characterize the wave.

	Quantity	Relation
wavenumber	k	$k = \dfrac{2\pi}{\lambda}$
wavelength	λ	$\lambda = \dfrac{2\pi}{k} = \dfrac{u}{\nu}$
angular frequency	ω	$\omega = \dfrac{2\pi}{T}$
period	T	$T = \dfrac{2\pi}{\omega} = \dfrac{1}{\nu}$
frequency	ν	$\nu = \dfrac{1}{T} = \dfrac{u}{\lambda}$

Table 3.4: Summary of quantities describing a one-dimensional harmonic wave.

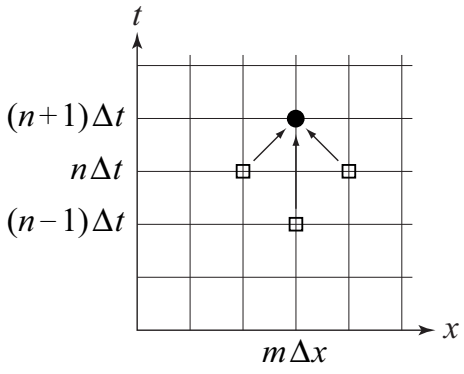

Figure 3.6: Illustration of the leap-frog scheme (CTCS) on a space-time grid.

3.5.2 Numerical solution using the CTCS scheme

We now solve the one-dimensional advection equation (3.15) numerically by discretising (3.15) in space and time as follows:

spatial discretisation:	$x = m\,\Delta x\ ,$	$m = 0,\ 1,\ 2,\ \ldots$
temporal discretisation:	$t = n\,\Delta t\ ,$	$n = 0,\ 1,\ 2,\ \ldots$

We adopt the following notation

$$C(x,t) = C(m\,\Delta x,\ n\,\Delta t) = C_{m,n} \tag{3.22}$$

for the values of the solution at the space-time grid points. The application of central differences in equation (3.15) yields

$$\frac{C_{m,n+1} - C_{m,n-1}}{2\,\Delta t} + u\,\frac{C_{m+1,n} - C_{m-1,n}}{2\,\Delta x} = 0\ . \tag{3.23}$$

Solving for the value at the most recent time point $(n+1)\,\Delta t$ yields

$$C_{m,n+1} = C_{m,n-1} - \frac{u\,\Delta t}{\Delta x}\,(C_{m+1,n} - C_{m-1,n})\ . \tag{3.24}$$

This scheme is called CTCS scheme (*central in time, central in space*). One can see that the identification of the value of solution C at a given time requires information from two neighboring grid points of the previous time step. This is schematically illustrated on a space-time grid in Fig. 3.6. With regard to the arrangement of the "predictors" this scheme is called *leap-frog scheme*. It must be noted that for the first time step from $t = 0$ to $t = \Delta t$ the CTCS scheme does not work. Instead, we must use the Euler forward scheme for time, therefore

$$C_{m,1} = C_{m,0} - \frac{u\,\Delta t}{2\,\Delta x}\,(C_{m+1,0} - C_{m-1,0})\ . \tag{3.25}$$

Here we used the FTCS scheme (*forward in time, central in space*). For $C_{m,0}$ the initial condition $C(x,0)$ is substituted.

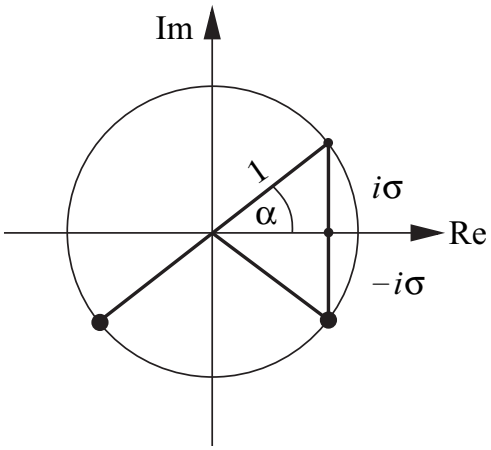

Figure 3.7: Illustration of the solutions (3.29) indicated as the large dots in the complex plane.

3.5.3 Numerical stability, CFL criterion

The following presentation is based on Haltiner and Williams (1980). Here we explore the characteristics of the leap-frog scheme (CTCS scheme). To this end, we assume the plane wave (3.20) as initial condition. Since we know the analytical solution, we can directly derive the discretized form,

$$C_{m,n} = B^{n\,\Delta t}\,\mathrm{e}^{\mathrm{i}\,k\,m\,\Delta x}\ , \tag{3.26}$$

where the time dependence is given in a particular form (with an appropriate choice of B in (3.26) this is identical to (3.21)). We insert (3.26) into (3.24) and obtain

$$\left(B^{\Delta t}\right)^2 + 2\,\mathrm{i}\,\sigma\,B^{\Delta t} - 1 = 0\ , \tag{3.27}$$

with

$$\sigma = \frac{u\,\Delta t}{\Delta x}\,\sin(k\,\Delta x)\ . \tag{3.28}$$

This is a quadratic equation in $B^{\Delta t}$ with the two solutions

$$B^{\Delta t} = -\mathrm{i}\,\sigma \pm \sqrt{1-\sigma^2}\ . \tag{3.29}$$

We distinguish two cases:

- **Stable case** $|\sigma| \le 1$:

  Both solutions $B^{\Delta t}$ have the absolute value 1, therefore they lie on the unit circle in the complex plane (Fig. 3.7). From the figure it follows:

$$B^{\Delta t} = \begin{cases} \mathrm{e}^{-\mathrm{i}\,\alpha} \\ \mathrm{e}^{\mathrm{i}(\alpha+\pi)} \end{cases}\ , \qquad \sin\alpha = \sigma\ . \tag{3.30}$$

  Therefore, the solution (3.26) can be written as

$$C_{m,n} = \left(M\,\mathrm{e}^{-\mathrm{i}\alpha\,n} + E\,\mathrm{e}^{\mathrm{i}(\alpha+\pi)\,n}\right)\mathrm{e}^{\mathrm{i}\,k\,m\,\Delta x} \tag{3.31a}$$

$$C_{m,0} = (M+E)\,\mathrm{e}^{\mathrm{i}\,k\,m\,\Delta x}\ . \tag{3.31b}$$

According to (3.20) we require $M + E = A$. Therefore, the discretised solution can be written as follows:

$$C_{m,n} = \underbrace{(A - E)\,\mathrm{e}^{\mathrm{i}\,k\left(m\,\Delta x - \frac{\alpha\,n}{k}\right)}}_{\mathrm{P}} + \underbrace{(-1)^n\ E\,\mathrm{e}^{\mathrm{i}\,k\left(m\,\Delta x + \frac{\alpha\,n}{k}\right)}}_{\mathrm{N}}\,, \tag{3.32}$$

where P denotes the physical mode and N the numerical mode (*computational mode*) of the solution. Note, that N changes its sign at every time step!

E remains to be identified. For the first time step we use (3.25). For the concentrations at time $t = 0$ we use (3.31b) and obtain

$$C_{m,1} = A\,(1 - \mathrm{i}\,\sin\alpha)\,\mathrm{e}^{\mathrm{i}\,k\,m\,\Delta x} = (A - E)\,\mathrm{e}^{\mathrm{i}\,k\,m\,\Delta x - \mathrm{i}\,\alpha} - E\,\mathrm{e}^{i\,k\,m\,\Delta x + \mathrm{i}\,\alpha}\,,$$

thus

$$E = A\,\frac{\cos\alpha - 1}{2\,\cos\alpha}\,.$$

Inserting this expression into (3.32) yields finally

$$C_{m,n} = \underbrace{A\,\frac{1 + \cos\alpha}{2\,\cos\alpha}\,\mathrm{e}^{\mathrm{i}\,k\left(m\,\Delta x - \frac{\alpha\,n}{k}\right)}}_{\mathrm{P}} + \underbrace{(-1)^{n+1}\ A\,\frac{1 - \cos\alpha}{2\,\cos\alpha}\,\mathrm{e}^{\mathrm{i}\,k\left(m\,\Delta x + \frac{\alpha\,n}{k}\right)}}_{\mathrm{N}}\,. \tag{3.33}$$

The convergence of (3.33) to (3.21) can be shown, as the following is valid:

$$\Delta x \to 0 \qquad \Longrightarrow \qquad \sigma = \frac{u\,\Delta t}{\Delta x}\,\sin(k\,\Delta x) \to u\,k\,\Delta t$$

and for $\Delta t \to 0$ it follows that $\sigma \ll 1$ and hence $\sigma = \sin\alpha \approx \alpha$. Therefore, (3.33) converges to

$$C_{m,n} \quad \to \quad \underbrace{A\,\frac{1 + \cos\alpha}{2\,\cos\alpha}\,\mathrm{e}^{\mathrm{i}\,k(x - u\,t)}}_{\mathrm{P}} + \underbrace{(-1)^{n+1}\ A\,\frac{1 - \cos\alpha}{2\,\cos\alpha}\,\mathrm{e}^{\mathrm{i}\,k(x + u\,t)}}_{\mathrm{N}}\,.$$

The term P describes the physical solution of a plane wave propagating to the right with an amplitude $A\,(1 + \cos\alpha)\,/\,(2\,\cos\alpha)$; for $\Delta t \to 0$ the amplitude is equal to A. The term N is the *computational mode* propagating to the left with an amplitude that vanishes for $\Delta t \to 0$.

The advection equation (3.15) was solved numerically for $u = 1$, $\Delta x = 1$, and $\Delta t = 0.1$ using scheme (3.24), while (3.25) was used for the first time step. The initial condition is a pulse of amplitude 10 at the origin, which, in the exact solution, ought to propagate to the right preserving its shape. The result is shown in Fig. 3.8. The numerical integration shows indeed a wave package moving to the right, physically well-founded, but also the numerical mode moving to the left and changing its sign at any grid point with each time step (Fig. 3.8). Additionally, the physical mode is subject to *numerical dispersion*, meaning that its form is not preserved. In this scheme, the propagation velocity of a wave depends on the wavelength. This causes the initially well-localized wave package to slowly disperse.

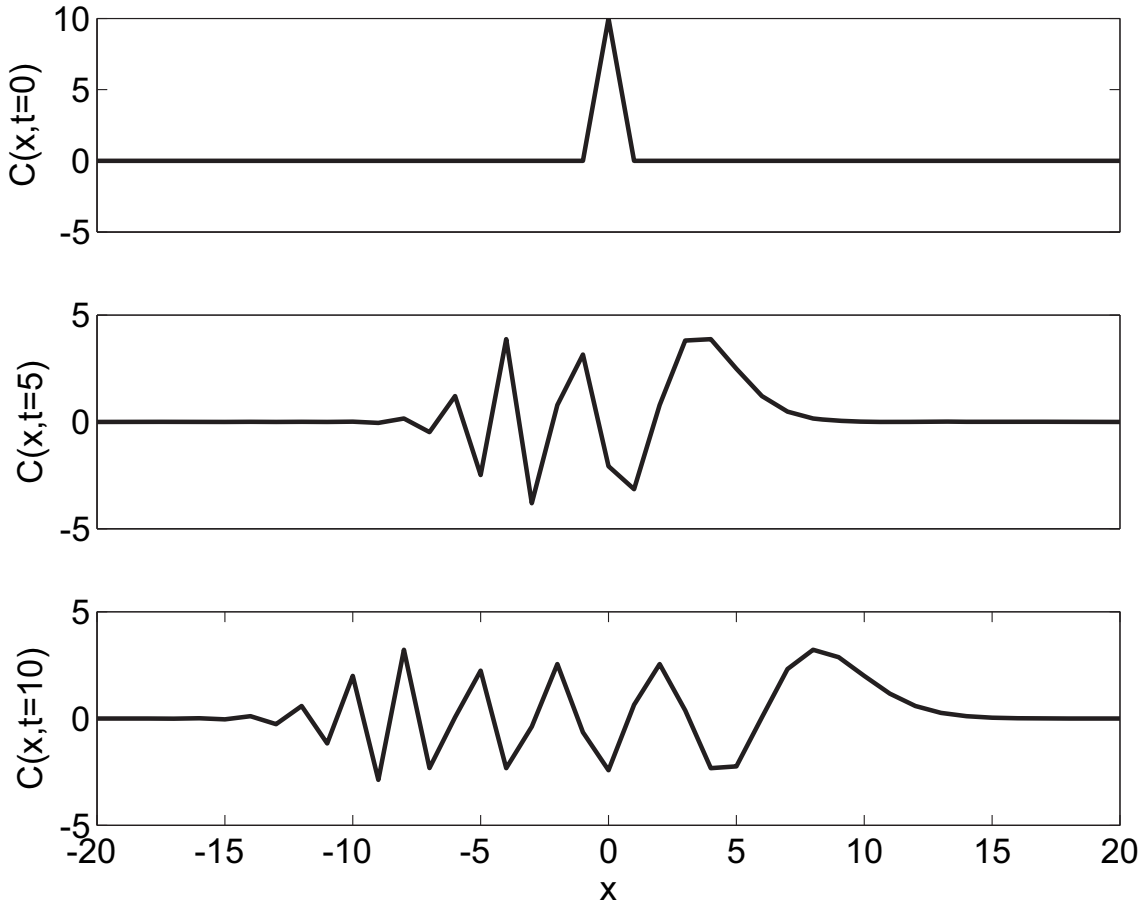

Figure 3.8: Dissipation of a wave package and generation of the numerical mode ($x < 0$) for the solution of the advection equation (3.15) for $u = 1$, $\Delta x = 1$, and $\Delta t = 0.1$ using CTCS.

- **Unstable case** $|\sigma| > 1$:

  In this case, we can rewrite (3.29):

  $$B^{\Delta t} = -\mathrm{i}\,(\sigma \pm S) \ , \qquad S = \sqrt{\sigma^2 - 1} > 0 \ .$$

  For $\sigma > 1$ we have $\sigma + S > 1$ and hence $\left|\left(B^{\Delta t}\right)^n\right| \to \infty$ for $n \to \infty$. For $\sigma < -1$ we have $\sigma - S < -1$ and $\left|\left(B^{\Delta t}\right)^n\right|$ diverges as well. The solution increases exponentially with time: it "explodes".

In consequence, the numerical solution using the CTCS scheme (3.24) only converges under the condition $|\sigma| \leq 1$, that is

$$\left|\frac{u\,\Delta t}{\Delta x}\,\sin\left(k\,\Delta x\right)\right| \leq 1 \ .$$

For this condition to be fulfilled for all wavenumbers k, the following very important condition must be satisfied:

$$\left|\frac{u\,\Delta t}{\Delta x}\right| \leq 1 \ . \tag{3.34}$$

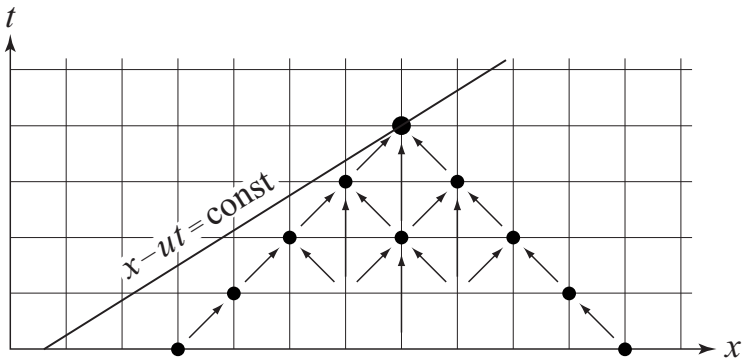

Figure 3.9: Space-time grid and area of influence of the CTCS scheme (3.24). In the case here, the characteristic of wave propagation lies outside the area of influence and thus violates the CFL criterion.

Condition (3.34) is called the *Courant-Friedrichs-Lewy criterion* (Courant et al., 1928), which must be satisfied in order to obtain stable numerical solutions using central differences. It is usually referred to as the *CFL criterion*. The CFL criterion links the velocity, at which signals are transported in the fluid, to the resolution of the space-time grid required to resolve the flow. At high transport velocities and a fixed spatial resolution, small time steps must be chosen. High flow velocities often occur in natural systems relevant for climate modelling. For example, the jet stream in the high troposphere/lower stratosphere of the mid-latitudes, or western boundary currents in ocean basins are difficult to resolve and require small time steps to satisfy the CFL criterion. Both, large u and small Δx conspire to requiring small time steps Δt. This may quickly result in a computational challenge.

Therefore, it is important to introduce numerical schemes which do not have to satisfy the CFL criterion. These are applied in difficult cases where the time step would have to be reduced too much.

We now present a more intuitive and physical way to understand the origin of the CFL criterion. The CFL criterion is a result of the wave propagation as described in the advection equation, and the area of influence of the chosen numerical scheme.

This is illustrated on a space-time grid in Fig. 3.9. A point (x, t) on this grid is visited by a wave which started at $t = 0$ from a specific location and has propagated in time t to location x. The wave propagates along its *characteristic*; here as a special case with a constant velocity u. The characteristic of a wave is defined as the geometric location of constant phase in the space-time-continuum. Here, the phase is given by $\Phi = x - u\,t$. The CFL criterion is the requirement that the characteristic that runs through point (x, t) is captured by the numerical scheme at all times.

The area of influence of the numerical scheme is determined by the specific formulation of the scheme. In the case of the leap-frog scheme (eq. 3.24, CTCS) a triangular area of influence in the space-time grid results. Its vertex is located at point (x, t). From Fig. 3.9 we see that the slope of the characteristic must be larger than the slope of the area of influence of the numerical scheme in order for all points to be captured by the waves reaching point (x, t). Therefore,

$$\frac{1}{u} \geq \frac{\Delta t}{\Delta x} \quad \Longleftrightarrow \quad \frac{u\,\Delta t}{\Delta x} \leq 1\,,$$

which yields the CFL criterion (3.34). Figure 3.9 also illustrates that the slope of

area of influence decreases either by increasing Δx or by decreasing Δt as is directly evident from (3.34).

Analogously, using (3.26) for the heat equation

$$\frac{\partial T}{\partial t} = \kappa \frac{\partial^2 T}{\partial x^2}$$

and solving it numerically using the FTCS-scheme we obtain the criterion for numerical stability

$$\frac{\kappa \Delta t}{\Delta x^2} \leq \frac{1}{2} \,. \tag{3.35}$$

3.6 Further methods for the solution of the advection equation

3.6.1 Euler forward in time, central in space (FTCS)

The numerical mode in (3.32) arose from the fact that the computation of the new time step required the information of two previous steps. In order to suppress the numerical mode we try an Euler forward method for time. Hence, equation (3.15) in a discretized form becomes

$$C_{m,n+1} = C_{m,n} - \frac{u \Delta t}{2 \Delta x} \left(C_{m+1,n} - C_{m-1,n} \right) \,. \tag{3.36}$$

We assume

$$C_{m,n} = B^{n \Delta t} \, \mathrm{e}^{\mathrm{i} \, k \, m \, \Delta x} \tag{3.37}$$

and obtain

$$B^{\Delta t} = 1 - \mathrm{i} \, \sigma = \sqrt{1 + \sigma^2} \, \mathrm{e}^{-\mathrm{i} \, \theta} \,, \tag{3.38}$$

where

$$\sigma = \frac{u \Delta t}{\Delta x} \sin(k \, \Delta x) \,, \qquad \tan \theta = \sigma \,.$$

Inserting (3.38) into (3.37) yields

$$C_{m,n} = \left(1 + \sigma^2 \right)^{n/2} \, \mathrm{e}^{\mathrm{i} \, k (m \, \Delta x - n \, \theta / k)} \,.$$

Since the above bracket is always greater than 1, the amplitude increases with time. Therefore we find $|C_{m,n}| \to \infty$ for $n \to \infty$. The solution „explodes“ using this scheme.

3.6.2 Euler forward in time, upstream in space (FTUS)

The following scheme takes into consideration the physics inherent in the simple advection equation (3.15). In a flow with speed u, the information originates from the negative x-direction and is carried at velocity u towards the grid point under consideration. It seems obvious to discretize the spatial derivative using a scheme that accounts for this situation. Instead of central differences, Euler backwards is

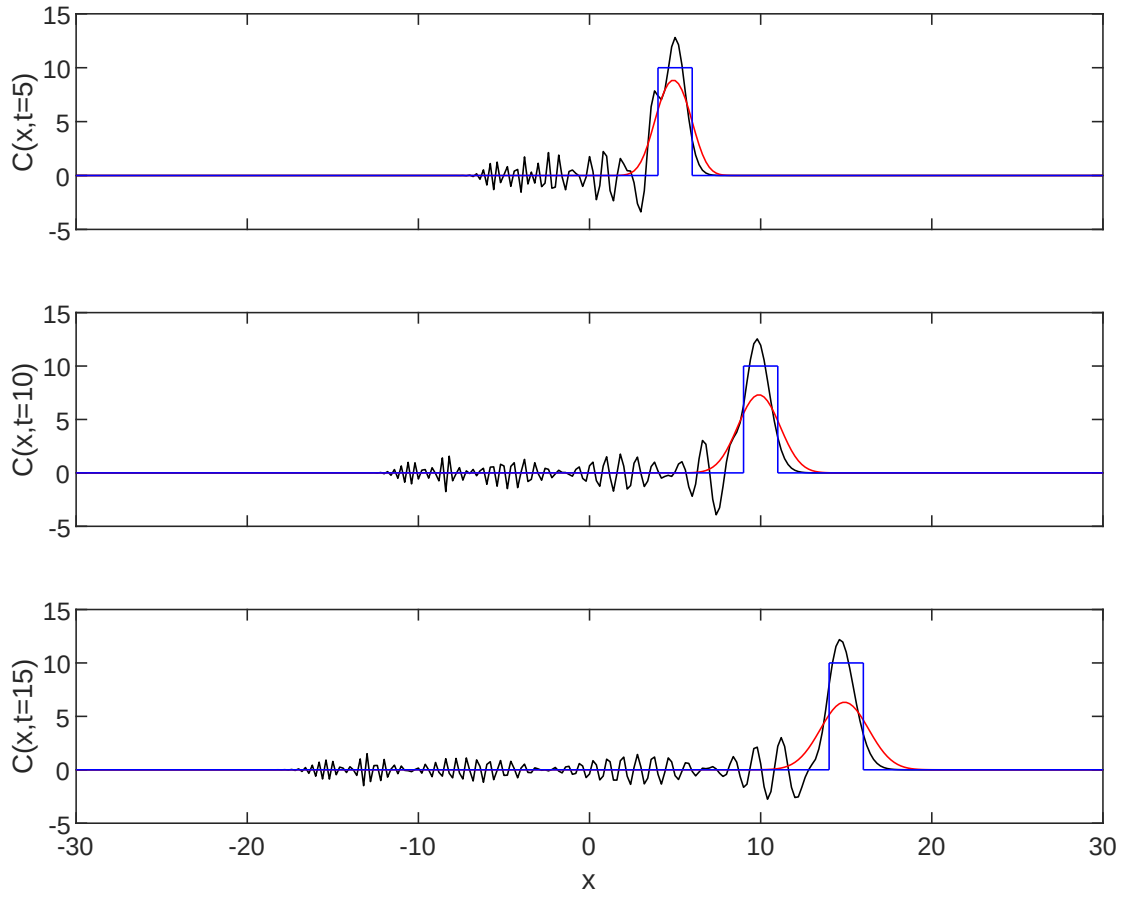

Figure 3.10: Comparison of the exact solution (*blue*) of the advection of a rectangular profile using different numerical solutions of the advection equation: central differences in t and x (CTCS, eq. (3.23), *black*), and upstream scheme, respectively (FTUS, eq. (3.39), *red*). For both, $\Delta x = 0.2$, $\Delta t = 0.1$ and $u = 1$ are used. The initial condition is $C = 1$ for $-1 \leq x \leq 1$ and $C = 0$ else. The numerical mode appearing when central differences (3.23) are used, is obvious. The upstream scheme does not produce a numerical mode but shows a very strong damping and dispersion.

used. It is clearer to use the term *upstream scheme* in this context, since spatial information originating from upstream locations is used. For $u > 0$ the discretized form of (3.15) therefore becomes

$$C_{m,n+1} = C_{m,n} - \frac{u\,\Delta t}{\Delta x}\left(C_{m,n} - C_{m-1,n}\right) \ . \tag{3.39}$$

Inserting (3.37) into (3.39) and simplifying, we obtain

$$B^{\Delta t} = 1 - \frac{u\,\Delta t}{\Delta x}\left(1 - \mathrm{e}^{-\mathrm{i}\,k\,\Delta x}\right) \ . \tag{3.40}$$

The numerical scheme stays stable if $\left|B^{\Delta t}\right| \leq 1$. Based on (3.40), it can be shown that this is satisfied for all wavenumbers k, provided

$$\frac{u\,\Delta t}{\Delta x} \leq 1 \ , \tag{3.41}$$

hence, if the CFL criterion (3.34) is satisfied. The disadvantage of the upstream scheme is a relatively strong damping and dispersion as illustrated in Fig. 3.10. In

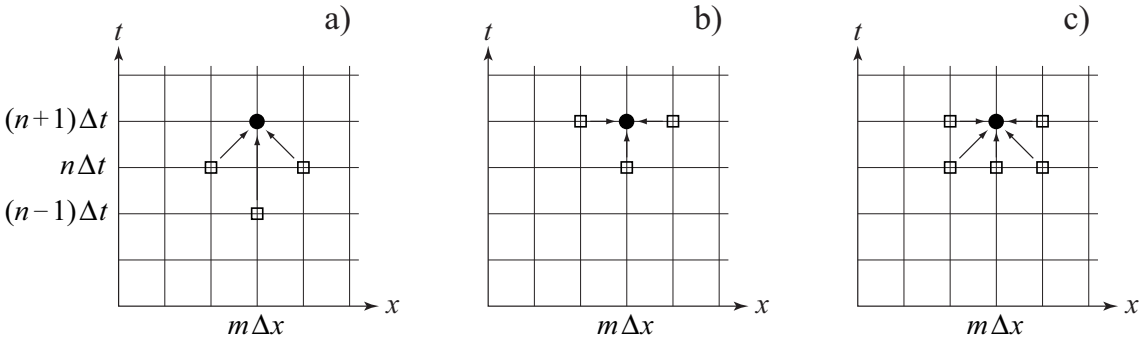

Figure 3.11: Schematic representation of an explicit and two implicit numerical schemes. **a)** explicit leap-frog scheme (3.23), **b)** the implicit leap-frog scheme (3.42), and **c)** the implicit trapezoidal scheme (3.44).

the upstream scheme, the damping increases with the reduction of Δt.

3.6.3 Implicit scheme

Often, the CFL criterion can only be satisfied if extremely short time steps are chosen. For example, in typical ocean models near the surface, where the isopycnal surfaces (surfaces of constant density) are steep, fluxes become large, and time steps on the order of seconds would be required to satisfy CFL. This is clearly not practical, and therefore an alternative must be found. The idea of the implicit scheme is that spatial derivatives are taken at the new time $(n+1)\,\Delta t$. There are various possibilities to do so, as is illustrated on a space-time grid in Fig. 3.11.

The implementation of the *implicit leap-frog scheme* for the advection equation (3.15) reads

$$\frac{C_{m,n+1} - C_{m,n}}{\Delta t} + u\,\frac{C_{m+1,n+1} - C_{m-1,n+1}}{2\,\Delta x} = 0\ . \tag{3.42}$$

We insert (3.37) into (3.42) and obtain

$$B^{\Delta t} = \frac{1}{1 + \mathrm{i}\,\sigma}\ , \qquad \sigma = \frac{u\,\Delta t}{\Delta x}\,\sin\left(k\,\Delta x\right)\ . \tag{3.43}$$

For any value for σ we find $\left|B^{\Delta t}\right| \leq 1$. Therefore, this scheme is stable without a constraint on the time step or the spatial grid resolution. However, there is significant damping.

If, instead, the spatial derivative is evaluated at the intermediate time level $(n+\frac{1}{2})\Delta t$, we obtain the *implicit trapezoidal scheme* for the advection equation (3.15)

$$\frac{C_{m,n+1} - C_{m,n}}{\Delta t} + u\,\frac{1}{2}\left(\frac{C_{m+1,n+1} - C_{m-1,n+1}}{2\,\Delta x} + \frac{C_{m+1,n} - C_{m-1,n}}{2\,\Delta x}\right) = 0\ , \tag{3.44}$$

where $\frac{1}{2}\,(\ldots)$ represents the average of the first spatial derivative at times $(n+1)\,\Delta t$ and $n\,\Delta t$. Again, we insert (3.37) into (3.44) and obtain

$$B^{\Delta t} = \frac{1 - \frac{1}{2}\,\mathrm{i}\,\sigma}{1 + \frac{1}{2}\,\mathrm{i}\,\sigma}\ . \tag{3.45}$$

For any value for σ we find $\left|B^{\Delta t}\right| = 1$. Therefore, this scheme is absolutely stable, and neither the CFL criterion has to be satisfied, nor a damping of the amplitude occurs. Unfortunately, the phase velocities of the waves become distorted.

It is evident from (3.44) that the implicit scheme leads to a large system of linear equations which requires a matrix inversion in order to solve for the new time step. We now write the equations resulting from using the implicit scheme in a compact way. Therefore, we collect the solutions at grid points $m = 1, 2, \ldots, M$ and time n in a vector:

$$\vec{C}_n = (C_{1,n}\,, C_{2,n}\,, \ldots\,, C_{M,n}) \ . \tag{3.46}$$

The discretized form (3.44) can then be written as a system of linear equations in the following way:

$$\begin{pmatrix} \vdots & \vdots & \vdots & \vdots & \vdots \\ \vdots & \vdots & \vdots & \vdots & \vdots \\ \ldots & -\dfrac{u\,\Delta t}{4\,\Delta x} & -1 & \dfrac{u\,\Delta t}{4\,\Delta x} & \ldots \\ \vdots & \vdots & \vdots & \vdots & \vdots \\ \vdots & \vdots & \vdots & \vdots & \vdots \end{pmatrix} \begin{pmatrix} \vdots \\ C_{m-1,n} \\ C_{m,n} \\ C_{m+1,n} \\ \vdots \end{pmatrix}$$

$$+ \begin{pmatrix} \vdots & \vdots & \vdots & \vdots & \vdots \\ \vdots & \vdots & \vdots & \vdots & \vdots \\ \ldots & -\dfrac{u\,\Delta t}{4\,\Delta x} & 1 & \dfrac{u\,\Delta t}{4\,\Delta x} & \ldots \\ \vdots & \vdots & \vdots & \vdots & \vdots \\ \vdots & \vdots & \vdots & \vdots & \vdots \end{pmatrix} \begin{pmatrix} \vdots \\ C_{m-1,n+1} \\ C_{m,n+1} \\ C_{m+1,n+1} \\ \vdots \end{pmatrix} = 0 \ ,$$

or in short

$$\mathbf{A}\,\vec{C}_n + \mathbf{B}\,\vec{C}_{n+1} = 0 \ . \tag{3.47}$$

The solution at time $n + 1$ is given by

$$\vec{C}_{n+1} = -\mathbf{B}^{-1}\,\mathbf{A}\,\vec{C}_n \ . \tag{3.48}$$

This means that for one time step, the solution at all spatial grid points is derived by the inversion of a linear equation system. $\mathbf{B}$ is a tridiagonal matrix; such matrices are regular, i.e. they can be inverted. The matrices are usually sparse, the solution can be obtained without using a full matrix inversion which is computationally expensive. In the case of (3.44), the matrix has non-zero elements only in the diagonal and the first off-diagonals. The numerical solution using the implicit scheme (3.44) for the same parameters Δt and Δx and the same initial conditions as in Fig. 3.10 is practically indistinguishable from the numerical solution using (3.23). However, the big advantage is the possibility of an arbitrary increase of the time step without sacrificing the quality of the numerical solution (Fig. 3.12).

3.6.4 Lax scheme

In Section 3.6.1 it was shown, that the scheme Euler forward in time, central in space (FTCS) is always unstable. Now, the idea in the Lax scheme is to stabilize the FTCS

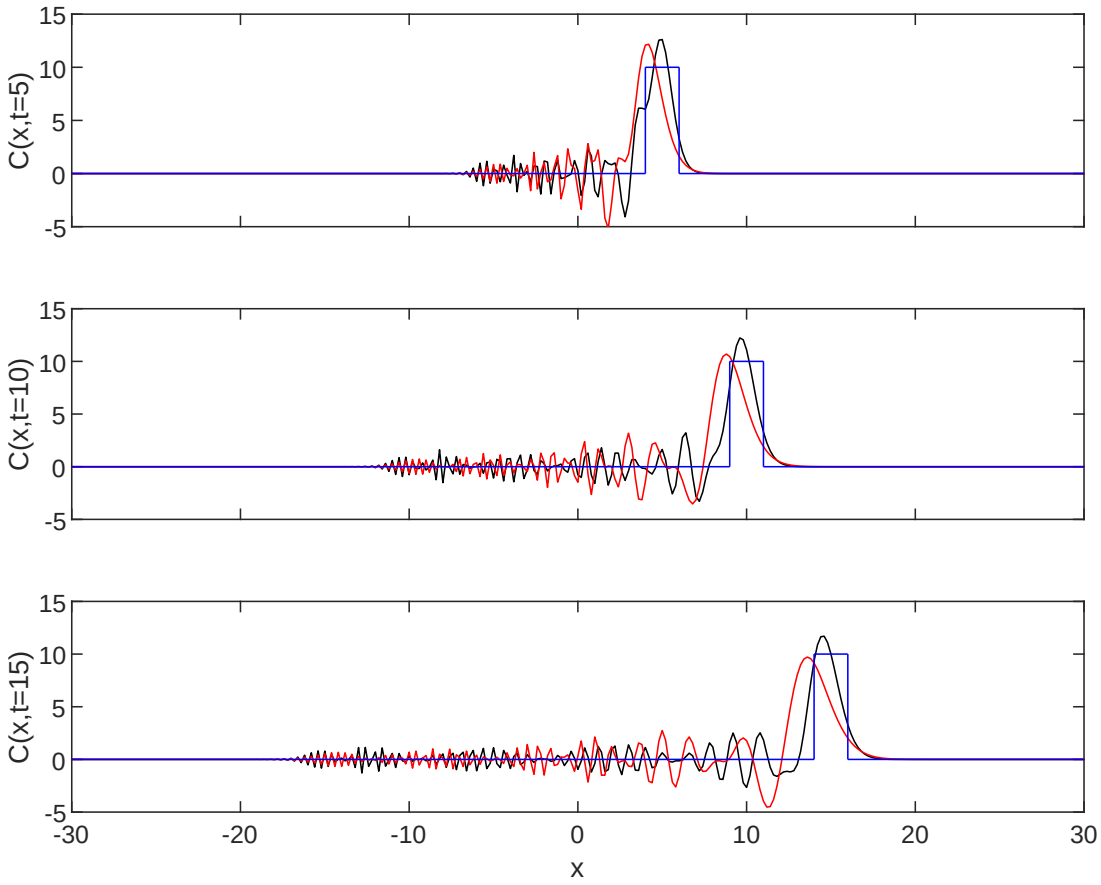

Figure 3.12: Comparison of the exact solution (*blue*) with the numerical solutions of the advection equation using the implicit-trapezoidal scheme (3.44) with two different time steps: $\Delta t = 0.1$ (*black*) and $\Delta t = 0.5$ (*red*) with $\Delta x = 0.2$ and $u = 1$. The latter violates the CFL criterion, but this is not relevant for the implicit scheme. The initial condition is $C = 1$ for $-1 \leq x \leq 1$, and $C = 0$ else. Both schemes reproduce the main maximum relatively well, but they also generate numerical modes propagating to the left. The method with the large time step exhibits a greater lag of the main maximum.

method by an additional diffusion term. This can be achieved by replacing $C_{m,n}$ by the spatial mean of two neighbouring grid points in (3.36). This leads to

$$C_{m,n+1} = \frac{1}{2}\left(C_{m+1,n} + C_{m-1,n}\right) - \frac{u\,\Delta t}{2\,\Delta x}\left(C_{m+1,n} - C_{m-1,n}\right) \ . \tag{3.49}$$

The scheme (3.49) is equivalent to (3.36) plus a diffusive term, because

$$C_{m,n+1} = \underbrace{C_{m,n} - \frac{u\,\Delta t}{2\,\Delta x}\left(C_{m+1,n} - C_{m-1,n}\right)}_{(3.36)} + \underbrace{\frac{1}{2}\left(C_{m+1,n} - 2\,C_{m,n} + C_{m-1,n}\right)}_{\mathrm{D}} \ ,$$

and term D is a discretized form of a diffusion term

$$\text{Term D} = \frac{\Delta x^2}{2}\,\frac{C_{m+1,n} - 2\,C_{m,n} + C_{m-1,n}}{\Delta x^2} \approx \Delta t\left(\frac{\Delta x^2}{2\,\Delta t}\right)\frac{\partial^2 C}{\partial x^2} \tag{3.50}$$

with a numerical diffusion constant $\Delta x^2/(2\,\Delta t)$. Therefore, the reduction of Δx decreases the diffusion quadratically, whereas a decrease of the time step increases

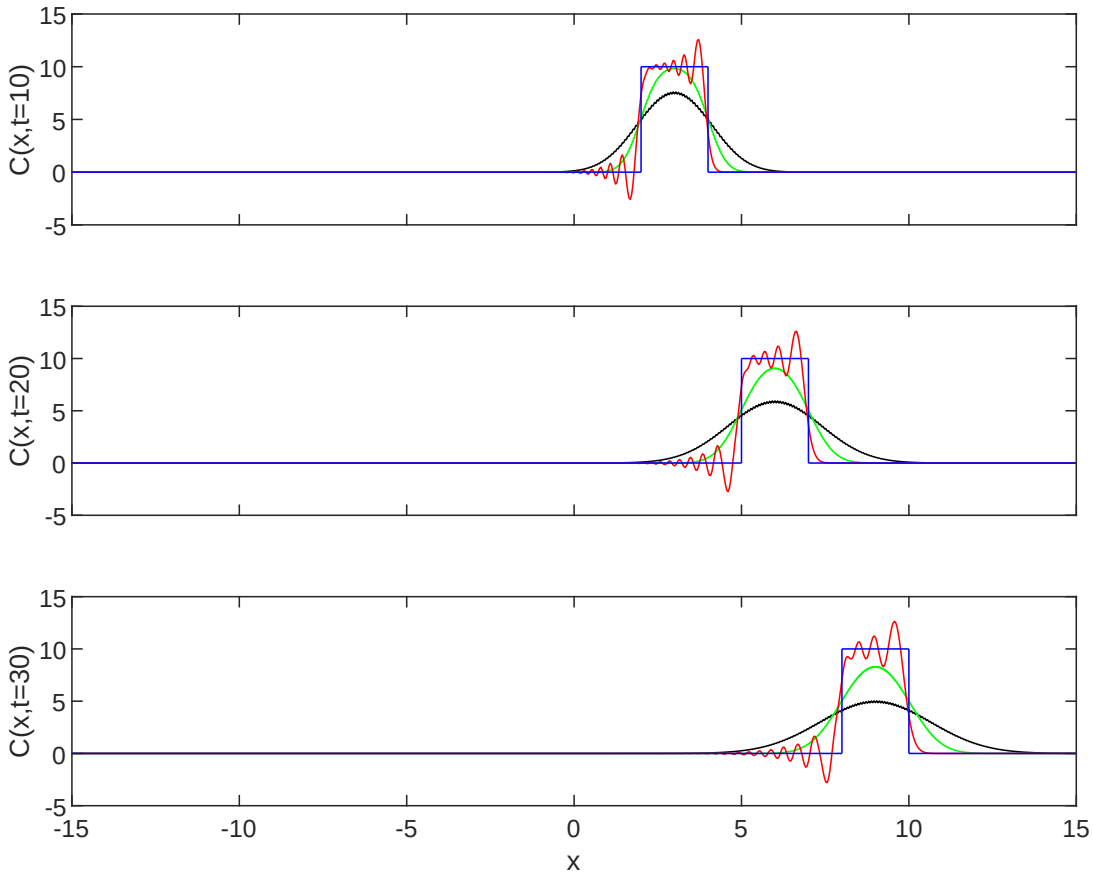

Figure 3.13: Comparison of the exact solution (*blue*) with different numerical solutions of the advection equation: Lax scheme (3.49) (*black and green*) and Lax-Wendroff scheme (3.53) (*red*). The parameters are: $\Delta x = 0.04$, $\Delta t = 0.02$ and $u = 0.3$. The initial condition is $C = 1$ for $-1 \leq x \leq 1$, $C = 0$ else. The Lax scheme (3.49) exhibits a strong damping and therefore a substantial underestimation of the gradients. The damping is reduced in the Lax scheme if the grid spacing is reduced ($\Delta x = 0.02$, *green*).

diffusion. But Δx and Δt cannot be chosen independent from one another because of the CFL criterion. This follows from using form (3.37) and inserting it into (3.49). This yields

$$B^{\Delta t} = \cos(k\,\Delta x) - \frac{u\,\Delta t}{\Delta x}\,\mathrm{i}\,\sin(k\,\Delta x)\ . \tag{3.51}$$

Hence, the scheme is stable only if

$$\left|B^{\Delta t}\right| \leq 1 \quad \Longleftrightarrow \quad \left|\frac{u\,\Delta t}{\Delta x}\right| \leq 1\ , \tag{3.52}$$

which is again the classical CFL criterion. The numerical solution is illustrated in Fig. 3.13; the parameters are identical to Fig. 3.10. The smaller the chosen time step, the stronger is the effect of diffusion of the first term in (3.49) and the scheme becomes useless.

The Lax scheme exhibits no numerical mode. But the clear disadvantage of the scheme is the rather large damping of gradients.

3.6.5 Lax-Wendroff Scheme

The Lax-Wendroff scheme addresses directly the problem of numerical diffusion from which the Lax scheme suffers. It reproduces gradients considerably better than the Lax scheme. This scheme is based on the idea to combine the Lax scheme for an intermediate time step with a subsequent leap-frog scheme (CTCS, with $\frac{1}{2}\Delta t$ and $\frac{1}{2}\Delta x$, see section 3.5.2). The intermediate or preparatory step is given by

$$\tilde{C}_{m+\frac{1}{2},n+\frac{1}{2}} = \frac{1}{2}\left(C_{m+1,n} + C_{m,n}\right) - \frac{u\,\Delta t}{2\,\Delta x}\left(C_{m+1,n} - C_{m,n}\right) \tag{3.53}$$

and then followed by CTCS-time stepping to time $(n+1)\,\Delta t$

$$C_{m,n+1} = C_{m,n} - \frac{u\,\Delta t}{\Delta x}\left(\tilde{C}_{m+\frac{1}{2},n+\frac{1}{2}} - \tilde{C}_{m-\frac{1}{2},n+\frac{1}{2}}\right) . \tag{3.54}$$

Inserting (3.53) into (3.54) reveals how the formerly unstable scheme (3.36) becomes stabilized:

$$\begin{aligned} C_{m,n+1} = & \underbrace{C_{m,n} - \frac{u\,\Delta t}{2\,\Delta x}\left(C_{m+1,n} - C_{m-1,n}\right)}_{(3.36)} \\ & + \underbrace{\frac{u^2\,\Delta t^2}{2\,\Delta x^2}\left(C_{m+1,n} - 2\,C_{m,n} + C_{m-1,n}\right)}_{\mathrm{D}} . \end{aligned} \tag{3.55}$$

Term D in (3.55) is a diffusion term, because

$$\begin{aligned} \text{Term D} &= \Delta t\,\frac{u^2\,\Delta t}{2}\,\frac{C_{m+1,n} - 2\,C_{m,n} + C_{m-1,n}}{\Delta x^2} \\ &\approx \Delta t\left(\frac{u^2\,\Delta t}{2}\right)\frac{\partial^2 C}{\partial x^2} . \end{aligned} \tag{3.56}$$

Here, the numerical diffusivity is $u^2\,\Delta t/2$ and thus much weaker than for the Lax scheme. It scales with Δt, and hence decreases when reducing the time step. The numerical solution is illustrated in Fig. 3.13. The representation of the steep gradients is significantly improved over the Lax scheme. However, the Lax-Wendroff scheme overestimates the maximum and shows trailing oscillations. Their spatial extent is much reduced compared to the trailing oscillations occuring with the CTCS, FTUS, and implicit schemes (see Figs. 3.10 and 3.12). This is because the oscillations emerging in the Lax-Wendroff scheme are primarily associated with the gradients rather than with a computational mode propagating to the $-x$-direction. These growing oscillations before the steep gradients are due to the *Gibbs phenomenon*.

It can be shown that also for the Lax-Wendroff Scheme the CFL criterion (3.52) has to be satisfied to ensure stability.

Comparing now the numerical diffusion constants of the Lax and the Lax-Wendroff schemes, respectively:

$$D_{\mathrm{N}}^{\mathrm{L}} = \frac{\Delta x^2}{2\Delta t} , \qquad D_{\mathrm{N}}^{\mathrm{LW}} = \frac{u^2 \Delta t}{2} , \tag{3.57}$$

and assuming that grid spacing and time step are unchanged, and that the CFL criterion (3.52) is satisfied as follows:

$$\frac{u\Delta t}{\Delta x} = r < 1 , \tag{3.58}$$

we find that

$$D_{\mathrm{N}}^{\mathrm{LW}} = r^2 D_{\mathrm{N}}^{\mathrm{L}} . \tag{3.59}$$

The Lax-Wendroff scheme has a numerical diffusion that is reduced by a factor of r^2 compared to the Lax scheme.

3.7 Numerical solution of the advection-diffusion equation

Let us now consider the one-dimensional advection-diffusion equation (3.5) with a source term proportional to $C(x,t)$:

$$\frac{\partial C}{\partial t} = D \frac{\partial^2 C}{\partial x^2} + u \frac{\partial C}{\partial x} + b\, C ; \tag{3.60}$$

D, u and b are constants. A generalized formulation of the discretized form of (3.60) is given by

$$\begin{aligned} \frac{C_{m,n+1} - C_{m,n}}{\Delta t} = D \frac{\theta\, \nabla_x^2 C_{m,n+1} + (1-\theta)\, \nabla_x^2 C_{m,n}}{\Delta x^2} \\ + u \frac{\nabla_x C_{m,n}}{2\,\Delta x} + b\, C_{m,n} \end{aligned} \tag{3.61}$$

using two central difference operators, defined as follows:

$$\begin{aligned} \nabla_x C_{m,n} &= C_{m+1,n} - C_{m-1,n} , \\ \nabla_x^2 C_{m,n} &= C_{m+1,n} - 2\, C_{m,n} + C_{m-1,n} . \end{aligned} \tag{3.62}$$

θ in (3.61) is a free weighting parameter, $0 \le \theta \le 1$, defining the "degree of implicity" of the scheme. For $\theta = 0$ the scheme is explicit and the right-hand side of (3.61) has no time index $n+1$. The explicit scheme is stable for $D\,\Delta t/\Delta x^2 \le \frac{1}{2}$.

For the parameter combination $u = 0$, $b = 0$ and $\theta = \frac{1}{2}$, (3.61) is called the *Crank-Nicholson scheme* which is absolutely stable. In general, stability of (3.61) requires

$$D \frac{\Delta t}{\Delta x^2} \le \frac{1}{2} \frac{1}{1 - 2\,\theta} \qquad \text{for} \quad 0 \le \theta < \tfrac{1}{2} \tag{3.63}$$

and for absolute stability: $\theta \ge \frac{1}{2}$.

3.8 Numerical Diffusion

Any numerical scheme exhibits non-physical properties due to the truncation. By neglecting higher-order terms in the Taylor expansion, errors are introduced. Numerical diffusion is one of them, and it becomes particularly obvious when the real diffusion of physical properties needs to be quantified (e.g., mixing of tracers in a fluid system, penetration of heat into the ocean, etc.). We have encountered this already in (3.49) and (3.54), but it is also evident in Fig. 3.10 (scheme (3.39)).

In order to examine the dependence of this numerical artifact from the choice of the discretization, we look at the one-dimensional advection equation (3.15) which represents one part of the classical wave equation:

$$\frac{\partial C}{\partial t} + u\,\frac{\partial C}{\partial x} = 0\ , \tag{3.64}$$

$$\frac{\partial^2 C}{\partial t^2} - u^2\,\frac{\partial^2 C}{\partial x^2} = 0\ . \tag{3.65}$$

We discretize in space (index m) and time (index n), and write the following Taylor expansions for the spatial and time steps, respectively:

$$\begin{aligned} C_{m+1,n} &= C_{m,n} + \frac{\partial C_{m,n}}{\partial x}\,\Delta x + \frac{1}{2!}\,\frac{\partial^2 C_{m,n}}{\partial x^2}\,\Delta x^2 + \ldots \\ C_{m,n+1} &= C_{m,n} + \frac{\partial C_{m,n}}{\partial t}\,\Delta t + \frac{1}{2!}\,\frac{\partial^2 C_{m,n}}{\partial t^2}\,\Delta t^2 + \ldots\ . \end{aligned} \tag{3.66}$$

In (3.66), we solve for the first derivatives and insert them into (3.64). We obtain

$$\begin{aligned} &\frac{C_{m,n+1} - C_{m,n}}{\Delta t} + u\,\frac{C_{m+1,n} - C_{m,n}}{\Delta x} \\ &\quad - \frac{1}{2!}\,\frac{\partial^2 C_{m,n}}{\partial t^2}\,\Delta t - u\,\frac{1}{2!}\,\frac{\partial^2 C_{m,n}}{\partial x^2}\,\Delta x - \ldots = 0\ . \end{aligned} \tag{3.67}$$

A solution of (3.64) is also a solution of (3.65). Therefore, the second time derivative in (3.67) can be substituted using (3.65). Finally, we get

$$\begin{aligned} &\frac{C_{m,n+1} - C_{m,n}}{\Delta t} + u\,\frac{C_{m+1,n} - C_{m,n}}{\Delta x} \\ &\quad - \left(\frac{1}{2}\,u^2\Delta t + \frac{1}{2}\,u\,\Delta x\right)\frac{\partial^2 C_{m,n}}{\partial x^2} - \ldots = 0\ . \end{aligned} \tag{3.68}$$

The third term in (3.68) is again a diffusion term. (3.68) reveals the fact that for all 1st-order schemes consisting of the numerical formulations of derivatives, diffusion occurs with diffusivity

$$D_{\mathrm{N}} = \frac{1}{2}\,u^2\Delta t + \frac{1}{2}\,u\,\Delta x\ \ . \tag{3.69}$$

D_{N} is the *numerical diffusivity* that scales with the time step and the grid spacing. Note that by marginally satisfying the CFL criterion and selecting Δx and Δt such

that $u\Delta t/\Delta x = 1$, we obtain from (3.69)

$$D_{\mathrm{N}} = \frac{\Delta x^2}{\Delta t} \quad . \tag{3.70}$$

This shows that by decreasing both Δx and Δt by a factor, the CFL criterion is unchanged, but the numerical diffusion reduces by that factor.

Various schemes exist that compensate for the numerical diffusion up to a certain point (see e.g., Smolarkiewicz, 1983). Such modern schemes are denoted FCT-schemes (*flux-corrected transport schemes*).

4 Energy transport in the climate system and its parameterisation

4.1 Basics

In the annual mean, the Earth takes up energy between 30°S and 30°N, while it has a negative energy balance towards the poles (Fig. 4.1). Since neither a continuous warming in the lower latitudes nor a cooling in the high latitudes are observed, a strong poleward transport of energy is required. The integration of the meridional radiation balance from the South Pole to the North Pole, as it is given in Fig. 4.1, yields the heat transport, required by the radiation balance (Fig. 4.2). In each hemisphere, about $5 \cdot 10^{15}$ J/s = 5 PW (Petawatt) are transported polewards. This flux is split about evenly between ocean and atmosphere. The maximum heat transport in the northern hemisphere occurs around 45°N in the atmosphere and around 20°N in the ocean. This fact points to the different mechanisms and boundary conditions (continents) responsible for the meridional heat transport. The atmosphere transports heat in a way fundamentally different from that of the ocean. The most important mechanisms are briefly explained in the following sections.

A central question is how climate models simulate heat transport and whether a certain model is able to reproduce the relevant processes of heat transport at all. It turns out that state-of-the-art three-dimensional climate models (position 3/3 in the model hierarchy of Table 2.1) simulate heat transport in the atmosphere as well as in the ocean in a physically adequate way. However, particularly models with a coarser resolution tend to underestimate the meridional heat transport in some of its important components and require unphysical corrections.

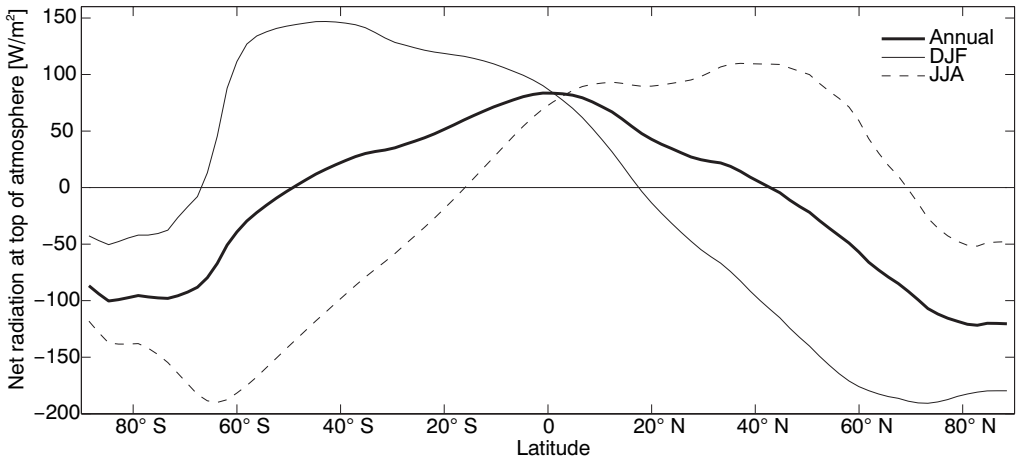

Figure 4.1: Radiation balance as a function of latitude. Shown are the annual mean as well as the two seasonal means DJF (December-January-February) and JJA (June-July-August). Data from NCEP reanalysis (Saha et al., 2006). Figure constructed by F. Lehner.

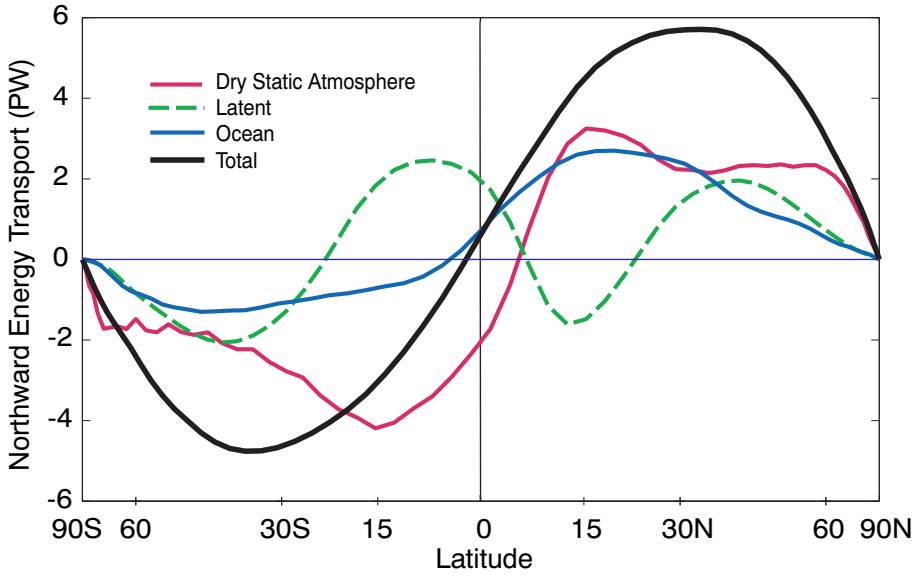

Figure 4.2: Annual mean meridional heat transport in the atmosphere (latent and dry) and in the ocean. Figure from Siedler et al. (2001).

4.2 Heat transport in the atmosphere

The total energy per unit mass in the atmosphere is given by

$$E = \underbrace{c_V\, T}_{\text{I}} + \underbrace{g\, z}_{\text{P}} + \underbrace{L\, q}_{\text{L}} + \underbrace{\frac{1}{2}\left(u^2 + v^2\right)}_{\text{K}}\,, \tag{4.1}$$

where c_V is the specific heat capacity of air at constant volume, T is the temperature, g is the gravity acceleration, z an altitude above a reference level, L the specific latent heat, q the humidity (mass of water vapour per mass of dry air), and u and v the horizontal components of the velocity (the vertical component is neglected). The four terms on the right-hand side denote the internal (I), the potential (P), the latent (L) and the kinetic (K) energy. The order of magnitude of the individual forms of energy in the atmosphere is given in Table 4.1.

		10^6 J m^{-2}	fraction (%)
Internal Energy	I	1800	70.2
Potential Energy	P	700	27.3
Latent Energy	L	64	2.5
Kinetic Energy	K	1.2	0.05
Total		2565	100

Table 4.1: Amount and distribution of energy per unit surface area in the global atmosphere (from Peixoto and Oort, 1992).

In order to explain the mechanisms of the temporal and zonal mean energy flux density $\vec{F} = \vec{u}\,\rho\,E$, we split the variables into a temporal mean and a temporal deviation on the one hand, as we have already done in Section 3.4, and, quite

analogously, into a zonal mean and a zonal deviation, on the other hand. The temporal and zonal means of a quantity A are defined as follows:

$$\overline{A} = \frac{1}{\tau} \int_{t_1}^{t_2} A \, \mathrm{d}t \, , \qquad [\, A \,] = \frac{1}{2\,\pi} \int_{0}^{2\,\pi} A \, \mathrm{d}\lambda \tag{4.2}$$

(time average taken over a time interval $\tau = t_2 - t_1$ of a few weeks, for example). We denote the temporal and zonal deviations from the respective means as

$$A' = A - \overline{A} \, , \qquad A^* = A - [\, A \,] \, . \tag{4.3}$$

From (4.3) follows, that

$$\overline{A'} = 0 \, , \qquad [\, A^* \,] = 0 \, , \tag{4.4}$$

as shown in (3.9).

Calculating fluxes such as the energy flux density $\vec{F} = \vec{u}\,\rho\,E$ involves products of quantities that vary in time and space. We write

$$\begin{aligned}
\overline{A\,B} &= \overline{\left(\overline{A} + A'\right)\left(\overline{B} + B'\right)} \\
&= \overline{\overline{A}\,\overline{B} + \overline{A}\,B' + A'\,\overline{B} + A'\,B'} \\
&= \overline{A}\,\overline{B} + \overline{A'\,B'} \\
&= \left([\,\overline{A}\,] + \overline{A}^*\right)\left([\,\overline{B}\,] + \overline{B}^*\right) + \overline{A'\,B'} \\
&= [\,\overline{A}\,][\,\overline{B}\,] + [\,\overline{A}\,]\overline{B}^* + \overline{A}^*[\,\overline{B}\,] + \overline{A}^*\,\overline{B}^* + \overline{A'\,B'} \, .
\end{aligned} \tag{4.5}$$

After zonal averaging of (4.5) we obtain

$$\begin{aligned}
[\,\overline{A\,B}\,] &= [\,\overline{A}\,][\,\overline{B}\,] + 0 + 0 + [\,\overline{A}^*\,\overline{B}^*\,] + [\,\overline{A'\,B'}\,] \\
&= [\,\overline{A}\,][\,\overline{B}\,] + [\,\overline{A}^*\,\overline{B}^*\,] + [\,\overline{A'\,B'}\,] \, .
\end{aligned} \tag{4.6}$$

The zonal and temporal mean of the product quantity $A\,B$ consists of the product of the means $[\,\overline{A}\,]$ and $[\,\overline{B}\,]$ of the respective individual quantities A and B *plus* the *zonal covariance* between the temporal means $\overline{A}$ and $\overline{B}$ *plus* the zonal mean of the *temporal covariance* $\overline{A'\,B'}$.

For illustration, we consider the first component of (4.1) in the following. By applying (4.6) onto the meridional flux density of internal energy $v\,\rho\,c_V\,T$, where ρ is the mass density, we get, ignoring both the approximately constant mass density and the approximately constant specific heat capacity, for the zonally and temporally averaged meridional flux of internal energy:

$$[\,\overline{v\,T}\,] = \underbrace{[\,\overline{v}\,][\,\overline{T}\,]}_{\mathrm{M}} + \underbrace{[\,\overline{v}^*\,\overline{T}^*\,]}_{\mathrm{SE}} + \underbrace{[\,\overline{v'\,T'}\,]}_{\mathrm{TE}} \, . \tag{4.7}$$

Hence, the zonally and temporally averaged meridional flux of internal energy consists of three components: the flux due to the mean meridional current (M), the flux due to stationary eddies (SE, caused, for example, by stationary high- and low-pressure systems) and the flux due to transient eddies (TE, caused, for example, by

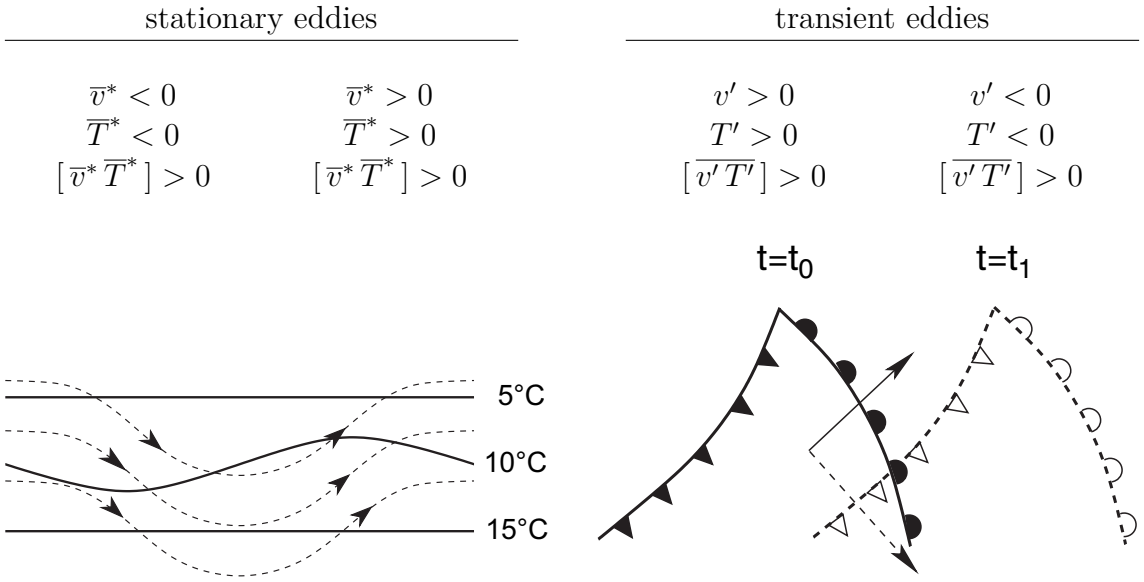

Figure 4.3: Schematic illustration of stationary and transient eddies in the atmosphere. In the situation above, both systems transport heat northwards.

moving high- and low-pressure systems).

Here, M is the classical advective heat flux as described in Section 3.2. The terms SE and TE in (4.7) originate from spatial and temporal correlations of v and T. An illustration is given in Fig. 4.3. The atmospheric meridional energy flux and its components, as determined from observations, are given in Fig. 4.4.

4.3 Meridional energy balance model

As can be inferred from Fig. 4.4, the annual mean meridional transport of total energy in the atmosphere is positive in the northern and negative in the southern hemisphere. In the zonal and annual mean, the meridional temperature gradient $\partial T/\partial\varphi$ is positive in the southern and negative in the northern hemisphere. Therefore, a negative correlation exists between $\partial T/\partial\varphi$ and $[\,\overline{v\,E}\,]$. This observation-based relation is now used to suggest a simple parameterisation of the meridional heat flux. We write

$$F = \rho\, c\, \overline{v'\,T'} = -\rho\, c\, K(\varphi)\, \frac{1}{R}\, \frac{\partial T}{\partial \varphi}\,, \tag{4.8}$$

where F is the meridional flux density of energy, ρ the air density, c the specific heat of air, v' and T' the eddy fluctuations of meridional air velocity and temperature, respectively. $K = K(\varphi)$ is a zonal eddy diffusivity dependent on latitude φ and on the order of 10^6 to 10^7 m^2/s, R the Earth radius and T the time mean of the local temperature.

It is obvious, that the spatial and temporal scales, where (4.8) can be regarded as valid, are strongly limited. Figure 4.4 shows, that during winter, when steeper temperature gradients are present, more energy is transported. It has been empirically shown that (4.8) is valid for time scales of ≥ 6 months and spatial scales of ≥ 1500 km (Lorenz, 1979).

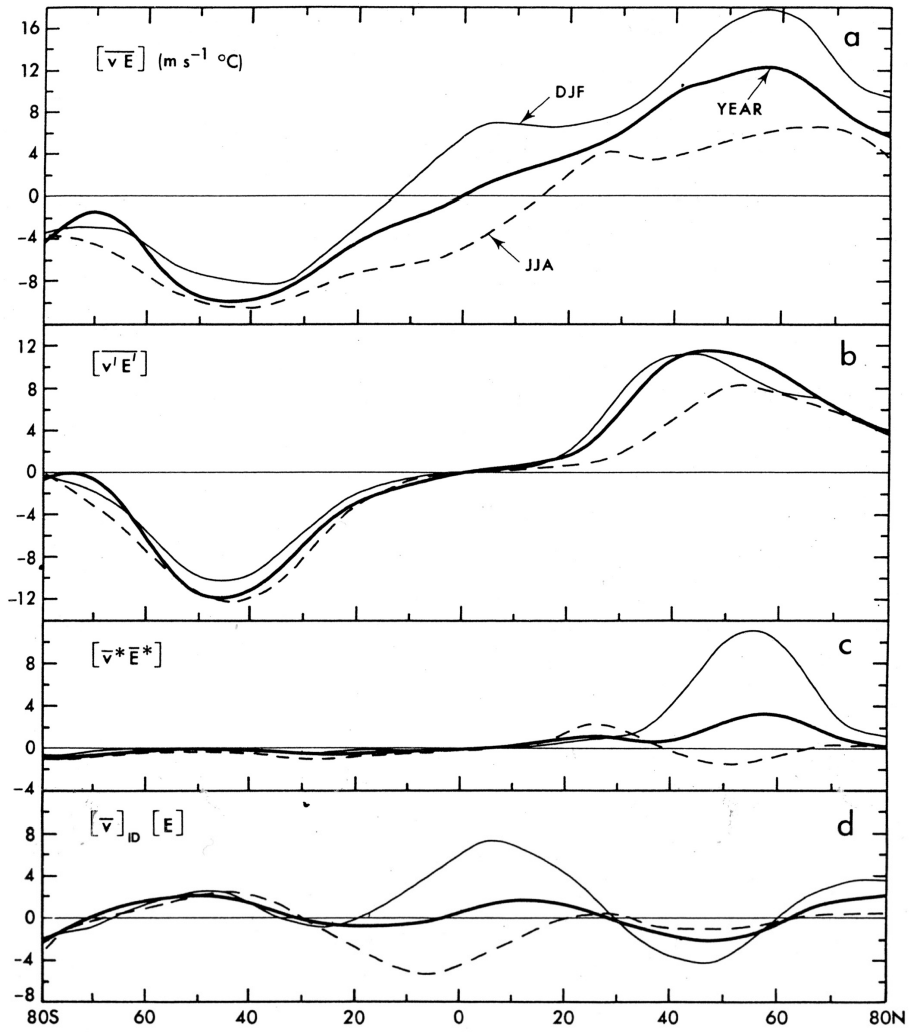

Figure 4.4: Profile of the zonally and vertically averaged atmospheric meridional transports of the total energy in (4.1) in $^\circ\mathrm{C\,m\,s^{-1}}$. **a)** total; **b)** transient eddies; **c)** stationary eddies; **d)** mean meridional flow, for the annual mean (*bold*), winter (*thin line*) and summer (*dashed*) months. In order to obtain units of PW, the factor $(2\,\pi R\,\cos\phi)\,c_\mathrm{p}\,(p_0/g)$ has to be multiplied. Figure from Peixoto and Oort (1992).

We now apply this to the point energy balance model (2.1) which can be extended to a one-dimensional energy balance model for which $t = T(\varphi)$ now depends on latitude. The balance equation is given by

$$h\,\rho\,c\,\frac{\partial T}{\partial t} = \frac{h}{R\,\cos\varphi}\,\frac{\partial}{\partial\varphi}\left(\rho\,c\,K(\varphi)\,\frac{1}{R}\,\frac{\partial T}{\partial\varphi}\,\cos\varphi\right) + \frac{1-\alpha(\varphi)}{4}\,S(\varphi) - \varepsilon(\varphi)\,\sigma\,T^4\,, \tag{4.9}$$

where the eddy diffusivity K, the albedo α, and the emissivity ε may be functions of latitude. The (mainly short-wave) incoming radiation $S(\varphi)$ is also a function of latitude. A good approximation for the annual mean is given by

$$S(\varphi) = S_0\left(0.5294 + 0.706\,\cos^2\varphi\right)\,,$$

where S_0 is the solar constant.

The first term on the right-hand side of (4.9) is the divergence of the meridional heat flux density multiplied by h, the vertical extent of the troposphere. The temperature is a function of time and latitude. Since (4.9) is a differential equation of 2nd order ($\partial^2/\partial\varphi^2$) in space, two boundary conditions must be satisfied. The boundary conditions at the two poles require the heat flux to vanish, hence

$$\frac{\partial T}{\partial \varphi} = 0 \qquad \text{for} \qquad \varphi = -\frac{\pi}{2},\ +\frac{\pi}{2}\ . \tag{4.10}$$

The one-dimensional energy balance model presented in (4.9) is referred to as the *Budyko-Sellers EBM*. Budyko (1969) and Sellers (1969) were the first to propose such a simplified climate model and to address fundamental questions concerning climate change using their models.

The EBM in (4.9) can be further generalized to two dimensions by additionally considering the zonal direction. Such models were developed in the 1980ies for studying the temperature difference between glacial and interglacial periods based on the changes in the radiation balance (North et al., 1983). Still today, they are implemented in some models of reduced complexity (Table 2.1, dimensions 2/2 and 2/3, e.g. Ritz et al. (2011)).

It must be emphasized that dynamic global circulation models of the atmosphere (AGCMs) compute the individual contributions to the energy transport (see (4.1) and (4.7)) based on the dynamics, and, to describe large-scale eddies and their effect on the heat transport, simplified parameterisations like (4.8) are not needed. This requires a minimum spatial resolution of 1000 km or less in the atmosphere in order to simulate eddies and their transport. As a result, a significantly increased computational burden is carried which in turn limits the length of the integrations and hence the applicability of AGCMs.

4.4 Heat transport in the ocean

The meridional heat transport in the ocean is caused by completely different mechanisms from those operating in the atmosphere, even though the equations describing the flow are analogous in both systems. The reason for this is on the one hand, that parameters in these equations are different (in certain cases by orders of magnitude) and that on the other hand, the ocean is restrained by basin boundaries. Along the latter, important current systems emerge which contribute significantly to the meridional heat flux.

In the ocean, eddies appear to play a minor role for the meridional heat transport except in some particular regions (equator, circumpolar current, southern tip of Africa). However, this statement is based on idealized model simulations and sparse observational data, for which reason the uncertainties are still quite high. An estimate for the meridional heat transport in the global ocean is given in Fig. 4.5. Some 2 PW are transported polewards by the ocean in both hemispheres, with the maximum in the northern hemisphere located more towards the equator than in the southern hemisphere.

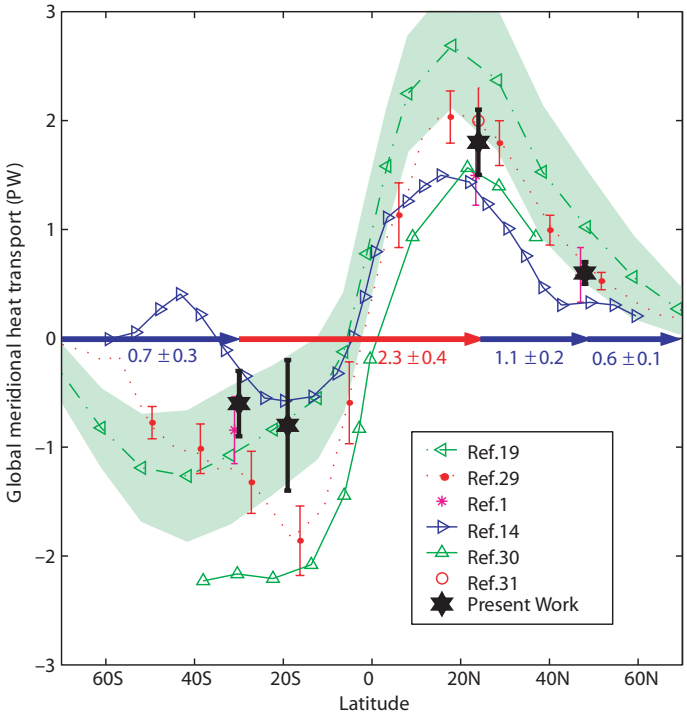

Figure 4.5: Zonally integrated heat transport in the ocean based on observations and inverse modelling. Figure from Ganachaud and Wunsch (2000).

In the different ocean basins different amounts of heat are transported. Ganachaud and Wunsch (2000) inferred the heat fluxes based from temperature and salinity measurements combined with inverse modelling. This is illustrated in Fig. 4.6. While heat is transported northwards at all latitudes in the Atlantic, a southward transport can be observed in the Indian Ocean. Despite its large extent, the transports in the Pacific are surprisingly small. Transport in the circumpolar current is largest with about 1.3 to 1.7 PW eastwards. The direction of the heat transport in the different ocean basins is qualitatively consistent with the strongly simplified depiction of the global oceanic conveyor belt introduced by *Wallace Broecker* (1931–2019) (Broecker, 1987).

In order to quantify the transport mechanisms of heat in the ocean, we define the vertical averaging of quantity A in the ocean according to

$$\widehat{A} = \frac{1}{H} \int_{-H}^{0} A \, \mathrm{d}z \,, \qquad A^+ = A - \widehat{A} \,. \tag{4.11}$$

The vertical average of a product, analogously to (4.7), is given by

$$\begin{aligned} \widehat{A\,B} &= (\widehat{A} + \widehat{A^+})(\widehat{B} + B^+) \\ &= \widehat{A}\,\widehat{B} + \widehat{A^+\,B^+} \\ &= \widehat{A}\,\widehat{B} + (\widehat{[\,A^+\,]} + \widehat{A^{+*}})(\widehat{[\,B^+\,]} + B^{+*}) \\ &= \widehat{A}\,\widehat{B} + \widehat{[\,A^+\,]\,[\,B^+\,]} + \widehat{A^{+*}\,B^{+*}} \,, \end{aligned} \tag{4.12}$$

where we have separated the quantities A^+ and B^+ further into a zonal mean and a zonal deviation according to (4.3b).

Now taking the zonal average of (4.12), and also splitting $\widehat{A}$ and $\widehat{B}$ into zonal mean

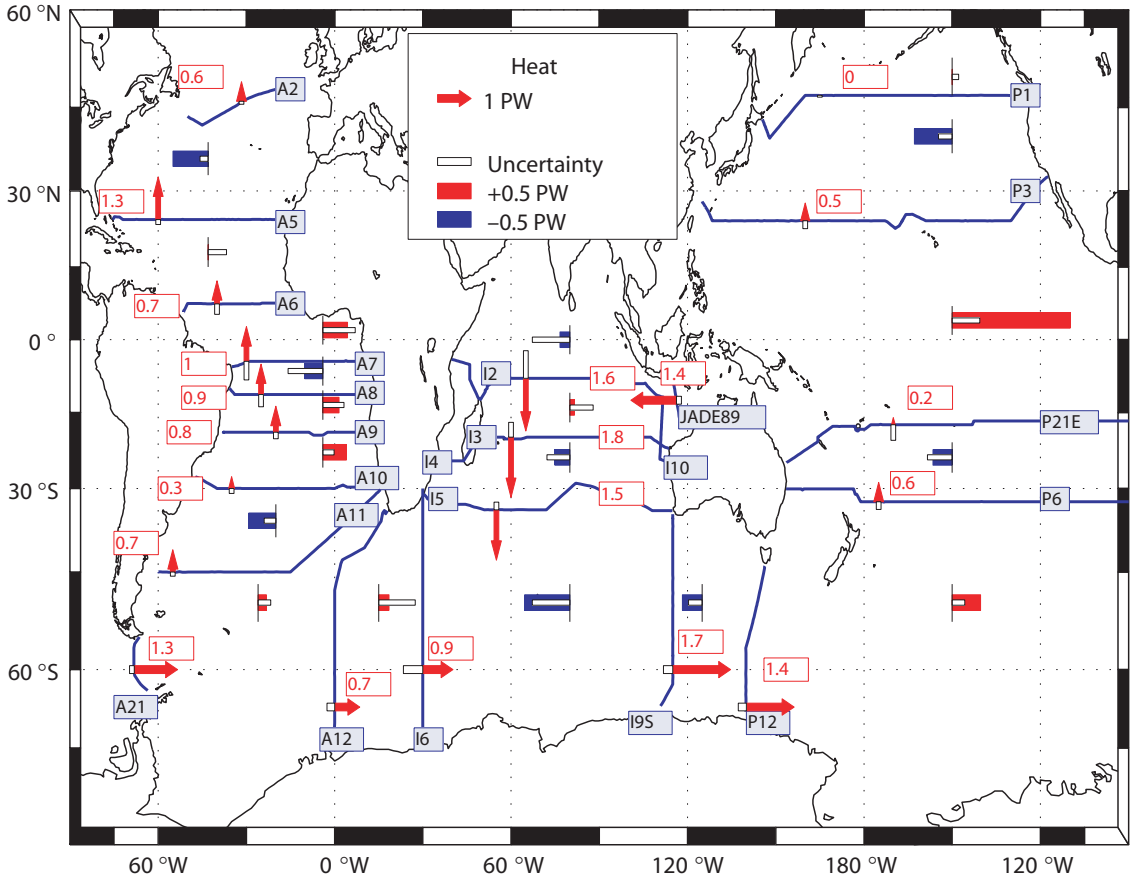

Figure 4.6: Meridional and vertical heat transports in the different regions of the world ocean. Numbers in boxes denote the meridional transport in PW. Horizontal bars represent the vertical transport (to the left = downwards). Figure from Ganachaud and Wunsch (2000).

and zonal deviation, we obtain

$$\begin{aligned}
\widehat{[A\,B]} &= [\widehat{A}\,\widehat{B}] + \widehat{[A^+][B^+]} + \widehat{[A^{+*}\,B^{+*}]} \\
&= [([\widehat{A}] + \widehat{A}^*)([\widehat{B}] + \widehat{B}^*)] + \widehat{[A^+][B^+]} + \widehat{[A^{+*}\,B^{+*}]} \\
&= [[\widehat{A}][\widehat{B}] + [\widehat{A}]\widehat{B}^* + \widehat{A}^*[\widehat{B}] + \widehat{A}^*\,\widehat{B}^*] + \widehat{[A^+][B^+]} + \widehat{[A^{+*}\,B^{+*}]} \\
&= [\widehat{A}][\widehat{B}] + [\widehat{A}^*\,\widehat{B}^*] + \widehat{[A^+][B^+]} + \widehat{[A^{+*}\,B^{+*}]}\,. \qquad (4.13)
\end{aligned}$$

The meridional heat transport $v\,T$, vertically and zonally averaged, therefore consists of four contributions:

$$\widehat{[v\,T]} = \underbrace{[\widehat{v}][\widehat{T}]}_{=0} + \underbrace{[\widehat{v}^*\,\widehat{T}^*]}_{\text{bG}} + \underbrace{\widehat{[v^+][T^+]}}_{\text{MOC+wG}} + \underbrace{\widehat{[v^{+*}\,T^{+*}]}}_{\text{EK}}\,, \qquad (4.14)$$

where the first term vanishes due to mass conservation in a closed basin, bG denotes the heat transport associated with horizontal *barotropic gyres* (i.e., ocean gyres with a one-to-one correspondence of density and pressure, so that isobaric surfaces are isopycnal surfaces, as further explained in Section 6.8), MOC+wG is the *meridional overturning circulation*, including the wind-driven *baroclinic gyre circulation*, and EK is the heat transport due to the surface- and bottom *Ekman circulation*. These

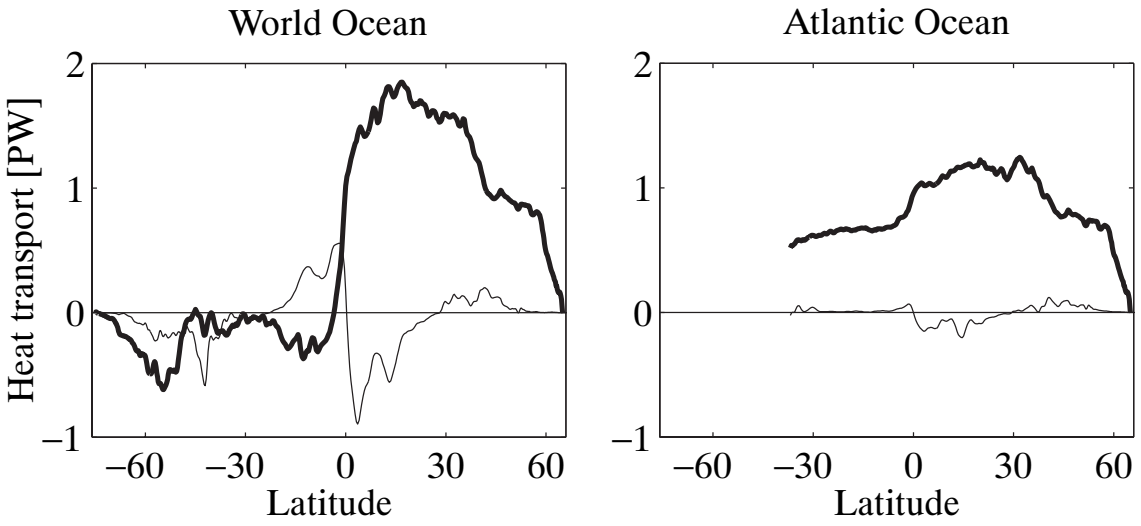

Figure 4.7: Zonally integrated meridional heat transport for the whole ocean and the Atlantic, total flux (*bold*) and contributions by eddies (*thin lines*), simulated with a high-resolution OGCM. Figure from Jayne and Marotzke (2002).

are induced by pressure forces, wind- and bottom-friction forces as well as Coriolis forces (see Sections 6.2 and 6.7).

Available data for the ocean does not yet permit to determine (4.14) by measurements. Therefore, Bryan (1987) simulated (4.14) in an ocean model of coarse resolution without eddies and found that around 80% of the meridional heat transport in the Atlantic is caused by the MOC. These results were later corroborated by a global OGCM of high resolution (Jayne and Marotzke, 2002). Thanks to a resolution of 0.25°, this model simulates individual eddies.

Globally, as well as in the Atlantic, the meridional transport of heat is predominantly associated with the term MOC in (4.14). Eddies only contribute in some limited regions to the total heat transport mainly in the tropical Pacific and in the western boundary currents (Fig. 4.7). For this reason, particularly in the Atlantic, the deep circulation, or *thermohaline circulation* (which is driven by ocean water density differences emerging from temperature and salinity differences), is the most relevant one for climate.

A rough estimate of the quantity of the term MOC in (4.14) yields the following values: In the northern Atlantic, the thermohaline circulation transports some $20 \cdot 10^6$ m^3 s^{-1} polewards near the surface at a temperature of around 18°C. Meanwhile, the same volume flows towards the equator at a depth of 2–3 km along the western boundary at a temperature of around 3°C. This corresponds to a meridional heat transport of $\rho\, c\, (\Delta V/\Delta t)\, \Delta T \approx 10^3 \cdot 4 \cdot 10^3 \cdot 20 \cdot 10^6 \cdot 15$ W $= 1.2$ PW. This is in rough agreement with the values of Fig. 4.6. The large vertical temperature contrast is therefore the reason for the meridional heat transport in the Atlantic.

Also in ocean models, sub-scale transports need to be parametrised due to the limitations imposed by the grid resolution. To this end, like in the energy balance model (4.9), a flux-gradient relationships for the transport of heat and momentum are chosen, because there are physical mechanisms (barotropic and baroclinic instabilities, see Vallis (2017)) that scale with the gradients of temperature (e.g., $K\partial T/\partial x$) and velocity (e.g., $K\partial v/\partial y$). Therefore, the assumptions shown in Table 4.2 are made.

$-A_{\mathrm{H}} \dfrac{\partial u}{\partial x}$,	$-A_{\mathrm{H}} \dfrac{\partial u}{\partial y}$	$-A_{\mathrm{H}} \dfrac{\partial v}{\partial x}$,	$-A_{\mathrm{H}} \dfrac{\partial v}{\partial y}$	Eddy-momentum flux in x- and y-direction
$-A_{\mathrm{V}} \dfrac{\partial u}{\partial z}$		$-A_{\mathrm{V}} \dfrac{\partial v}{\partial z}$		Eddy-momentum flux in z-direction
$-K_{\mathrm{H}} \dfrac{\partial T}{\partial x}$,	$-K_{\mathrm{H}} \dfrac{\partial T}{\partial y}$	$-K_{\mathrm{H}} \dfrac{\partial S}{\partial x}$,	$-K_{\mathrm{H}} \dfrac{\partial S}{\partial y}$	Eddy-heat and -salt flux in x- and y-direction
$-K_{\mathrm{V}} \dfrac{\partial T}{\partial z}$		$-K_{\mathrm{V}} \dfrac{\partial S}{\partial z}$		Eddy-heat and -salt flux in z-direction

Table 4.2: Components of eddy fluxes, namely x-, y- and z-components of eddy fluxes of horizontal momentum, eddy fluxes of heat and eddy fluxes of salt.

The values of the eddy viscosities A_{H}, A_{V} and the eddy diffusivities K_{H}, K_{V} are insufficiently constrained by data and hence, they are very uncertain. The value of A_{H} depends on the grid resolution of the ocean model: the smaller Δx, the smaller A_{H}, since the model is able to resolve more scales for smaller Δx. Table 4.3 lists typical values used in ocean models.

Table 4.3: Ranges of values for eddy viscosities and eddy diffusivities in ocean models of coarse resolution.

	$(\mathrm{m}^2/\mathrm{s})$
A_{H}	$10^1 \ldots 10^5$
A_{V}	$10^{-5} \ldots 10^{-1}$
K_{H}	$10^3 \ldots 10^4$
K_{V}	$10^{-5} \ldots 10^{-4}$

The role of eddies in mixing the water masses and their realistic and consistent parameterisation in models is a current topic of research. In which way the mixing effect of the tides and their interaction with the ocean topography could be accounted for, also remains an unresolved question.

5 Initial value and boundary value problems

5.1 Basics

The linear approximations of the energy balance models by Sellers (1969) and Budyko (1969) result in a linear partial differential equation of 1st order in time and 2nd order in space (4.9). The first term on the right-hand side is the divergence of the temperature gradient in one dimension, the second term is a source term, independent from the solution itself, and finally there is a term proportional to T^4 which in its linear approximation about the temperature T_o reads

$$T^4 \approx T_\mathrm{o}^4 + \left.\frac{\mathrm{d}\,(T^4)}{\mathrm{d}T}\right|_{T_\mathrm{o}} (T - T_\mathrm{o}) = T_\mathrm{o}^4 + 4\,T_\mathrm{o}^3\,(T - T_\mathrm{o}) = -3\,T_\mathrm{o}^4 + 4\,T_\mathrm{o}^3\,T\ .$$

If the eddy diffusivity K in (4.9) is taken as a constant, (4.9) is therefore approximately of the general type

$$\frac{\partial C}{\partial t} + K\,\vec{\nabla}^2 C + \tilde{\alpha}\,C = \tilde{\rho}(\vec{x})\ , \tag{5.1}$$

with the solution function $C(\vec{x}, t)$, e.g., $T(\varphi, t)$, and where $\tilde{\alpha}$ is constant and $\tilde{\rho}(\vec{x})$ a given function of $\vec{x}$, and defined on a (not necessarily finite) domain Ω. It describes numerous linear or linearized phenomena in physics, chemistry or mathematical biology.

Functions $C = C(\vec{x}, t)$, $\vec{x} \in \Omega$, solve (5.1) for suitable boundary and initial conditions. If such a solution satisfies an *initial condition*

$$C(\vec{x}, 0) = f(\vec{x})\ , \tag{5.2}$$

where $f(\vec{x})$ is a suitable function defined on the domain Ω, then the differential equation (5.1) and the initial condition (5.2) together represent an *initial value problem*. Instead, if the problem is independent of time,

$$\vec{\nabla}^2 C + \alpha\,C = \rho(\vec{x})\,, \tag{5.3}$$

with the constant α and the function $\rho(\vec{x})$, for example

$\vec{\nabla}^2 C = 0$	Laplace Equation,
$\vec{\nabla}^2 C = \rho(\vec{x})$	Poisson Equation,
$\vec{\nabla}^2 C + \alpha\,C = 0$	Helmholtz Equation,

and the solution $C = C(\vec{x})$ satifies *boundary conditions*

$$\alpha(\vec{x}_\mathrm{b})\,\frac{\partial C(\vec{x}_\mathrm{b})}{\partial n} + \beta(\vec{x}_\mathrm{b})\,C(\vec{x}_\mathrm{b}) = \gamma(\vec{x}_\mathrm{b})\;, \tag{5.4}$$

where $\partial/\partial n$ is the derivative perpendicular to the boundary $\vec{x}_\mathrm{b}$ of the domain Ω, and $\alpha(\vec{x}_\mathrm{b})$, $\beta(\vec{x}_\mathrm{b})$ as well as $\gamma(\vec{x}_\mathrm{b})$ are suitable functions defined on this boundary, then the differential equation (5.3) and the boundary condition (5.4) together constitute a *boundary value problem*. For boundary conditions (5.4) at a point $\vec{x}_\mathrm{b}$ on the boundary the following names are commonly used:

$\alpha(\vec{x}_\mathrm{b}) = 0$	Dirichlet boundary condition,
$\beta(\vec{x}_\mathrm{b}) = 0$	Neumann boundary condition,
else	Cauchy boundary condition.

One of the most common boundary value problem is Poisson's Equation

$$\vec{\nabla}^2 C = \rho(\vec{x}) \tag{5.5}$$

along with boundary conditions, i.e., specifically in two dimensions using Cartesian coordinates,

$$\frac{\partial^2 C}{\partial x^2} + \frac{\partial^2 C}{\partial y^2} = \rho(x, y)\;. \tag{5.6}$$

Equations (5.5) and (5.6) describe such diverse examples as stationary temperature distributions (T instead of C) in regions where heat sources are present, also stationary distributions of the electrostatic potential (φ instead of C) in regions containing electric charges, or the stationary flow of an incompressible and inviscid fluid (velocity potential instead of C) in the presence of mass sources and sinks.

5.2 Direct numerical solution of Poisson's equation

This section is given only for introductory purposes and in order to demonstrate the principles. The numerical solution of a boundary value problem would not be calculated using this method because of its computational inefficiency. Superior methods are available which will be presented below.

For simplification, we first assume, that the region, in which the equation is to be solved, is quadratic in shape. For the numerical solution of (5.6) a grid with a grid spacing of Δx and Δy is overlaid on the region (Fig. 5.1). Circles are termed *inner points*, diamonds denote *boundary points*. Further, we assume that Dirichlet boundary conditions are formulated, i.e. the values of the boundary points are given. The derivatives in (5.6) are discretized according to Table 2.2:

$$\frac{\partial^2 C}{\partial x^2} = \frac{C_{i,j+1} - 2\,C_{i,j} + C_{i,j-1}}{\Delta x^2} + \mathrm{O}(\Delta x^2) \tag{5.7a}$$

$$\frac{\partial^2 C}{\partial y^2} = \frac{C_{i+1,j} - 2\,C_{i,j} + C_{i-1,j}}{\Delta y^2} + \mathrm{O}(\Delta y^2)\;. \tag{5.7b}$$

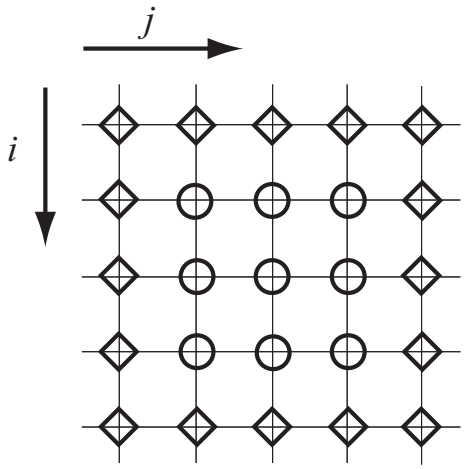

Figure 5.1: Grid with inner points (*circles*) and boundary points (*diamonds*).

Inserting (5.7) into (5.6), assuming $\Delta x = \Delta y$, and neglecting terms of higher order in (5.7), we obtain:

$$C_{i+1,j} + C_{i-1,j} + C_{i,j+1} + C_{i,j-1} - 4\,C_{i,j} = \Delta x^2\,\rho_{i,j}\ . \tag{5.8}$$

(5.8) states, that the deviation of the sum of the four closest neighbors from the value in the centre is equal to the source term at this point. Equation (5.8) is a system of linear equations of dimension $N\,M \times N\,M$ of the unknowns $C_{i,j}$, $i = 1, \ldots, N$; $j = 1, \ldots, M$. By appropriately numbering the indices of the inner points, a vector C_k, $k = 1, \ldots, N\,M$ can be constructed. We choose the following numbering, here illustrated for $N = 3$ and $M = 3$, a total of 9 inner points as in Fig. 5.1,

$$\begin{pmatrix} C_{1,1} & C_{1,2} & C_{1,3} \\ C_{2,1} & C_{2,2} & C_{2,3} \\ C_{3,1} & C_{3,2} & C_{3,3} \end{pmatrix} \equiv \begin{pmatrix} C_1 & C_4 & C_7 \\ C_2 & C_5 & C_8 \\ C_3 & C_6 & C_9 \end{pmatrix}\ , \tag{5.9}$$

which converts (5.8) into the system of linear equations

$$\left(\begin{array}{ccc|ccc|ccc} -4 & 1 & 0 & 1 & 0 & 0 & 0 & 0 & 0 \\ 1 & -4 & 1 & 0 & 1 & 0 & 0 & 0 & 0 \\ 0 & 1 & -4 & 0 & 0 & 1 & 0 & 0 & 0 \\ \hline 1 & 0 & 0 & -4 & 1 & 0 & 1 & 0 & 0 \\ 0 & 1 & 0 & 1 & -4 & 1 & 0 & 1 & 0 \\ 0 & 0 & 1 & 0 & 1 & -4 & 0 & 0 & 1 \\ \hline 0 & 0 & 0 & 1 & 0 & 0 & -4 & 1 & 0 \\ 0 & 0 & 0 & 0 & 1 & 0 & 1 & -4 & 1 \\ 0 & 0 & 0 & 0 & 0 & 1 & 0 & 1 & -4 \end{array}\right) \begin{pmatrix} C_1 \\ C_2 \\ C_3 \\ C_4 \\ C_5 \\ C_6 \\ C_7 \\ C_8 \\ C_9 \end{pmatrix} = \begin{pmatrix} r_1 \\ r_2 \\ r_3 \\ r_4 \\ r_5 \\ r_6 \\ r_7 \\ r_8 \\ r_9 \end{pmatrix}\ , \tag{5.10}$$

where the vector on the right side of the equation contains the values $\Delta x^2\,\rho_{i,j}$ plus possible boundary values. The matrix in (5.10) is symmetric and has a block structure. By inverting the matrix in (5.10), C can easily be solved for. However, this method quickly leads to very large systems, which can hardly be handled. By numbering (5.9) in a different way, we obtain a different structure of the matrix. The conditioning of the matrix depends on this numbering. This has an impact on the accuracy of the solution C.

We have seen that the numerical solution of partial differential equations rapidly leads to large systems of linear equations which have to be solved using appropriate numerical methods. For a typical grid resolution of 50×50 already a matrix of dimension 2500×2500 has to be inverted.

5.3 Iterative methods

The inversion of a large matrix is costly. To avoid this obstacle, we consider here iterative methods, first methods of *relaxation* and then the method of *successive overrelaxation*.

5.3.1 Methods of relaxation

The solution of (5.6) is a special solution of the time-dependent partial differential equation

$$\frac{1}{K}\frac{\partial C}{\partial t} = \frac{\partial^2 C}{\partial x^2} + \frac{\partial^2 C}{\partial y^2} - \rho(\vec{x}) \;, \tag{5.11}$$

namely the one for which $\partial C/\partial t = 0$. We seek the stationary solution of (5.11). Discretization in space and time yields

$$C_{i,j}^{n+1} = C_{i,j}^n + \frac{K\,\Delta t}{\Delta x^2}\left(C_{i+1,j}^n + C_{i-1,j}^n + C_{i,j+1}^n + C_{i,j-1}^n - 4\,C_{i,j}^n\right) - K\,\Delta t\,\rho_{i,j} \;, \tag{5.12}$$

where again $\Delta x = \Delta y$ and the upper index n denotes the time step. For the time discretization in (5.12), Euler forward was used. The simultaneous solution of a system of linear equations is replaced by an iterative calculation rule given by (5.12). In the course of a relaxation iteration procedure the values $C_{i,j}$ converge to the values of the stationary solution $\partial C/\partial t = 0$. For the solution to be stable, the appropriate CFL criterion (3.35) in two dimensions must be satisfied, i.e.

$$\frac{K\,\Delta t}{\Delta x^2} \le \frac{1}{4} \;. \tag{5.13}$$

By considering the maximum allowable time step derived from (5.13), (5.12) transforms to the classical *Jacobi method*:

$$C_{i,j}^{n+1} = \frac{1}{4}\left(C_{i+1,j}^n + C_{i-1,j}^n + C_{i,j+1}^n + C_{i,j-1}^n\right) - \frac{\Delta x^2}{4}\,\rho_{i,j} \;. \tag{5.14}$$

The Jacobi method converges only very slowly. A related method is the *Gauss-Seidel method*, which uses already computed values of the consecutive time steps in (5.14). Hence, when we proceed along the rows (i = constant) from small to large j, (5.14) can be modified to

$$C_{i,j}^{n+1} = \frac{1}{4}\left(C_{i+1,j}^n + C_{i-1,j}^{n+1} + C_{i,j+1}^n + C_{i,j-1}^{n+1}\right) - \frac{\Delta x^2}{4}\,\rho_{i,j} \;. \tag{5.15}$$

Even the Gauss-Seidel method is not very efficient. In order to reduce the error of the solution by p orders of magnitude, i.e., by a factor of 10^p, about $\frac{1}{2}\,p\,J^2$ iterations are required, where J is the number of grid points.

5.3.2 Method of successive overrelaxation (SOR)

The method of successive overrelaxation (SOR) described in this section is a good and appropriate method for simple boundary value problems that do not have to be designed for efficiency. It is an iterative method based on the discretization given in equation (5.8).

The solution matrix C in (5.9) is again numbered as a vector: C_k, $k = 1, \ldots, J$, $J = M\,N$. For clarity, the solution vector here will be denoted x, instead of C. Hence, (5.8) reads

$$\mathbf{A}\,x = b\;. \tag{5.16}$$

Any matrix can be written as the sum of a diagonal matrix $\mathbf{D}$, a left-triangular matrix $\mathbf{L}$, and a right-triangular matrix $\mathbf{R}$, with zeroes in the diagonals of the latter two. Applying this for matrix $\mathbf{A}$ we have

$$\mathbf{A} = \mathbf{D} + \mathbf{L} + \mathbf{R}\;. \tag{5.17}$$

In this notation, the methods we have previously presented read:

$$\textit{Jacobi method} \qquad \mathbf{D}\,x^{n+1} = -\left(\mathbf{L} + \mathbf{R}\right) x^n + b\;, \tag{5.18}$$

$$\textit{Gauss-Seidel method} \qquad \left(\mathbf{D} + \mathbf{L}\right) x^{n+1} = -\mathbf{R}\,x^n + b\;. \tag{5.19}$$

We subtract $\left(\mathbf{D} + \mathbf{L}\right) x^n$ from both sides of (5.19) and solve for x^{n+1}:

$$x^{n+1} = x^n - \Big(\mathbf{D} + \mathbf{L}\Big)^{-1} \underbrace{\Big(\left(\mathbf{D} + \mathbf{L} + \mathbf{R}\right) x^n - b\Big)}_{=\,\xi^n}\;. \tag{5.20}$$

The quantity ξ^n is called the residual of equation (5.16) at time step n, because $\xi^n = \mathbf{A}\,x^n - b$. Hence, the iteration reads

$$x^{n+1} = x^n \underbrace{- \left(\mathbf{D} + \mathbf{L}\right)^{-1} \xi^n}_{=\,\Delta x^{n+1}}\;, \tag{5.21}$$

where $\Delta x^{n+1} = x^{n+1} - x^n = -\left(\mathbf{D} + \mathbf{L}\right)^{-1} \xi^n$ is the correction at iteration step $n+1$ (the first iteration step goes from $n = 0$ to $n = 1$).

The idea of the method of successive overrelaxation is to accelerate the convergence by scaling the correction in (5.21) by a factor ω with $1 < \omega < 2$. This amounts to increasing the correction term by up to 100%. Accordingly, the SOR method reads

$$x^{n+1} = x^n - \omega\left(\mathbf{D} + \mathbf{L}\right)^{-1} \xi^n\;, \tag{5.22}$$

and $\omega = 1$ would be the Gauss-Seidel method.

It can be shown that in order to reduce the error by a factor 10^p, here only $\frac{1}{3}\,p\,J$

iterations are required. The computational burden therefore only scales linearly with J rather than quadratically ($\frac{1}{2}\,p\,J^2$) as for the Jacobi and the Gauss-Seidel methods. However, this only holds if an optimum value for ω is used in (5.22), and this is the difficulty in the SOR method. Luckily, there are some prior estimates for ω_{opt} (see Press et al., 1992, chapter Relaxation Methods). For smaller problems, ω_{opt} can be found by a search algorithm.

The matrix formulation (5.22) of the algorithm is only of theoretical value. The practical implementation is straightforward.

The discrete form of a partial differential equation of second order can be written in a generalized way as follows:

$$a_{i,j}\,x_{i+1,j} + b_{i,j}\,x_{i-1,j} + c_{i,j}\,x_{i,j+1} + d_{i,j}\,x_{i,j-1} + e_{i,j}\,x_{i,j} = f_{i,j}\ . \tag{5.23}$$

The new estimate for $x_{i,j}$ is then calculated analogously to (5.22):

$$x_{i,j}^{n+1} = x_{i,j}^{n} - \omega\,\frac{\xi_{i,j}^{n}}{e_{i,j}}\ , \tag{5.24}$$

where $\xi_{i,j}^{n}$ is the residual of the nth iteration:

$$\xi_{i,j}^{n} = a_{i,j}\,x_{i+1,j}^{n} + b_{i,j}\,x_{i-1,j}^{n} + c_{i,j}\,x_{i,j+1}^{n} + d_{i,j}\,x_{i,j-1}^{n} + e_{i,j}\,x_{i,j}^{n} - f_{i,j}\ . \tag{5.25}$$

In 1950, *D. M. Young* and *S. P. Frankel* proposed independently from each other an optimized SOR method which uses previously computed $x_{i,j}^{n+1}$ in (5.25). This method has become a standard SOR method and is outlined in Appendix A. The description there should also illuminate the relation between the relaxation factor ω and the speed of convergence of any SOR method.

6 Large-scale circulation in the ocean

Every fluid parcel in the atmosphere and the ocean obeys the fundamental laws of fluid mechanics including the equation of motion and the continuity equation. In the following we describe approximate forms of these two equations for large-scale circulations in the ocean. Analogous equations apply for large-scale circulations in the atmosphere. As a preparatory step, we consider a special time derivative.

6.1 Material derivative

Given a small water parcel moving through the ocean on a path

$$\vec{r}(t) = \begin{pmatrix} x(t) \\ y(t) \\ z(t) \end{pmatrix} \ .$$

Hence, at time t the water parcel passes the coordinates $x(t)$, $y(t)$ and $z(t)$ with the velocity

$$\vec{u}(t) = \frac{\mathrm{d}\vec{r}(t)}{\mathrm{d}t} = \begin{pmatrix} \frac{\mathrm{d}x(t)}{\mathrm{d}t} \\ \frac{\mathrm{d}y(t)}{\mathrm{d}t} \\ \frac{\mathrm{d}z(t)}{\mathrm{d}t} \end{pmatrix} = \begin{pmatrix} u(t) \\ v(t) \\ w(t) \end{pmatrix} \ , \tag{6.1}$$

where $u(t)$, $v(t)$ and $w(t)$ are the x-, y- and z-components of the velocity, respectively.

Any physical property A of the water parcel—such as the velocity, the pressure, the density, the temperature, or the salinity—is a function of time and space, $A = A(t, x, y, z)$. The total derivative with respect to time of this mathematical function is

$$\frac{\mathrm{d}A}{\mathrm{d}t} = \frac{\partial A}{\partial t} + \frac{\mathrm{d}x}{\mathrm{d}t}\,\frac{\partial A}{\partial x} + \frac{\mathrm{d}y}{\mathrm{d}t}\,\frac{\partial A}{\partial y} + \frac{\mathrm{d}z}{\mathrm{d}t}\,\frac{\partial A}{\partial z} \ . \tag{6.2}$$

Determining the derivative along the path of the water parcel, where $\mathrm{d}x/\mathrm{d}t = u$, $\mathrm{d}y/\mathrm{d}t = v$ and $\mathrm{d}z/\mathrm{d}t = w$ according to (6.1), we get the *material derivative*, also called Lagrangian derivative or advective derivative,

$$\frac{\mathrm{D}A}{\mathrm{D}t} = \frac{\partial A}{\partial t} + u\,\frac{\partial A}{\partial x} + v\,\frac{\partial A}{\partial y} + w\,\frac{\partial A}{\partial z} \ , \tag{6.3}$$

corresponding to the time rate of change of the physical quantity A measured by an observer moving with the water parcel. The first term on the right-hand side of this equation is the partial derivative of A with respect to time t (the space coordinates x, y and z are held constant), called *Eulerian derivative*, corresponding to the rate of change of the physical quantity A measured by an observer at a fixed position in space (x, y, z = constant). The difference between the material derivative $\mathrm{D}A/\mathrm{D}t$ and the Eulerian derivative $\partial A/\partial t$ is due to the transport with the flow, of which the

water parcel is part, namely due to advection. Equation (6.3) can also be written in vector notation:

$$\begin{aligned}\frac{\mathrm{D}A}{\mathrm{D}t} &= \frac{\partial A}{\partial t} + (u,\, v,\, w)\cdot \begin{pmatrix} \frac{\partial A}{\partial x} \\ \frac{\partial A}{\partial y} \\ \frac{\partial A}{\partial z} \end{pmatrix} \\ &= \frac{\partial A}{\partial t} + \vec{u}\cdot\vec{\nabla}A\ . \end{aligned} \tag{6.4}$$

6.2 Equation of motion

The small water parcel satisfies the conservation equation for momentum, namely the equation of motion based on the 2nd Law of Newton. With respect to an Earth-fixed coordinate system it is

$$\frac{\mathrm{D}\vec{u}}{\mathrm{D}t} = \vec{a} + \vec{a}_{\mathrm{I}}\ , \tag{6.5}$$

where $\vec{a}$ signifies the acceleration (force per unit mass) due to the sum of all *real forces* (pressure gradient force, friction force, gravity force) and $\vec{a}_{\mathrm{I}}$ analogously the acceleration due to the sum of all *inertial forces* (also called *apparent forces*) arising from Earth's rotation in an Earth-fixed reference system (Coriolis force, centrifugal force).

Denoting the nearly constant angular velocity of Earth's rotation with $\vec{\Omega}$, where $\Omega = 2\pi/86,400\ \mathrm{s} = 7.272\cdot 10^{-5}\ \mathrm{s}^{-1}$, the acceleration of the water parcel due to inertial forces relative to an Earth-fixed reference system is given by

$$\vec{a}_{\mathrm{I}} = -2\,\vec{\Omega}\times\vec{u} - \vec{\Omega}\times\left(\vec{\Omega}\times\vec{r}\right)\ , \tag{6.6}$$

as shown for example in Peixoto and Oort (1992). The first term on the right-hand side is the Coriolis acceleration, the second term is the centrifugal acceleration. Due to the centrifugal acceleration, the Earth surface is approximately a rotational ellipsoid so that the horizontal component of the centrifugal acceleration is nearly cancelled out by the horizontal component of the gravity acceleration $\vec{g}$. Therefore, in contrast to the Coriolis force, the horizontal component of the centrifugal force can be neglected.

Every realistic version of the equation of motion has to consider that the oceanic currents are flowing on the approximately spherical surface of the Earth. But there are good approximations, especially for circulations on smaller scales, which assume oceanic flows to occur on a plane (Fig. 6.1). This plane is called *f-plane* or *β-plane*, depending on the approximations assumed (see below). A Cartesian coordinate system (x, y, z), in which the equations are formulated, is defined on this plane. The coordinate system is attached to the sphere and rotates with it. The Coriolis acceleration in this system is given by

$$\vec{a}_{\mathrm{C}} = -2\begin{pmatrix} 0 \\ \Omega\cos\varphi \\ \Omega\sin\varphi \end{pmatrix}\times\begin{pmatrix} u \\ v \\ 0 \end{pmatrix} = \begin{pmatrix} 2\,\Omega\,\sin\varphi\, v \\ -2\,\Omega\,\sin\varphi\, u \\ 2\,\Omega\,\cos\varphi\, u \end{pmatrix}\ ; \tag{6.7}$$

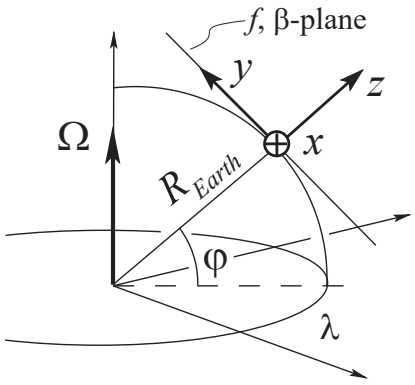

Figure 6.1: Local Cartesian coordinate system on a rotating sphere.

considering inertial forces, we will neglect vertical motions by setting $w = 0$. In both horizontal components the common factor

$$f = 2\,\Omega\,\sin\varphi \tag{6.8}$$

appears. This is the *Coriolis parameter* which, due to the spherical shape of the Earth, depends on latitude φ. Linearisation of $f(\varphi)$ yields

$$\begin{aligned} f(\varphi) &\approx f(\varphi_0) + \left.\frac{\mathrm{d}f}{\mathrm{d}\varphi}\right|_{\varphi_0} (\varphi - \varphi_0) \\ &= 2\,\Omega\,\sin\varphi_0 + 2\,\Omega\,\cos\varphi_0\,(\varphi - \varphi_0) \\ &= f_0 + \frac{2\,\Omega\,\cos\varphi_0}{R_{Earth}}\,y \\ &= f_0 + \beta\,y\;. \end{aligned} \tag{6.9}$$

If we only account for the constant term f_0 in the equations of motion in the (x, y, z)-coordinate system, we consider the dynamics on an *f-plane*. On the *β-plane* one uses the linear approximation (6.9) when considering the dynamics. This is especially important if the plane's origin is at the equator where $f_0 = 0$.

Next, we work out the most important real forces acting on the fluid. These are the pressure gradient force, the friction force due to shear stress and the gravity force. Pressure forces (caused by pressure p) and friction forces (caused by shear stress τ) act on a mass element as follows (see Fig. 6.2):

$$\begin{aligned} \rho\,\delta x\,\delta y\,\delta z\,a_x = {} & p(x)\,\delta y\,\delta z - p(x+\delta x)\,\delta y\,\delta z \\ & + \tau_{xy}(y+\delta y)\,\delta z\,\delta x - \tau_{xy}(y)\,\delta z\,\delta x \\ & + \tau_{xz}(z+\delta z)\,\delta x\,\delta y - \tau_{xz}(z)\,\delta x\,\delta y\,. \end{aligned}$$

The water density ρ is taken as constant. Friction forces within the ocean arise especially from eddy shear stress due to eddy fluxes of momentum going through the frictional surface considered (viscous shear stress, however, is generally negligible for large-scale motions), so that according to Table 3.3 $\tau_{xy} = -\rho\,\overline{u'\,v'}$, $\tau_{xz} = -\rho\,\overline{u'\,w'}$,

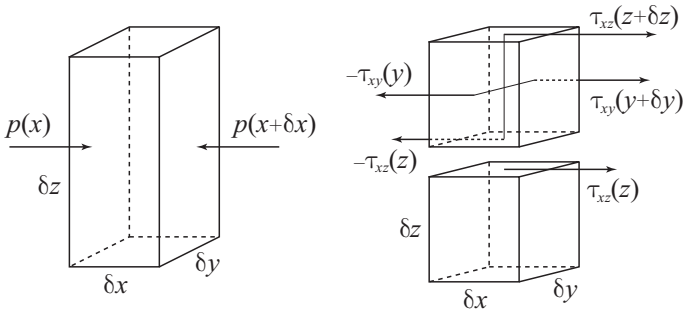

Figure 6.2: Denominations of the pressure and of the shear stress for the derivation of the pressure gradient accelerations and friction accelerations.

except at the boundaries. We obtain for the components of the acceleration,

$$\begin{aligned} a_x &= -\frac{1}{\rho}\frac{\partial p}{\partial x} + \frac{1}{\rho}\frac{\partial \tau_{xy}}{\partial y} + \frac{1}{\rho}\frac{\partial \tau_{xz}}{\partial z}\,, \\ a_y &= -\frac{1}{\rho}\frac{\partial p}{\partial y} + \frac{1}{\rho}\frac{\partial \tau_{yx}}{\partial x} + \frac{1}{\rho}\frac{\partial \tau_{yz}}{\partial z}\,, \\ a_z &= -\frac{1}{\rho}\frac{\partial p}{\partial z} + \frac{1}{\rho}\frac{\partial \tau_{zx}}{\partial x} + \frac{1}{\rho}\frac{\partial \tau_{zy}}{\partial y} - g\,, \end{aligned} \tag{6.10}$$

where g denotes the free-fall acceleration, i.e., the resultant acceleration due to the gravity force and the vertical components of centrifugal force and Coriolis force. As the horizontal shears of large-scale ocean circulations are commonly negligibly small compared to the vertical shear we write approximately

$$a_x = -\frac{1}{\rho}\frac{\partial p}{\partial x} + \frac{1}{\rho}\frac{\partial \tau_{xz}}{\partial z}\,, \tag{6.11a}$$

$$a_y = -\frac{1}{\rho}\frac{\partial p}{\partial y} + \frac{1}{\rho}\frac{\partial \tau_{yz}}{\partial z}\,, \tag{6.11b}$$

$$a_z = -\frac{1}{\rho}\frac{\partial p}{\partial z} - g\,. \tag{6.11c}$$

With this we obtain from (6.5) the equation of motion approximated for large-scale horizontal circulations,

$$\frac{\mathrm{D}u}{\mathrm{D}t} = -\frac{1}{\rho}\frac{\partial p}{\partial x} + \frac{1}{\rho}\frac{\partial \tau_{xz}}{\partial z} + f\,v\,, \tag{6.12a}$$

$$\frac{\mathrm{D}v}{\mathrm{D}t} = -\frac{1}{\rho}\frac{\partial p}{\partial y} + \frac{1}{\rho}\frac{\partial \tau_{yz}}{\partial z} - f\,u\,, \tag{6.12b}$$

$$\frac{\mathrm{D}w}{\mathrm{D}t} = -\frac{1}{\rho}\frac{\partial p}{\partial z} - g\,, \tag{6.12c}$$

i.e., written out in full, using the relation (6.3),

$$\frac{\partial u}{\partial t} + u\,\frac{\partial u}{\partial x} + v\,\frac{\partial u}{\partial y} + w\,\frac{\partial u}{\partial z} = -\frac{1}{\rho}\,\frac{\partial p}{\partial x} + \frac{1}{\rho}\,\frac{\partial \tau_{xz}}{\partial z} + f\,v\,, \tag{6.13a}$$

$$\frac{\partial v}{\partial t} + u\,\frac{\partial v}{\partial x} + v\,\frac{\partial v}{\partial y} + w\,\frac{\partial v}{\partial z} = -\frac{1}{\rho}\,\frac{\partial p}{\partial y} + \frac{1}{\rho}\,\frac{\partial \tau_{yz}}{\partial z} - f\,u\,, \tag{6.13b}$$

$$\frac{\partial w}{\partial t} + u\,\frac{\partial w}{\partial x} + v\,\frac{\partial w}{\partial y} + w\,\frac{\partial w}{\partial z} = -\frac{1}{\rho}\,\frac{\partial p}{\partial z} - g\,. \tag{6.13c}$$

6.3 Continuity equation

The equation system (6.13) is not yet complete. In order to account for the mass conservation, we assume that the ocean water is incompressible and satisfies therefore the continuity equation (3.8):

$$\frac{\partial u}{\partial x} + \frac{\partial v}{\partial y} + \frac{\partial w}{\partial z} = 0\,. \tag{6.14}$$

6.4 Special case: Shallow water equations

6.4.1 General derivation of one-layer model

We now assume that the ocean is a homogeneous layer of water of average thickness H, its surface everywhere at height $z = 0$ in the stationary equilibrium but generally at height $z = \eta$, the ocean bottom at height $z = -H + \eta_\mathrm{b}$ (Fig. 6.3). Thus, the local instantaneous layer thickness is $h = H + \eta - \eta_\mathrm{b}$. If the average thickness H of the water layer is much smaller than its horizontal extent—a precondition of the subsequently described *shallow water model*—then the vertical accelerations in the water mass will be rather small ($\mathrm{D}w/\mathrm{D}t \approx 0$), so that the ocean will be approximately in the so-called *hydrostatic equilibrium*, defined by the *hydrostatic equation* following from the vertical component of the equation of motion (6.12c):

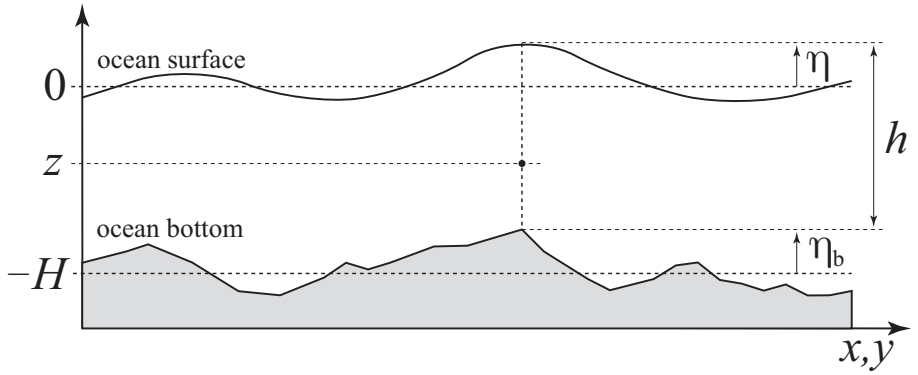

Figure 6.3: Vertical cross section showing a part of the ocean. Average layer thickness H, water surface at height $z = \eta$, bottom at height $z = -H + \eta_\mathrm{b}$, local layer thickness $h = H + \eta - \eta_\mathrm{b}$.

$$\frac{\partial p}{\partial z} = -\rho\, g \ . \tag{6.15}$$

Under these conditions, the *hydrostatic pressure* at height z within the water layer is given by

$$\begin{aligned} p(z) &= p(\eta) + \Big(p(z) - p(\eta)\Big) \\ &= p(\eta) + \int\limits_{\eta}^{z} \frac{\partial p}{\partial z}\, \mathrm{d}z \\ &= p(\eta) + \rho\, g\, (\eta - z) \ . \end{aligned}$$

It is therefore equal to the sum of the atmospheric air pressure at the surface of the ocean water, $p(\eta)$, and the weight per unit area of the water column above, $\rho\, g\, (\eta - z)$. Assuming the atmospheric air pressure to be constant, we get for the pressure gradients $\partial p/\partial x$ and $\partial p/\partial y$

$$\begin{aligned} \frac{\partial p}{\partial x} &= \rho\, g\, \frac{\partial \eta}{\partial x} \\ \frac{\partial p}{\partial y} &= \rho\, g\, \frac{\partial \eta}{\partial y} \ . \end{aligned}$$

Obviously, the pressure gradients within the layer in hydrostatic equilibrium are independent of z. Due to this important fact, the horizontal components of the velocity u and v are constant with height for all time, if this had already been the case at the beginning. Provided this case, the friction forces due to shear stress vanish and the horizontal components of the equation of motion (6.12) become

$$\frac{\partial u}{\partial t} + u\, \frac{\partial u}{\partial x} + v\, \frac{\partial u}{\partial y} = -g\, \frac{\partial \eta}{\partial x} + f\, v \tag{6.16a}$$

$$\frac{\partial v}{\partial t} + u\, \frac{\partial v}{\partial x} + v\, \frac{\partial v}{\partial y} = -g\, \frac{\partial \eta}{\partial y} - f\, u \ , \tag{6.16b}$$

where we have written out in full the material derivative, as in (6.13), and the vertical motions neglected.

In order to close the equation system for the three unknowns u, v and η, we integrate the continuity equation (6.14) from the bottom of the ocean water layer to its surface. To be sufficiently exact, we take the vertical motions into account:

$$\begin{aligned} &\int\limits_{-H+\eta_\mathrm{b}}^{\eta} \left(\frac{\partial u}{\partial x} + \frac{\partial v}{\partial y} + \frac{\partial w}{\partial z}\right) \mathrm{d}z \\ &\qquad = \int\limits_{-H+\eta_\mathrm{b}}^{\eta} \frac{\partial u}{\partial x}\, \mathrm{d}z + \int\limits_{-H+\eta_\mathrm{b}}^{\eta} \frac{\partial v}{\partial y}\, \mathrm{d}z + \int\limits_{-H+\eta_\mathrm{b}}^{\eta} \frac{\partial w}{\partial z}\, \mathrm{d}z \quad = \quad 0 \ . \end{aligned} \tag{6.17}$$

The limits of integration $z_1 = -H + \eta_\mathrm{b}$ and $z_2 = \eta = z_1 + h$ are functions of x and y, i.e. $z_1 = z_1(x, y) = -H + \eta_\mathrm{b}(x, y)$ and $z_2 = \eta(t, x, y) = z_1(x, y) + h(t, x, y)$. Using the Leibniz integral rule (rule for the differentiation of a definite integral) and

noting that the velocities u and v are constant, we get

$$\begin{aligned}
\int_{-H+\eta_\mathrm{b}}^{\eta} \frac{\partial u}{\partial x}\,\mathrm{d}z &= \frac{\partial}{\partial x}\int_{-H+\eta_\mathrm{b}}^{\eta} u\,\mathrm{d}z - u\,\frac{\partial \eta}{\partial x} + u\,\frac{\partial \eta_\mathrm{b}}{\partial x} \\
&= \frac{\partial\Big(u\,(H+\eta-\eta_\mathrm{b})\Big)}{\partial x} - u\,\frac{\partial \eta}{\partial x} + u\,\frac{\partial \eta_\mathrm{b}}{\partial x} \\
&= \frac{\partial\,(u\,h)}{\partial x} - u\,\frac{\partial \eta}{\partial x} + u\,\frac{\partial \eta_\mathrm{b}}{\partial x}\,, \\
\int_{-H+\eta_\mathrm{b}}^{\eta} \frac{\partial v}{\partial y}\,\mathrm{d}z &= \frac{\partial}{\partial y}\int_{-H+\eta_\mathrm{b}}^{\eta} v\,\mathrm{d}z - v\,\frac{\partial \eta}{\partial y} + v\,\frac{\partial \eta_\mathrm{b}}{\partial y} \\
&= \frac{\partial\,(v\,h)}{\partial y} - v\,\frac{\partial \eta}{\partial y} + v\,\frac{\partial \eta_\mathrm{b}}{\partial y}\,, \\
\int_{-H+\eta_\mathrm{b}}^{\eta} \frac{\partial w}{\partial z}\,\mathrm{d}z &= w(\eta) - w(-H+\eta_\mathrm{b})
\end{aligned}$$

and with this from (6.17)

$$\begin{aligned}
&\frac{\partial\,(u\,h)}{\partial x} - u\,\frac{\partial \eta}{\partial x} + u\,\frac{\partial \eta_\mathrm{b}}{\partial x} \\
&\quad + \frac{\partial\,(v\,h)}{\partial y} - v\,\frac{\partial \eta}{\partial y} + v\,\frac{\partial \eta_\mathrm{b}}{\partial y} \\
&\qquad + w(\eta) - w(-H+\eta_\mathrm{b}) = 0\,.
\end{aligned} \tag{6.18}$$

The difference between the vertical velocity at the surface $w(\eta)$ and the vertical velocity at the bottom $w(-H+\eta_\mathrm{b})$ corresponds to the change in height per unit time of the water column between $-H+\eta_\mathrm{b}$ and η and therefore to the material derivative (with respect to the horizontal motion) of the column height $h(t,x,y) = H + \eta(t,x,y) - \eta_\mathrm{b}(x,y)$:

$$\begin{aligned}
w(\eta) - w(-H+\eta_\mathrm{b}) &= \frac{\mathrm{D}h}{\mathrm{D}t} \\
&= \frac{\partial h}{\partial t} + u\,\frac{\partial h}{\partial x} + v\,\frac{\partial h}{\partial y} \\
&= \frac{\partial \eta}{\partial t} + u\,\frac{\partial \eta}{\partial x} + v\,\frac{\partial \eta}{\partial y} - u\,\frac{\partial \eta_\mathrm{b}}{\partial x} - v\,\frac{\partial \eta_\mathrm{b}}{\partial y}\,.
\end{aligned}$$

So, we obtain from (6.18)

$$\frac{\partial \eta}{\partial t} + \frac{\partial\,(u\,h)}{\partial x} + \frac{\partial\,(v\,h)}{\partial y} = 0\,,$$

or, because $h = H + \eta - \eta_\mathrm{b}$, where H as well as η_b are time independent,

$$\frac{\partial h}{\partial t} + \frac{\partial\,(u\,h)}{\partial x} + \frac{\partial\,(v\,h)}{\partial y} = 0\,. \tag{6.19}$$

The equation of motion (6.16) and continuity equation (6.19) represent the funda-

mental equations of the shallow water model, namely the shallow water equations

$$\frac{\partial u}{\partial t} + u\,\frac{\partial u}{\partial x} + v\,\frac{\partial u}{\partial y} = -g\,\frac{\partial \eta}{\partial x} + f\,v\,, \tag{6.20a}$$

$$\frac{\partial v}{\partial t} + u\,\frac{\partial v}{\partial x} + v\,\frac{\partial v}{\partial y} = -g\,\frac{\partial \eta}{\partial y} - f\,u\,, \tag{6.20b}$$

$$\frac{\partial h}{\partial t} + u\,\frac{\partial h}{\partial x} + v\,\frac{\partial h}{\partial y} = -h\left(\frac{\partial u}{\partial x} + \frac{\partial v}{\partial y}\right)\,, \qquad h = H + \eta - \eta_\mathrm{b}\;; \tag{6.20c}$$

the continuity equation (6.20c) follows from (6.19) with the aid of the product rule of differentiation.

We now consider briefly a few approximations of (6.20) which demonstrate that the shallow water equations permit solutions that represent various types of propagating waves. These waves are of central importance to understand the effect of local anomalies in e.g., surface elevation, temperature or salinity, on the large scale circulation. Waves are also key to enable various modes of natural variability in the climate system, e.g., El Niño-Southern Oscillation (see Section 8.6.2). The waves that we discuss here occur in principle both in the ocean and the atmosphere, but we will focus on the ocean.

We first simplify the shallow water equations by assuming a flat bottom ($\eta_\mathrm{b} = 0$), small velocities u, v and elevations $\eta \ll H$, as well as small space derivatives of u, v and h. In this case the non-linear terms are negligible:

$$\frac{\partial u}{\partial t} - f\,v = -g\,\frac{\partial \eta}{\partial x} \tag{6.21a}$$

$$\frac{\partial v}{\partial t} + f\,u = -g\,\frac{\partial \eta}{\partial y} \tag{6.21b}$$

$$\frac{\partial \eta}{\partial t} = -H\left(\frac{\partial u}{\partial x} + \frac{\partial v}{\partial y}\right)\,. \tag{6.21c}$$

6.4.2 Gravity waves in a non-rotating ocean

Further restricting considerations to a non-rotating Earth ($f = 0$), taking the time derivative $\partial/\partial t$ of the continuity equation (6.21c), the space derivative $\partial/\partial x$ of the equation of motion (6.21a) and the space derivative $\partial/\partial y$ of the equation of motion (6.21b) we obtain a single equation for the surface elevation:

$$\frac{\partial^2 \eta}{\partial t^2} = g\,H\,\vec{\nabla}^2 \eta\,. \tag{6.22}$$

This is a classical 2-dimensional wave equation, formally identical to (3.17). Solutions of the simplified shallow water equations (6.21) in the non-rotating case are therefore, among others, harmonic dispersion-free gravity waves. The solutions are

given by

$$\eta(x, y, t) = \tilde{\eta}\, \mathrm{e}^{\mathrm{i}(kx+ly-\omega t)}\,, \tag{6.23}$$

where the following dispersion relation between angular frequency ω and the horizontal wavenumbers k and l must be satisfied:

$$\omega = \sqrt{gH}\, K\,, \quad \text{with} \quad K = \sqrt{k^2 + l^2}\,. \tag{6.24}$$

K is the magnitude of the wavenumber vector (k, l) which points in the direction of wave propagation. The phase speed is given by $c_{ph} = \omega/K = \sqrt{gH}$, and is constant, i.e. it does not depend on the angular frequency of the gravity wave. Therefore, gravity waves in a non-rotating frame are dispersion-free.

6.4.3 Poincaré waves and Kelvin waves

The effect of the Earth's rotation brings about important modifications of the wave propagation and also generates new types of waves which do not exist in non-rotating environments. Here we consider the case of a constant Coriolis parameter $f \neq 0$; waves propagate on an f-plane. Seeking a wave solution to (6.21), we assume that also u and v take the form (6.23) with amplitudes $\tilde{u}$ and $\tilde{v}$, respectively. Inserting these into (6.21) yields a system of three linear equations which permits non-trivial solutions for $(\tilde{u}, \tilde{v}, \tilde{\eta})$ only if

$$\omega\,(\omega^2 - gH\,K^2 - f^2) = 0\,. \tag{6.25}$$

The dispersion relation therefore reads

$$\omega = \sqrt{gH\,K^2 + f^2}\,, \tag{6.26}$$

and is shown in Fig. 6.4. The phase speed of the wave, $c_{ph} = \omega/K$, here depends on the wavenumber, and therefore gravity waves in a rotating frame are dispersive. There are two limiting cases based on the characteristic length scales relative to the *Rossby radius* which is defined as $L_R = \sqrt{gH}/f$. Typical values for the Rossby radius in an ocean of depth 4 km at mid-latitudes are about 2000 km, for a shallower layer of only 400 m, we have $L_R \approx 600\,\mathrm{km}$.

The Rossby radius separates two distinct gravity wave regimes in a rotating environment. For wavelengths much shorter than the Rossby radius, i.e., $\lambda = 2\pi/K \ll L_R$, rotation becomes unimportant and the waves are non-dispersive with $\omega = \sqrt{gH}\, K$. For wavelengths longer than the Rossby radius, ω approaches f. These waves are called *Poincaré waves*. Their angular frequency has a lower bound f, whereas in the non-rotating case, ω will approach 0 for very long gravity waves.

A special case occurs at lateral boundaries in a rotating ocean. Such boundaries act as wave guides. For illustration we assume that there is a north-south wall at $x = 0$ which requires $u = 0$. Equations (6.21b) and (6.21c) can then be combined as follows:

$$\frac{\partial^2 \eta}{\partial t^2} = g\,H\,\frac{\partial^2 \eta}{\partial y^2}\,, \tag{6.27}$$

with the general solution $\eta(x,y,t) = \tilde{\eta}(x)\,\mathrm{e}^{\mathrm{i}(ly-\omega t)}$, provided $\omega = \pm\sqrt{gH}\,l$. This is a wave travelling in the y-direction at phase speed $c_{ph} = \sqrt{gH}$. Assuming a formally identical solution for v, inserting it into (6.21a) and (6.21b), and using the dispersion relation, we obtain

$$\frac{\partial \tilde{\eta}}{\partial x} = \pm\frac{f}{\sqrt{gH}}\,\tilde{\eta}\,. \tag{6.28}$$

A finite solution for $x > 0$ is therefore:

$$\tilde{\eta}(x) = \hat{\eta}\,\mathrm{e}^{-x/L_R}\,, \tag{6.29}$$

where we have used the definition of the Rossby radius $L_R = \sqrt{gH}/f$, and the appropriate sign in (6.28) for the domain of propagation. Exponential decay away from a boundary is the salient property of *Kelvin waves*. This highlights the fact that the Rossby radius is also the characteristic length scale of a Kelvin wave. In the northern hemisphere, where $f > 0$, Kelvin waves propagate with the boundary to their right: northward at eastern boundaries, southward at western boundaries, and westward at northern boundaries and eastward at southern boundaries. The dispersion relation is shown in Fig. 6.4.

It turns out that also the equator, where $f = 0$, acts as a wave guide along which waves can travel. This is due to the fact that f changes sign at the equator where we have $f = \beta y$ (see eq. 6.9). Since the boundary needs to be to the right of a Kelvin wave travelling in the northern hemisphere, and to the left in the southern hemisphere, equatorial Kelvin waves propagate from west to east with $c_{ph} = \sqrt{gH}$. The amplitude of an equatorial Kelvin wave decays as $\mathrm{e}^{-1/2(y/L_E)^2}$ away from the equator, where $L_E = (\sqrt{gH}/\beta)^{1/2}$ is the *equatorial Rossby radius*. This is one key element in the equatorial ocean to understand the dynamics of El Niño-Southern Oscillation.

6.4.4 Rossby waves

The shallow water equations (6.21) support yet another class of waves which arise due to the dependence of the Coriolis parameter f on latitude. Such changes become important at scales larger than the Rossby radius. To extract these waves we build $-\partial/\partial y$(6.21a)$+\partial/\partial x$(6.21b) which eliminiates the pressure gradients in the momentum equations:

$$\frac{\partial}{\partial t}\left(\frac{\partial v}{\partial x} - \frac{\partial u}{\partial y}\right) + f\left(\frac{\partial u}{\partial x} + \frac{\partial v}{\partial y}\right) + \beta v = 0\,. \tag{6.30}$$

Note that we used $f = f_0 + \beta y$. We further assume that $\partial\eta/\partial t = 0$, in which case, according to (6.21c), the divergence of the flow field vanishes. This permits the

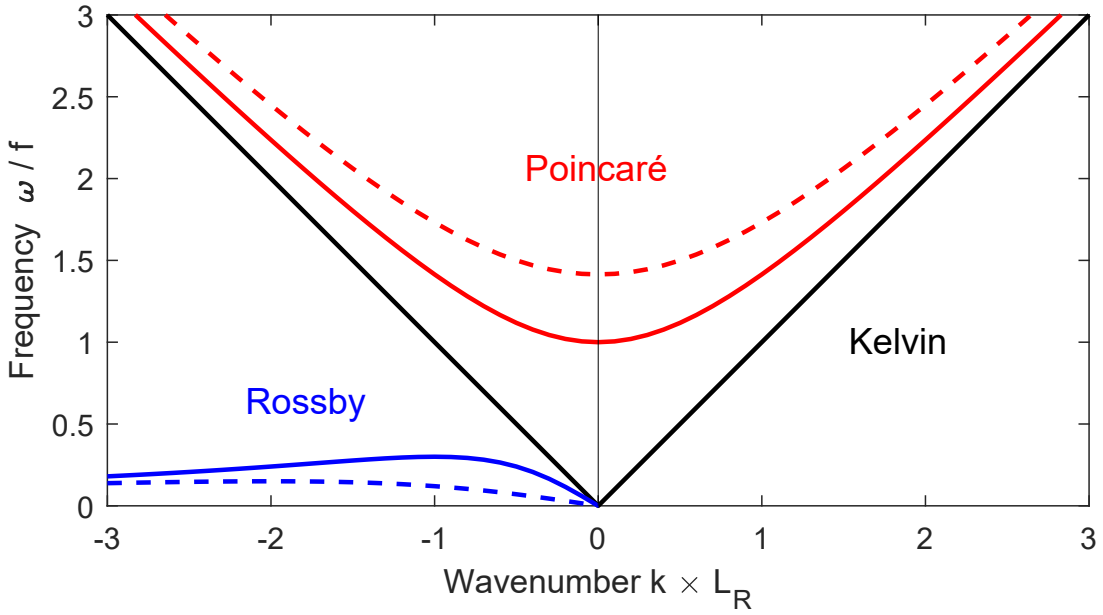

Figure 6.4: Dispersion relations for the various types of midlatitude shallow water waves on an f-plane (Poincaré and Kelvin waves) and on a β-plane (Rossby waves), according to the approximations in subsections 6.4.3 and 6.4.4. The next mode with meridional wavenumber l is shown in dashed lines.

introduction of a stream function $\psi(x, y)$ as follows:

$$u = -\frac{\partial \psi}{\partial y} \quad , \quad v = \frac{\partial \psi}{\partial x} \, . \tag{6.31}$$

Replacing u and v in (6.30) by $\psi(x, y)$ we get

$$\frac{\partial}{\partial t}\left(\frac{\partial^2 \psi}{\partial x^2} + \frac{\partial^2 \psi}{\partial y^2}\right) + \beta \frac{\partial \psi}{\partial x} = 0 \, , \tag{6.32}$$

which supports wave solutions of the form $\psi(x, y, t) = \tilde{\psi}\, \mathrm{e}^{\mathrm{i}(kx+ly-\omega t)}$, provided the dispersion relation

$$\omega = -\frac{\beta\, k}{k^2 + l^2} \tag{6.33}$$

holds (Fig. 6.4). Note that the phase of the Rossby wave only propagates in one direction, as indicated in the fixed sign relation between wavenumber and angular frequency in (6.33): Rossby waves propagate from east to west in a fluid at rest.

A similar analysis can be carried out for a fluid with a background flow U. In this case, an additional term $U\, k$ appears in (6.33), and for a particular wavelength, Rossby waves can become stationary ($c_{ph} = \omega/k = 0$), if the background flow is eastward ($U > 0$). The equatorial wave guide also supports *equatorial Rossby waves*, in addition to the equatorial Kelvin waves. For a much more extended presentation of the dynamics the reader is referred to Vallis (2017).

6.4.5 Further considerations on the shallow water waves

To obtain the dispersion relations for the Poincaré and Rossby waves above, we have made simplifications which are, however, not necessary. The full dispersion relation of (6.21) on a mid-latitude β-plane can be determined by first bringing all terms in (6.21) to the left-hand side and then building $\partial^2/\partial t^2$(6.21b) $- g\,\partial^2/\partial t\partial y$(6.21c) $- gH\,\partial/\partial x(\partial/\partial x$(6.21b)$-\partial/\partial y$(6.21a)$) - f\,(\partial/\partial t$(6.21a)$- g\,\partial/\partial x$(6.21c)$)$. This eliminates u and η, and by assuming $v(x,y,t) = \tilde{v}\,\mathrm{e}^{\mathrm{i}(kx+ly-\omega t)}$, we obtain the full dispersion relation.

The shallow water equations (6.20) include non-linear terms which preclude analytical solutions in most cases. Therefore, numerical methods must be employed to calculate the flow on discretized grids. Because of the presence of waves on different time and space scales the numerical implementation is not straightforward. A comprehensive exposition of the problem is found in Griffies (2005).

In the next section we provide a short overview of the most commonly used two-dimensional grids that are employed to numerically solve the partial differential equations that describe the circulations in the ocean and the atmosphere.

6.5 Different types of grids in climate models

The solution of the partial differential equations describing the dynamics in climate models requires discretization of the equations. Up to now, we only considered one-dimensional problems (Section 3.5). Furthermore, we have assumed that all quantities are evaluated at the same grid points. However, in most cases this is not the best choice. It will be shown in simple examples that other arrangements of grids, which represent the physical reality better, lead to much more efficient schemes. This will be illustrated using the one-dimensional version of the simplified shallow water equations (6.21).

Here we focus, for simplicity and clarity, on Cartesian grids which are suitable for equations formulated in Cartesian coordinates. Generally, climate models use spherical coordinates. Because of basin boundaries in the ocean component of these models, the equations are generally solved on a grid which discretizes along the spherical coordinates (r, λ, φ). However, for atmospheric models which cover the entire globe, an alternative technique based on the transformation into spectral space is also frequently used. The basics are presented in Section 6.6.

The simplified shallow water equations (6.21) in one dimension and in a non-rotating frame are given by

$$\frac{\partial u}{\partial t} = -g\,\frac{\partial \eta}{\partial x}\,, \tag{6.34a}$$

$$\frac{\partial \eta}{\partial t} = -H\,\frac{\partial u}{\partial x}\,, \tag{6.34b}$$

where the two unknown functions $u(x,t)$ and $\eta(x,t)$ are to be determined. It is important to realize that the two equations in (6.34) are tightly coupled. If we choose the common discretization in space according to $x = i\,\Delta x$ with the denominations

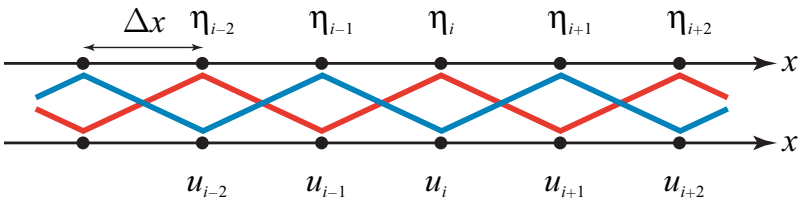

Figure 6.5a: Simple spatial grid for the shallow water equations. The structure of the two equations dictates two independent sub-grids (red and blue lines).

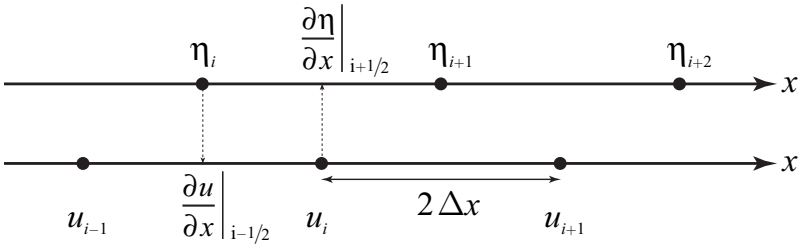

Figure 6.5b: Staggered grid for the shallow water equations. Flux quantities (u) and volume quantities (η) are evaluated at different points.

$u_i \equiv u(i\,\Delta x, t)$, and $\eta_i \equiv \eta(i\,\Delta x, t)$, both functions are evaluated at identical grid points (Fig. 6.5a). The discretized forms of equations (6.34) read

$$\frac{\partial u_i}{\partial t} = -g\,\frac{\eta_{i+1} - \eta_{i-1}}{2\,\Delta x}\,, \tag{6.35a}$$

$$\frac{\partial \eta_i}{\partial t} = -H\,\frac{u_{i+1} - u_{i-1}}{2\,\Delta x}\,. \tag{6.35b}$$

Thus, it appears that the two schemes are applied on two independent sub-grids, the solution vectors (η_{2k}, u_{2k+1}) and (η_{2k+1}, u_{2k}) are mutually independent and no information is interchanged. The error of the schemes in (6.35) is of order Δx^2.

By shifting one axis in Fig. 6.5a, we consider a *staggered grid* as it is shown in Fig. 6.5b. Here, twice the grid spacing as before is chosen. Therefore, only half the number of values needs to be computed. The discretized forms of equations (6.34) for this grid are given by

$$\frac{\partial u_i}{\partial t} = -g\,\left.\frac{\partial \eta}{\partial x}\right|_{i+1/2} = -g\,\frac{\eta_{i+1} - \eta_i}{2\,\Delta x}\,, \tag{6.36a}$$

$$\frac{\partial \eta_i}{\partial t} = -H\,\left.\frac{\partial u}{\partial x}\right|_{i-1/2} = -H\,\frac{u_i - u_{i-1}}{2\,\Delta x}\,. \tag{6.36b}$$

By evaluating derivatives in (6.36) at the intermediate points, they can be regarded as central differences with an equivalent grid spacing of Δx, even though indices only include immediate neighbors. For this reason, the schemes in (6.36) are of the same accuracy as the ones in (6.35), where twice the number of values need to be computed. Hence, the staggered grid affords a significant improvement with regard to the present differential equations.

These findings can be generalized to two dimensions. To illustrate this, we consider again the equation system (6.20), where the three unknown functions $u(x, y, t)$,

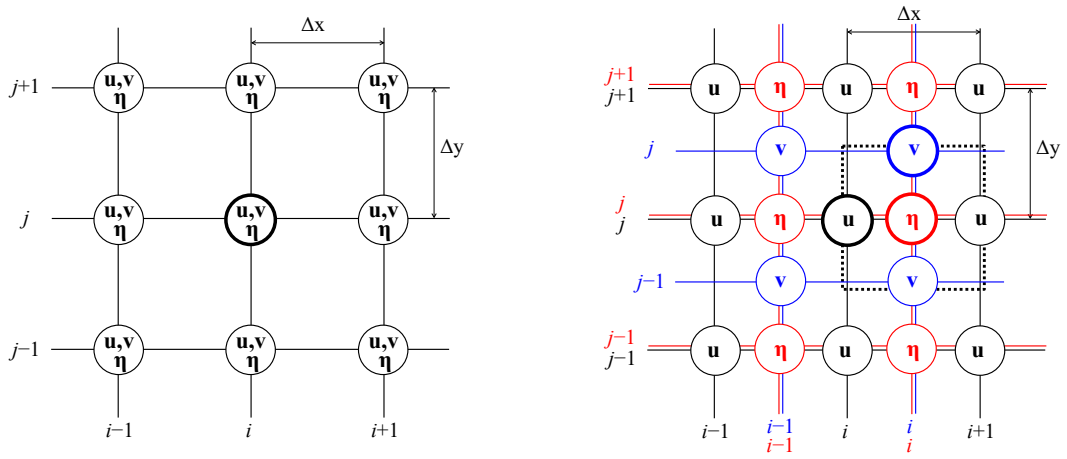

Figure 6.6: Left: Two-dimensional Arakawa A-grid in which all quantities are evaluated at identical grid points. Right: Arakawa C-grid which consists of three sub-grids, one for each field to be calculated. The dashed square indicates a hypothetical physical grid box. Flux quantities u and v are evaluated at the center of the faces of the box, whereas volume quantities η are taken in the centre of the box. Grid positions at indices (i, j) of the respective sub-grid are circled bold.

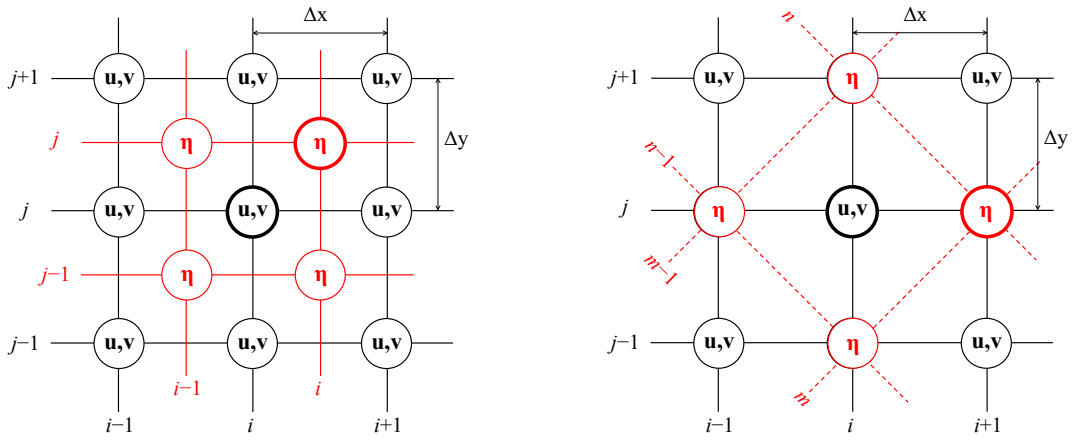

Figure 6.7: Left: The two-dimensional Arakawa B-grid consists of two subgrids, one for the velocities which are evaluated at identical grid points, and one for η. Right: Arakawa E-grid which has only one grid whose points are alternatively occupied by velocities and η. This grid can also be set up consisting of two subgrids, one for (u, v) and one for η, as indicated by the red dashed grid, rotated by 45°. The B- and E-grids are structurally identical. Grid positions at indices (i, j) are circled bold.

$v(x, y, t)$ and $\eta(x, y, t)$ have to be computed on a two-dimensional grid (Figs. 6.6 and 6.7). In case all functions are evaluated at the same grid points (Fig. 6.6, left), we denote this an A-grid (*Arakawa A-grid*). This structurally most simple grid has disadvantages in representing spatial gradients.

A commonly used grid is the C-grid (*Arakawa C-grid*). It results from the A-grid by defining a subgrid for each unknown u, v, and η and staggering them by half a grid length $\frac{1}{2}\Delta x$ and $\frac{1}{2}\Delta y$, respectively. Velocity components of different directions are evaluated at different locations (Fig. 6.6, right). This grid structure represents the physics of fluid motion appropriately with respect to the conservation of mass and momentum, because *flux quantities*, such as the velocities, energy fluxes, etc., are defined at the boundaries of a hypothetical physical box (dashed square box in Fig. 6.6, right), while *volume quantities*, such as the surface elevation, temperature,

salinity, density, concentrations of tracers, etc., are represented in the center of this box. When using the C-grid in solving the shallow water equations (6.20) the spatial gradients can be easily represented, but evaluating the Coriolis term at a specific velocity grid point requires averaging the values of the nearest neighbors.

For illustration we here give the discretized version of (6.20a) for the Arakawa-C grid, and we use central differences for the time discretization $t = n \cdot \Delta t$:

$$\frac{u_{i,j}^{n+1} - u_{i,j}^{n-1}}{2\Delta t} = -u_{i,j}^{n} \frac{u_{i+1,j}^{n} - u_{i-1,j}^{n}}{2\Delta x} - \overline{v_{i,j}^{n}} \frac{u_{i,j+1}^{n} - u_{i,j-1}^{n}}{2\Delta y} - g \frac{\eta_{i,j}^{n} - \eta_{i-1,j}^{n}}{\Delta x} + f\, \overline{v_{i,j}^{n}} \quad (6.37)$$

with $\overline{v_{i,j}^{n}} = \frac{1}{4}(v_{i,j}^{n} + v_{i-1,j}^{n} + v_{i-1,j-1}^{n} + v_{i,j-1}^{n})$. It is evident that the Arakawa-C grid is not ideal for the representation of the meridional advection and Coriolis terms. For simplicity here we have chosen central differences for time stepping, but the Lax-Wendroff scheme (see Section 3.6.5) would be preferable.

Alternative choices of grids that are used in ocean models are the B-grid (*Arakawa B-grid*) and the E-grid (*Arakawa E-grid*) for which the velocity components are evaluated at grid points between the η points (Fig. 6.7). Therefore, they consist of two subgrids, one for the two velocity components and one for η, and the subgrids are staggered by $\frac{1}{2}\Delta x$ or $\frac{1}{2}\Delta y$. Note that for $\Delta x = \Delta y$ the B- and E-grids are structurally identical: By rotation of 45° and stretching by a factor of $\sqrt{2}$ the B-grid is transformed into an E-grid.

It is important to note that each grid has special properties regarding conservation of physical quantitites and characteristics of wave propagation in the two-dimensional space. Dispersion and damping of waves, e.g., the gravity and planetary Rossby waves in (6.20), depend on the grid on which the system of equations is solved. More details on the properties of these grids are given in Randall (1994).

So far we have discussed two-dimensional horizontal grids. In the atmosphere or ocean model components, the vertical dimension is also discretized, and this can be achieved by applying the considerations above. In atmosphere models, pressure coordinates are preferred, in ocean models most often depth is used, but there are also so called *isopycnal ocean models* that employ density as the vertical coordinate.

We now consider a simple, one-dimensional application of a staggered grid. This choice is convenient when solving the one-dimensional energy balance model. Equation (4.9) can be simplified to

$$\frac{\partial T}{\partial t} = a + b\,T^4 + c\,\frac{\partial}{\partial \varphi}\left(e\,\frac{\partial T}{\partial \varphi}\right) \ , \quad (6.38)$$

with spatially dependent coefficients a, b, c and e. In this model, temperature is the volume quantity while the meridional temperature gradient represents a flux quantity. If an A-grid is selected (Fig. 6.8a), the discretized form of (6.38) reads

$$\frac{\partial T_i}{\partial t} = a_i + b_i\,T_i^4 + c_i\,\frac{e_{i+1}\,T'_{i+1} - e_{i-1}\,T'_{i-1}}{2\,\Delta\,\varphi} \quad (6.39a)$$

$$\left(\frac{\partial T}{\partial \varphi}\right)_i = T'_i = \frac{T_{i+1} - T_{i-1}}{2\,\Delta\,\varphi} \ , \quad (6.39b)$$

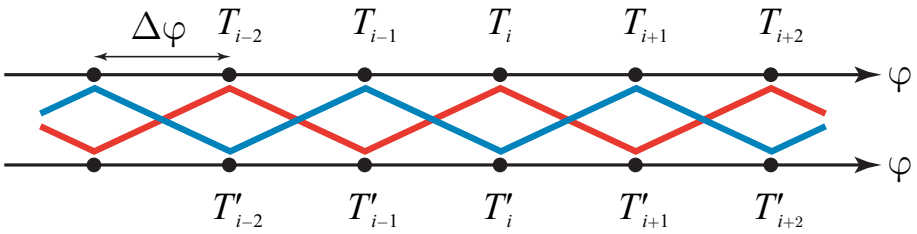

Figure 6.8a: A-grid for the one-dimensional energy balance model. The scheme (6.39) for the solution of (6.38) results in two independent sub-grids (colored lines).

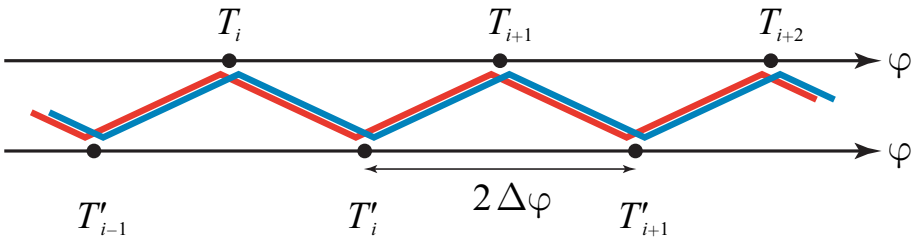

Figure 6.8b: C-grid for the one-dimensional energy balance model.

where again (T_{2k}, T'_{2k+1}) and (T_{2k+1}, T'_{2k}) are independent solution vectors. The solution is evaluated on two non-connected sub-grids.

In a C-grid configuration (Fig. 6.8b) with double grid spacing, only half the number of functions has to be evaluated and, accordingly, the discretized form reads

$$\frac{\partial T_i}{\partial t} = a_i + b_i\, T_i^4 + c_i\, \frac{e_i\, T'_i - e_{i-1}\, T'_{i-1}}{2\,\Delta\varphi}\,, \tag{6.40a}$$

$$T'_i = \frac{T_{i+1} - T_i}{2\,\Delta\varphi}\,, \tag{6.40b}$$

which is of the same accuracy, but requires only half the computational resources. In addition, the implementation of boundary conditions with respect to the flux quantities (4.10) is straightforward, since they can be set to zero: $T'_0 = 0$ and $T'_M = 0$.

6.6 Spectral models

Here, a short section on an important alternative method to solve partial differential equations in spherical coordinates (r, λ, φ) is presented. Up to now, we have treated several methods that make use of finite differences. For the atmosphere component of global climate models, the integration domain covers a sphere, which enables the use of particular functions for the solution of the partial differential equations. Therefore, in order to solve equations of the type given in (6.22) on a sphere, spectral methods are often applied.

Usually, the atmospheric components of global climate models are spectral models. In global ocean models they are employed rarely, or only for the vertical component as the strong gradients of properties near the surface (e.g., temperature) can be better accounted for.

Instead of spanning a grid over the sphere and then replacing the differential equations by a system of equations in finite differences, the unknown functions are expanded by appropriate basis functions which satisfy certain boundary conditions.

Consider eigenfunctions of the Laplace operator on a sphere of radius R,

$$\vec{\nabla}^2 Y_\ell^m = -\frac{\ell\,(\ell+1)}{R^2}\,Y_\ell^m\ , \tag{6.41}$$

namely *spherical harmonics*, which are given by

$$Y_\ell^m(\varphi,\lambda) = P_\ell^m(\sin\varphi)\,\mathrm{e}^{\mathrm{i}\,m\,\lambda}\ , \tag{6.42}$$

where $P_\ell^m(\sin\varphi)$ are *associated Legendre functions of the 1st kind*. The quantities m and ℓ are wavenumbers: $2\,m$ is the number of knot meridians (zeroes on a circle of latitude), $\ell - m$ is the number of knot latitudes excluding the two poles. The following orthogonality relation is valid:

$$\frac{1}{4\,\pi}\int\limits_{-1}^{1}\mathrm{d}\,(\sin\varphi)\int\limits_{0}^{2\,\pi}\mathrm{d}\lambda\ Y_\ell^m\,Y_{\ell'}^{m'} \quad = \quad \begin{cases} 1 & \text{if} \quad m=m',\ \ell=\ell' \\ 0 & \text{else} \end{cases} \tag{6.43}$$

which is consistent with the fact, that (6.42) constitutes a complete basis of functions.

The unknown solution of (6.22) is now expressed as a linear combination of basis functions $Y_\ell^m(\varphi,\lambda)$ with time-dependent coefficients $\Phi_\ell^m(t)$:

$$\eta(t,\varphi,\lambda) = \sum_{|m|\le\ell}\ \sum_{\ell}\Phi_\ell^m(t)\,Y_\ell^m(\varphi,\lambda)\ . \tag{6.44}$$

Inserting (6.44) into (6.22) and using (6.41) we obtain following ordinary differential equations for the coefficient functions:

$$\frac{\mathrm{d}^2\Phi_\ell^m}{\mathrm{d}t^2} = -\ell\,(\ell+1)\,\frac{g\,H}{R^2}\,\Phi_\ell^m\ . \tag{6.45}$$

Hence, the partial differential equation (6.22) is replaced by a set of ordinary differential equations for the coefficient functions $\Phi_\ell^m(t)$. In this special case, the solutions are simply the harmonic modes $\Phi_\ell^m(t) = \phi_\ell^m\cdot\mathrm{e}^{\mathrm{i}\,\omega_\ell\,t}$ with $\omega_\ell^2 = \ell(\ell+1)gH/R^2$.

The expansion in (6.44) theoretically ranges from $\ell = 0,\ \ldots,\ \infty$, $m = -\ell,\ \ldots\ ,+\ell$, but in practice, the summation needs to be truncated at an appropriate point. This results in finite spatial resolution determined by the highest wavenumbers. The most commonly used truncations are *triangular* and *rhomboidal* truncations, schematically illustrated in Fig. 6.9.

Early GCMs used R15 and R21. Transient eddies, important features of the atmosphere, are barely resolved in R15. Hence, the partitioning—in absolute terms—of the meridional heat transport in the atmosphere is not realistically simulated. This is one of the reasons for coupled models of low resolution to require flux corrections (see also Section 8.7). Typical spectral resolutions used today are T42 for coupled

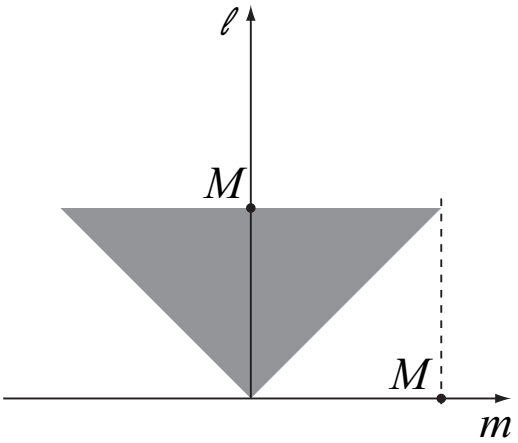

Figure 6.9a: Triangular truncation

$$\eta(t,\varphi,\lambda) = \sum_{m=-M}^{M} \sum_{\ell=|m|}^{M} \Phi_\ell^m(t)\, Y_\ell^m(\varphi,\lambda)$$

denomination: T(M)

e.g., T21, T31, T42, T63, T85, T106

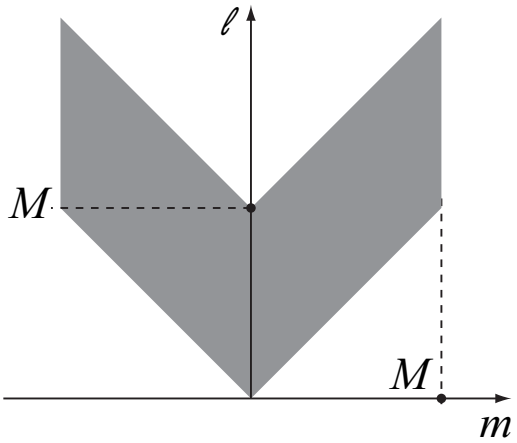

Figure 6.9b: Rhomboidal truncation

$$\eta(t,\varphi,\lambda) = \sum_{m=-M}^{M} \sum_{\ell=|m|}^{|m|+M} \Phi_\ell^m(t)\, Y_\ell^m(\varphi,\lambda)$$

denomination: R(M)

e.g., R15, R21, R30

atmosphere-ocean GCMs used for ensemble or long-term paleoclimate simulations, T639 for the ERA5 reanalysis product, and T7999 for the currently highest resolved spectral model (Wedi et al., 2020).

The choice of the basis function already satisfies some of the boundary conditions. This is a distinct advantage of spectral models. However, one difficulty arises with the treatment of the non-linear and Coriolis terms which are part of the full equations of motion. When these effects are considered, spectral models become much more complicated, and coupling between the individual wavenumbers occurs.

6.7 Wind-driven flow in the ocean (Stommel model)

Since the beginning of inter-continental marine navigation in the 15$^{\text{th}}$ century, it is well known that the surface flow in the ocean is characterized by large-scale gyres (in the northern hemisphere clock-wise subtropical gyre, counter-clockwise subpolar gyre). These gyres are not spatially uniform but feature a strongly intensified current along the western boundary of the ocean basin, namely a strong northward current in the northern hemisphere and a strong southward current in the southern hemisphere, while in the eastern part the currents are weak.

The well-known Gulf stream is part of the western part of the North Atlantic's subtropical gyre. This then turns into the Transatlantic Drift Current as soon as it leaves the American East Coast and moves northward towards the eastern part of the subpolar gyre. Its effects on temperature and salinity are observed as far as Spitsbergen. The Kuroshio Current, the Brazil Current and others form dynamically similar circulation systems.

The wind, i.e., the Westerlies in the mid-latitudes and the pronounced Easterlies more towards the equator, have quickly been identified as causes of these currents. However, the dynamical problem, why the ocean currents only intensify along the

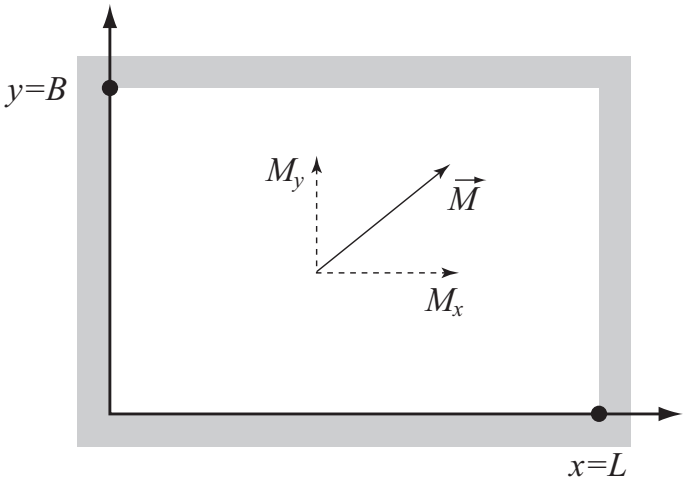

Figure 6.10: Geometry of the ocean basin and mass transport in a Cartesian coordinate system, which is tangent to the Earth's sphere at a given latitude.

western basin boundaries, has not been resolved until 1948 when a landmark paper was published by *Henry Stommel* (1920–1992). Using an elegant model, he demonstrated that the spherical shape of the rotating Earth is the origin of this prominent phenomenon (Stommel, 1948).

Stommel considered a homogenous fluid (ρ = constant) in a flat rectangular basin (Fig. 6.10) on the β-plane; vertical cross-section as shown in Fig. 6.3. He assumed the bottom to be flat, $\eta_\mathrm{b} = 0$, further the atmospheric air pressure at the surface of the ocean water $p(\eta)$ to be constant, and finally the vertical elevation to be much smaller than the mean layer thickness, i.e. $\eta \ll H$. Multiplication of the horizontal components of the equation of motion (6.13) with ρ, integration over the entire depth from the height of the bottom $z = -H$ to the height of the water surface $z = \eta$, plus the assumption of stationarity $\partial/\partial t = 0$ and linearity, yields

$$-f \int_{-H}^{\eta} \rho\, v \,\mathrm{d}z = -\int_{-H}^{\eta} \frac{\partial p}{\partial x}\,\mathrm{d}z + \tau_{xz}(\eta) - \tau_{xz}(-H)\;, \tag{6.46a}$$

$$f \int_{-H}^{\eta} \rho\, u \,\mathrm{d}z = -\int_{-H}^{\eta} \frac{\partial p}{\partial y}\,\mathrm{d}z + \tau_{yz}(\eta) - \tau_{yz}(-H)\;. \tag{6.46b}$$

We define the mass transport as follows:

$$\vec{M} = \int_{-H}^{\eta} \rho\, \vec{u}\,\mathrm{d}z \tag{6.47}$$

and substitute this in (6.46). Equation (6.46) reveals that the mass transport is driven by the shear at the surface and slowed by the friction on the ocean floor. Hence, at the surface the effect of the wind is to transfer momentum into the fluid. The flux of momentum must be passed on to the fluid by internal friction or friction at the bottom of the ocean basin.

Stommel chose the simplest possible parameterisation for this effect by postulating that the shear exerted by the bottom is proportional to the velocity, or the mass

transport, respectively. Hence, (6.46) becomes

$$-f\,M_y = -\int_{-H}^{\eta} \frac{\partial p}{\partial x}\,\mathrm{d}z + \tau_{xz}(\eta) - R\,M_x\ , \tag{6.48a}$$

$$f\,M_x = -\int_{-H}^{\eta} \frac{\partial p}{\partial y}\,\mathrm{d}z + \tau_{yz}(\eta) - R\,M_y\ , \tag{6.48b}$$

where R is an inverse characteristic spin-down time of the circulation due to friction.

6.7.1 Determination of the stream function

By cross-differentiation $\partial(6.48\mathrm{b})/\partial x - \partial(6.48\mathrm{a})/\partial y$ the pressure gradient terms in (6.48) are eliminated. Taking (6.9) into account, we obtain

$$\beta\,M_y + f\left(\frac{\partial M_x}{\partial x} + \frac{\partial M_y}{\partial y}\right) = \frac{\partial \tau_{yz}}{\partial x} - \frac{\partial \tau_{xz}}{\partial y} - R\left(\frac{\partial M_y}{\partial x} - \frac{\partial M_x}{\partial y}\right)\ , \tag{6.49}$$

where the functions τ_{xz} and τ_{yz} are now written without argument.

The two unknown components of the mass transport are not mutually independent, since in a closed basin mass conservation must be satisfied. The vertical integration of the continuity equation (6.14) yields, analogously to the derivation leading to (6.19) but with $\partial/\partial t = 0$,

$$\vec{\nabla}\cdot\vec{M} = \frac{\partial M_x}{\partial x} + \frac{\partial M_y}{\partial y} = 0\ , \tag{6.50}$$

where the unknown vector function $\vec{M}$ can now be replaced by a scalar choosing

$$M_x = -\frac{\partial \Psi}{\partial y}\ , \tag{6.51a}$$

$$M_y = \frac{\partial \Psi}{\partial x}\ . \tag{6.51b}$$

The scalar function $\Psi(x, y)$ is called *stream function*. Streamlines are lines of constant stream function, along which the current moves tangentially.

Definition (6.51) satisfies (6.50) automatically, and we can use (6.51) in (6.49) in order to obtain the Stommel equation which was first formulated in 1948 (Stommel, 1948):

$$\beta\,\frac{\partial \Psi}{\partial x} = \frac{\partial \tau_{yz}}{\partial x} - \frac{\partial \tau_{xz}}{\partial y} - R\left(\frac{\partial^2 \Psi}{\partial x^2} + \frac{\partial^2 \Psi}{\partial y^2}\right)\ . \tag{6.52}$$

This equation contains the phenomenon of western boundary currents in an ocean basin in principle. Equation (6.52) is a partial differential equation of 2nd order in x and y for the function $\Psi(x, y)$.

Boundary conditions still remain to be formulated. Since the transport must be parallel to the boundaries, we require along the boundaries in the y-direction $M_x = -\partial\Psi/\partial y = 0$, and along the boundaries in the x-direction $M_y = \partial\Psi/\partial x = 0$. Hence,

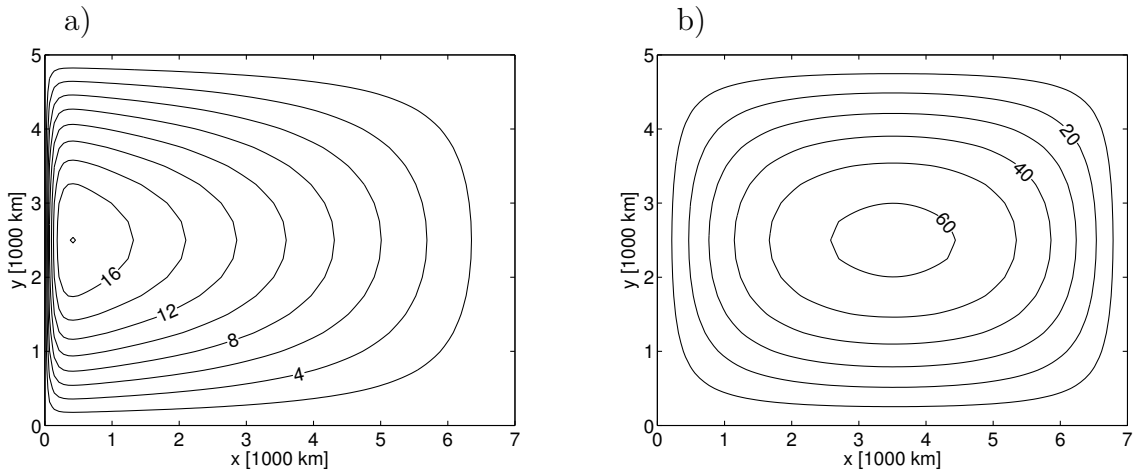

Figure 6.11: Stream function Ψ (in Sverdrup, 1 Sv $= 10^6$ m^3 s^{g-1}) of the Stommel model (6.52) for **a)** $\beta = 2 \cdot 10^{-11}$ m^{-1} s^{-1} and **b)** $\beta = 0$, with $R = 1/(6$ days), and $T = 0.1$ N m^{-2} in (6.54). The numerical solution was computed on a grid with $N_x \times N_y = 100 \times 20$ and using the Method of Successive Overrelaxation (5.22). The current flows clockwise and is parallel to the stream lines.

Ψ is constant along the boundary. Because (6.52) only contains derivatives of Ψ, we can set, without loss of generality,

$$\Psi = 0 \qquad \text{at the boundaries.} \tag{6.53}$$

Therefore, the Stommel model is a boundary value problem with *Dirichlet boundary conditions* (Section 5.1). In order to find the solution, the wind stress must be prescribed. For particularly simple spatial relationships of the stress, the boundary problem may even be solved analytically. To this end, Stommel chose a purely zonal wind stress, typical of the mid-latitude northern hemisphere, given by

$$\tau_{xz} = -\tau_0 \cos\left(\frac{\pi}{B}\, y\right) , \tag{6.54a}$$

$$\tau_{yz} = 0 . \tag{6.54b}$$

Thus, (6.52) can be solved analytically by separation of the variables. But for more complicated profiles of the wind stress, numerical methods presented in Chapter 5, need to be applied. We will not explain this analytical solution but are going to discuss numerical solutions of this problem.

The numerical solutions of the boundary value problem (6.52), (6.53) in a rectangular basin between $0 \le x \le 7000$ km and $0 \le y \le 5000$ km are illustrated in Fig. 6.11. We have employed the Method of Successive Overrelaxation described in Section 5.3.2. On a β-plane, a western boundary current develops; for $\beta = 0$, a symmetric solution results which exhibits no boundary current. The western boundary current in this model appears as soon as the Coriolis parameter f depends on the latitude, implying that the spherical shape of the Earth plays a fundamental role in the establishment of the dynamics.

In case a boundary current is present, the x derivatives of the stream function in (6.52) become dominant at the boundary. Assuming a typical lateral width δ of the

boundary current and inserting $\Psi \sim 1 - \mathrm{e}^{-x/\delta}$ into (6.52), we obtain

$$\beta \, \frac{1}{\delta} \sim R \, \frac{1}{\delta^2} \qquad \text{hence} \qquad \delta \sim \frac{R}{\beta} \, . \tag{6.55}$$

The width of the boundary current (Stommel boundary layer) scales with the friction coefficient and is inversely proportional to β.

6.7.2 Determination of the surface elevation

According to (6.48), wind-driven flow induces pressure gradients, which become manifest as an elevation η of the water surface. This effect shall be quantified in the following. It will lead to a boundary value problem with *Neumann boundary conditions* (Section 5.1).

Analogously to (6.47), we define the pressure integrated over the depth as

$$P = \int_{-H}^{\eta} p \, \mathrm{d}z \tag{6.56}$$

and take $\partial(6.48\mathrm{a})/\partial x + \partial(6.48\mathrm{b})/\partial y$, assuming $\eta \ll H$. Using (6.50) and (6.51), we obtain now the following Poisson equation for $P(x, y)$:

$$\vec{\nabla}^2 P = f \, \vec{\nabla}^2 \Psi + \beta \, \frac{\partial \Psi}{\partial y} + \frac{\partial \tau_{xz}}{\partial x} + \frac{\partial \tau_{yz}}{\partial y} \, . \tag{6.57}$$

With the previous choice of the wind stress (6.54) the last two terms in (6.57) vanish. The boundary conditions for $P(x, y)$ may be derived from (6.48) and the fact that the transport must be parallel to the boundaries:

$$\frac{\partial P}{\partial x} = f \, \frac{\partial \Psi}{\partial x} + \tau_{xz} \qquad \text{at} \quad x = 0 \quad \text{and} \quad x = L \, , \tag{6.58a}$$

$$\frac{\partial P}{\partial y} = f \, \frac{\partial \Psi}{\partial y} + \tau_{yz} \qquad \text{at} \quad y = 0 \quad \text{and} \quad y = B \, . \tag{6.58b}$$

Consequently, the derivatives of P perpendicular to the boundary are fixed (Neumann boundary conditions). It must be noted, that (6.57) and (6.58) restrict the solution up to a single constant.

By calculating $P(x, y)$ based on (6.57) and considering (6.58), we can determine the elevation of the water surface using (6.56) and assuming hydrostatic equilibrium:

$$P(x, y) = \int_{-H}^{\eta} \rho \, g \, (\eta - z) \, \mathrm{d}z = \frac{1}{2} \, \rho \, g \, (H + \eta)^2 \, . \tag{6.59}$$

We expand (6.59) with regard to $\eta \ll H$,

$$P(x, y) = \frac{1}{2} \, \rho \, g \, H^2 \left(1 + \frac{\eta}{H} \right)^2 \approx \frac{1}{2} \, \rho \, g \, H^2 + \rho \, g \, H \, \eta \, ,$$

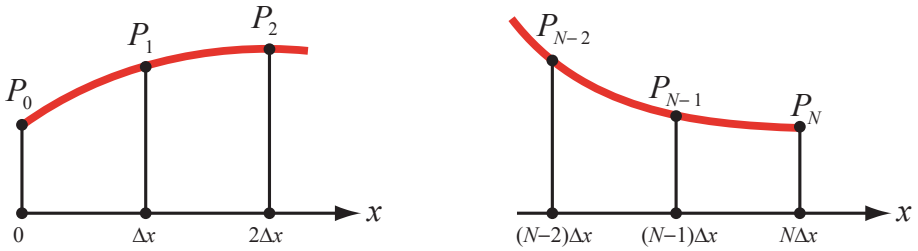

Figure 6.12: Interpolation of the solution at the western and eastern boundary using parabolas.

and find with this

$$\eta(x,y) \approx \frac{P(x,y)}{\rho\, g\, H} - \frac{H}{2}\ . \tag{6.60}$$

The numerical solution of a boundary value problem with Neumann boundary conditions requires some additional considerations. For Dirichlet boundary conditions, such as (6.53), the boundary values are accounted for naturally by setting the values in the numerical scheme directly. However, Neumann boundary conditions require additional information from the points next to the boundary in order to find the values at the boundary itself.

We derive the discretized schemes for the Neumann boundary conditions by calculating the derivatives at the boundary using the values of the grid points inside and assuming an appropriate interpolation. There are various possibilities for this: linear, parabolic, etc. We explain the approach for the boundaries $x = 0$ and $x = L$; corresponding formulations for the other boundaries can be inferred analogously.

In x-direction, the discretisation $\Delta x = L/N$, with $x = i\,\Delta x$ is chosen. We evaluate the solution function $P(x)$ at the grid points, that is $P(i\,\Delta x) \equiv P_i$, where P_0 and P_N are located at the respective boundaries $x = 0$ and $x = L$ (Fig. 6.12). A parabola is assumed to interpolate the solution between the boundary point and the two points closest to the boundary. For the boundary $x = 0$, we assume the quadratic function

$$P(x) = a\,x^2 + b\,x + P_0\ . \tag{6.61}$$

In order to assure that the parabola goes through the values P_1 and P_2, the following must be valid

$$P_1 = a\,(\Delta x)^2 + b\,(\Delta x) + P_0 \qquad \text{and} \qquad P_2 = a\,(2\,\Delta x)^2 + b\,(2\,\Delta x) + P_0\ , \tag{6.62}$$

and analogous expressions hold for the boundary at $x = L$. Solving (6.62) for the coefficients of the interpolation parabola we obtain

$$a = \frac{P_2 - 2\,P_1 + P_0}{2\,\Delta x^2} \qquad \text{and} \qquad b = \frac{-P_2 + 4\,P_1 - 3\,P_0}{2\,\Delta x}\ . \tag{6.63}$$

With this, the first derivative at the boundary can be computed using (6.61):

$$\left.\frac{\mathrm{d}P}{\mathrm{d}x}\right|_{x=0} = b\ . \tag{6.64}$$

Hence, for the derivative to be given as a boundary condition at the boundaries, we

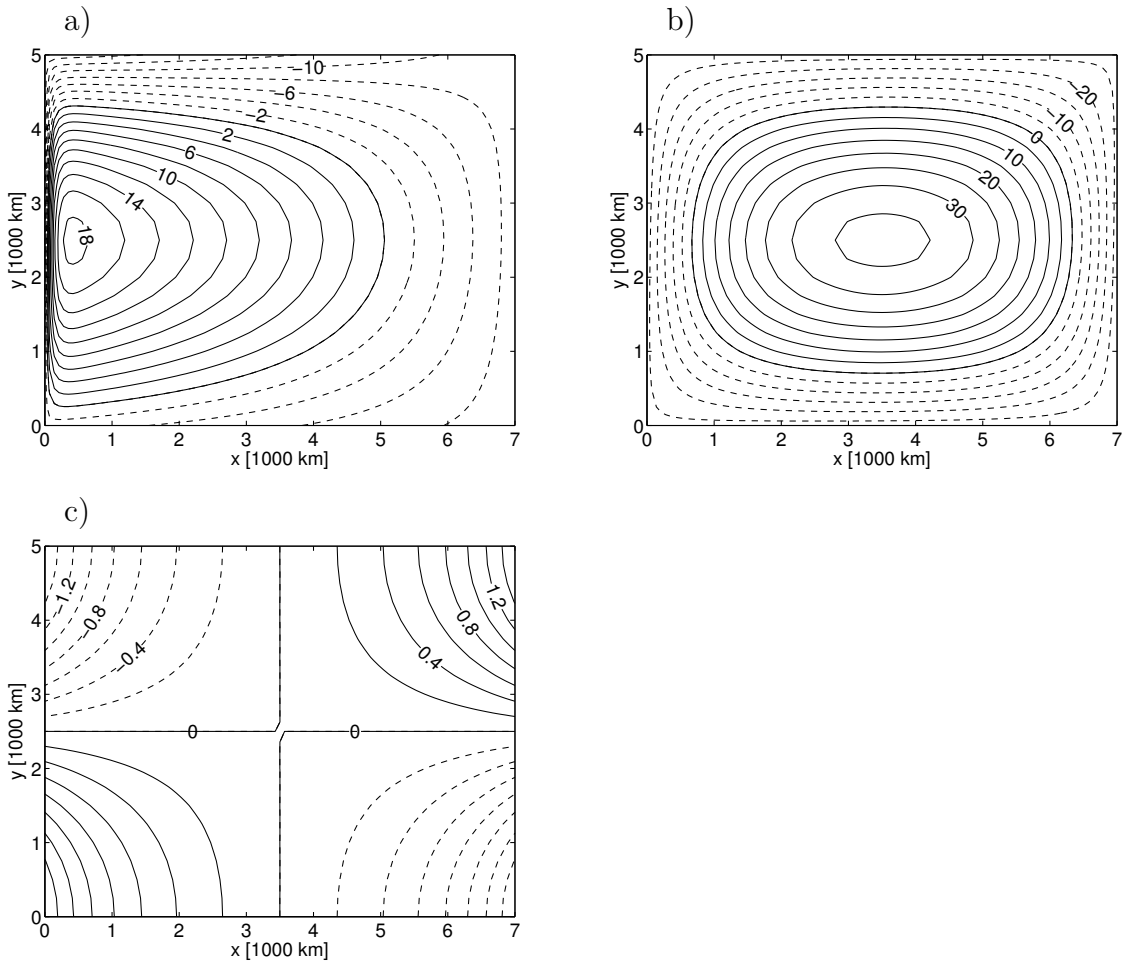

Figure 6.13: Surface elevation η (in cm) calculated using the Stommel model (6.52). Panel **a)** $\beta = 2 \cdot 10^{-11}$ m^{-1} s^{-1}; Panel **b)** $\beta = 0$, and Panel **c)** $f = 0$. The parameters are $R = 1/(6$ days), $H = 1000$ m and $T = 0.1$ N m^{-2} in (6.54). The numerical solution of (6.57) and (6.58) was calculated on a grid with $N_x \times N_y = 100 \times 20$ using the Method of Successive Overrelaxation (5.22).

can apply (6.63) and (6.64) in order to calculate the value of the function at the boundary. We find

$$P_0 = \frac{4\,P_1 - P_2}{3} - \frac{2}{3}\,\Delta x\,\left.\frac{\mathrm{d}P}{\mathrm{d}x}\right|_{x=0}, \tag{6.65a}$$

$$P_N = \frac{4\,P_{N-1} - P_{N-2}}{3} + \frac{2}{3}\,\Delta x\,\left.\frac{\mathrm{d}P}{\mathrm{d}x}\right|_{x=L}. \tag{6.65b}$$

The numerical solution of (6.57), shown for different parameter values in Fig. 6.13, was computed inside the domain using the Method of Successive Overrelaxation according to (5.22). Therefore, $\Psi(x, y)$ needs to be determined first by solving the Dirichlet boundary value problem given by (6.52) and (6.53). The boundary conditions (6.58) are accounted for by computing the boundary values according to (6.65).

The current is clock-wise (Fig. 6.11). Inside the western boundary current, pressure gradient, Coriolis and inertial forces are in equilibrium with the wind stress (Fig. 6.13, a). On an f-plane ($\beta = 0$, Fig. 6.13, b), the current is approximately

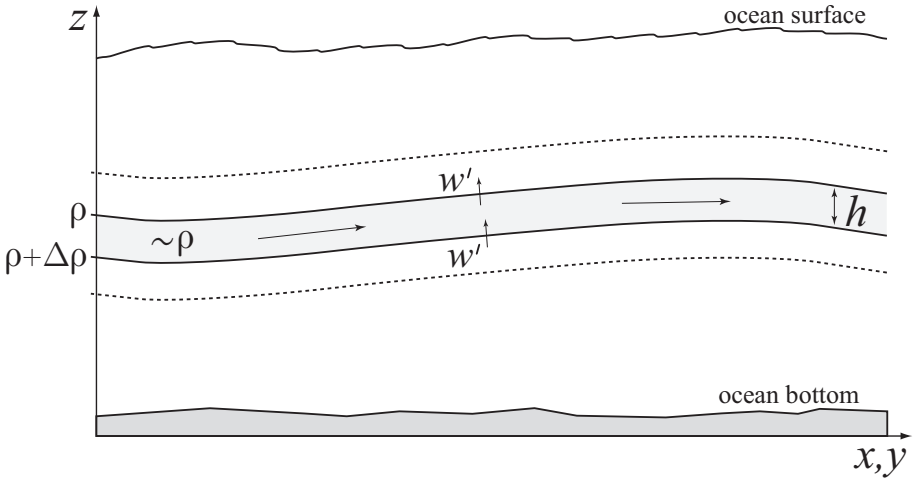

Figure 6.14: Vertical cross section showing a part of a discontinuously stratified ocean. Providing that the stratification is stable, the water of the lower layers are denser than the water of the upper layers ($\Delta\rho > 0$). Eddy fluctuations w' of the vertical velocity w occur and yield mean eddy mass fluxes $\pm\overline{w'\,\rho'} = \pm\overline{w'\,\Delta\rho}$ between the layers.

in a geostrophic equilibrium (Coriolis forces are balanced mainly by the pressure gradients, friction compensates for the wind stress). It must be noted, that due to the friction, currents do not exactly follow the lines of constant pressure, although $\nabla^2 P = f\,\vec{\nabla}^2\Psi$ is valid inside the domain. This follows from the equation of motion (6.48). In case the reference system is not rotating ($f = 0$, Fig. 6.13, c), the meridional flow is directed parallel to the negative pressure gradients, i.e. "downhill", and the zonal flow is forced to flow "uphill", i.e. against the pressure gradient, owing to the zonal wind stress that drives the zonal flow.

6.8 Potential vorticity: An important conserved quantity

Conservation theorems are fundamental statements in physics and enable a more profound understanding of various processes responsible for the dynamics. Hence, conservation theorems and related quantities are also very useful in geophysical fluid dynamics and climate modelling. A conservation equation for large-scale ocean flow is derived from the equations of motion (6.13) in this section.

The following explanations of this section are based on a simple model of a large-scale ocean flow in hydrostatic equlibrium (Section 6.4). It approximates the continuous stratification of the real ocean water by a discontinuous stratification formed by superimposed thin layers, shallow water layers indeed, as illustrated in Fig. 6.14. Any of these layers has a constant density ρ and a variable thickness $h(x, y)$ and slides between the underlying denser layer and the overlying lighter layer, thereby moving along surfaces of constant density (isopycnals). The function $\rho\,h(x, y)$ represents the mass per unit area in this layer and obeys the relation

$$\frac{\partial\,(\rho\,h)}{\partial t} + \frac{\partial}{\partial x}\,(u\,\rho\,h) + \frac{\partial}{\partial y}\,(v\,\rho\,h) = Q\;. \tag{6.66}$$

This is a generalized version of the continuity equation (6.19) of the shallow water

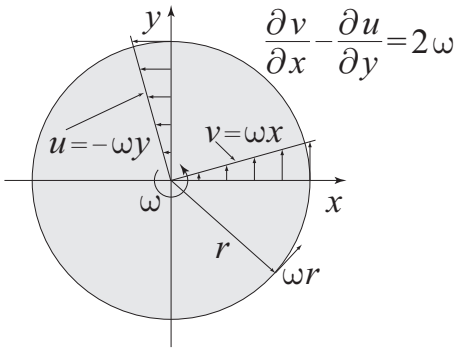

Figure 6.15: Vortex in the form of a solid disk rotating with angular velocity ω about an Earth-fixed z-axis. The velocity of the points of the vortex at a distance r from the center is $\omega\, r$ and always tangential. Hence, the relative vorticity is $2\,\omega$.

model taking into account a *cross-isopycnal mass flux* Q (in kg/(m^2 s)) as well, which could arise for example from eddy mass fluxes $\pm\overline{w'\,\rho'}$ (covariance between vertical velocity w and density ρ) going through the upper and the lower boundaries of the layer. Using definition (6.3) for horizontal motions and neglecting density changes (but not volume changes) within the layer, (6.66) can be written as

$$\frac{\mathrm{D}h}{\mathrm{D}t} + h\left(\frac{\partial u}{\partial x} + \frac{\partial v}{\partial y}\right) = \frac{Q}{\rho}\,. \tag{6.67}$$

We now define the *vorticity* measured relatively to the Earth's surface, namely the *relative vorticity* ζ, as the vertical component of the curl of the velocity field $\vec{u}$, which is measured relatively to the Earth's surface, according to

$$\zeta = \left(\vec{\nabla}\times\vec{u}\right)\cdot\hat{z} = \frac{\partial v}{\partial x} - \frac{\partial u}{\partial y}\,. \tag{6.68}$$

$\hat{z}$ is the unit vector normal to the Earth's surface. It can be shown that the relative vorticity ζ equals twice the angular velocity of an infinitesimal vortex on Earth as illustrated in Fig. 6.15.

To examine the time evolution of relative vorticity inside the layer, we consider the equations of motion (6.13) — namely a generalized version of the equations of motion of the shallow water model (6.20) — and calculate $\partial/\partial y(6.13a)$ and $\partial/\partial x(6.13b)$ assuming $w = 0$. Observing (6.11) we obtain

$$\frac{\partial(6.13a)}{\partial y}: \quad \frac{\partial}{\partial t}\frac{\partial u}{\partial y} + \frac{\partial u}{\partial y}\frac{\partial u}{\partial x} + u\,\frac{\partial^2 u}{\partial x\,\partial y} + \frac{\partial v}{\partial y}\frac{\partial u}{\partial y} + v\,\frac{\partial^2 u}{\partial y^2} = \frac{\partial a_x}{\partial y} + \frac{\partial f}{\partial y}\,v + f\,\frac{\partial v}{\partial y}\,,$$

$$\frac{\partial(6.13b)}{\partial x}: \quad \frac{\partial}{\partial t}\frac{\partial v}{\partial x} + \frac{\partial u}{\partial x}\frac{\partial v}{\partial x} + u\,\frac{\partial^2 v}{\partial x^2} + \frac{\partial v}{\partial x}\frac{\partial v}{\partial y} + v\,\frac{\partial^2 v}{\partial y\,\partial x} = \frac{\partial a_y}{\partial x} - \frac{\partial f}{\partial x}\,u - f\,\frac{\partial u}{\partial x}\,,$$

so that $\partial/\partial x(6.13b) - \partial/\partial y(6.13a)$ reads

$$\begin{aligned}
&\frac{\partial}{\partial t}\left(\frac{\partial v}{\partial x} - \frac{\partial u}{\partial y}\right) + u\,\frac{\partial}{\partial x}\left(\frac{\partial v}{\partial x} - \frac{\partial u}{\partial y}\right) + v\,\frac{\partial}{\partial y}\left(\frac{\partial v}{\partial x} - \frac{\partial u}{\partial y}\right)\\
&+ \frac{\partial u}{\partial x}\left(\frac{\partial v}{\partial x} - \frac{\partial u}{\partial y}\right) + \frac{\partial v}{\partial y}\left(\frac{\partial v}{\partial x} - \frac{\partial u}{\partial y}\right)\\
&= \frac{\partial a_y}{\partial x} - \frac{\partial a_x}{\partial y} - \frac{\partial f}{\partial x}\,u - f\,\frac{\partial u}{\partial x} - \frac{\partial f}{\partial y}\,v - f\,\frac{\partial v}{\partial y}
\end{aligned}$$

and with (6.68) and $\partial f/\partial t = 0$

$$\frac{\partial \zeta}{\partial t} + u\,\frac{\partial \zeta}{\partial x} + v\,\frac{\partial \zeta}{\partial y} + \left(\frac{\partial u}{\partial x} + \frac{\partial v}{\partial y}\right)\zeta$$
$$= \frac{\partial a_y}{\partial x} - \frac{\partial a_x}{\partial y} - \frac{\partial f}{\partial t} - u\,\frac{\partial f}{\partial x} - v\,\frac{\partial f}{\partial y} - f\left(\frac{\partial u}{\partial x} + \frac{\partial v}{\partial y}\right) ,$$

that is,

$$\frac{\mathrm{D}}{\mathrm{D}t}\,(\zeta + f) = \underbrace{-\,(\zeta + f)\left(\frac{\partial u}{\partial x} + \frac{\partial v}{\partial y}\right)}_{\text{CON}} + \underbrace{\frac{\partial a_y}{\partial x} - \frac{\partial a_x}{\partial y}}_{\text{PRO}} . \tag{6.69}$$

$\zeta + f$ is the *absolute vorticity*, i.e. the vorticity taken relative to an unaccelerated reference system ($f = 2\,\Omega\,\sin\varphi$ is the vorticity of the rotating surface of the Earth at latitude φ).

We consider the terms on the right-hand side of (6.69). They signify two distinct sources of absolute vorticity: (i) convergence of the flow (CON), and (ii), production by real forces (PRO). From (6.11), and with $\rho =$ constant, we have

$$\frac{\partial a_y}{\partial x} - \frac{\partial a_x}{\partial y} = \frac{1}{\rho}\,\frac{\partial^2 \tau_{yz}}{\partial x\,\partial z} - \frac{1}{\rho}\,\frac{\partial^2 \tau_{xz}}{\partial y\,\partial z} .$$

In such a fluid the production by real forces (PRO) is independent of the pressure gradient forces. Such a fluid is called *barotropic*, all the others are *baroclinic* (Section 4.4). In a barotropic fluid the change of the absolute vorticity results solely from circulation convergence and vorticity production due to friction.

Equation (6.67) allows us to simplify the term CON in (6.69) applied to the shallow water layer emphasized in Fig. 6.14:

$$\frac{\mathrm{D}}{\mathrm{D}t}\,(\zeta + f) = -\frac{\zeta + f}{h}\left(\frac{Q}{\rho} - \frac{\mathrm{D}h}{\mathrm{D}t}\right) + \frac{\partial a_y}{\partial x} - \frac{\partial a_x}{\partial y} ,$$

i.e.

$$\frac{1}{h}\,\frac{\mathrm{D}}{\mathrm{D}t}\,(\zeta + f) - \frac{\zeta + f}{h^2}\,\frac{\mathrm{D}h}{\mathrm{D}t} = -\frac{\zeta + f}{h}\,\frac{Q}{\rho\,h} + \frac{1}{h}\left(\frac{\partial a_y}{\partial x} - \frac{\partial a_x}{\partial y}\right)$$

and consequently

$$\frac{\mathrm{D}}{\mathrm{D}t}\left(\frac{\zeta + f}{h}\right) = -\left(\frac{\zeta + f}{h}\right)\frac{Q}{\rho\,h} + \frac{1}{h}\left(\frac{\partial a_y}{\partial x} - \frac{\partial a_x}{\partial y}\right) . \tag{6.70}$$

The quantity $(\zeta + f)\,/h$ is the *potential vorticity* in the shallow water layer. Potential vorticity is a conservative quantity in a barotropic and frictionless ocean circulation, if no mass is supplied or removed.

Regarding (6.70), wind-driven flow described in Section 6.7 can now be understood in a coherent framework. In the Stommel model, a closed flat basin ($Q = 0$ and $\eta_\mathrm{b} = 0$, Fig. 6.3) with only one shallow water layer was considered. We integrate (6.70) over the layer thickness h, assuming $\eta \ll H$ (so that $h = H + \eta \approx H =$ constant), and substitute a_x and a_y for the right-hand side of (6.48). We assume $\tau_{yz} = 0$ according

Direction of flow	1 $\rho\, h \dfrac{\mathrm{D}\zeta}{Dt}$	2 $+\rho\, h \dfrac{\mathrm{D}f}{\mathrm{D}t}$	$\approx$	3 $-\dfrac{\partial \tau_{xz}}{\partial y}$	4 $-R \dfrac{\partial M_y}{\partial x}$	5 $+R \dfrac{\partial M_x}{\partial y}$
N $\rightarrow$ S	≈ 0	< 0		< 0	≈ 0	≈ 0
S $\rightarrow$ N	≈ 0	> 0		< 0	$\gg 0$	≈ 0

Table 6.1: Signs of the individual terms in (6.71) for the Stommel model of the subtropical gyre in the northern hemisphere. The relation *shaded in grey* is required in order to close the balance of terms. The large gradients imply a strong, confined flow, i.e., a boundary current.

to the Stommel model. This results in the approximation

$$\rho\, h \frac{\mathrm{D}\zeta}{\mathrm{D}t} + \rho\, h \frac{\mathrm{D}f}{\mathrm{D}t} \approx -\frac{\partial \tau_{xz}}{\partial y} - R \frac{\partial M_y}{\partial x} + R \frac{\partial M_x}{\partial y} \,. \tag{6.71}$$

An estimate for the individual terms in (6.71) for large-scale circulation of typical spatial scales of 10^6 m reveals the individual contributions given in Table 6.1 and provides substantial insight into the dynamics of large-scale geophysical flow.

We now consider the signs and magnitudes of the five terms in (6.71) for northward and southward flow. The dominant term on the left-hand side is $\mathrm{D}f/\mathrm{D}t$ (term 2 in Table 6.1), and the material derivative of the relative vorticity (term 1) can be neglected in comparison. Southward flow implies decreasing f, and for northward flow f increases. The sign of term 3 is always negative, and the west-east mass transport M_x (term 5) vanishes towards the eastern and western boundary. We therefore are left with term 4 to close the vorticity balance. For southward flow both left-hand side and right-hand side of (6.71) are negative, so term 4 is not required to achieve vorticity balance. This is the *Sverdrup transport* determined by the wind stress curl and the β-effect.

In contrast, for northward flow, term 2 and 3 have opposite sign and only a strongly positive term 4 can achieve vorticity balance. $-R\,\partial M_y/\partial x \gg 0$ is, however, only possible at the western boundary. Therefore, friction in the boundary current produces enough positive vorticity that the negative vorticity input by the wind is overcompensated. This enables the movement of the water parcel from south to north.

Henry Stommel examined the deep circulation, as well. He used a similar model which is generally referred to as the Stommel-Arons model presented in two landmark papers (Stommel, 1958; Stommel and Arons, 1960). These articles led to the remarkable prediction of a western boundary current that is supposed to be located in the Atlantic at a depth of 2–3 km, flowing from north to south! Consequently, physical oceanographers set up an intensive search for this current in order to verify the theoretical prediction. It was finally identified off Cape Hatteras using current meters. Maximum velocities in the core at a depth of 2500 m are around 20 cm/s.

At this depth, the effect of the wind can be neglected, however, the mass flux, also a source term of potential vorticity in (6.70), must be accounted for. Stommel postulated a large-scale, extremely slow upwelling in the deep ocean in order to

Direction of flow	1 $\rho\, h \dfrac{\mathrm{D}\zeta}{Dt}$	2 $+\rho\, h \dfrac{\mathrm{D}f}{\mathrm{D}t}$	3 $\approx -(\zeta + f)\, Q$	4 $-R \dfrac{\partial M_y}{\partial x}$	5 $+R \dfrac{\partial M_x}{\partial y}$
N $\rightarrow$ S	≈ 0	< 0	> 0	$\ll 0$	≈ 0
S $\rightarrow$ N	≈ 0	> 0	> 0	≈ 0	≈ 0

Table 6.2: Signs of the terms in (6.71) for the Stommel-Arons model of the subtropical gyre in the northern hemisphere. The relation *shaded in grey* is required in order to close the balance of terms. The large gradients imply a strong, confined flow, i.e., a boundary current.

compensate for the deep water formation occurring in polar regions. This signifies that water leaves the layer h and hence $Q < 0$ in (6.70). Analogously, Table 6.2 can be compiled.

The vorticity balance requires a deep western boundary current flowing southward. It supplies the inner geostrophic flow with water and therefore continuously loses strength. Just this prediction could not be confirmed by observations, which points to a much more complicated picture of deep currents, in particular, the assumption of large-scale uniform upwelling seems inconsistent with measurements. A critical overview is given in Lozier (2010).

In a highly simplified view, Fig. 6.16 displays the structure of the current systems in the northern hemisphere Atlantic schematically.

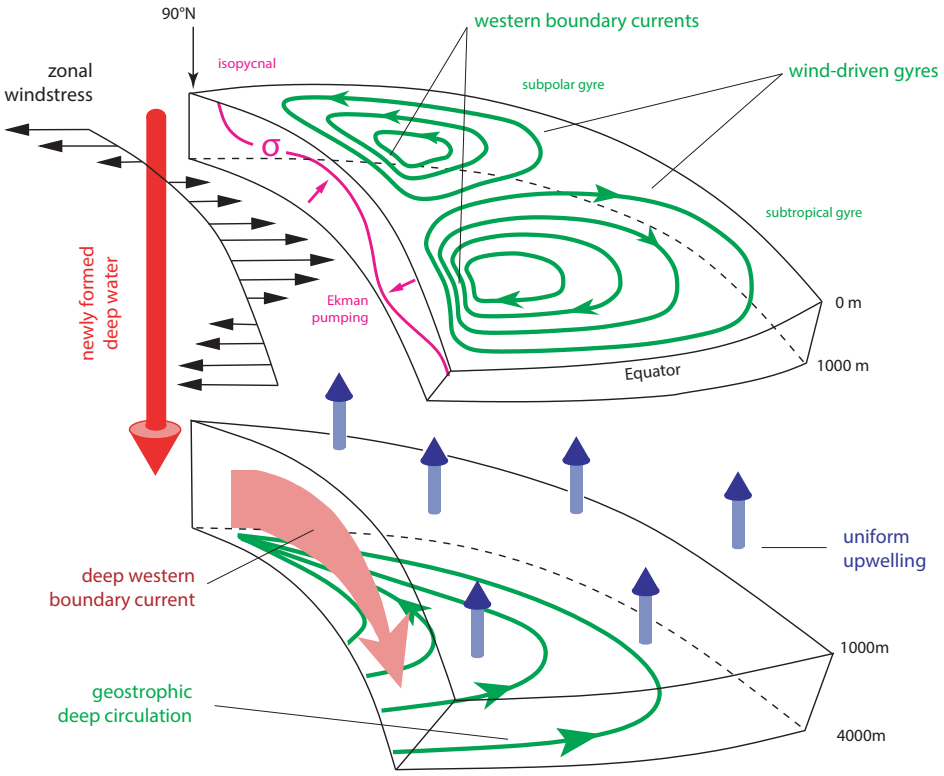

Figure 6.16: Panoramic and simplified view of the large-scale currents in the northern hemisphere Atlantic based on the Stommel and Stommel-Arons models.

7 Large-scale circulation in the atmosphere

7.1 Zonal and meridional circulation

In this chapter the general circulation in the atmosphere is presented in a simplified form. A comprehensive description of the dynamics of the atmosphere can be found in Holton and Hakim (2013).

The consideration in Chapter 4 of zonally and temporally averaged quantities and their deviations was useful for the analysis of the meridional heat fluxes. Here, we follow the same approach. Applying suitable time averages the short-term weather events are filtered out and the general circulation can be separated into a quasi-stationary component, a monsoon component that changes its direction during the seasonal cycle, and a component describing low-frequency variations.

The mean flow in the atmosphere is mainly directed from west to east, and so are the highest wind velocities (Figs. 7.1 and 7.2). This is a result of the conservation of the air masses' angular momentum on the rotating Earth. Their movement is driven by the meridional temperature distribution.

The specific angular momentum (angular momentum per mass) of an air parcel that moves along the latitude φ at velocity u relative to the Earth's surface is given by

$$L = (\Omega\, R\, \cos\varphi + u)\, R\, \cos\varphi\ , \tag{7.1}$$

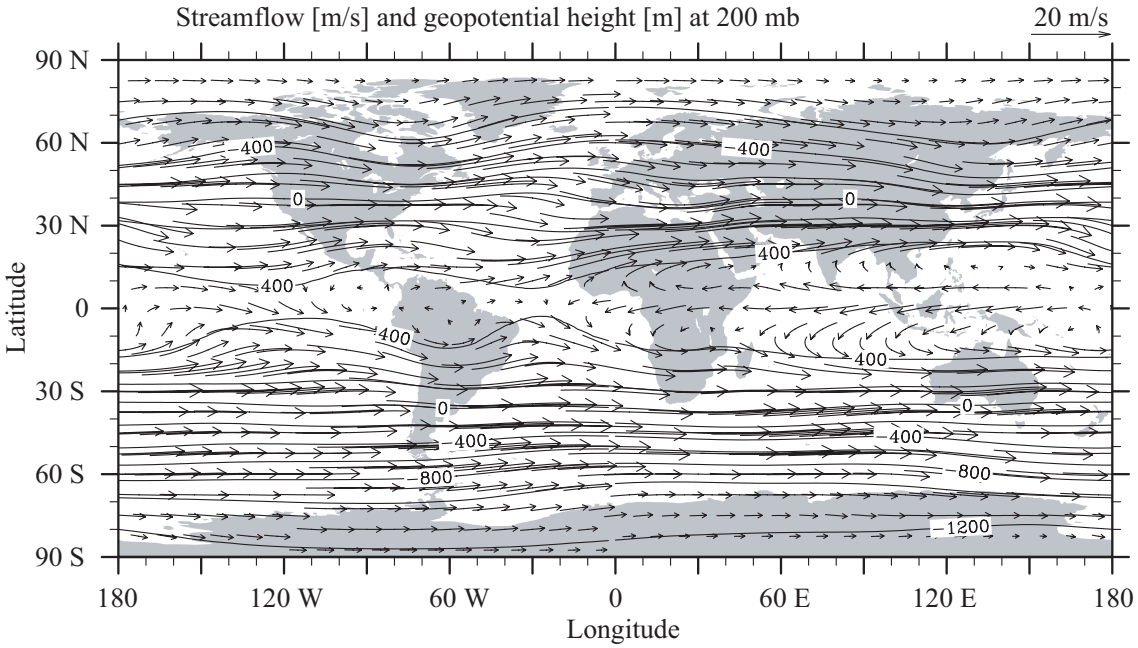

Figure 7.1: Mean wind field at an altitude of around 12 km. Data from ERA-40 (Uppala et al., 2005). Figure constructed by F. Lehner.

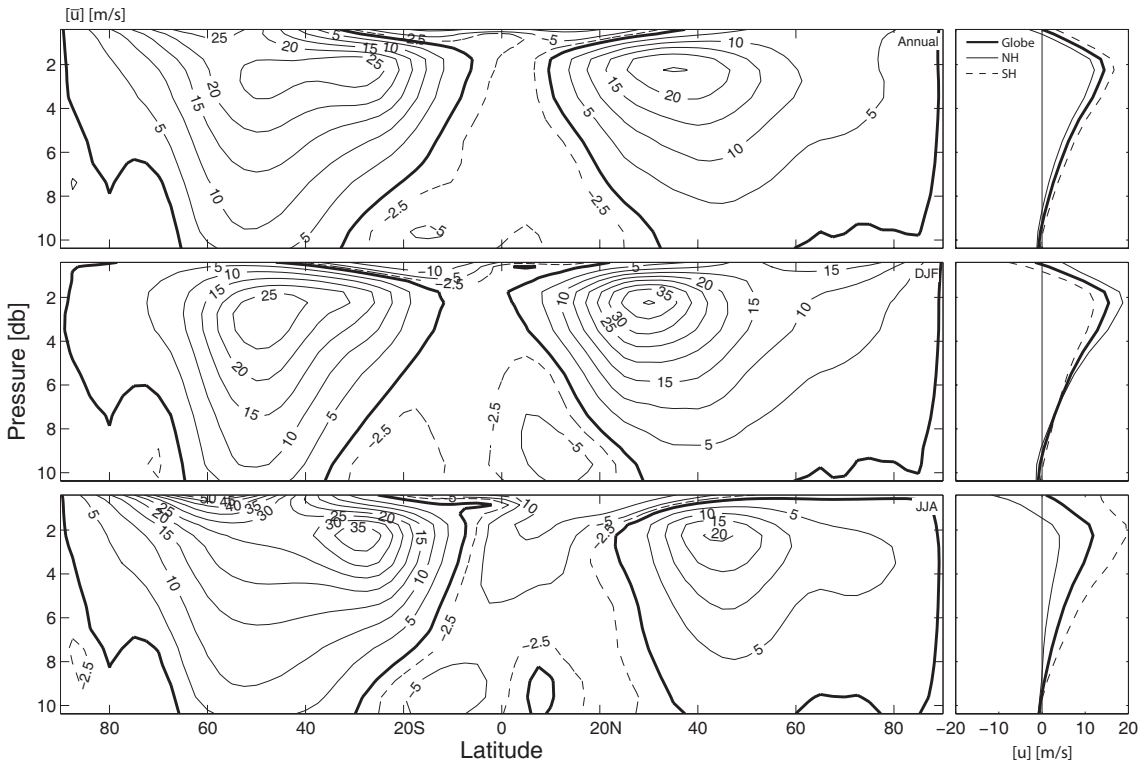

Figure 7.2: Mean wind in $\mathrm{m\,s^{-1}}$ in a meridional transect of the atmosphere. The strong west-east jets in the northern- and southern hemisphere at an altitude of around 12 km are clearly visible. Data from ERA-40 (Uppala et al., 2005). Figure constructed by F. Lehner.

where Ω and R are the angular velocity and the Earth radius, respectively. If no forces act on the air parcel, the angular momentum L is conserved. Consider an air parcel which starts from rest at the equator and reaches latitude φ. Accounting for the conservation of its angular momentum, its zonal velocity reaches

$$u(\varphi) = \frac{\Omega\, R\, \sin^2 \varphi}{\cos \varphi}\ . \tag{7.2}$$

This means, that at 30°N a westerly wind with a velocity of $u = 134\ \mathrm{m\,s^{-1}}$ would result. This calculation, however, overestimates the speed of the zonal jet stream by about a factor of 3. The observed jet stream maximum is located at 35°N and at an altitude of about 12 km (Fig. 7.2). But this simple computation shows that the transport of angular momentum is by far sufficient for an explanation of the high zonal wind velocities at mid-latitudes. However, it also leads to the conclusion that angular momentum must be constantly removed from the flow. This is caused by eddies and the associated transport of angular momentum. The mean meridional advective transport of angular momentum is given by

$$\begin{aligned}[\,\overline{v\,L}\,] = &\underbrace{[\,\overline{v}\,]\,(\Omega\, R\, \cos\varphi + [\,\overline{u}\,])\, R \cos\varphi}_{\mathrm{M}} \\ &+ \Big(\underbrace{[\,\overline{u}^*\,\overline{v}^*\,]}_{\mathrm{SE}} + \underbrace{[\,\overline{u'\,v'}\,]}_{\mathrm{TE}} \Big) R\, \cos\varphi\ ,\end{aligned} \tag{7.3}$$

in analogy to (4.7). The meridional transport of angular momentum is achieved by

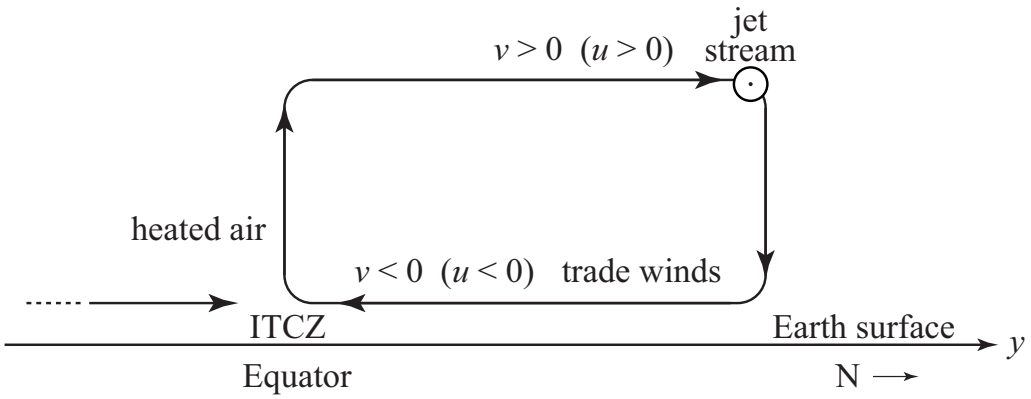

Figure 7.3: A simple depiction of the Hadley circulation in the northern hemisphere. Heated air at the equator rises first, then moves polewards, descends at higher latitudes and finally returns to the equator as a near-surface flow.

the combination of the mean flow (M), stationary eddies (SE) and transient eddies (TE). Observations show that at latitudes between 20° and 50° TE is the largest contribution to angular momentum transport.

In the 18$^{\text{th}}$ century, *George Hadley* (1685-1768) proposed that the strong solar radiation in the tropics heats up the air and causes it to rise. On the northern hemisphere the resulting near-surface flow is directed towards the equator and converges finally at the so-called intertropical convergence zone (ITCZ). Its deviation towards the west (so that the zonal velocity is westward, $u < 0$) is a result of angular momentum conservation. This causes the well-known *trade winds*. The return flow at higher levels is analogously deviated towards the east ($u > 0$) inducing a zonal jet stream at higher latitudes where it passes over to descending air motions. The resulting meridionally closed circulation is referred to as *Hadley circulation* or *Hadley cell*, schematically depicted in Fig. 7.3.

The effect of the Coriolis force, or of the conservation of angular momentum respectively, is hence a south-west-directed flow at the surface and a north-east-directed flow at high altitudes. Hadley expected the circulation cell to extend all the way to the pole. However, observations indicated that the Hadley cell does not even reach the mid-latitudes, because there, the mean winds are directed to the east at the surface, as well as at high altitudes (westerlies). The simple picture of a merely thermally-driven flow is therefore not sufficient to explain observations outside the tropics.

For a deeper understanding the balance equations for momentum, mass and energy in the atmosphere need to be solved. The equation of motion is basically analogous to (6.13) and the continuity equation is given with (3.7); in addition, the thermodynamic energy equation must be taken into account. For a complete derivation of the equations, the reader is referred to Holton and Hakim (2013).

We consider the zonally and temporally averaged equations, where terms of the form (4.6) will occur. The flow in a meridional plane can be described by a meridional

stream function $\chi(y, z)$, defined as follows:

$$\rho_0 \, \overline{v} = -\frac{\partial \overline{\chi}}{\partial z} \,, \tag{7.4a}$$

$$\rho_0 \, \overline{w} = \frac{\partial \overline{\chi}}{\partial y} \,, \tag{7.4b}$$

where v and w are meridional and vertical velocities and $\rho_0 = \rho_0(z)$ is the density of air. The overbars denote appropriate time averaging. As derived in Holton and Hakim (2013), the stream function satisfies the following partial differential equation:

$$\begin{aligned} &\frac{N^2}{\rho_0} \frac{\partial^2 \overline{\chi}}{\partial y^2} + f_0^2 \frac{\partial}{\partial z} \left(\frac{1}{\rho_0} \frac{\partial \overline{\chi}}{\partial z} \right) \\ &\qquad = \underbrace{\frac{\kappa}{H} \frac{\partial \overline{J}}{\partial y}}_{\mathrm{D}} - \underbrace{\frac{R^*}{H} \frac{\partial^2 \overline{v' \, T'}}{\partial y^2}}_{\mathrm{TEH}} - \underbrace{f_0 \frac{\partial^2 \overline{v' \, u'}}{\partial z \, \partial y}}_{\mathrm{TEM}} + \underbrace{f_0 \frac{\partial \overline{X}}{\partial z}}_{\mathrm{R}} \,. \end{aligned} \tag{7.5}$$

Here, N is the Brunt-Väisälä frequency, the angular frequency of free vertical oscillations in a stable atmosphere given by

$$N^2 = \frac{R^*}{H} \left(\frac{\kappa \, T_0}{H} + \frac{\mathrm{d}T_0}{\mathrm{d}z} \right) \,, \tag{7.6}$$

which is approximately constant in the troposphere. R^* is the specific gas constant of the air and $\kappa = R^*/c_p$; furthermore, $H = R^* \, \hat{T}_0 / g$ is the isothermal scale-height of the atmospheric layer considered here with temperature $T_0 = T_0(z)$ and a layer mean temperature $\hat{T}_0$. The physical quantity $\overline{J}(y, z)$ in (7.5) is a mean diabatic heating rate (induced by heat fluxes at the ground or latent heat from condensation processes) and $\overline{X}$ is a mean drag in a zonal direction by friction at the ground. Finally, the coordinate z in (7.5) signifies the so-called log-pressure coordinate $z = -H \, \ln(p/p_\mathrm{s})$ with p_s the air pressure on the underside of the layer. In the troposphere, the log-pressure coordinate is nearly equal to the usual z-coordinate which represents a geometric height coordinate. According to (7.5), the stream function is driven by four processes: (i), diabatic heat sources (D), (ii), heat fluxes associated with transient eddies (TEH), (iii), fluxes of momentum associated with transient eddies (TEM) and, (iv), friction (R).

Equation (7.5) is a generalized form of the Poisson equation and needs to be complemented by boundary conditions. Therefore, we consider a domain, reaching from the equator nearly to the pole and in the vertical dimension from the Earth surface up to the tropopause. Transport is assumed to be confined within these boundaries, and hence $\overline{\chi} = 0$ on the boundary. The domain is illustrated in Fig. 7.4.

For the qualitative discussion of (7.5), we assume that $\overline{\chi}$ can be represented by appropriate sin-functions in y and z which satisfy the boundary conditions. Hence, the left-hand side of (7.5) is proportional to $-\overline{\chi}$ and we can derive the following

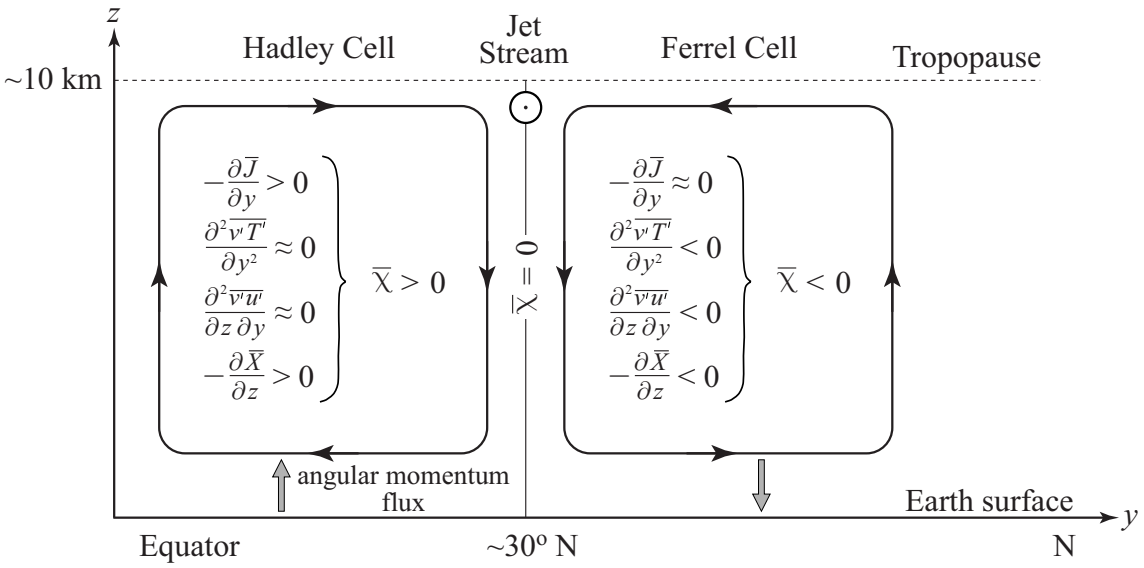

Figure 7.4: Schematic illustration of the stream function $\overline{\chi}$ in the northern hemisphere. $\overline{\chi} > 0$ is the thermally direct Hadley cell, $\overline{\chi} < 0$ describes the thermally indirect Ferrel cell. Angular momentum is supplied to the atmosphere south of about 30°N and removed from the atmosphere north of it.

relations:

$$\overline{\chi} \propto -\frac{\partial}{\partial y}\,(\text{diabatic heat sources}) + \frac{\partial^2}{\partial y^2}\,(\text{meridional eddy heat flux}) + \frac{\partial^2}{\partial z\,\partial y}\,(\text{meridional eddy momentum flux}) - \frac{\partial}{\partial z}\,(\text{zonal shear})\ . \tag{7.7}$$

Close to the equator, a large amount of latent heat is released and hence, $\overline{J} > 0$, while at around 30°N and further to the north cooling caused by radiative losses dominates, hence $\overline{J} < 0$. Between the equator and 30°N $\overline{J}$ decreases and hence $\partial\overline{J}/\partial y < 0$. In these latitudes the eddy fluxes TEH and TEM are small; their contribution to the zonal wind stress, that is directed towards the east due to the trade winds, is only to be considered at its lower boundary. Term D prevails in (7.5) and contributes, together with the smaller term R, to the observed Hadley cell, a meridional cell with $\overline{\chi} > 0$. This is denoted as a *thermally direct* cell, i.e., warm air rises, while colder air sinks (Fig. 7.4).

The eddy activity has a maximum at around 30° to 60°N where the storm tracks are located. The latitudinal and altitudinal dependence of the meridional eddy fluxes are illustrated in Fig. 7.5. It can be shown that at these latitudes the two respective terms are negative in (7.7). Due to the westerlies, the drag is directed towards the west and decreases in magnitude with increasing altitude, hence $-f_0\,\partial\overline{X}/\partial z < 0$. Therefore, according to (7.7), $\overline{\chi} < 0$ and an *indirect* cell is formed. This indirect cell in the region of 40° to 60°N is called *Ferrel cell* (Fig. 7.4). The Ferrel cell is thermally indirect, i.e., cold air rises and warm air sinks.

A part of the specific angular momentum (7.1) of the northern hemisphere is produced in the Hadley cell in the region of the trade winds, where $u < 0$. Here, the air is accelerated by friction at the Earth surface so that a flux of angular momentum

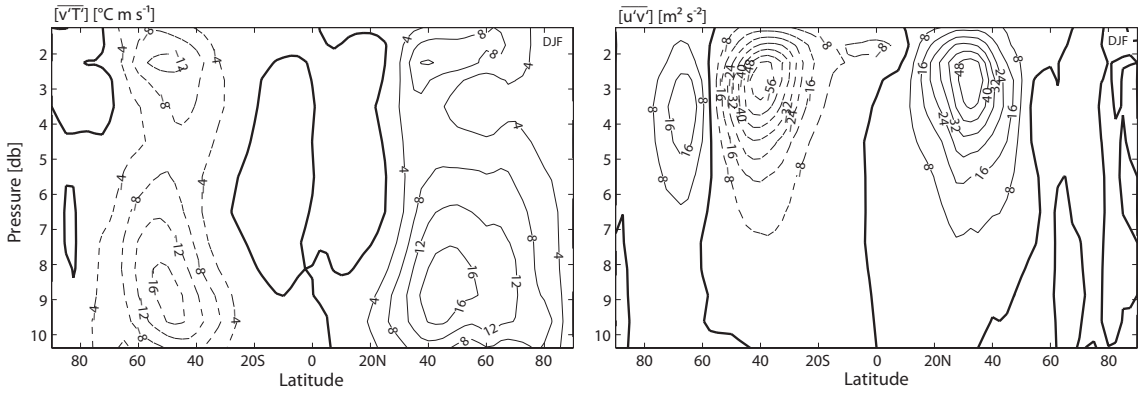

Figure 7.5: Observed distribution of eddy fluxes of heat (**left**, in $^\circ\mathrm{C\,m\,s^{-1}}$) and momentum (**right**, in $\mathrm{m^2\,s^{-2}}$) for northern winter. Positive fluxes are directed northward. Data from ERA-40 (Uppala et al., 2005). Figure constructed by F. Lehner.

from the Earth to the atmosphere is induced (Fig. 7.4). This angular momentum is transported polewards to the Ferrel cell and subsequently again lost to the Earth surface in mid-latitudes, where $u > 0$.

The observed meridional circulation (Fig. 7.6) shows strong Hadley cells in the respective winter hemisphere. The Ferrel cells in the southern and northern hemispheres can also be identified. The simplified theoretical model in (7.5) captures this structure quite well.

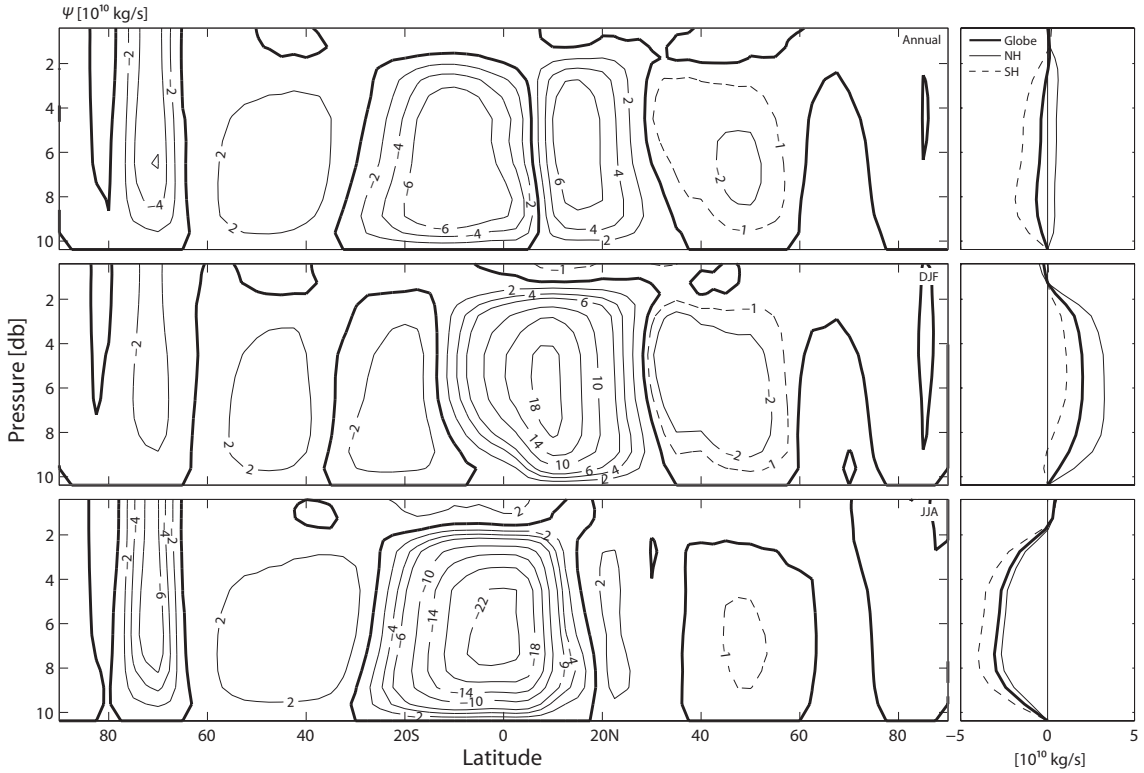

Figure 7.6: Observed meridional circulation (stream function in $10^{10}\ \mathrm{kg\,s^{-1}}$), annually averaged (**upper**), for the northern winter (**middle**) and the northern summer (**lower**). Data from ERA-40 (Uppala et al., 2005). Figure constructed by F. Lehner.

7.2 The Lorenz-Saltzman model

In order to examine the thermally-driven flow, *Barry Saltzman* (1931–2001) derived an approximation of the governing equations of a viscous, stably stratified flow consisting of a non-linear system of ordinary differential equations (Saltzman, 1962). The fundamental significance of this equation system was recognized by *Edward Lorenz* (1917–2008) who numerically solved this system and interpreted it (Lorenz, 1963). Beyond the particular application for viscous incompressible fluids, the system may be interpreted as the simplest form of a description of non-linear processes in relation with the general circulation in the atmosphere. The model is of particular significance, because it was the first system to describe deterministic chaos and, based on it, *Chaos theory* was developed.

Deterministic chaos can occur in a non-linear system (non-linearity is a necessary but not satisfactory condition) and is based on the fact that the instantaneous time derivative is given functionally, however, the temporal evolution of the system cannot be predicted over long periods. Mathematically speaking, the system is determined by several coupled ordinary differential equations of first order in time. Its changes can be calculated exactly at all times: the system is therefore deterministic. This system is generally referred to as the Lorenz model. But since the original equations were derived by B. Saltzman, we shall call it *Lorenz-Saltzman model*.

The following derivation of the Lorenz-Saltzman model is somewhat technical. Nevertheless, it will be described here since in the literature only the dimensionless system is usually given. The Lorenz-Saltzman model is formulated on a meridional plane in the non-rotating reference system (y, z). A generalization for the f-plane was presented later (Lorenz, 1984). Solutions are assumed uniform in the x-direction. We further assume that diabatic effects, e.g., heat sources, drive the flow clock-wise. Additionally, a constant vertical temperature gradient is chosen as a background state. The solution domain is shown schematically in Fig. 7.7.

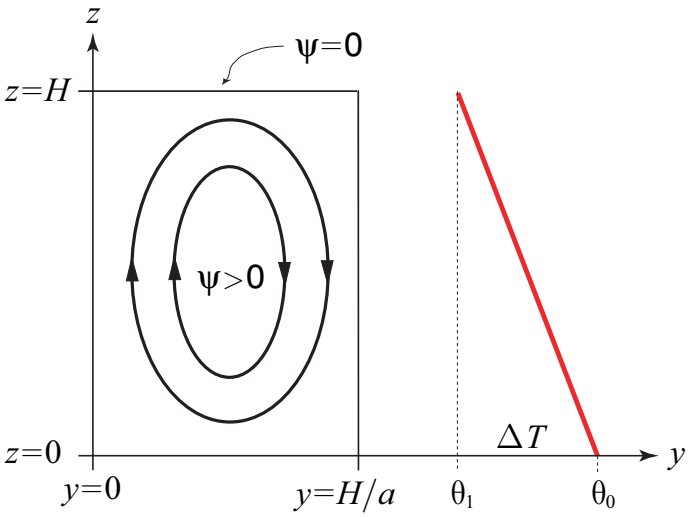

Figure 7.7: Coordinates and solution domain for the Lorenz-Saltzman model. A constant vertical temperature gradient is chosen.

The fluid is considered incompressible (in fact, not a valid approximation for the atmosphere, but applicable to a water body), therefore, mass conservation is given

by the continuity equation (6.14),

$$\frac{\partial v}{\partial y} + \frac{\partial w}{\partial z} = 0 \; . \tag{7.8}$$

With this, a stream function can be defined as follows:

$$v = -\frac{\partial \Psi}{\partial z} \; , \qquad w = \frac{\partial \Psi}{\partial y} \; . \tag{7.9}$$

Thus, the relative vorticity in the meridional y-z-plane, i.e. $\zeta = \partial w/\partial y - \partial v/\partial z$, is given by

$$\zeta = \vec{\nabla}^2 \Psi \; . \tag{7.10}$$

The formulation of the conservation equation of vorticity reveals that vorticity is dissipated by molecular diffusion and produced by meridional temperature gradients $\partial\theta/\partial y$ (buoyancy). In order to derive the vorticity equation, we start from the momentum equations

$$\frac{\mathrm{D}v}{\mathrm{D}t} = -\frac{1}{\rho_0}\frac{\partial p}{\partial y} + \nu \vec{\nabla}^2 v \, , \tag{7.11a}$$

$$\frac{\mathrm{D}w}{\mathrm{D}t} = -\frac{1}{\rho_0}\frac{\partial p}{\partial z} + \nu \vec{\nabla}^2 w - \frac{g}{\rho_0}\tilde{\rho} \, , \tag{7.11b}$$

where ν is the kinematic viscosity and the last term in (7.11b) describes the acceleration due to buoyancy, caused by a small deviation $\tilde{\rho}$ from the constant density ρ_0 (Archimedes' principle). Cross-differentiating $\partial(7.11\mathrm{b})/\partial y - \partial(7.11\mathrm{a})/\partial z$ and considering (7.8) yields

$$\frac{\mathrm{D}\zeta}{\mathrm{D}t} = \nu \vec{\nabla}^2 \zeta - \frac{g}{\rho_0}\frac{\partial \tilde{\rho}}{\partial y} \; . \tag{7.12}$$

Using the volume coefficient of expansion

$$\alpha = -\frac{1}{\rho_0}\frac{\partial \tilde{\rho}}{\partial \theta} \; , \tag{7.13}$$

(7.12) can be rewritten as

$$\frac{\mathrm{D}\zeta}{\mathrm{D}t} = \nu \vec{\nabla}^2 \zeta + g\,\alpha \frac{\partial \theta}{\partial y} \; ,$$

that is,

$$\frac{\partial \zeta}{\partial t} + v\frac{\partial \zeta}{\partial y} + w\frac{\partial \zeta}{\partial z} = \nu \vec{\nabla}^2 \zeta + g\,\alpha \frac{\partial \theta}{\partial y} \; . \tag{7.14}$$

We now assume the following temperature distribution

$$\theta(y,z,t) = \theta_0 - \frac{\Delta T}{H} z + \tilde{\theta}(y,z,t) \; , \tag{7.15}$$

where $\tilde{\theta}$ is the deviation from a stable linear temperature profile $\theta_0 - \Delta T/H \; z$ with $\Delta T = \theta_0 - \theta_1$ (Fig. 7.7). The conservation of thermal energy can be captured by

the heat equation

$$\frac{\mathrm{D}\theta}{\mathrm{D}t} = \kappa\,\vec{\nabla}^2\theta\;; \tag{7.16}$$

considering (7.15), we obtain

$$\frac{\partial\tilde{\theta}}{\partial t} + v\,\frac{\partial\tilde{\theta}}{\partial y} - w\,\frac{\Delta T}{H} + w\,\frac{\partial\tilde{\theta}}{\partial z} = \kappa\,\frac{\partial^2\tilde{\theta}}{\partial y^2} + \kappa\,\frac{\partial^2\tilde{\theta}}{\partial z^2}\;. \tag{7.17}$$

Here, κ is the thermal diffusivity. Inserting (7.9) and (7.10) into (7.14) and (7.17) results with (7.15) in the following system:

$$\frac{\partial}{\partial t}\vec{\nabla}^2\Psi - \frac{\partial\Psi}{\partial z}\,\frac{\partial}{\partial y}\vec{\nabla}^2\Psi + \frac{\partial\Psi}{\partial y}\,\frac{\partial}{\partial z}\vec{\nabla}^2\Psi = \nu\,\vec{\nabla}^4\Psi + g\,\alpha\,\frac{\partial\tilde{\theta}}{\partial y}\,, \tag{7.18}$$

$$\frac{\partial\tilde{\theta}}{\partial t} - \frac{\partial\Psi}{\partial z}\,\frac{\partial\tilde{\theta}}{\partial y} + \frac{\partial\Psi}{\partial y}\,\frac{\partial\tilde{\theta}}{\partial z} = \kappa\,\vec{\nabla}^2\tilde{\theta} + \frac{\Delta T}{H}\,\frac{\partial\Psi}{\partial y}\;. \tag{7.19}$$

Equations (7.18) and (7.19) represent a coupled, non-linear system of partial differential equations which has to be completed by boundary conditions. We postulate no transport across the boundaries and no heat flux across the meridional boundaries. Furthermore, fixed temperatures at the ground and at the upper boundary shall be given, hence

$$\Psi = 0 \qquad \text{at the boundary}\;, \tag{7.20a}$$

$$\frac{\partial\tilde{\theta}}{\partial y} = 0 \qquad \text{for } y = 0 \text{ and } y = H/a\;, \tag{7.20b}$$

$$\tilde{\theta} = 0 \qquad \text{for } z = 0 \text{ and } z = H\;. \tag{7.20c}$$

The solution of this system is supposed to be found approximately by only considering the rough spatial structure inside the solution domain. To do so, we assume a truncated *Fourier expansion* satisfying the boundary conditions:

$$\Psi(y,z,t) = X(t)\,\sin\left(\frac{\pi\,a\,y}{H}\right)\,\sin\left(\frac{\pi\,z}{H}\right)\,, \tag{7.21a}$$

$$\tilde{\theta}(y,z,t) = Y(t)\,\cos\left(\frac{\pi\,a\,y}{H}\right)\sin\left(\frac{\pi\,z}{H}\right) - Z(t)\,\sin\left(\frac{2\,\pi\,z}{H}\right)\;. \tag{7.21b}$$

The space dependence is prescribed, the time dependence is given by the coefficient functions $X(t)$, $Y(t)$ and $Z(t)$. This *a priori* choice allows solutions with the simplest possible structure and, due to the truncation of the expansion only represents approximate solutions. Inserting (7.21) into (7.18), and eliminating the common factor $\sin(\pi\,a\,y/H)\sin(\pi\,z/H)$ we find

$$\left(\frac{\pi}{H}\right)^2\left(1+a^2\right)\frac{\mathrm{d}X}{\mathrm{d}t} = -\nu\left(\frac{\pi}{H}\right)^4\left(1+a^2\right)^2 X + g\,\alpha\,\frac{\pi\,a}{H}\,Y\;. \tag{7.22}$$

Similarly, inserting (7.21) into (7.19) yields

$$\cos\left(\frac{\pi\,a\,y}{H}\right)\sin\left(\frac{\pi\,z}{H}\right)\left\{\frac{\mathrm{d}Y}{\mathrm{d}t}-\frac{\pi\,a}{H}\,\frac{2\,\pi}{H}\,X\,Z\,\cos\left(\frac{2\,\pi\,z}{H}\right)\right.$$
$$\left.+\,\kappa\left(\frac{\pi}{H}\right)^2\left(1+a^2\right)Y-\frac{\Delta T}{H}\,\frac{\pi\,a}{H}X\right\}$$
$$=\sin\left(\frac{2\,\pi\,z}{H}\right)\left\{\frac{\mathrm{d}Z}{\mathrm{d}t}-\frac{1}{2}\,\frac{\pi\,a}{H}\,\frac{\pi}{H}\,X\,Y+\kappa\left(\frac{2\,\pi}{H}\right)^2 Z\right\}\ ,$$

i.e., with $\sin\left(\frac{2\,\pi\,z}{H}\right)=2\,\sin\left(\frac{\pi\,z}{H}\right)\,\cos\left(\frac{\pi\,z}{H}\right)$,

$$\cos\left(\frac{\pi\,a\,y}{H}\right)\left\{\frac{\mathrm{d}Y}{\mathrm{d}t}-\frac{\pi\,a}{H}\,\frac{2\,\pi}{H}\,X\,Z\,\cos\left(\frac{2\,\pi\,z}{H}\right)\right.$$
$$\left.+\,\kappa\left(\frac{\pi}{H}\right)^2\left(1+a^2\right)Y-\frac{\Delta T}{H}\,\frac{\pi\,a}{H}X\right\}$$
$$=2\,\cos\left(\frac{\pi\,z}{H}\right)\left\{\frac{\mathrm{d}Z}{\mathrm{d}t}-\frac{1}{2}\,\frac{\pi\,a}{H}\,\frac{\pi}{H}\,X\,Y+\kappa\left(\frac{2\,\pi}{H}\right)^2 Z\right\}\ . \tag{7.23}$$

Since this equation has to be valid for all values $0\le y\le H/a$ and $0\le z\le H$, the sums in the two {}-brackets have to vanish. Finally, we assume that the dynamics are determined by processes inside the vertical range $1/4\,H<z<3/4\,H$ and hence, the rough approximation $\cos\left(2\,\pi\,z/H\right)\approx-1$ is applicable.

The system of ordinary differential equations for the coefficient functions $X(t)$, $Y(t)$ and $Z(t)$ then reads:

$$\frac{\mathrm{d}X}{\mathrm{d}t}=-c\,X+d\,Y\ , \tag{7.24a}$$

$$\frac{\mathrm{d}Y}{\mathrm{d}t}=-e\,X\,Z+f\,X-g\,Y\ , \tag{7.24b}$$

$$\frac{\mathrm{d}Z}{\mathrm{d}t}=h\,X\,Y-k\,Z\ , \tag{7.24c}$$

with the seven constants

$$c=\nu\left(\frac{\pi}{H}\right)^2\left(1+a^2\right),\qquad d=\frac{g\,\alpha\,a\,H}{\pi\,(1+a^2)},$$
$$e=\frac{2\,\pi^2\,a}{H^2},\qquad f=\frac{\Delta T\,\pi\,a}{H^2},\qquad g=\kappa\left(\frac{\pi}{H}\right)^2\left(1+a^2\right), \tag{7.25}$$
$$h=\frac{\pi^2\,a}{2\,H^2},\qquad k=4\,\kappa\left(\frac{\pi}{H}\right)^2\ .$$

By introducing new dimensionless physical quantities t, X, Y and Z in the following

way,

$$\begin{aligned}
(\frac{\pi}{H})^2 \left(1+a^2\right) \kappa\, t &\rightarrow t \\
\frac{a}{\kappa\,(1+a^2)}\, X &\rightarrow X \\
\frac{a}{\kappa\,(1+a^2)}\, \frac{g\,\alpha\,a\,H^3}{\pi^3\,(1+a^2)^2\,\nu}\, Y &\rightarrow Y \\
2\,\frac{a}{\kappa\,(1+a^2)}\, \frac{g\,\alpha\,a\,H^3}{\pi^3\,(1+a^2)^2\,\nu}\, Z &\rightarrow Z\ ,
\end{aligned}$$

the classical Lorenz-Saltzman model can be derived:

$$\frac{\mathrm{d}X}{\mathrm{d}t} = -\sigma\, X + \sigma\, Y \tag{7.26a}$$

$$\frac{\mathrm{d}Y}{\mathrm{d}t} = -X\, Z + r\, X - Y \tag{7.26b}$$

$$\frac{\mathrm{d}Z}{\mathrm{d}t} = X\, Y - b\, Z \tag{7.26c}$$

with

$$\sigma = \frac{\nu}{\kappa}\ , \qquad r = \frac{g\,\alpha\,H^3\,\Delta T}{\nu\,\kappa}\,\frac{a^2}{\pi^4\,(1+a^2)^3}\ , \qquad b = \frac{4}{1+a^2}\ . \tag{7.27}$$

Note, the quantities t, X, Y and Z in (7.26) are the scaled forms of the quantities t, X, Y and Z in (7.24); for simplicity we do not introduce a new notation.

Figs. 7.8 and 7.9 illustrate the solution of (7.26) for a given set of parameters. The time series exhibit a chaotic behaviour, where the variables, here $Y(t)$, change from one regime ($Y > 0$) to the other ($Y < 0$) in an irregular way (Fig. 7.8). The residence time in a certain regime is erratic and considerably longer than the transition between the regimes itself. The system obviously evolves on two different time scales: one for the transition and one for the residence time in one regime. The Lorenz-Saltzman model is a prime example for abrupt changes in a dynamical system. These transitions are not a response to external disturbances, but are *spontaneously* triggered by the dynamics of the system itself.

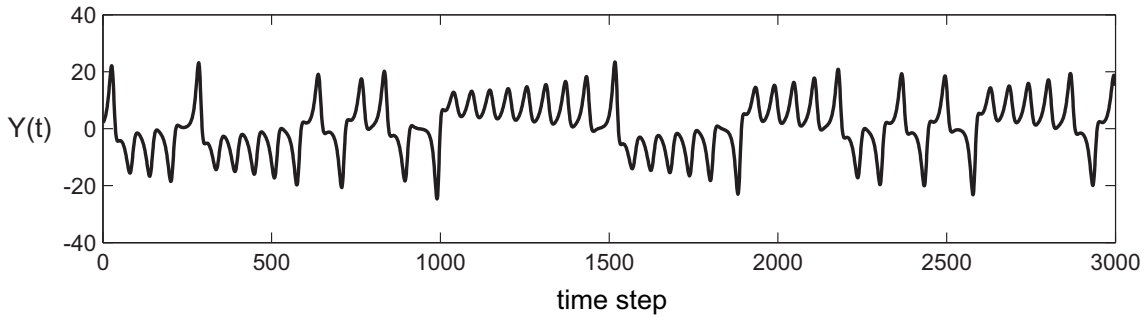

Figure 7.8: First 3000 time steps of the time series $Y(t)$ of the Lorenz-Saltzman model with the classical parameter values $r = 28$, $\sigma = 10$, $b = 8/3$. The Runge-Kutta scheme (2.23) with $\Delta t = 0.012$ and initial conditions $(1, 2, 11.02)$ is used. Shown is the chaotic regime with abrupt transitions after a period of growing amplitudes.

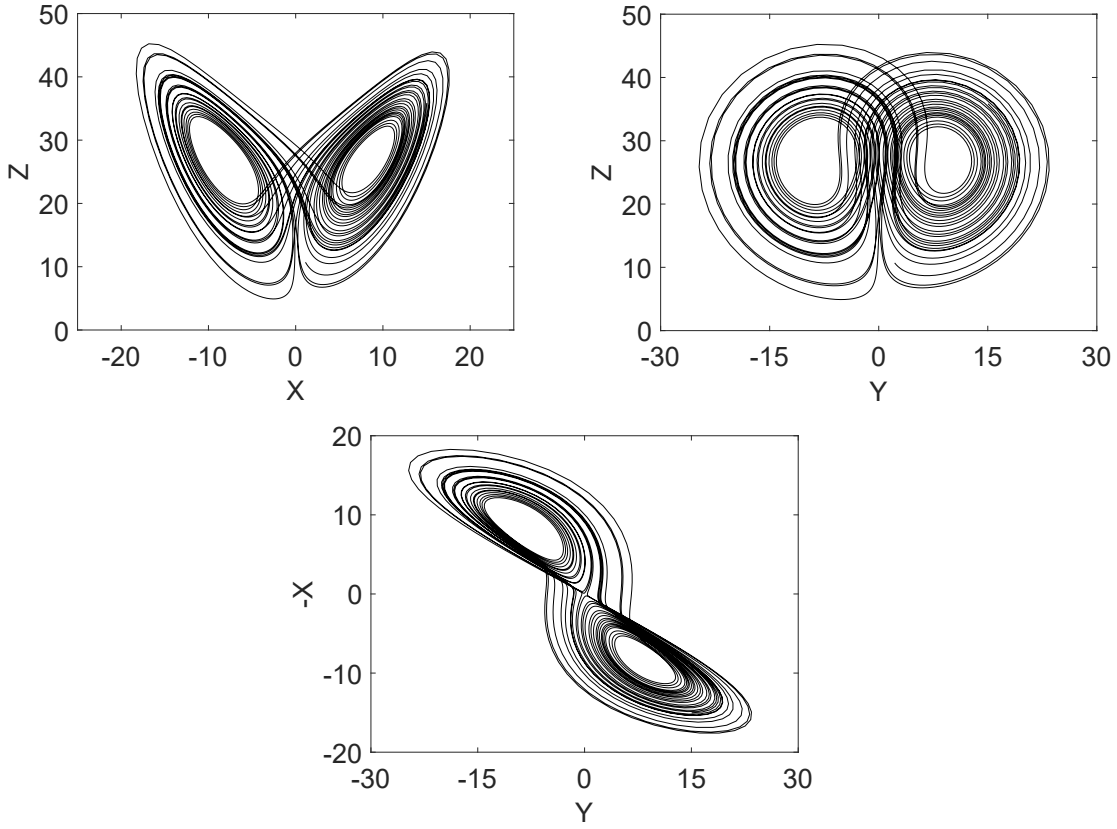

Figure 7.9: Cross-sections through the different planes in the (X, Y, Z)-space of the Lorenz-Saltzman model with the classical parameter values used in Fig. 7.8. Shown is the chaotic regime which is established after a transient phase.

Figure 7.9 shows the trajectories of the Lorenz model at subsequent time steps in the three-dimensional variable space (X, Y, Z). The points ($X = \pm 8.49$, $Y = \pm 8.49$, $Z = 27$) represent unstable equilibria. Trajectories originating in their surroundings move away from these points in spirals. For chaotic behaviour, as is the case in Figs. 7.8 and 7.9, the trajectories will never cross in the (X, Y, Z)-space. Another particular point is the origin $(0, 0, 0)$, representing another stationary solution of the equations (7.26). It is located in the center of the *transition point* from one regime to the other and hence, is the location of maximum *non-predictability* in the Lorenz-Saltzman system.

It is remarkable that this system can exhibit chaotic, periodic or stationary behaviour depending on the choice of parameters (7.27). The chaotic behaviour of the Lorenz-Saltzman model only occurs in certain parameter windows. Outside these windows, either a stable equilibrium is reached after a relatively long transient phase (Fig. 7.10) or a periodic behaviour can be observed. These are *self-sustained oscillations*, as shown in Fig. 7.12. They develop after a transient phase.

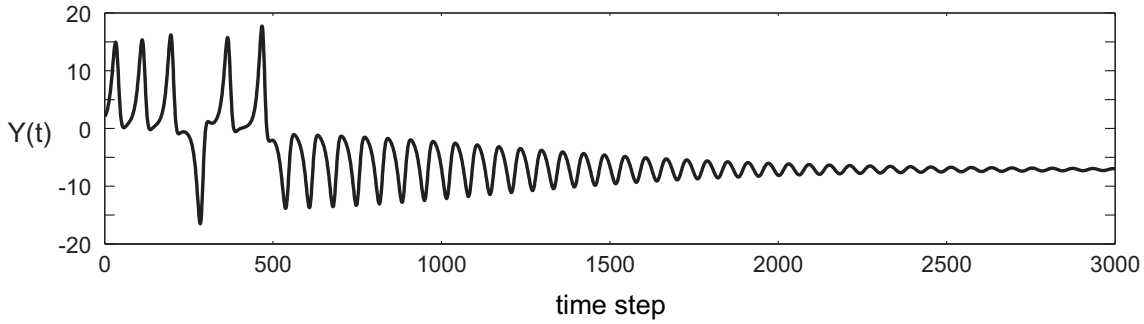

Figure 7.10: As Fig. 7.8 but with $r = 20$, $\sigma = 10$, $b = 8/3$. Shown is the damped regime approaching a steady state after a transient phase.

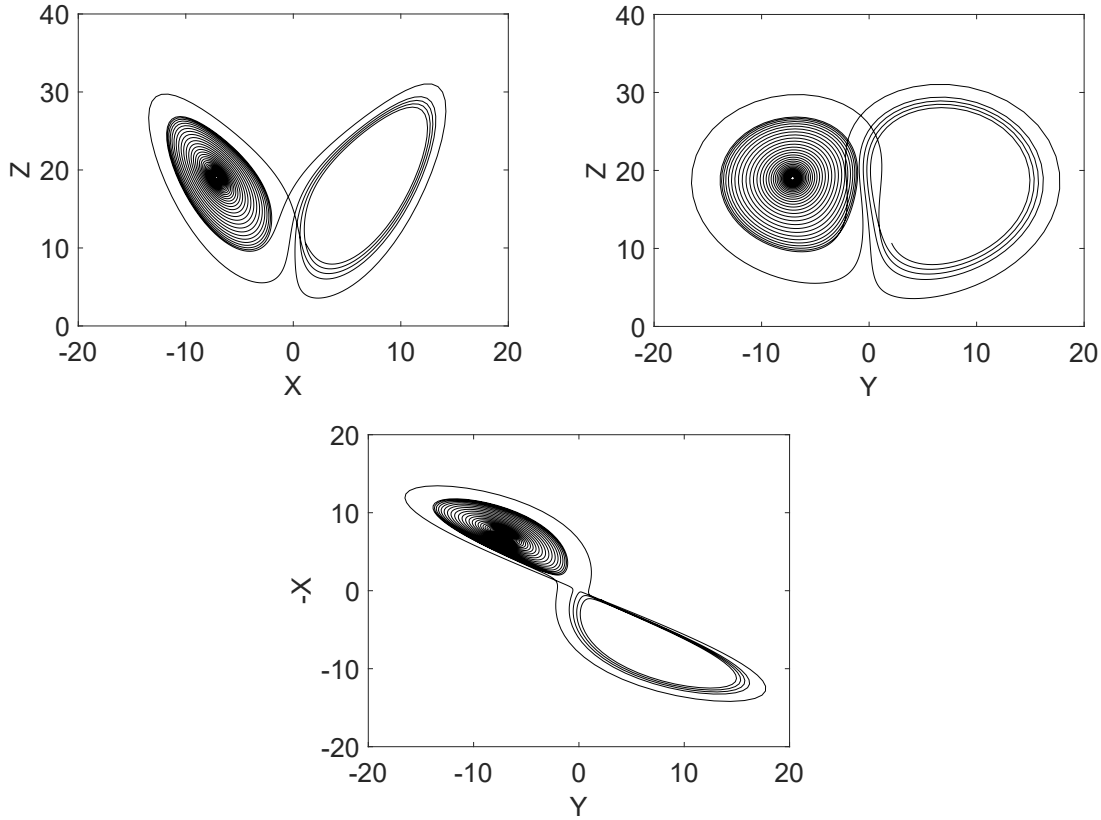

Figure 7.11: As Fig. 7.9 but with $r = 20$, $\sigma = 10$, $b = 8/3$. Shown is the damped regime approaching a steady state after a transient phase.

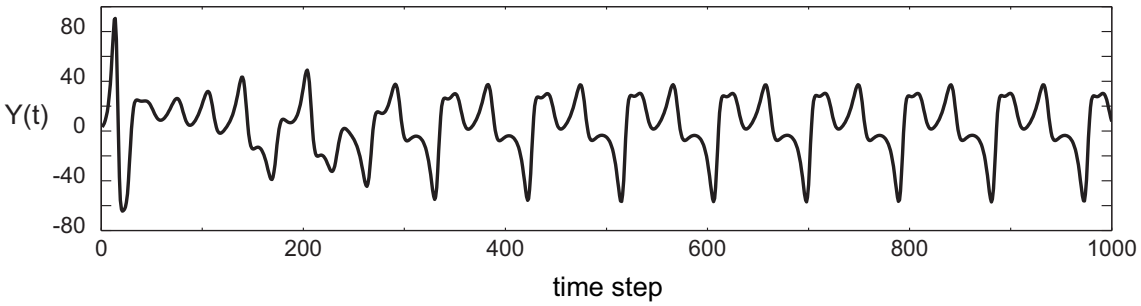

Figure 7.12: As Fig. 7.8 but with $r = 100$, $\sigma = 10$, $b = 8/3$. Shown is the periodic regime which is established after a transient phase.

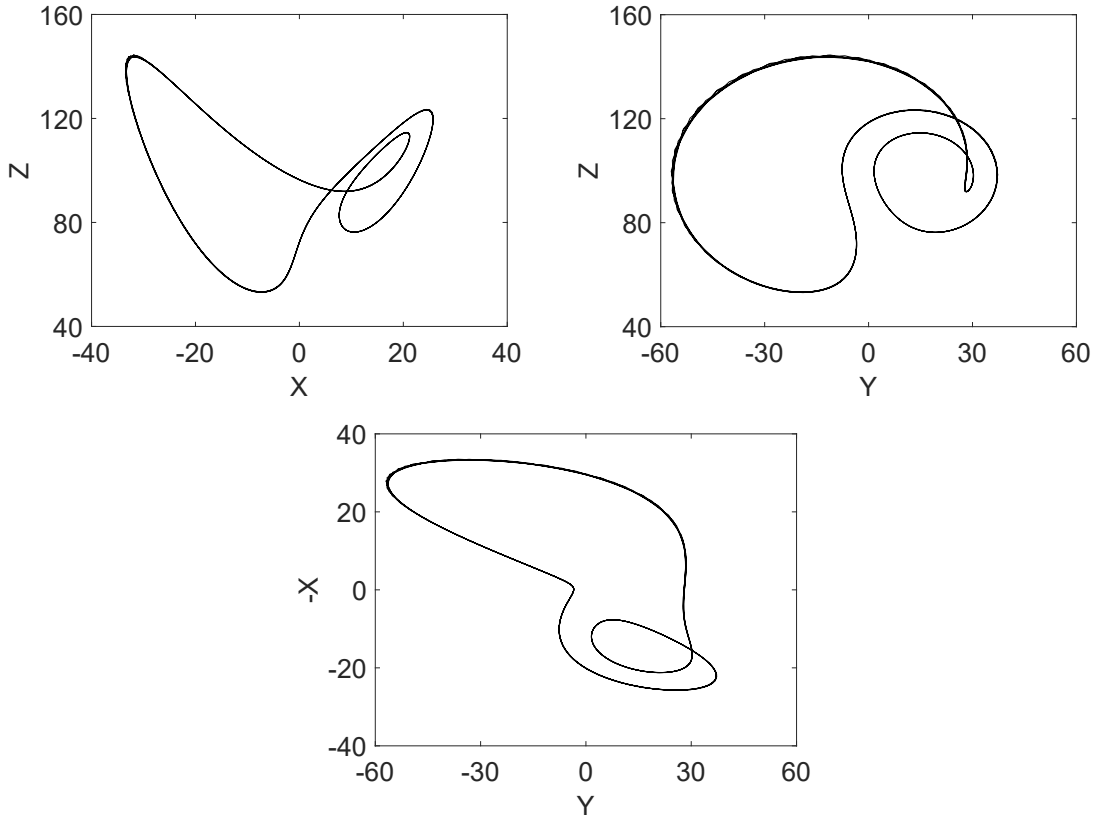

Figure 7.13: As Fig. 7.9 but with $r = 100$, $\sigma = 10$, $b = 8/3$. Shown is the periodic regime from time step 2500 to 3000.

8 Atmosphere-ocean interactions

8.1 Coupling of physical model components

Energy, momentum and matter (water, carbon, nitrogen, ...) are exchanged between the ocean and the atmosphere. Most of the movements in the ocean, particularly the large-scale flow, are caused by these exchange fluxes. Consequently, they need to be reproduced in a climate model as realistically as possible. In the context of these lecture notes we will not treat micro-scale fluxes, occurring on a cm- or smaller scale. An in-depth description is provided by Kraus and Businger (1994). We will only present the parameterisations that are implemented mainly in climate models of coarse resolution. Formulations of so-called *boundary layers* in the atmosphere and ocean are also not discussed.

In the present chapter, we consider primarily heat fluxes (fluxes of thermal or latent energy), water fluxes and momentum fluxes (Fig. 8.1). They are influenced by the dynamics of the atmosphere and the ocean, whilst they influence these dynamics. For the individual model components, the fluxes can be considered and formulated as boundary conditions.

Similar considerations have to be made for the coupling of sea ice, ice sheets, and land surface modules.

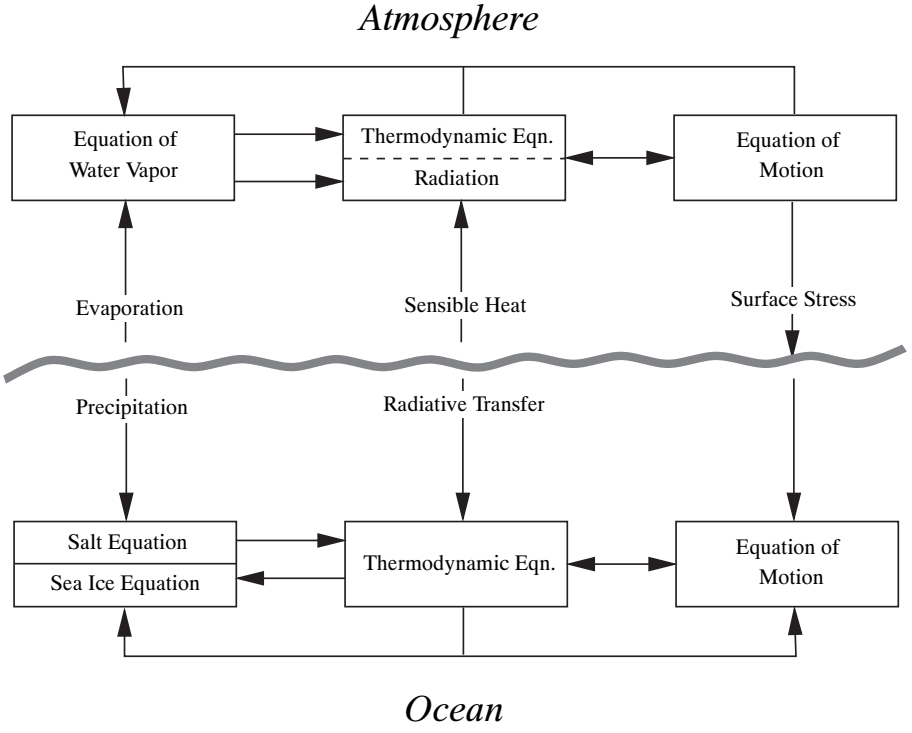

Figure 8.1: Diagram of the different model parts and fluxes of water, heat and momentum. Redrawn from Fig. 1 in Manabe and Stouffer (1988).

8.2 Thermal boundary conditions

The complete thermal boundary condition for the heat flux from the ocean to the atmosphere $F^{\mathrm{O}\to\mathrm{A}}$ is given by

$$F^{\mathrm{O}\to\mathrm{A}} = -\underbrace{(1-\alpha_{\mathrm{O}})\,Q^{\mathrm{short}}}_{\mathrm{SW}} + \underbrace{\varepsilon_{\mathrm{O}}\,\sigma\,T_{\mathrm{O}}^4}_{\mathrm{LW}} - \underbrace{\varepsilon_{\mathrm{A}}\,\sigma\,T_{\mathrm{A}}^4}_{\mathrm{LB}} + \underbrace{D\;(T_{\mathrm{O}}-T_{\mathrm{A}})}_{\mathrm{S}} + \underbrace{E(T_{\mathrm{O}},T_{\mathrm{A}})}_{\mathrm{E}}\;, \tag{8.1}$$

where T_{O} and T_{A} are the surface temperatures of the ocean and the atmosphere, respectively, Q^{short} denotes the (mainly short-wave) solar radiation reaching the ocean surface, α_{O} the albedo of the ocean surface, ε_{O} and ε_{A} the emissivities at the ocean surface and the atmosphere, respectively, D a transfer coefficient for the sensible heat flux and finally $E(T_{\mathrm{O}},T_{\mathrm{A}})$ a relation describing the evaporation on the ocean surface. The heat flux consists of five components: short-wave solar radiation (SW), long-wave radiation of the ocean (LW), long-wave back radiation of the atmosphere (LB), sensible heat flux (S) and evaporation (E). A positive sign denotes a flux from the ocean to the atmosphere. The global distribution of ocean-atmosphere fluxes is given in Fig. 8.2 and for the Atlantic in Fig. 8.3.

Typical values for the parameters in (8.1) are

$$\alpha_{\mathrm{O}} = 0.2\;, \quad \varepsilon_{\mathrm{O}} = 0.96\;, \quad \varepsilon_{\mathrm{A}} = 0.7\;\ldots\;0.9\;, \quad D = 10\;\mathrm{W\,K^{-1}\,m^{-2}}\;. \tag{8.2}$$

For certain parameterisations, the transfer coefficient D for the sensible heat flux may depend on wind speed.

The temperature dependence of the evaporation E can be expressed as a Taylor series expanded about the temperature of the atmosphere T_{A} (Haney, 1971),

$$E(T_{\mathrm{O}},T_{\mathrm{A}}) = E(T_{\mathrm{O}}=T_{\mathrm{A}},T_{\mathrm{A}}) + \left.\frac{\mathrm{d}E(T_{\mathrm{O}},T_{\mathrm{A}})}{\mathrm{d}T_{\mathrm{O}}}\right|_{T_{\mathrm{O}}=T_{\mathrm{A}}} (T_{\mathrm{O}}-T_{\mathrm{A}}) + \ldots\;.$$

An appropriate linear truncated Taylor series, which is in accordance with the Clausius-Clapeyron equation, reads (Gill, 1982; Stocker et al., 1992)

$$E(T_{\mathrm{O}},T_{\mathrm{A}}) = c_{\mathrm{E}}\;\mathrm{e}^{14.7-\frac{5418\;\mathrm{K}}{T_{\mathrm{A}}}}\left(0.2 + 5418\;\mathrm{K}\,\frac{T_{\mathrm{O}}-T_{\mathrm{A}}}{T_{\mathrm{A}}^2}\right)\;, \tag{8.3}$$

where c_{E} is a transfer coefficient depending on the wind speed.

For simplicity, in (8.1), the long-wave heat fluxes are given as grey body radiation with their associated emissivities. However, particularly LB may originate from the individual contributions of the free atmosphere and the reflection of clouds (high, as well as low clouds) and hence, may depend on modeled variables of the atmosphere component in a complex way. They also affect the solar radiation Q^{short}, which is prescribed in (8.1) but in reality is influenced by the state of the atmosphere. In principle, the heat flux between ocean and atmosphere depends on the temperatures in both components as well as on the wind speeds. These are all quantities that are simulated in a coupled climate model.

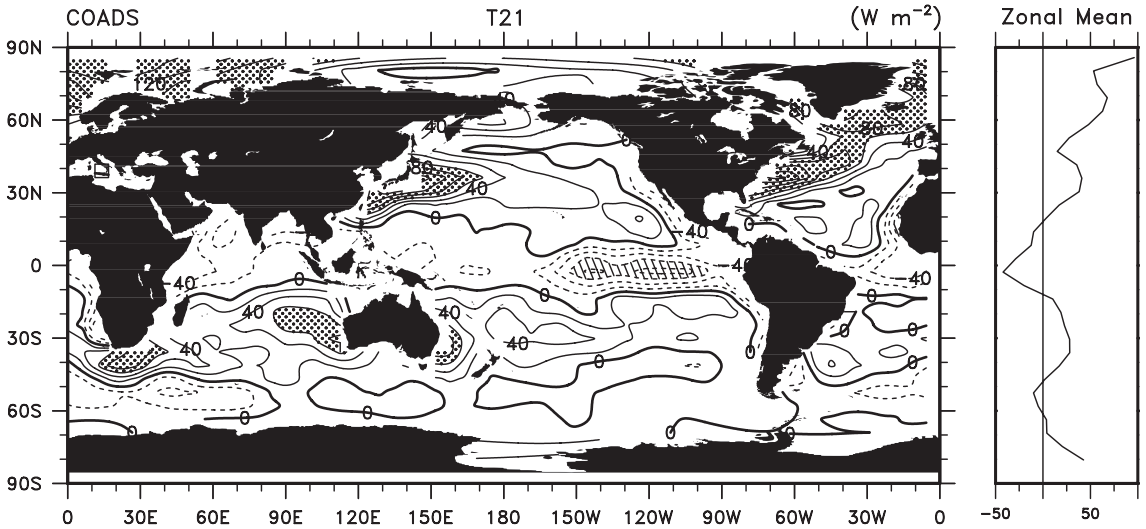

Figure 8.2: Left: Annually averaged heat fluxes in $\mathrm{W\,m^{-2}}$ based on the *Comprehensive Ocean Atmosphere Data Set* (COADS), Woodruff et al. (1987). Areas with heat fluxes exceeding $60\ \mathrm{W\,m^{-2}}$ are hatched. **Right**: Zonal average. Figure from Trenberth et al. (2001).

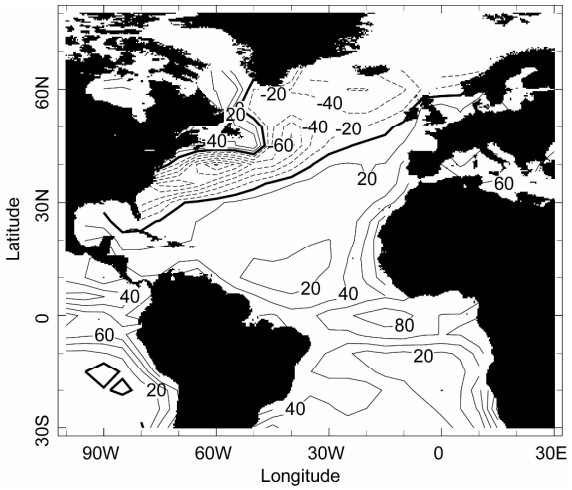

Figure 8.3: Heat flux $-F^{\mathrm{O}\to\mathrm{A}}$ in the Atlantic in $\mathrm{W\,m^{-2}}$. The map was compiled on the internet (http://ingrid.ldeo.columbia.edu), where many data sets are available. Here we have used the Cayan data set, Cayan (1992).

In climate modelling, simplified forms of (8.1) are often applied, especially when a single model component (e.g., the ocean) is integrated individually or in models of reduced complexity. This is often the case at the beginning of a simulation, when a stable equilibrium climate has to be reached. An adequately simplified form of (8.1) for an ocean model is found by linearizing this relation using a truncated Taylor series about the temperature of the atmosphere T_{A}, which is assumed to be constant (for an atmospheric model analogously):

$$
\begin{aligned}
F^{\mathrm{O}\to\mathrm{A}}(T_{\mathrm{O}}) &= F^{\mathrm{O}\to\mathrm{A}}(T_{\mathrm{A}}) + \left.\frac{\mathrm{d}F^{\mathrm{O}\to\mathrm{A}}}{\mathrm{d}T_{\mathrm{O}}}\right|_{T_{\mathrm{O}}=T_{\mathrm{A}}} (T_{\mathrm{O}} - T_{\mathrm{A}}) \\
&= F_0 + D^* \left(T_{\mathrm{O}} - T_{\mathrm{A}}\right) \ , \qquad (8.4)
\end{aligned}
$$

where

$$F_0 = F^{\mathrm{O}\to\mathrm{A}}(T_\mathrm{A}) \ ,$$

$$D^* = \left.\frac{\mathrm{d}F^{\mathrm{O}\to\mathrm{A}}}{\mathrm{d}T_\mathrm{O}}\right|_{T_\mathrm{O}=T_\mathrm{A}} \ .$$

F_0 is the net heat flux through the ocean surface of the temperature $T_\mathrm{O} = T_\mathrm{A}$ and $D^* \approx 45\ \mathrm{W\,K^{-1}\,m^{-2}}$ is a typical transfer coefficient. Note, that $D^* > D$, since (8.4) contains the effects of temperature-dependence of evaporation and of the net long-wave radiation. Haney (1971) proposed a further simplification of (8.4),

$$F^{\mathrm{O}\to\mathrm{A}}(T_\mathrm{O}) = D^*\,(T_\mathrm{O} - T_\mathrm{O}^*) \ , \tag{8.5}$$

with the so-called *restoring temperature*

$$T_\mathrm{O}^* = T_\mathrm{A} - \frac{F_0}{D^*} \ , \tag{8.6}$$

which is assumed to be constant. The formulation (8.5) is called *restoring heat flux*. This is due to the fact that heat fluxes are directed in a way that the variable surface temperature T_O asymptotically approximates the fixed temperature T_O^* when no other heat fluxes (e.g., advective heat fluxes) are present.

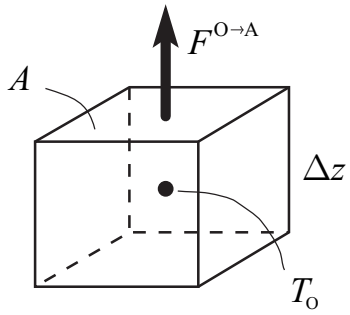

Figure 8.4: 1-box model for the illustration of restoring fluxes.

The effect of the restoring heat fluxes and the role of D^* shall be briefly illustrated by means of a 1-box model. The energy balance in the 1-box model (Fig. 8.4) with surface area A and volume $V = A\,\Delta z$ is given by

$$\rho\,V\,c\,\frac{\mathrm{d}T_\mathrm{O}}{\mathrm{d}t} = -A\,F^{\mathrm{O}\to\mathrm{A}}(T_\mathrm{O}) = -A\,D^*\,(T_\mathrm{O} - T_\mathrm{O}^*) \ . \tag{8.7}$$

ρ is the mass density and c the specific heat capacity of the ocean water. Equation (8.7) can be written as follows:

$$\frac{\mathrm{d}\,(T_\mathrm{O} - T_\mathrm{O}^*)}{\mathrm{d}t} = -\frac{D^*}{\rho\,c\,\Delta z}\,(T_\mathrm{O} - T_\mathrm{O}^*)$$

and the solution is

$$T_\mathrm{O}(t) = T_\mathrm{O}^* + \left(T_\mathrm{O}(t=0) - T_\mathrm{O}^*\right)\mathrm{e}^{-\frac{t}{\tau}} \ ,$$

where τ is a typical time scale of the relaxation. Accordingly, disturbances decay

on a time scale τ. An estimate of this *restoring time scale* yields:

$$\tau = \frac{\rho\, c\, \Delta z}{D^*} \approx \frac{1028 \cdot 3900}{45}\ \frac{\mathrm{s}}{\mathrm{m}}\, \Delta z \approx 1\ \frac{\mathrm{day}}{\mathrm{m}}\, \Delta z\ . \tag{8.8}$$

In an ocean model used in an uncoupled mode, *restoring heat fluxes* are commonly used, and for the *restoring temperature* T_O^* the observed surface temperature is applied. This guarantees that the surface values of temperature never deviate too far from the observations and that a defined equilibrium state is reached. In atmosphere models, one can proceed analogously.

The formulation (8.5), as part of an ocean model, may be regarded as the simplest form of a specific parameterisation of the effect of the not dynamically modeled atmosphere. A closer investigation of two extreme cases of ocean models demonstrates this:

- Constant temperature of the atmosphere T_A: The atmosphere acts as a "heat reservoir" with infinite heat capacity. These are *infinite heat capacity models*.
- Constant flux from the ocean to the atmosphere: We select $D^* = 0$ in (8.4), and hence $F^{\mathrm{O}\to\mathrm{A}}(T_\mathrm{O}) = F_0$, and therefore independent of a possible deviation from the mean temperatures of ocean and atmosphere. The heat capacity of the atmosphere vanishes, the atmosphere radiates the heat energy immediately to space. This is referred to as *zero heat capacity models*, and is also the case for very long relaxation times τ.

Again analogous considerations apply for atmospheric models.

The fact that (8.5) ignores a possible scale-dependence of the relaxation time is an important problem. Small-scale temperature anomalies at the sea surface are eliminated at a rate of ≈ 1 m/day by direct heat exchange. But large-scale anomalies may persist much longer, since they penetrate deeper into the ocean, and hence require a significantly higher amount of heat for equilibration. Under certain circumstances this heat energy cannot be provided by the atmosphere alone (e.g., in the form of rapidly passing storms).

In order to account for the scale-dependence, we would have to write

$$F(\vec{x}) = \int \Lambda(\vec{x}, \vec{x}\,')\, \{T(\vec{x}\,') - T^*(\vec{x}\,')\}\, \mathrm{d}\vec{x}\,' \ , \tag{8.9}$$

which contains a non-local dependence of the fluxes at location $\vec{x}$. Here, the determination of the form function $\Lambda(\vec{x}_1, \vec{x}_2)$ is a challenge. A step towards scale dependence of τ or D was proposed by Willebrand (1993),

$$F^{\mathrm{O}\to\mathrm{A}}(T_\mathrm{O}) = D_1\, (T_\mathrm{O} - T_\mathrm{O}^*) - D_2\, \vec{\nabla}^2\, (T_\mathrm{O} - T_\mathrm{O}^*)\ , \tag{8.10}$$

with $D_1 \approx 2\ \mathrm{W\,K^{-1}\,m^{-2}}$ and $D_2 \approx 10^{13}\ \mathrm{W\,K^{-1}}$. Small-scale anomalies at a typical spatial scale of 500 km, given a surface ocean layer of 50 m thickness, are equilibrated on a time scale of $\tau_2 = \rho\, c\, \Delta z\, L^2/D_2 \approx 60$ days, while large-scale anomalies decay on a time scale of $\tau_1 = \rho\, c\, \Delta z/D_1 \approx 3.5$ years. Formulation (8.10) may also be interpreted as a compact form of an atmospheric energy balance model.

8.3 Hydrological boundary conditions

The coupling of the water cycle is of fundamental significance for the transport of energy in the form of latent heat in the atmosphere and for the change in density of the surface water, induced by precipitation and evaporation. Evaporation not only represents an important heat flux (see 8.1), but also separates water and salt and only the latter remains in the ocean.

Accordingly, evaporation leads to an increase of the salinity in the surface ocean. The density of sea water at the surface $\rho(T, S)$ can be expressed as a Taylor series expanded about a temperature T_0 and a salinity S_0. An appropriately truncated Taylor series reads

$$\rho(T,S) = \rho_0\Big(1 + \alpha\,(T - T_0) + \beta\,(S - S_0) + \gamma\,(T - T_0)^2\Big)\ , \tag{8.11}$$

where

$$\begin{aligned} \rho_0 &= 1028\ \mathrm{kg\,m^{-3}}\ , & \alpha &= -5.4128 \cdot 10^{-5}\ \mathrm{K^{-1}}\ , \\ T_0 &= 0°\mathrm{C}\ , & \beta &= 7.623 \cdot 10^{-4}\ , \\ S_0 &= 35\ , & \gamma &= -5.0804 \cdot 10^{-6}\ \mathrm{K^{-2}}\ . \end{aligned} \tag{8.12}$$

ρ decreases with increasing temperature T and increases with increasing salinity S (S in g salt per kg water).

In analogy to (8.5), ocean models are run to equilibrium with the boundary condition

$$F_{\mathrm{S}}^{\mathrm{O}\to\mathrm{A}}(S) = D_{\mathrm{S}}^{*}\,(S - S^{*}) \tag{8.13}$$

with a transfer coefficient D_{S}^{*} that has the units $\mathrm{kg\,m^{-2}\,s^{-1}}$. This guarantees surface salinity values to remain close to the observational data S^{*}. Formulation (8.13) is called *restoring salt flux*. Here, the *restoring time scale*

$$\tau = \frac{\rho\,\Delta z}{D_{\mathrm{S}}^{*}} \tag{8.14}$$

is most commonly selected to be identical with the restoring time scale of the thermal boundary conditions (8.8). In case both fluxes, as given by (8.5) and (8.13), are applied in ocean models, we refer to *restoring boundary conditions*.

Analogously, atmosphere models require a condition for the lower boundary. Above water, it usually reads

$$F_{\mathrm{W}}^{\mathrm{O}\to\mathrm{A}}(q) = D_{\mathrm{W}}^{*}\,(q - q^{*})\ , \tag{8.15}$$

where q^{*} is a prescribed specific humidity. For land surfaces, simple hydrological models (*bucket models*) are commonly used. The coupling of atmosphere and ocean models requires that the salt fluxes in (8.13) are consistent with the water fluxes in (8.15). This is approximately accounted for by dividing the salt fluxes by a constant conversion factor $\rho\,S_0$, S_0 is a reference salinity:

$$p - e = \frac{1}{\rho\,S_0}\,F_{\mathrm{S}}^{\mathrm{O}\to\mathrm{A}} \tag{8.16}$$

and $p - e$ is the net water balance in m/s (or mm/yr). The distribution of $p - e$ is

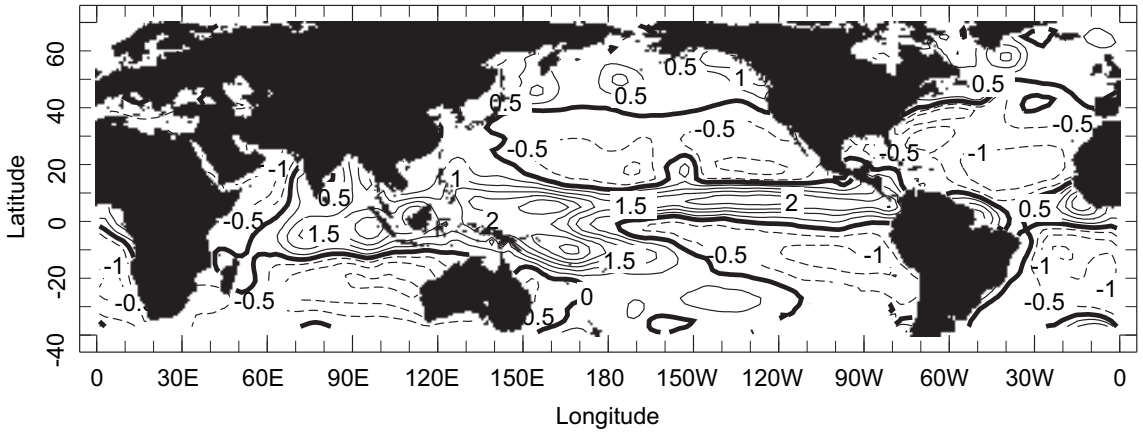

Figure 8.5: Distribution of water fluxes $p - e$ in m/year, at a contour interval of 0.5 m/year. The map was compiled on the internet (http://ingrid.ldeo.columbia.edu), where numerous data sets are available (here we used the Oberhuber data set).

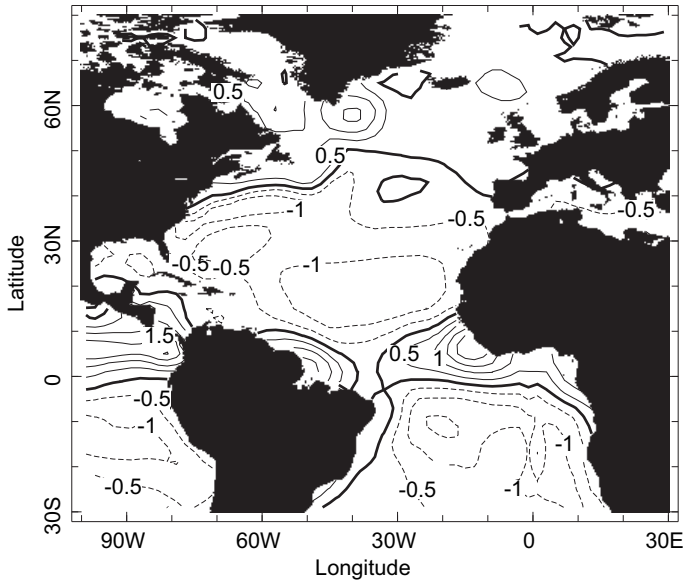

Figure 8.6: Water fluxes $p - e$ in the Atlantic in m/year. The map was compiled on the internet (http://ingrid.ldeo.columbia.edu), where numerous data sets are available (here we used the Oberhuber data set).

shown in Figs. 8.5 and 8.6. The conversion to energy fluxes is done according to

$$E = \rho\, L\, e\,, \qquad P = \rho\, L\, p\,, \tag{8.17}$$

with $L = 2.5 \cdot 10^6\ \mathrm{J\,kg^{-1}}$ for the specific latent heat of water.

8.4 Momentum fluxes

Any wind stress τ on the ocean surface is due to a momentum flux between ocean and atmosphere. It is a function of the horizontal wind speed $v_\mathrm{h} = \sqrt{u^2 + v^2}$. For dimensional reasons of the units, the following parameterisation is used,

$$\tau = c_\mathrm{D}\, \rho\, v_\mathrm{h}^2\,, \tag{8.18}$$

where ρ is the density of air and c_D is a dimensionless transfer coefficient for momentum. Based on wind tunnel experiments, one may select for atmosphere-ocean fluxes

$$c_\mathrm{D} = \begin{cases} 1.1 \cdot 10^{-3} & 0 < |u| < 6\,\frac{\mathrm{m}}{\mathrm{s}} \\ 0.61{\cdot}10^{-3} + 6.3{\cdot}10^{-5}\,\frac{\mathrm{s}}{\mathrm{m}} \cdot |u| & 6\,\frac{\mathrm{m}}{\mathrm{s}} < |u| < 22\,\frac{\mathrm{m}}{\mathrm{s}}\ , \end{cases} \tag{8.19}$$

but many other parameterisations have been proposed to account for different conditions at the interface. In the models, vertical momentum fluxes are implemented as forces acting on the uppermost layer of the ocean model (or the lowest layer in the atmosphere model).

8.5 Mixed boundary conditions

Restoring boundary conditions as given by (8.5) are useful when equilibria of ocean models are sought for which the surface temperatures and salinities should be in good agreement with the data. Analogously, they are used in atmosphere-only models when surface temperatures are prescribed. For heat fluxes it may plausibly be argued that fluxes are proportional to temperature differences. In fact, this is a discretized formulation of the heat flux according to Fick's first law. In physical terms, this means that for example a warm anomaly of the surface temperature in the ocean leads to an increased heat flux from the ocean to the atmosphere and hence causes a cooling of the ocean tending to restore the previous equilibrium.

However, the same argument cannot be used for water fluxes. A locally increased salinity at the surface of the ocean, for example induced by an oceanic eddy, does not lead to increased precipitation (Fig. 8.7). Such anomalies are therefore not eliminated on a typical time scale and have a much longer lifetime. Hence, (8.13) lacks a physical justification.

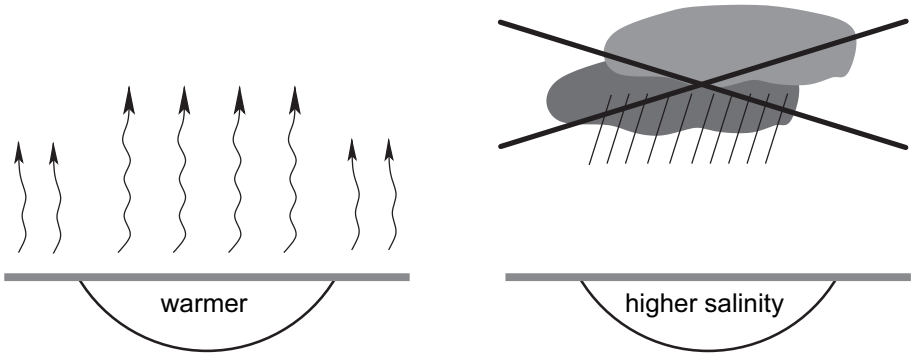

Figure 8.7: Schematic illustration of temperature and salinity anomalies at the surface ocean and the different responses of heat and water fluxes. A warm SST anomaly causes an increased ocean-to-atmosphere heat flux which removes the anomaly. On the other hand, a SSS anomaly does not influence the amount of precipitation in the atmosphere.

In order to account for this fact in ocean models that have reached equilibrium (after several 1000 years for T and S), equation (8.13) is replaced by a constant flux

$$\hat{F}_\mathrm{S}^{\mathrm{O}\to\mathrm{A}} = D_\mathrm{S}^* \left(S_\infty - S^*\right)\ , \tag{8.20}$$

where S_∞ is the salinity attained in equilibrium. According to (8.20), $\hat{F}_\mathrm{S}^{\mathrm{O}\to\mathrm{A}}$ is

not time-dependent. The combination of the two boundary conditions (8.5) and (8.20) is denoted *mixed boundary conditions*. In principle, they represent a first approximation to the different nature of feedback processes associated with heat and water fluxes.

For mixed boundary conditions, the salinity, and hence the density at the surface ocean can deviate arbitrarily from a fixed prescribed distribution S^* without water fluxes to react and to counteract the emerging changes. This implies that salinity anomalies could permanently alter the structure of the circulation. This hypothesis was first formulated by Stommel (1961), and later confirmed by Bryan (1986) in a three-dimensional ocean model. The surprising result was the detection of *multiple equilibria*, qualitatively different ocean circulations were simulated. The relevance of this finding to understand the dynamics of the climate system is further discussed in Chapter 9.

8.6 Simple coupled models

We have seen the amount of fundamental insight that comes from simple models in the consideration of the thermally-driven flow in the atmosphere (see Section 7.2). Here we present two further examples of dynamical systems that address entirely different space and time scales. The first concerns the question of ice ages and thus includes processes operating on time scales of 10^5 to 10^6 years, while the second simulates the atmosphere-ocean interactions in the equatorial Pacific that give rise to the ENSO-phenomenon with characteristic time scales of a few months to years.

8.6.1 Global model of Pleistocene ice ages

Due to the long time scales of glacial-interglacial cycles, for many years general circulations models could not be applied to these questions due to their computational limitations. In the past few years, EMICs could be applied to these problems, and predictably soon, low-resolution coupled climate models will do so, too. Fundamental feedback relations between global climate system components can be investigated by systematically reducing conservation equations to a lower-dimensional problem (Saltzman, 2001). The insights gleaned from such reduced climate models pave the way for targeted investigations using models of gradually increasing complexity (see Table 2.1).

The approach is very similar to that already presented in Section 7.2. The model of Saltzman and Maasch (1991) considers three global-scale variables: global ice volume $I(t)$, CO_2-concentration in the atmosphere, $C(t)$, and deep ocean temperature, $T(t)$ which are coupled through feedbacks between them:

$$\frac{\mathrm{d}I}{\mathrm{d}t} = \alpha_1 - \alpha_2\, C - \alpha_3\, I - \alpha_4\, T - r(t) + \varepsilon_I(t)\ , \tag{8.21a}$$

$$\frac{\mathrm{d}C}{\mathrm{d}t} = \beta_1 - \beta_2\, C + \beta_3\, C^2 - \beta_4\, C^3 - \beta_5\, T + \varepsilon_C(t)\ , \tag{8.21b}$$

$$\frac{\mathrm{d}T}{\mathrm{d}t} = \gamma_1 - \gamma_2\, I - \gamma_3\, T + \varepsilon_T(t)\ , \tag{8.21c}$$

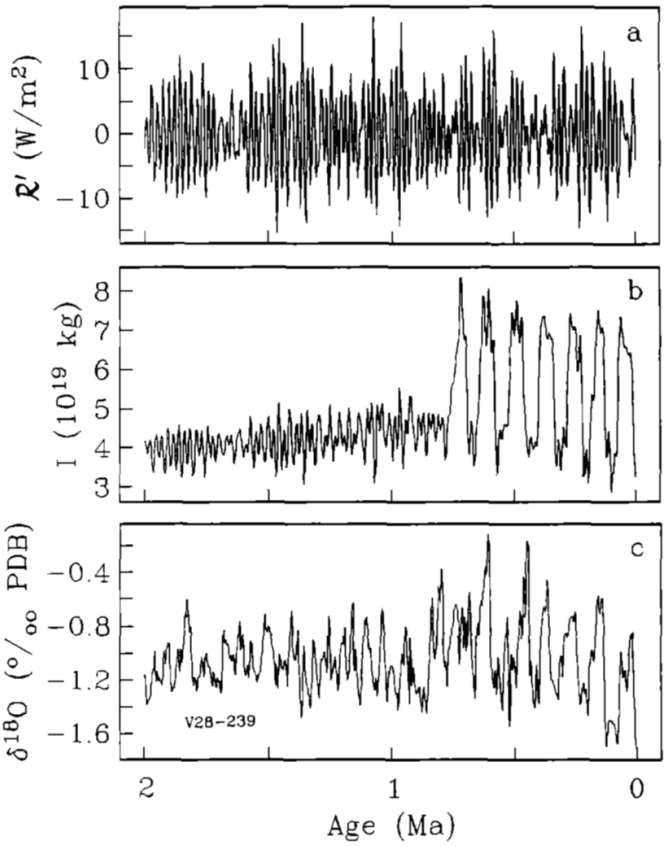

Figure 8.8: Pleistocene ice ages as simulated by the dynamical system (8.21). **(a)**: Prescribed changes in high-latitude solar irradiation; **(b)**: simulated changes in ice volume; **(c)**: reconstructed evolution of sea level based on stable isotope measurements on marine sediments. The Mid Pleistocene Transition from the 40,000 to the 100,000-year ice age cycles occurred around 1 million years ago. Figure from Saltzman and Maasch (1991).

where α_i, β_i, and γ_i are positive coupling constants, $r(t)$ is the prescribed variation in high-latitude irradiation, and $\varepsilon_i(t)$ are small stochastic forcings for each variable representing the effects of internal variability. With the exception of β_2 all feedbacks are negative and hence stabilizing. The parameters can be tuned within plausible ranges. In addition, Saltzman and Maasch (1991) prescribed slow trends of the background climate, consistent with the known slow cooling, decreasing CO_2 and increasing ice volume over the past 5 M years. By then focusing on the millennial-scale changes by separating $I(t) = I_0 + I'(t)$, etc., they could simulate the transient change in global climate over the past 2 M years. The time evolution is remarkably consistent with the paleoclimatic records as known by then (Fig. 8.8c). In particular, the Mid Pleistocene Transition (MPT) at around 1 M years ago is captured as a relatively rapid switch from 40,000-year, small amplitude to 100,000-year, large amplitude ice age cycles.

Such studies with simplified climate models are not meant to definitely resolve the mysteries around the MPT but to demonstrate the dominating processes that may generate this transition. It is concluded that the switch is caused by a non-linear interaction between the ice sheet extent, the ocean temperature, and the atmospheric CO_2 concentration, against a varying background climate due to other, much slower processes such as weathering, ice-bedrock interactions, or tectonic responses. Remarkably, more recent simulations using an EMIC come to similar conclusions (Willeit et al., 2019).

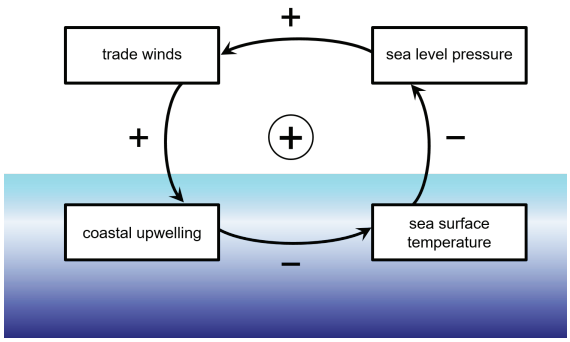

Figure 8.9: Bjerknes positive feedback loop involving atmosphere and ocean and responsible for maintaining the normal conditions in the Eastern equatorial Pacific.

8.6.2 Simplified models of the El Niño-Southern Oscillation

El Niño-Southern Oscillation is the most prominent mode of natural variability in the climate system and an iconic example of atmosphere-ocean interaction. It consists of two elements: (i), a pressure seesaw between Tahiti and Darwin which drives anomalies of the trade winds over the equatorial Pacific and determines the location of the tropical convection (Southern Oscillation), and (ii), anomalies of sea surface temperature and associated upwelling in the eastern equatorial Pacific and ocean wave propagation along and near the equator. A key process maintaining normal conditions in the equatorial Pacific is the so-called *Bjerknes feedback* (Bjerknes, 1969). This was proposed by *Jacob Bjerknes* (1897–1975), the son of Vilhelm Bjerknes (page 11). Cold anomalies at the sea surface in the Eastern equatorial Pacific increase sea level pressure, promote atmospheric subsidence and increase trade winds. These in turn, force coastal upwelling which further cools the sea surface (Fig. 8.9).

Figure 8.10 shows the three states of the ENSO cycle. *Normal conditions* are characterized by a tilted thermocline – the location between the cold deeper water and the warm surface water at around 150 m depth at the equator –, resulting in cold sea surface temperatures in the east and a warm pool in the west. Cold surface conditions generate high sea level pressure, whereas low pressure and convection prevail over the western warm pool. This promotes trade winds which drive warm surface waters westward and shallow the thermocline in the east. This is the lower branch of the atmospheric *Walker circulation*. Under normal conditions, coastal waters supplied by the upwelling are cool and nutrient-rich. If the trade winds relax and the Walker circulation weakens, the entire equatorial Pacific adjusts, and *El Niño conditions* start to develop. First, the upwelling in the east weakens and cuts off the supply of colder deeper waters. A strong warming and deepening of the thermocline follows in the east, the western warm pool starts to extend towards the central equatorial Pacific, and the convective area in the atmosphere shifts eastward. *La Niña conditions* are the opposite of El Niño with anomalously cold conditions in the eastern equatorial Pacific and a stronger Walker circulation.

The cycle is irregular and has a typical time scale of 3 to 7 years. Recent analyses show that there is also a decadal component to the Pacific variability: phases with several El Niño-years follow a series of La Niñas, or several years of normal conditions. Furthermore, observations suggest that these three states described here are not sharply defined and there may exist different flavors of ENSO with different degrees of predictability (Timmermann et al., 2018).

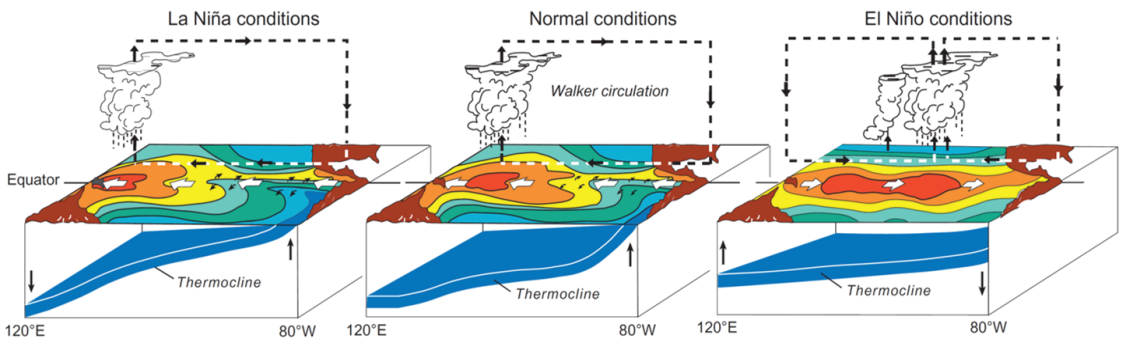

Figure 8.10: The three states of the ENSO cycle showing the location of the main convective system and circulation in the atmosphere, sea surface temperature anomalies and the location of the ocean thermocline. Figure adapted from McPhaden et al. (1998).

To understand ENSO cycle one needs to consider the propagation of anomalies in the equatorial atmosphere-ocean system. Key is the fact that the equator is a wave guide for Kelvin and Rossby waves (see Sections 6.4.3 and 6.4.4). Anomalies at the east (e.g., sea surface temperature or thermocline thickness) propagate westward as slow Rossby waves. When they reach the western basin boundary they are reflected and transform into eastward propagating fast equatorial Kelvin waves. Once arrived at the eastern boundary, they generate coastal Kelvin waves escaping into both hemispheres, and a new westward travelling Rossby wave, closing the oceanic wave cycle. The sequence of waves not only transports anomalies but also dissipates them and causes an adjustment of the state. It is through this equatorial wave action, tightly coupled to the tropical atmosphere, that the different states of the ENSO cycle are generated.

Simple models therefore must represent the coupling of the key variables of surface temperature, thermoclimate thickness, and wind strength, and the temporal sequence of perturbations. Various simple models have been proposed. For illustration we present two of them briefly, and then close with a dynamical model that is based on the shallow water equations on the equatorial β-plane.

The simplest model, exhibiting some key characteristics of ENSO, is the *Delayed Oscillator* for the eastern Pacfic surface temperature T:

$$\frac{\mathrm{d}T}{\mathrm{d}t} = a\,T(t) - b\,T(t-\delta) - r\,T^3\,. \tag{8.22}$$

The strength of the positive Bjerknes feedback is described by a, and the delayed negative feedback, mediated by the Rossby and Kelvin waves at delay time δ, is captured by the second term. The third term is a nonlinear dissipation term. This empirical model exhibits a stable and oscillatory regime depending on model parameters r and b/a. More details are given in Boutle et al. (2007) and Vallis (2017).

The second, more complex model is the *Recharge–Discharge Oscillator* which describes the coupled interaction between anomalies of sea surface temperature in the eastern Pacific T and thermocline thickness h:

$$\frac{\mathrm{d}T}{\mathrm{d}t} = a\,T + F\,h\,, \quad \frac{\mathrm{d}h}{\mathrm{d}t} = -\varepsilon h - \alpha\,T\,, \tag{8.23}$$

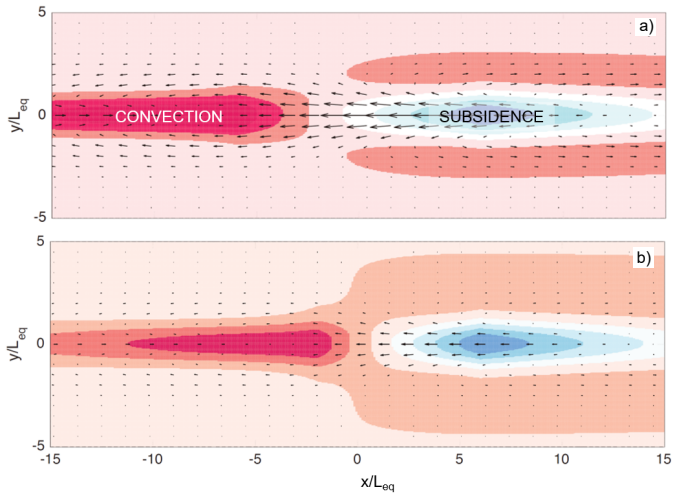

Figure 8.11: Simulated anomalous atmospheric circulation on an equatorial β-plane, caused by a localized heat anomaly for two states of ENSO. Shown are velocities (*arrows*) and divergence (*blue*) and convergence (*red*) of the velocity field. **(a)**: heating and cooling in the west and the east, respectively, with maximum heating at $x = -6$ (normal state). **(b)**: weaker heating and cooling with maximum heating shifted eastward to $x = -2$ (El Niño state). The location of maximum cooling is unchanged. Figure from Vallis (2017).

where F provides the warming through thermocline thickening, while the thermocline undergoes discharge (ε) and recharge (α), via meridional Sverdrup transport towards (caused by easterly wind anomalies), and away from the equator (caused by westerly wind anomalies).

Due to the direct impacts on people and livelihoods in the entire tropical Pacific, chiefly in the coastal regions of South America, but also beyond the Pacific regions through teleconnections, there is a strong economic interest to reliably predict ENSO (see Section 1.5.5). Simple models are unable to provide this information and therefore, coupled models based on the detailed dynamics in the equatorial Pacific need to be employed. They are based on the shallow water equations 6.20, formulated on the equatorial β-plane and supplemented by a suitable atmospheric component coupled to it. The relevant ocean dynamics occur in the equatorial thermocline layer which occupies the top 150 m and rests on a colder water body. Therefore, we need to employ in (6.20) *reduced gravity* g'. It is defined as $g' = g\,(\rho_2 - \rho_1)/\rho_1$, with ρ_1 and ρ_2 the densities of the thermocline layer and the layer below, respectively. All waves are understood to pertain to the first baroclinic mode, i.e., they propagate on the thermocline.

The first model that was employed for an ENSO forecast was formulated by Zebiak and Cane (1987). Here we follow essemtially Vallis (2017) and present the system of equations which results from the shallow water equations in the ocean and the atmosphere, formulated on an equatorial β-plane where $f = \beta\, y$. First, the equations for the ocean are given by:

$$\begin{aligned}
\frac{\partial u}{\partial t} - \beta\, y\, v &= -g' \frac{\partial h}{\partial x} - r\, u + \tilde{\tau}_x \,, \\
\frac{\partial v}{\partial t} + \beta\, y\, u &= -g' \frac{\partial h}{\partial y} - r\, v + \tilde{\tau}_y \,, \\
\frac{\partial h}{\partial t} + H \left(\frac{\partial u}{\partial x} + \frac{\partial v}{\partial y} \right) &= 0 \,,
\end{aligned} \tag{8.24}$$

where (u, v) is the horizontal velocity vector of the flow in the thermocline layer with an undisturbed thickness of H. The thickness anomaly is given by h and caused by the combination of the elevation of the sea surface and a much larger change

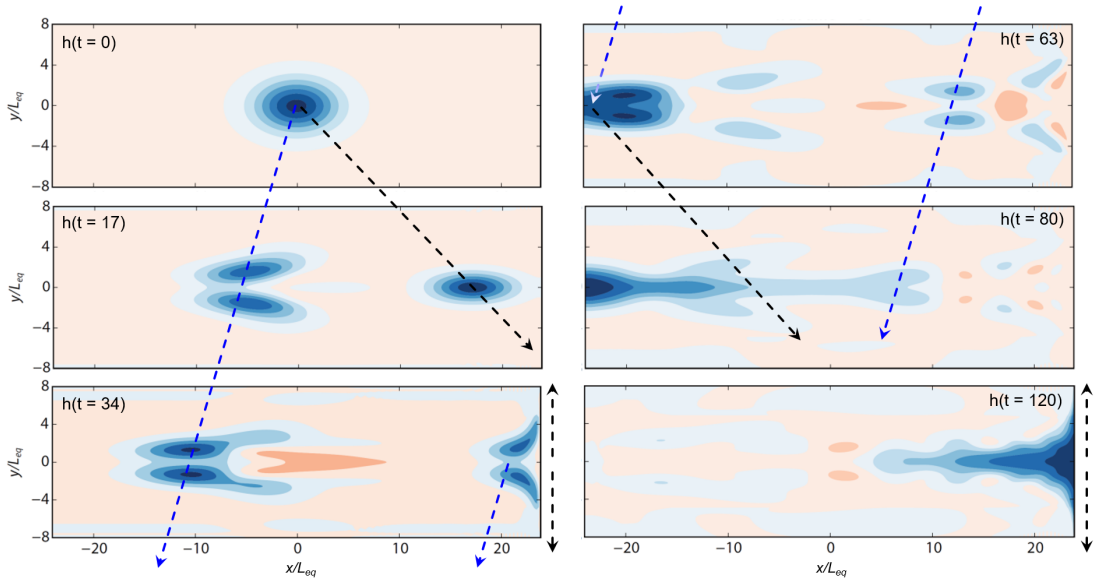

Figure 8.12: Simulated time evolution of the thermocline thickness anomalies on an equatorial β-plane. The simulation shows the effect of equatorial wave propagation initiated by a central-equatorial thickness anomaly at $t = 0$. The locations of anomaly maxima are joined by *dashed arrows* through time: *black*: eastward propagating Kelvin wave at speed $c_{ph} = 2.8\,\mathrm{m\,s^{-1}}$; *blue*: westward propagating Rossby wave at speed $c_{ph} = 0.9\,\mathrm{m\,s^{-1}}$. Figure adapted from Vallis (2017).

in the depth of the thermocline. It is the latter that is important for the ENSO phenomenon. In this case, the pressure gradient acceleration driving the flow is dominated by $-g'\nabla h$, with reduced gravity $g' = 5.6 \cdot 10^{-2}\,\mathrm{m\,s^{-2}}$, $r = (2.5\mathrm{yr})^{-1}$ is a dissipation coefficient, and $\tilde{\tau}_x = \tau_x/\rho H$ is the zonal wind stress acting on the thermocline layer of undisturbed thickness $H = 150\,\mathrm{m}$. Here, it is assumed that the meridional wind stress $\tilde{\tau}_y$ and all non-linear advection terms are neglected.

The atmospheric component of this ENSO model is formally very similar to (8.24), namely

$$\begin{aligned} \frac{\partial U}{\partial t} - \beta\, y\, V &= -\frac{\partial \Phi}{\partial x} - r_a\, U\ , \\ \frac{\partial V}{\partial t} + \beta\, y\, U &= -\frac{\partial \Phi}{\partial y} - r_a\, V\ , \\ \frac{\partial \Phi}{\partial t} + c_a^2 \left(\frac{\partial U}{\partial x} + \frac{\partial V}{\partial y} \right) &= Q_a\ . \end{aligned} \tag{8.25}$$

(U, V) is the horizontal velocity vector of the baroclinic circulation in the atmosphere, driven by geopotential gradients of Φ. With the baroclinic velocity (U, V), appropriate to describe the Walker circulation (see Fig. 8.10), the near-surface wind velocity would be $-\frac{1}{2}(U, V)$ and the wind aloft $+\frac{1}{2}(U, V)$. Parameter values are taken from Hirst (1986). $r_a = 5 \cdot 10^{-6}\,\mathrm{s^{-1}}$ is the atmospheric drag coefficient. The zonal wind speed U creates a wind stress driving ocean currents: $\tilde{\tau}_x = -K_S\, U$, with $K_S = 8 \cdot 10^{-8}\,\mathrm{s^{-1}}$. The negative sign is due to the fact that τ_x is in the direction of the near-surface wind velocity. $c_a = 60\,\mathrm{m\,s^{-1}}$ is the speed of the first baroclinic mode of atmospheric gravity waves.

The atmospheric dynamics are driven by heat anomalies Q_a caused by sea surface

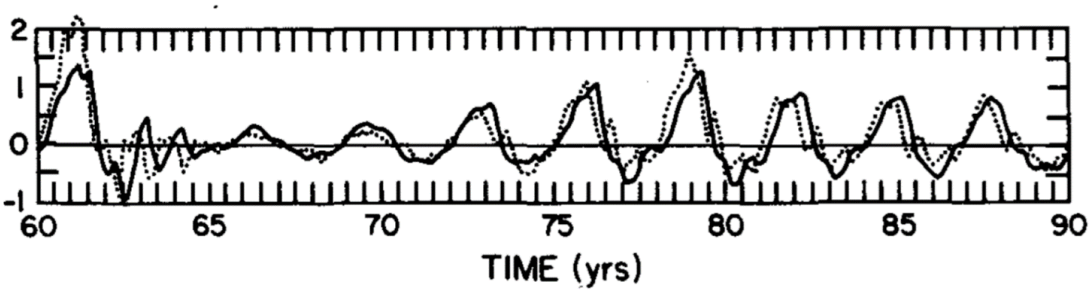

Figure 8.13: Evolution of the zonal wind anomalies (in $\mathrm{m\,s^{-1}}$) in the western (*solid*) and central-eastern (*dotted*) equatorial Pacific as simulated by the Zebiak-Cane model (Zebiak and Cane, 1987). The non-periodic nature of the ENSO cycle is evident with strong events, quiet periods, and near-oscillatory behaviour. Figure from Zebiak and Cane (1987).

temperature anomalies T. An empirical parameterization is therefore $Q_a = K_Q\, T$ with $K_Q = 7 \cdot 10^{-3}\,\mathrm{m^2 s^{-3} K^{-1}}$ (Hirst, 1986). The Zebiak and Cane (1987) model also includes a balance equation for the thermocline temperature. A simplification was proposed by Hirst (1986) who shows that the temperature anomaly T is approximately proportional to the thermocline thickness anomaly h, and hence $Q_a = \alpha\, h$. Heating of the overlying atmosphere occurs where the thermocline is deep. Parameter $\alpha = 2.1 \cdot 10^{-4}\,\mathrm{m\,s^{-3}}$ represents the strength of the positive Bjerknes feedback (Fig. 8.9). Coupling of ocean and atmosphere in (8.24) and (8.25) occurs through $\tilde{\tau}_x = -K_S\, U$ and $Q_a = \alpha\, h$, respectively. (8.24) and (8.25) form a complete set of PDEs for the six variables (u, v, h, U, V, Φ).

For the solution of the PDEs we need to employ numerical techniques as outlined in Section 6.5. A simulation of the uncoupled atmospheric flow anomalies generated by an equatorial heat source (west: $x < 0$) and heat sink (east: $x > 0$) is shown Fig. 8.11a. This heat distribution is characteristic of normal ENSO conditions and generates easterly flow and resulting convergence with ensuing convection in the west, while divergence and subsidence are located in the east. This is the lower branch of the Walker circulation. Upon an eastward shift and weakening of the heat source (Fig. 8.11b), the Walker circulation reduces and the area of convergence widens towards the east. This is the El Niño condition.

A simulation of the ocean component of the ENSO model (8.24) is depicted in Fig. 8.12. The system (8.24) is solved on the equatorial β-plane where perturbations are meridionally confined by the equatorial Rossby radius $L_E \approx 350\,\mathrm{km}$. The model is initiated with a Gaussian perturbation in the central Pacific which launches a slow Rossby wave westward and a fast Kelvin wave eastward. Once the latter arrives at the eastern basin boundary ($t \approx 34$), the Kelvin wave splits and propagates meridionally as a coastal Kelvin wave away from the equator. This is an efficient dissipation mechanism for wave energy. Additionally, a weaker equatorial Rossby wave is generated that, again, moves westward. When the Rossby waves hit the western boundary ($t = 63$), the energy is transferred to an equatorial Kelvin wave which starts travelling eastward (see also Fig. 8.10).

Finally, we show the historical simulation by Zebiak and Cane (1987) in Fig. 8.13. Their coupled ENSO model was based essentially on equations (8.24)-(8.25) and was able to reproduce the main characteristics of the observed ENSO cycle. Irregular fluctuations of zonal wind stress, themocline thickness and heat content

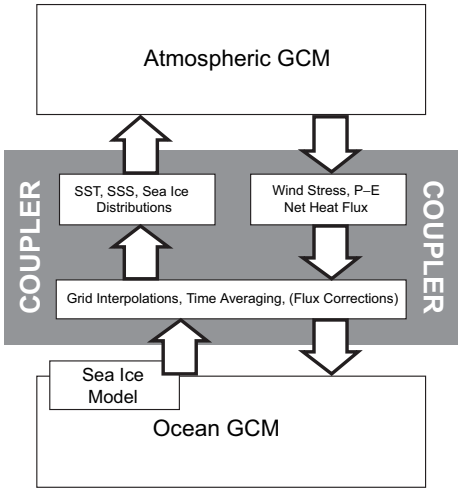

Figure 8.14: Scheme of the coupling of atmosphere and ocean model components. Figure from Trenberth (1992).

show episodes of significantly larger anomalies (El Niño conditions), several years of normal conditions, and nearly-regular El Niño-La Niña cycles. Such models, supplemented with essential observations in the tropical Pacific, form the basis of today's ENSO forecast system.

8.7 Coupled models

The biggest challenge in climate modelling is the construction of consistent coupled models that incorporate and quantitatively simulate the components ocean, atmosphere, cryosphere, land surface, biosphere as well as the physical-biogeochemical interactions. Over the years, large progress in the coupling has been achieved as illustrated in Fig. 1.12. A particular difficulty is to simulate climatologies of the ocean, the atmosphere, and the cryosphere, that agree well with the observations. For a long period, the fact that the ocean and the atmosphere required different fluxes in order to reach equilibrium, was a major obstacle in modelling. This implies, that at the time of coupling, the two model components cannot be driven by the same fluxes. This inevitably leads to drift of the two components and possibly to completely unrealistic states.

Ideally, the coupling follows the scheme presented in Fig. 8.14 without flux corrections. In climate models of earlier generations, this often led to climate drift. A stable state agreeing with the climatology could not be attained. This is especially difficult, when the model state is in a range where several equilibria are possible.

Such a climate drift simulated with a coupled model of reduced complexity is shown in Fig. 8.15. The ocean component is first brought to equilibrium for 4000 years under *restoring boundary conditions*. Subsequently, a simple energy balance model is coupled to the ocean model. From this point on, more degrees of freedom are available, therefore, T and S may also change.

As mentioned earlier, the prevention of drift is based on an unphysical approach: so-called *flux corrections* or *flux adjustments*. Although the latest generation of coupled models no longer requires such flux corrections, they shall be discussed here, also with respect to their order of magnitude.

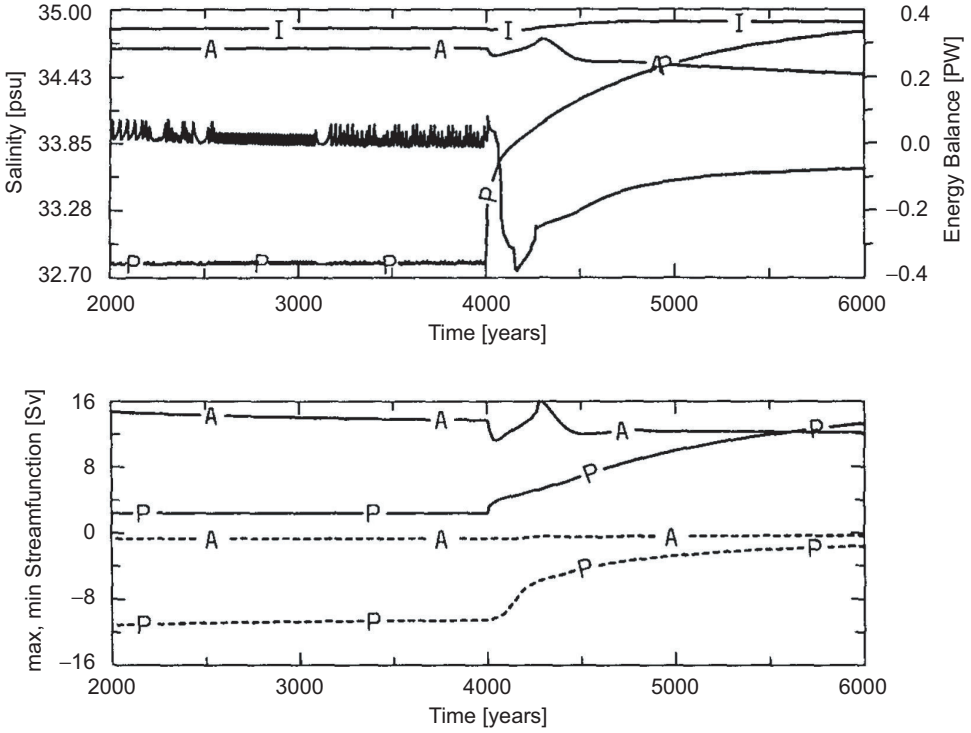

Figure 8.15: Climate drift in a coupled model of reduced complexity, the Bern 2.5D model, initiating at the time of coupling ($t = 4000$ years). The salinity of the Pacific (P) is increasing, the energy balance is perturbed and an approach to a different equilibrium state is simulated (**upper panel**). This leads to a change in the meridional circulation (**lower panel**), apparent in the drift of the stream functions. Figure from Stocker et al. (1992).

Flux corrections for heat, water and momentum fluxes are implemented as constant artificial sources and sinks at the boundaries of the individual model components. In doing so, the different model components are not fully coupled, but are rather linked via their deviations from an independently maintained equilibrium state. This is also referred to as *anomaly coupling*.

Flux corrections may be described as follows. $F(\mathrm{o},\mathrm{a})$ denotes the heat flux from the ocean (o) to the atmosphere (a), as it results from a fully coupled model, hence it is computed based on the variables T_O and T_A in (8.1). $F(\mathrm{o_u},\mathrm{a_u})$ denotes the heat flux that the *uncoupled* model requires in which $T_\mathrm{O,u}$ and $T_\mathrm{A,u}$ are used. In contrary, $F(\mathrm{o_u},\mathrm{a_m})$ denotes the heat flux based on fixed observational data of the atmosphere based on *measurements* ($\mathrm{a_m}$) and values of the *uncoupled* ocean model ($\mathrm{o_u}$). This is illustrated in Fig. 8.16.

Instead of driving the ocean model with the fully coupled fluxes $F(\mathrm{o},\mathrm{a})$, $F(\mathrm{o},\mathrm{a})$ is replaced by

$$\tilde{F}_\mathrm{o}(\mathrm{o},\mathrm{a}) = F(\mathrm{o},\mathrm{a}) + \underbrace{\{F(\mathrm{o_u},\mathrm{a_m}) - F(\mathrm{o_u},\mathrm{a_u})\}}_{FO} , \tag{8.26}$$

where FO is the flux correction for the ocean model. $FO = 0$, in the ideal case that the variables from the uncoupled atmosphere model completely agree with the measured quantities, i.e., $\mathrm{a_u} = \mathrm{a_m}$. Analogously, for the atmosphere model we write

$$\tilde{F}_\mathrm{a}(\mathrm{o},\mathrm{a}) = F(\mathrm{o},\mathrm{a}) + \underbrace{\{F(\mathrm{o_m},\mathrm{a_u}) - F(\mathrm{o_u},\mathrm{a_u})\}}_{FA} , \tag{8.27}$$

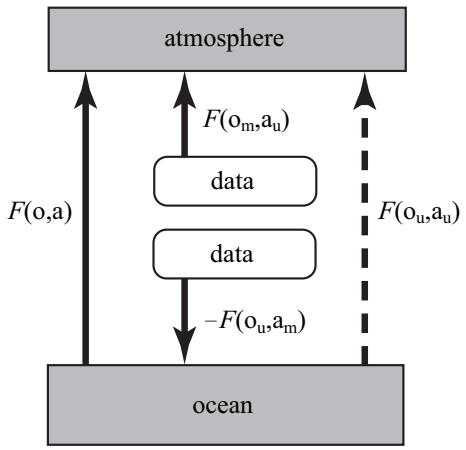

Figure 8.16: Schematic depiction of the different fluxes with a flux correction in coupled climate models; "data" denotes measured climatologies.

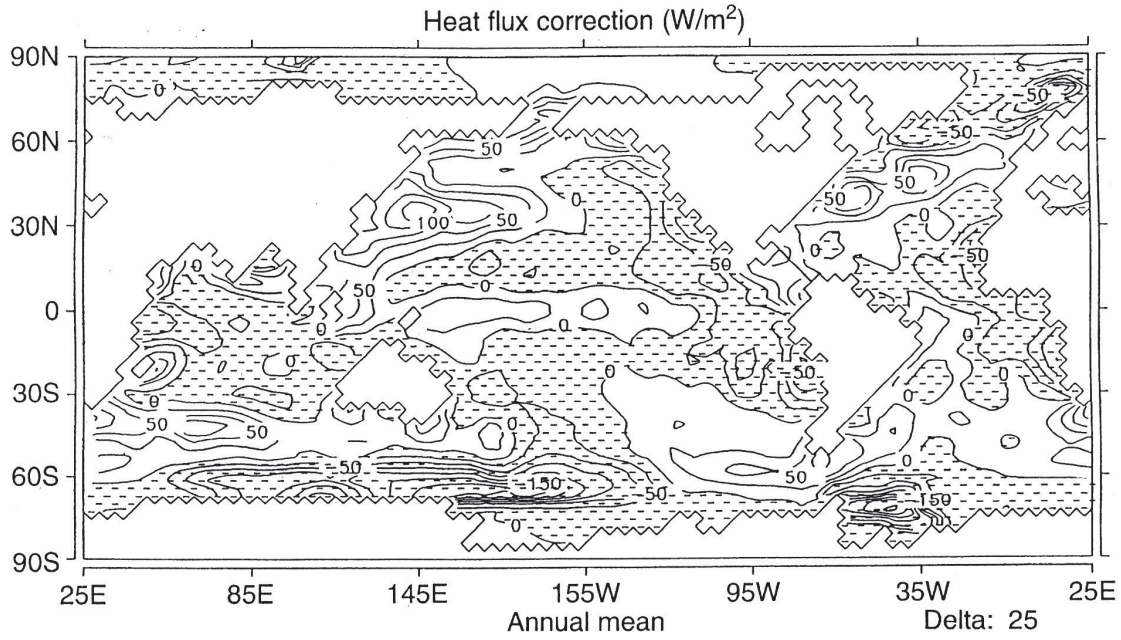

Figure 8.17: Correction of the heat flux. Particularly in areas with strong oceanic currents (Gulf stream and Kuroshio), as well as in areas of deep water formation (Norwegian and Weddell Seas), very large fluxes result. Figure from Schiller et al. (1997).

where FA is the flux correction for the atmosphere model. The difference $\tilde{F}_o - \tilde{F}_a$ is the artificial net source of heat, induced by the deviations of the modeled fluxes in the uncoupled model from the measured fluxes. The corrections in (8.26) and (8.27) may reach the same order of magnitude as the fluxes themselves. For the heat flux, this is shown in Fig. 8.17, for the flux of water in Fig. 8.18, for two illustrative examples of coupled climate model.

By means of simple models and other considerations, it can be demonstrated, that for relatively small changes (e.g., the simulation of the next 50 year's climate) flux corrections do not yield fundamentally different results compared to the ones without flux correction (Egger, 1997). However, one has to be generally cautious when interpreting such models.

As mentioned above, most of current climate models no longer employ flux corrections. This is evidence for significant progress in the understanding of processes in the climate system components (ocean, atmosphere, land, sea ice, snow, vegeta-

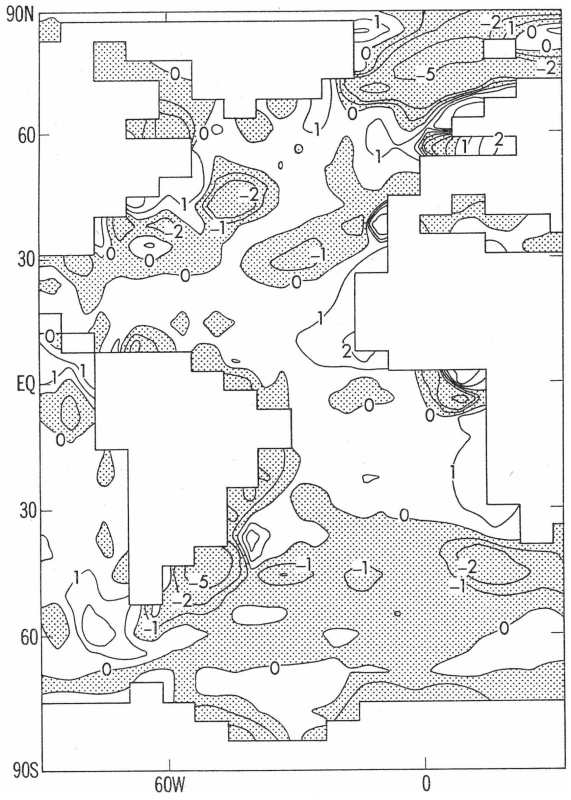

Figure 8.18: Correction of the water flux in m/year. Particularly in areas with strong oceanic currents (Gulf stream and Brazil Current), as well as in areas of deep water formation (Norwegian Sea), very large fluxes result. Figure from Manabe and Stouffer (1988).

tion, etc.) and their representation in coupled models. Improved parameterisations (used in climate models), and to some extent a higher model grid resolution, have contributed to this progress.

However, occasionally coupled models still use other forms of flux correction, e.g., an imposed additional freshwater flux from the Atlantic to the Pacific in order to enhance deep water formation in the North Atlantic and improve the global ocean circulation (e.g., Zaucker et al., 1994; Renssen et al., 2005; Ritz et al., 2011).

9 Multiple equilibria in the climate system

9.1 Abrupt climate change recorded in polar ice cores

The most detailed information about past climate states of the last 800,000 years can be retrieved from polar ice cores (Jouzel et al., 2007). One example for the last 90,000 years is presented in Fig. 9.1. The Holocene, the present interglacial, has started after the abrupt end of the last glacial period, 11,650 years ago. The transition from the last ice age to the Holocene, called Termination I, started about 20,000 years ago. An increase in the concentrations of particular isotopes could be detected in Antarctic ice cores. Stable isotopes of the water molecule are a measure for the local temperature. The temperature indicators also show that the climate changed in an abrupt way 25 times in Greenland during the last glacial period. These abrupt warming events, numbered in Fig. 9.1, are now referred to as *Dansgaard-Oeschger events (D/O events)* in remembrance of the research of the two pioneers in ice core science *Willy Dansgaard* (1922–2011) and *Hans Oeschger* (1927–1998) from the University of Copenhagen and the University of Bern.

These D/O events all show an abrupt warming of the northern hemisphere within one decade and a subsequent continuous cooling over about 1000 to 3000 years. Interestingly, the isotope maxima and minima during the glacial periods are all at the same level. Already in 1984, Hans Oeschger proposed that the climate system may have operated similar to a physical flip-flop and that the ocean circulation in the Atlantic Ocean is likely to be responsible for these climate jumps (Oeschger et al., 1984). Flip-flop systems are characterized by several stable equilibria. The Lorenz-Saltzman model (Section 7.2) is a classical example.

When Bryan (1986) demonstrated, using a three-dimensional ocean circulation model, that several states of the thermohaline circulation can be realized, *Wally Broecker* (1931–2019) synthesized the results from different climate archives and argued that rapid oscillations of the "Atlantic heat pump" (the thermohaline circulation) are responsible for the abrupt climate changes found in the Greenland ice cores, in tree rings, in sea and lake sediments, stalagmites, and in numerous other paleoclimatic archives (Broecker et al., 1985; Broecker and Denton, 1989). Some relevant sources of subsequent research on abrupt climate change are Alley et al. (2003), Barker et al. (2009), Blunier et al. (1998), Broecker (1997), Clark et al. (2002), Dansgaard et al. (1984), Dansgaard et al. (1993), EPICA Community Members (2006), Huber et al. (2006), Manabe and Stouffer (1988), Manabe and Stouffer (1994), Oeschger et al. (1984), Pedro et al. (2018), Stocker (2000), Stocker and Johnsen (2003), Stocker and Marchal (2000), Stocker and Wright (1991), Stocker et al. (1992), For an introductory overview on the role of the ocean in the climate system we refer to Stocker (2013b).

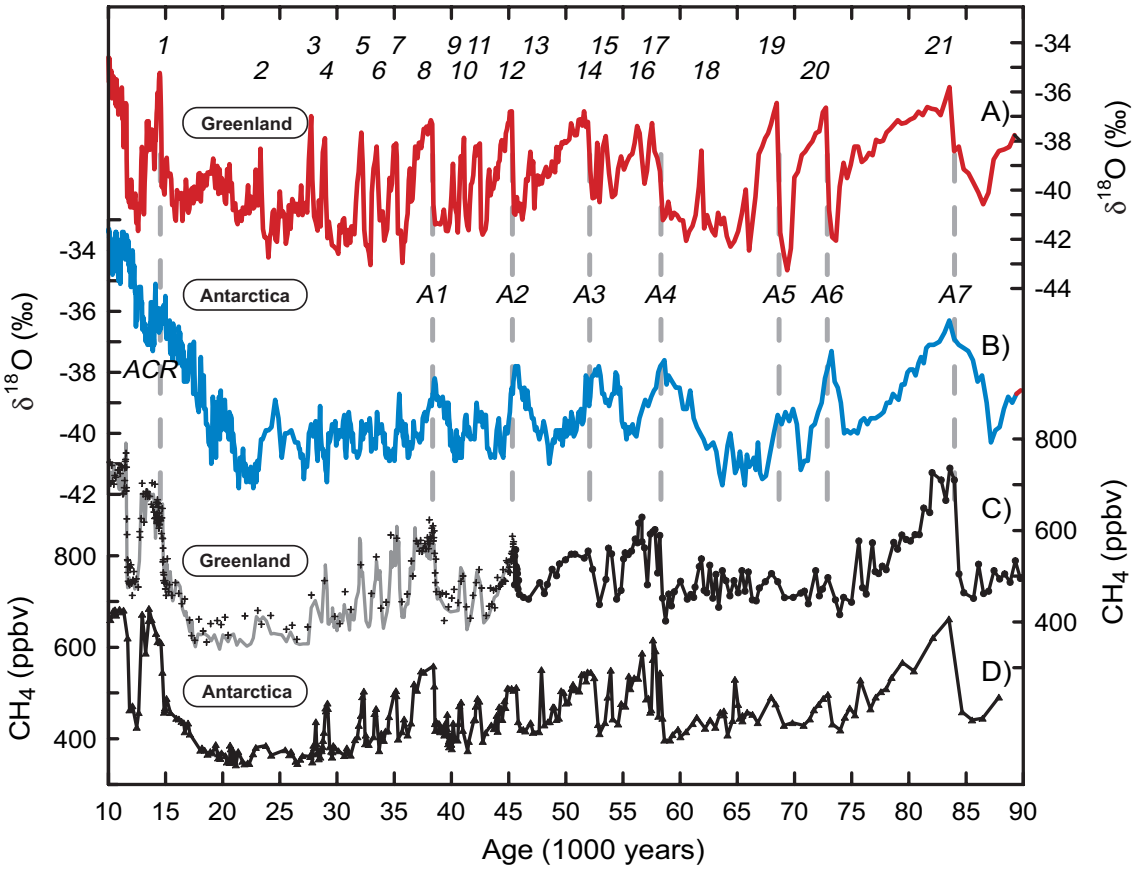

Figure 9.1: Climate history of the last 90,000 years recorded in ice cores from Greenland and Antarctica. **A)** Oxygen-isotope ratio ^{18}O (in per mille deviation from a predefined standard) in the GRIP ice core from Greenland; **B)** ^{18}O in the Byrd core from Antarctica; **C)** Methane concentration in the GRIP core; **D)** Methane concentration in the Byrd core. In the Greenland ice core, 21 Dansgaard/Oeschger events are recorded. The longest D/O events exhibit a corresponding warm event in the Antarctic core; labeled A1 to A7. All of the D/O events are marked by abrupt peaks in the methane, enabling a synchronization of the time scales of Greenland and Antarctic ice cores. Figure from Blunier and Brook (2001).

9.2 The bipolar seesaw

Evidence from many climate archives supports the hypothesis that the ocean is primarily responsible for these abrupt changes. A sudden shut-down of the North Atlantic deep water formation causes a reduction of the meridional heat flux and therefore an abrupt cooling in the North Atlantic region. An active meridional current draws heat from the Southern Atlantic and therefore a weakening will cause a warming of the Southern Atlantic and should be noticeable in distinct teleconnections. This has led to the formulation of the so-called "Bipolar Seesaw" as a paradigm for the interaction of the northern and southern hemisphere during abrupt climate transitions (Broecker, 1998; Stocker, 1998). The bipolar seesaw is shown in Fig. 9.2 (right part) and suggests that an abrupt warming in the north leads to an abrupt cooling of the Southern Atlantic and vice-versa. This hypothesis makes distinct predictions that can be tested in climate archives.

A slightly more elaborate concept is the thermal bipolar seesaw proposed by Stocker and Johnsen (2003). It results from coupling a large heat reservoir to the southern end of the seesaw and leads to a fundamentally different temporal response of the

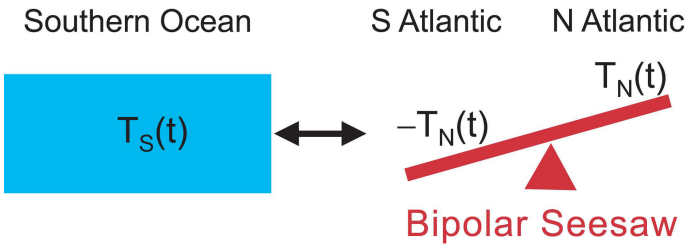

Figure 9.2: Bipolar seesaw coupled with a southern heat reservoir to form the thermal bipolar seesaw. Figure from Stocker and Johnsen (2003).

Southern Ocean to abrupt temperature changes in the north. An abrupt cooling in the South Atlantic (i.e., abrupt warming in the North Atlantic) induces a slow continuous cooling in the whole Southern Ocean. In this simple manner, the very different characteristics of temperature signals extracted from ice cores of Greenland and Antarctica and shown in Fig. 9.1 can be explained.

The thermal bipolar seesaw is formulated as an energy balance for the Southern Ocean temperature:

$$\frac{\mathrm{d}T_\mathrm{S}(t)}{\mathrm{d}t} = \frac{1}{\tau}\Big(- T_\mathrm{N}(t) - T_\mathrm{S}(t)\Big) \,, \tag{9.1}$$

where T_S is the temperature anomaly of the Southern Ocean and T_N may represent the temperature anomaly of Greenland. With this, $-T_\mathrm{N}$ is the temperature anomaly of the South Atlantic adjacent to the Southern Ocean assuming the instantaneous seesaw. τ is a characteristic time scale for the heat equilibration in the Southern Ocean. If $T_\mathrm{N}(t)$ is given, the temporal evolution of $T_\mathrm{S}(t)$ can be determined by a *Laplace transformation* of (9.1):

$$T_\mathrm{S}(t) = -\frac{1}{\tau}\int_0^t T_\mathrm{N}(t-t')\,\mathrm{e}^{-t'/\tau}\,\mathrm{d}t' + T_\mathrm{S}(0)\,\mathrm{e}^{-t/\tau} \,. \tag{9.2}$$

Hence, T_S is completely determined by the temporal evolution of T_N and reflects the northern temperature with a "damped memory". Let us consider this simple model in order to explain the different temporal evolution of the temperatures in Greenland and Antarctica. By tuning the only free parameter τ we aim at producing the largest possible correlation between the modelled T_S based on (9.2), with the known temperature from the ice core T_N as input and the measured T_S derived from the Antarctic ice core. For $\tau \approx 1,100$ years a maximum correlation of 0.77 is achieved. This allows us to predict the Antarctic temperature based on the temperature of Greenland in a surprisingly accurate way (Fig. 9.3). The bipolar seesaw *predicts* that not only the most prominent D/O events have a southern counterpart, but that *all D/O events* should coincide with a peak in temperature that is achieved by a prior slow warming and a subsequent slow cooling (A events in Fig. 9.3).

Although this simple concept explains a large part of the variability, the required long time scale τ of over 1000 years seems incompatible with the results from Ocean General Circulation Models (OGCMs), simulating only around 100 to 200 years as a typical exchange duration for the Southern Ocean.

There is another interesting consequence of the bipolar seesaw which follows from (9.2). Consider a very simple case of a northern temperature signal that has the

shape of a periodic step function:

$$T_{\mathrm{N}}(t) = \begin{cases} -\dfrac{1}{2}\,\Delta T & \text{for} \quad (2\,i)\,t_0 < t < (2\,i+1)\,t_0 \\ +\dfrac{1}{2}\,\Delta T & \text{for} \quad (2\,i+1)\,t_0 < t < 2\,(i+1)\,t_0\ , \end{cases} \tag{9.3}$$

where $i = 0,\ 1,\ 2,\ \ldots$ and ΔT the temperature amplitude of abrupt changes in the north. In this case, we can determine $T_{\mathrm{S}}(t)$ easily using (9.2). Assuming $T_{\mathrm{S}}(0) = 0$ we get in the first interval $0 \le t < t_0$:

$$T_{\mathrm{S}}(t) = \frac{1}{2}\,\Delta T\left(1 - \mathrm{e}^{-t/\tau}\right)\ . \tag{9.4}$$

Values for $T_{\mathrm{S}}(t)$ in later intervals are calculated similarly. From the Taylor series expansion of this function about $t = 0$ truncated to first order, we obtain

$$\begin{aligned} T_{\mathrm{S}}(t) &\approx T_{\mathrm{S}}(0) + \left.\frac{\mathrm{d}T_{\mathrm{S}}}{\mathrm{d}t}\right|_{t=0} t \\ &\approx \frac{\Delta T}{2\,\tau}\,t\ , \end{aligned}$$

which is a good approximation for $t \ll \tau$. We find a remarkable linear dependence of the maximum southern warming on the duration t_0 of the northern cooling,

$$T_{\mathrm{S}}(t_0) \approx \frac{\Delta T}{2\,\tau}\,t_0\ . \tag{9.5}$$

The longer the cooling in the northern Atlantic lasts due to the cessation of the meridional overturning circulation, the larger the warming will be in Antarctica. The warming further depends on the overall cooling, ΔT, in the north.

This linear relationship could be confirmed using the most recent information from the EPICA ice core from Dronning Maud Land (Antarctica). This ice core was drilled in a location geographically relatively close the Southern Atlantic Ocean where one would expect the largest influence of the bipolar seesaw. The duration of the stadials prior to the Dansgaard-Oeschger events was determined from the temperature reconstructions of the Greenland ice core from North GRIP; the amplitude of the warming in the south was obtained from the isotopic measurements on the EPICA ice core from Dronning Maud Land (EPICA Community Members, 2006).

Figure 9.4 shows this impressive linear relationship for Marine Isotope Stage 3 during the last ice age and provides therefore the most convincing and independent evidence that much of the variability during an ice age can be captured by the very simple concept of the bipolar seesaw. It is remarkable that such a strong connection of the climatic behaviour on millennial time scales operates across the hemispheres.

More recent paleoclimatic reconstructions suggest that this mechanism also operated during the last Termination, i.e. the transition from the last ice age to the Holocene, a time period which was punctuated by large and abrupt climate changes such as the Bølling/Allerød warming and the Younger Dryas cooling in the North Atlantic region, and the Antarctic Cold Reversal in the south (Barker et al., 2009), as hypothesized earlier (Stocker, 2003), as well as during previous ice ages (Nehrbass-Ahles

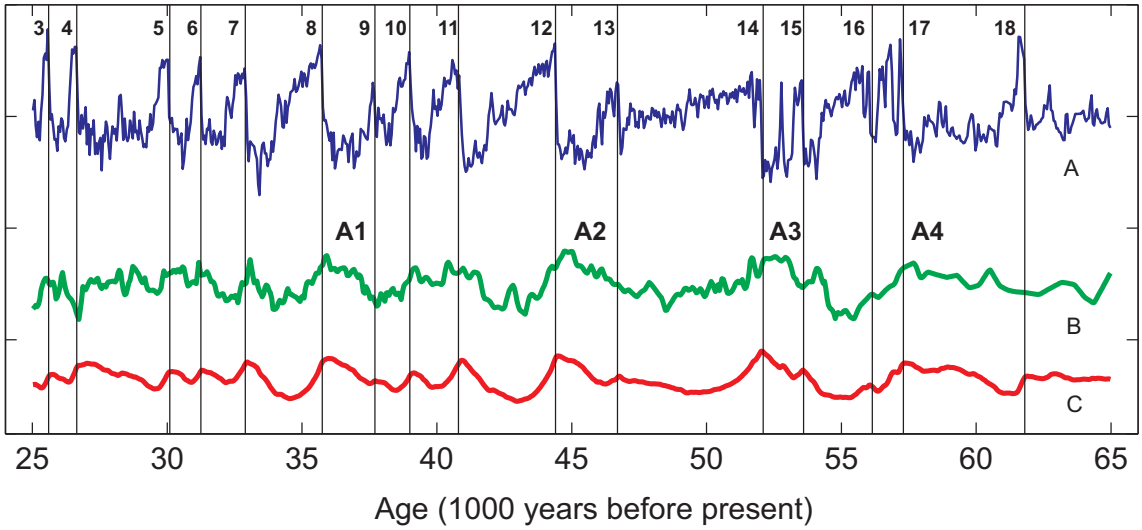

Figure 9.3: High-pass filtered time series of the temperatures in Greenland **(A)** and Antarctica **(B)** derived from ice cores. **(C)** is the simulated temperature according to (9.2) with input (A). The abrupt Dansgaard-Oeschger events of the north hence become manifest in the local isotope maxima in Antarctica (A1, A2, ...). For each D/O event 3 to 18, an individual Antarctic warming event is predicted in (C). Figure from Stocker and Johnsen (2003).

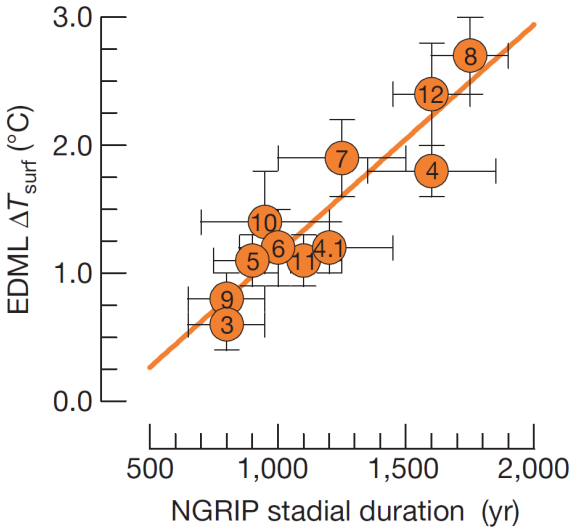

Figure 9.4: Linear correlation between the duration of the cold stadials preceding the Dansgaard-Oeschger events in Greenland, and the temperature amplitudes of the warmings in Antarctica. The numbers indicate the D/O events in Fig. 9.3. Figure from EPICA Community Members (2006).

et al., 2020).

Naturally, the bipolar seesaw os a climate model reduced to the max. As more high-resolution paleoclimate records become available and more coupled climate model simulations are carried out, the picture of north-south globa teleconnection becomes more complex (Pedro et al., 2018).

9.3 Multiple equilibria in a simple atmosphere model

Geological evidence suggests that the Earth has gone through several phases of almost complete glaciation ("Snowball Earth" hypothesis, Hoffman et al. (2017)). How could this happen, given a roughly constant solar irradiation?

The energy balance model presented in Section 2.2 already gives a possible answer in

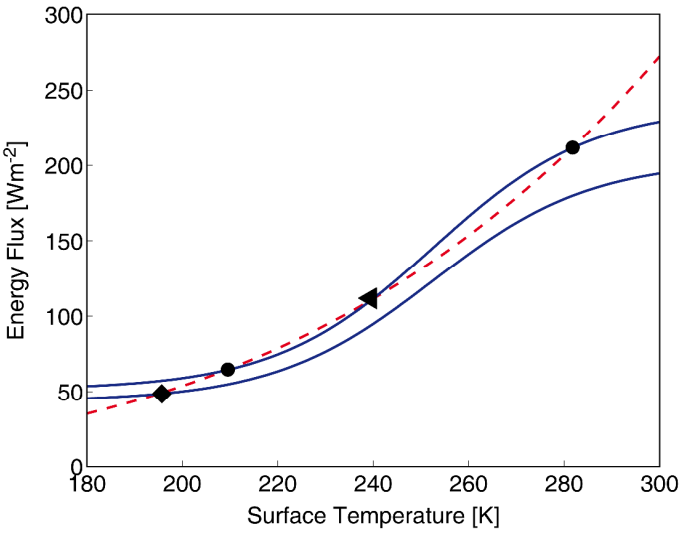

Figure 9.5: Right-hand side (*dashed*) and left-hand sides of (9.7) for S_0 (*upper curve*) and $0.85\,S_0$. The temperature dependence of the albedo produces several equilibrium solutions: stable states (*filled circles* and *diamond*) and an unstable state (*triangle*).

case the ice-albedo feedback is accounted for (Section 2.4.1). Considering the equilibria of the energy balance (2.1) and parameterizing the albedo according to (2.35) but in a mathematically differentiable form as illustrated in Fig. 2.12 according to

$$\alpha(T) = 0.575 - 0.275 \tanh\left(\frac{T - 252.5\ \mathrm{K}}{30.3\ \mathrm{K}}\right) , \tag{9.6}$$

an energy balance equation results that is non-linear in T:

$$\Big(1 - \alpha(T)\Big)\frac{S_0}{4} = \varepsilon\,\sigma\,T^4 . \tag{9.7}$$

The left- and right-hand sides of (9.7) are shown in Fig. 9.5 for the two cases of a solar constant of $S_0 = 1361\ \mathrm{W\,m^{-2}}$ and one which is reduced by 15%, $S_0^* = 0.85\,S_0$. For today's value of the solar constant (S_0) three equilibria exist, of which two are stable as indicated by filled circles. They represent a "warm" and a "cold" climate state. In the case of a 15% weaker solar constant (S_0^*, *faint young Sun*), only a single stable equilibrium exists corresponding to a very cold climate. Likewise, Fig. 9.5 reveals that the structure of the solution strongly depends on the specific form of the ice-albedo parameterisation. For example, if an albedo parameterisation with a flatter slope were chosen, the two stable equilibria would shift towards the unstable one and finally merge into a single stable equilibrium.

The question remains, whether multiple equilibria also exist in more complex climate models, e.g. in a coupled atmosphere-ocean model. This is discussed in Section 9.5.

9.4 Multiple equilibria in a simple ocean model

The deep circulation in the Atlantic is associated with a large heat transport that considerably affects climate in the North Atlantic region (conveyor belt). This heat transport is responsible for a comparatively mild climate. Already at the beginning of the 20$^{\mathrm{th}}$ century geologists assumed that the change in the ocean circulation may be responsible for part of the climate variability. In 1961, Henry Stommel presented a conceptual model that is able to reproduce such changes since it contains several

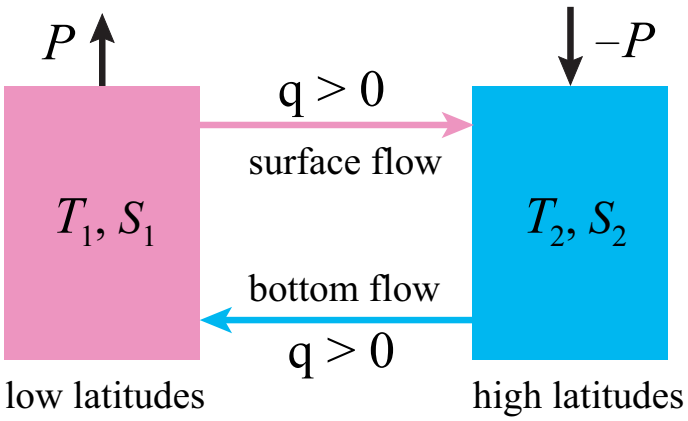

Figure 9.6: 2-Box model of the thermohaline circulation, representing a low-latitude warm water pool with evaporation dominating, and a high-latitude cold water pool with precipitation dominating. Figure after Stommel (1961) and Marotzke (2000).

equilibria (Stommel, 1961). This model is presented in its simplified form following Marotzke (2000). The reason for the existence of multiple equilibria is linked to the fact that heat and water fluxes respond differently to anomalies. Mixed boundary conditions account for this phenomenon (see Fig. 8.7). Different relaxation times in (8.8) and (8.14) can also lead to several equilibria.

In this simple model the ocean is represented as two boxes: one for latitudes where evaporation dominates (warm, a positive water flux P) and one for the cold, high latitudes where precipitation dominates (Fig. 9.6). T_i und S_i represent the temperatures and salinities of the two boxes, respectively. A fixed temperature difference ΔT between the boxes is assumed. It is maintained by heat fluxes between the atmosphere and the ocean. Between high and low latitudes a water transport q operates and is driven by the density difference according to

$$q = k\,(\rho_2 - \rho_1) = k\,\rho_0\Big(\alpha\,(T_2 - T_1) + \beta\,(S_2 - S_1)\Big)\;, \tag{9.8}$$

in which (8.11) with $\alpha < 0$ and $\beta > 0$ but with $\gamma = 0$ was used. The balance of the salinity in the two boxes is

$$\frac{\mathrm{d}S_1}{\mathrm{d}t} = |q|\,(S_2 - S_1) + P\;, \qquad \frac{\mathrm{d}S_2}{\mathrm{d}t} = |q|\,(S_1 - S_2) - P\;, \tag{9.9}$$

where $P > 0$ denotes the net water flux. In (9.9) the absolute value of q appears, because for the exchange the direction of the current is irrelevant. Stationary solutions for (9.9) can only be found if

$$\Delta S = S_2 - S_1 = \begin{cases} -\dfrac{\alpha\,\Delta T}{2\,\beta} \pm \sqrt{\left(\dfrac{\alpha\,\Delta T}{2\,\beta}\right)^2 - \dfrac{P}{\rho_0\,k\,\beta}} & q > 0\;, \\[2ex] -\dfrac{\alpha\,\Delta T}{2\,\beta} - \sqrt{\left(\dfrac{\alpha\,\Delta T}{2\,\beta}\right)^2 + \dfrac{P}{\rho_0\,k\,\beta}} & q < 0\;, \end{cases} \tag{9.10}$$

where $\Delta T = T_2 - T_1 < 0$. For the *direct circulation*, $q > 0$ and hence $\rho_2 > \rho_1$, two solutions are possible: one with a smaller contrast in salinity $\Delta S < 0$ and one with

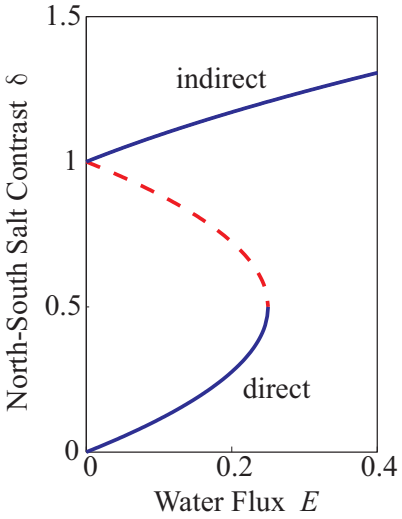

Figure 9.7: Multiple equilibria (*dashed* indicates unstable state) of the thermohaline circulation for different values of the water flux in the Stommel box model.

a large negative ΔS. For an even smaller ΔS an *indirect circulation* exists, $q < 0$ and $\rho_2 < \rho_1$. We put

$$\delta = -\frac{\beta\,\Delta S}{\alpha\,\Delta T}\;, \qquad E = \frac{\beta\,P}{\rho_0\,k\,(\alpha\,\Delta T)^2}\;, \tag{9.11}$$

and obtain from (9.10)

$$\delta = \begin{cases} \dfrac{1}{2} \pm \sqrt{\dfrac{1}{4} - E} & q > 0\;, \\[2ex] \dfrac{1}{2} + \sqrt{\dfrac{1}{4} + E} & q < 0\;. \end{cases} \tag{9.12}$$

The transport q is given by

$$q = k\,\rho_0\,\alpha\,\Delta T\,(1-\delta)\;. \tag{9.13}$$

For $\delta > 1$ the circulation is *indirect*, i.e., water sinks where it is warmer. In order to attain a sufficiently high density that permits a sinking, the salinity must be accordingly high. For $\delta < 1$ two solutions result, of which one is unstable (Fig. 9.7). For the *direct* circulation (water sinks where it is colder) $q > 0$. In case P increases, E and δ increase as well. But this leads to a decrease of q. An amplified hydrological cycle slows down the thermohaline circulation.

For $0.5 < \delta < 1$ and hence $0 < q < \frac{1}{2}\,k\,\rho_0\,\alpha\,\Delta T$ the circulation is unstable. The model shows a threshold for q, below which the thermohaline circulation does not exist. It must be noted, that in this simple model the meridional temperature contrast directly determines this threshold.

The existence of multiple equilibria of the thermohaline circulation can be qualitatively understood by considering the heat and water transport as schematically illustrated in Fig. 9.8. In Fig. 9.8 a) the circulation is direct. Under the typical depth-profiles of T and S in the ocean (with respectively high values at the surface) the ocean transports heat and salt northwards. The cycle of the fluxes is closed by

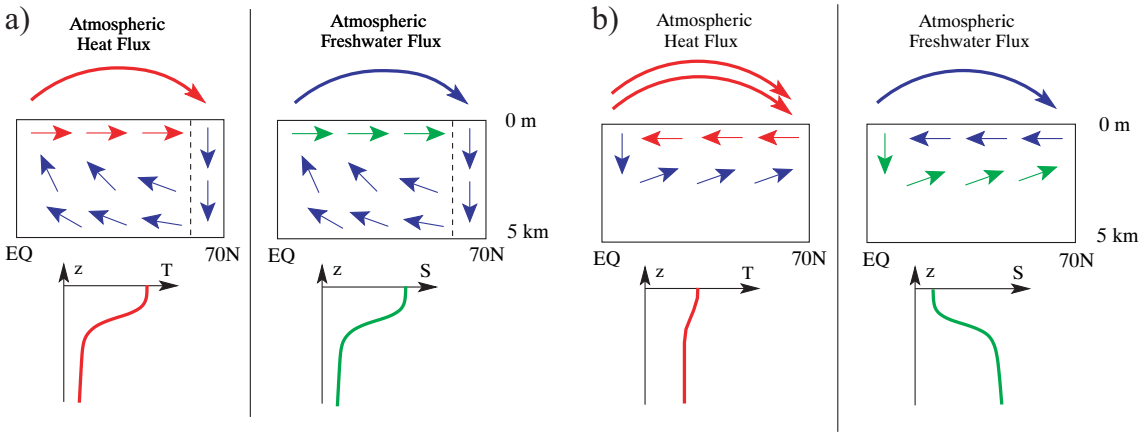

Figure 9.8: Schematic depiction of the thermohaline circulation and the meridional heat and water fluxes. **a)** direct circulation: water sinks where it is cold; **b)** indirect circulation: water sinks in warm areas. Arrows of the water circulation are color coded: *red* (warm), *blue* (cold/fresh), *green* (salty).

an excess of heat in the equatorial region and a cooling in the north, and by the atmospheric water transport. However, the same water transport can also result from an opposite circulation as shown in (b) in case the vertical gradient of S changes sign.

Hence, significant relocations of salinity in the ocean are necessary in order to provoke basin-scale changes in the oceanic circulation. In the context of mixed boundary conditions for ocean models the salinity at the surface may change in an unlimited way which is a precondition for attaining state (b) in Fig. 9.8. The question whether this bears any realism is addressed in the next section.

9.5 Multiple equilibria in coupled models

Model simulations by Manabe and Stouffer (1988) revealed for the first time results from a coupled climate model, in which for present climate conditions, two different states were found. They primarily differed in their thermohaline circulation in the Atlantic. One of the states had an active deep water formation in the North Atlantic, the other state showed a circulation similar to the one in the Pacific. Transitions can be triggered by short-term differences in the water balance in the North Atlantic. Similar results were also found with other coupled models (Ferreira et al., 2018; Kilic et al., 2017, 2018).

Therefore, it is probable that the deep water circulation in the Atlantic sensitively responds to changes in the surface water balance. This is a plausible mechanism to explain the abrupt changes found in climate time series (e.g., Fig. 9.1). One hypothesis claims that during glacial periods the ice sheets located around the North Atlantic discharged large amounts of freshwater caused by advancing ice streams. This situation was reinforced towards the end of the last glacial period, when the melting of the northern hemispheric ice sheets led to a sea level rise of about 120 m. During that time, the last sequence of abrupt climate changes was observed.

The lessons from the past clearly raise the question whether limited stability of the climate system, observed in many paleoclimatic records, may also be an issue

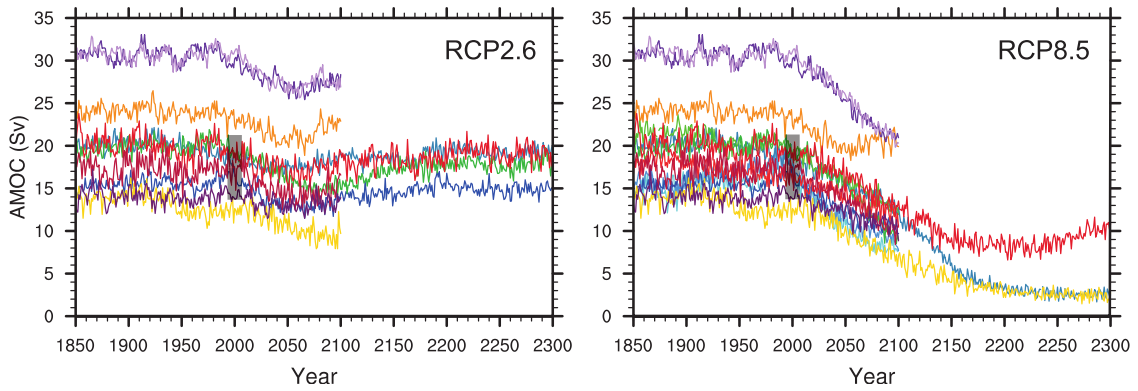

Figure 9.9: Atlantic Meridional Overturning Circulation (AMOC) strength at 30°N as a function of year, from 1850 to 2300 as simulated by CMIP5 models in response to scenario RCP2.6 (**left**) and RCP8.5 (**right**). The vertical *grey bar* at year 2000 shows the range of AMOC strength measured at 26°N, from 2004 to 2011. Figure from IPCC (2013), Technical Summary TFE.5.

today, when the increase of greenhouse gas concentrations represents a significant perturbation to the climate system. The anthropogenic warming in the atmosphere not only increases sea surface temperatures but also alters the freshwater balance in a profound way. First, the melting of Greenland, which is proceeding at rapid rates, delivers freshwater to the Atlantic Ocean. Second, a warmer climate intensifies the water cycle due to the increased amount of water vapour in the atmosphere and to the higher evaporation rates induced by higher temperatures. This leads to a stronger meridional transport of water in the atmosphere. All three processes (warming of the SST, melting of Greenland and more precipitation) conspire to decrease the sea surface density in the North Atlantic and, in consequence, have the potential to reduce the formation of deep water in the North Atlantic.

The question remains, whether this has basin-scale implications with the possibility that the Atlantic meridional overturning circulation may weaken in the future. Whether a threshold will be exceeded and a complete shut-down of this circulation system follows, is the object of current research. Coupled climate models will take centre-stage to shed light on this important issue.

The Intergovernmental Panel on Climate Change has addressed this issue (IPCC, 2013, Chap. 12). Fig. 9.9 illustrates the change in the meridional overturning circulation of the Atlantic for the coming 300 years based on different coupled models. Large differences between models exist; some models are inconsistent with observational estimates of the Atlantic meridional overturning.

Nevertheless, a general weakening trend during the 21st century emerges. None of the models simulates an intensification or an abrupt shut-down under these scenarios within the coming 100 to 200 years.

Models of reduced complexity show that a threshold of the circulation exists beyond which a complete shut-down of the current results without additional external inputs. Therefore, a transition to a second stable equilibrium occurs. This behaviour might also be observable in more complete models (three-dimensional coupled atmosphere-ocean models without flux corrections), according most recent simulations (Mikolajewicz et al., 2007) and as suggested by two of the three longest simulations for the RCP8.5 scenario in Fig. 9.9 (Hu et al., 2013). Multiple equi-

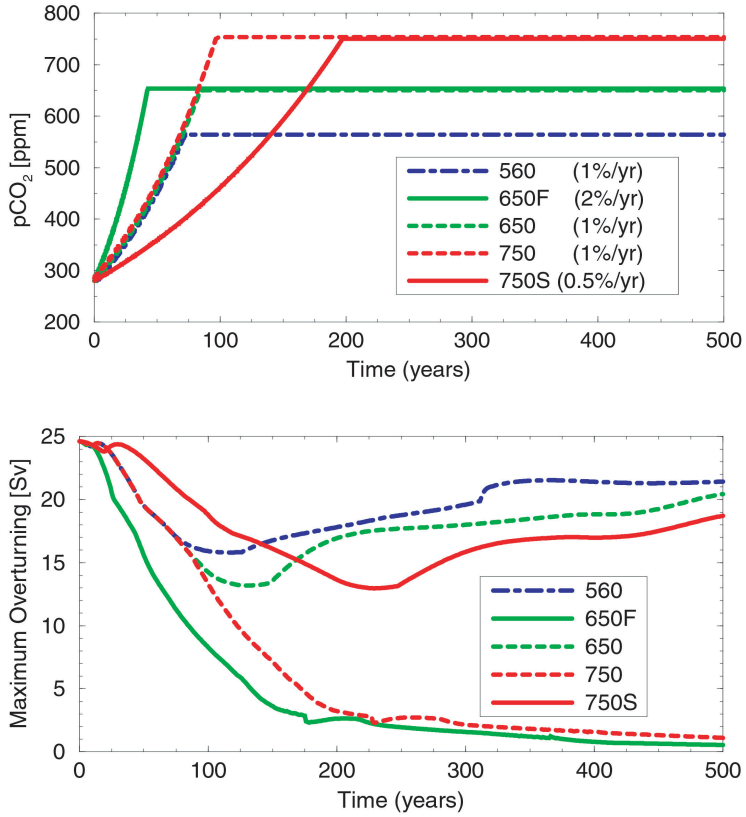

Figure 9.10: Simulations with the Bern 2.5D model for the evolution of the meridional overturning circulation (MOC) in the Atlantic considering a warming scenario. The different simplified CO_2-scenarios (**upper panel**) consist of an exponential increase at different rates, levelling off at a given maximum value. The MOC reveals a bifurcation in its behaviour (**lower panel**): for small maximum values or slow rates of CO_2 increase, the threshold for a complete shut-down may be avoided. Figure from Stocker and Schmittner (1997).

libria were also shown in a fully coupled AOGCM, in an aquaplanet configuration (Ferreira et al., 2011), and an Earth with idealized continental distribution (Ferreira et al., 2018).

Simulations with a simplified coupled model (Bern 2.5D model), consisting of a zonally averaged 3-basin ocean model and an energy balance model for the atmosphere, show that the threshold depends on several important quantities in the climate system, as well as the history of the perturbation. Figure 9.10 gives a summary of the results. For the respective simulations, simplified CO_2-scenarios were chosen: after an exponential growth at different rates, the CO_2 concentration was held constant. The evolution of the thermohaline circulation may be split into two cases. One exhibits a linear behaviour in which a temporarily strong reduction of the circulation is followed by a recovery over a few centuries. The reduction of the overturning circulation depends on the maximum value of the CO_2 increase and hence on the warming. In the second case, the circulation shuts down completely and does not recover. An irreversible transition to the second stable equilibrium has been realized.

It is interesting to notice that a reduction of the maximum concentration of CO_2 (from experiment 750 to 650) as well as a reduction of the rate of CO_2 increase (from experiment 750 to 750S) avoids the crossing of the critical threshold. Hence, the rate of future warming in the climate system plays a significant role. Depending

on the rate and amount of warming, irreversible changes may result.

There is evidence that a similar behaviour can be produced by a more complex model. However, it must be considered that these models contain more degrees of freedom and hence respond to disturbances in a much more sophisticated way. The question, whether multiple equilibria can also occur in the models of highest resolution, remains anaread of active research.

In its latest assessment report, the IPCC draws a cautious conclusion regarding this potentially serious consequence of anthropogenic climate change in the Summary for Policymakers, IPCC (2021):

> The Atlantic Meridional Overturning Circulation is *very likely* to weaken over the 21st century for all emission scenarios. While there is *high confidence* in the 21st century decline, there is only *low confidence* in the magnitude of the trend. There is *medium confidence* that there will not be an abrupt collapse before 2100. If such a collapse were to occur, it would *very likely* cause abrupt shifts in regional weather patterns and water cycle, such as a southward shift in the tropical rain belt, weakening of the African and Asian monsoons and strengthening of Southern Hemisphere monsoons, and drying in Europe.

Recent research has focused on the question whether there exist other components in the climate system which may exhibit instabilities or which are forced into new, quite different, equilibrium states. One example of intensive debate is the fate of the Greenland ice sheet. Recent observations confirm sustained mass losses for both Greenland and Antarctica (Rignot et al., 2019; Mouginot et al., 2019). Some model simulations suggest that there exist thresholds for warming in the area of the Greenland ice sheet and if crossed, this may lead to an irreversible melt-down of the ice sheet with a massive sea level rise of more than 6 meters over the next several 100 years. However, paleoclimatic information suggests that during the last interglacial about 120,000 years ago, which was about 4°C warmer than today, the Greenland ice sheet was still present, although much smaller in extent, and hence additional sea level rise remains a real threat.

Also, the Amazonian rainforest is supposed to respond to anthropogenic climate change both directly to the warming and, of course, due to direct deforestation. Some model simulations suggest that in this area a steppe-like vegetation cover may develop which then would feed back to the regional hydrological cycle and produce a new state of stable, but much drier regional climate. Even if the large-scale climate conditions were reset to pre-industrial values, the change in vegetation would not be reversible.

Permafrost in the boreal areas of Siberia and North America is also a system which is increasingly investigated. Large amounts of methane are trapped in the permafrost. With the warming, permafrost is melting which could release methane from these areas. As a powerful greenhouse gas, this would enhance the greenhouse effect. However, due to natural sinks for methane in the atmosphere and the short lifetime of methane (about 10 years), such a perturbation would disappear rather rapidly.

There is therefore the general concern that anthropogenic perturbations may have already caused irreversible climate change. In this context, one often refers to "Tipping Points" in the climate system (Lenton, 2011), although this concept is difficult to quantify. Obviously, predictability is extremely low, if not impossible, for such climate instabilities, but warning signals may be identified in the climate system.

10 Concluding remarks

The goal of these lecture notes was to provide some basic knowledge in climate modelling. In addition to theoretical concepts and recent results from climate research, we have framed the material in a sequence of simple problems which were solved numerically. This afforded the opportunity to introduce some basic numerical solution techniques and expose specific characteristics of them. A further goal was to introduce a few fundamental concepts of the dynamics of the climate system. Surely, these notes could only provide an initial, very limited insight into this fascinating topic. Hopefully, it was made clear, that questions remain unresolved and that therefore many areas of activity are open for good ideas and creative model design.

Climate modelling is the only, however by far not perfect, method to make quantitative statements concerning past climate change. For predictions of future changes, climate modelling is the only scientific basis. An ongoing analysis of observed data and climate variables, as well as a more profound understanding of the fundamental processes guarantees a continuous improvement of these models. The scientific assessment of the impact of human activities on this planet, and to foresee dangerous developments becomes an important duty of a responsible modern society.

Global heating is a scientific fact. This is succinctly captured by the 'warming stripes' (Fig. 10.1). Climate models are the basis for designing strategies of a sustainable future. A stable climate is a crucial resource for humanity, as it is now realized in the light of increasingly frequent and intense extreme climate events such as heat waves, flooding, drought, and tropical storms. Many of these events can now be attributed to anthropogenic emissions of greenhouse gases (IPCC, 2021).

A stable climate is also a essential for uninterrupted ecosystem services. Each modification of a resource implies a risk and disruptions may follow. In this sense, the changes observed to date should be considered as both a reminder and starting point for resolute actions. These are required as humanity has set a clear goal: Holding the increase in the global average temperature to well below 2°C above preindustrial levels (UNFCCC, 2015). However, with every year of constant, or even increasing, CO_2 emissions the door for climate targets is closing irreversibly (Stocker, 2013a).

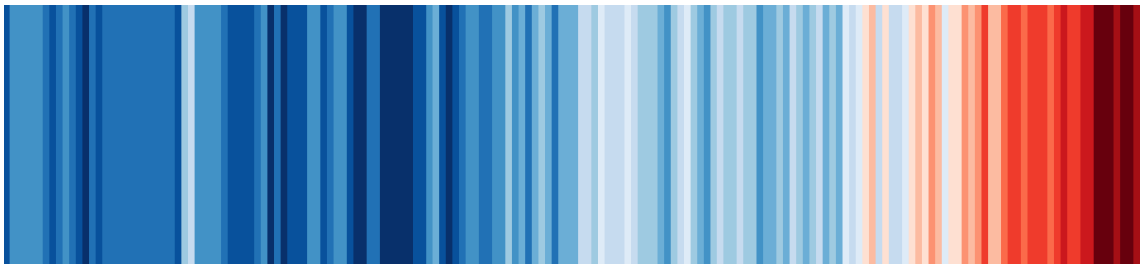

Figure 10.1: Global mean surface temperature anomalies from 1850 to 2021 shown as 'warming stripes', a compelling visual by Ed Hawkins, University of Reading (`showyourstripes.info`).

In closing, I note that art is able to provide an orthogonal and deeply emotional access to the greatest challenge of our century. As an early and impressive example of an artist's engagement against anthropogenic climate change we reproduce, as the last display item of these Lecture Notes, the compelling drawing *Global Warming*, created by *Niki de Saint Phalle* (1930–2002) in 2001 (Fig. 10.2).

Niki de Saint Phalle was an internationally acclaimed sculptor, painter, and filmmaker. She is most famous for her colourful and voluminous 'Nanas' which are powerful reminders of joyful, liberated and self-confident women. A huge Nana, *L'ange protecteur*, is flying high in the 19th-century arrival hall of Zurich's main train station since 1997.

Niki de Saint Phalle's œuvre is very rich and surprising, sometimes eccentric. Her drawing reproduced here is a prescient call of the many problems created by humans polluting the atmosphere and the environment. Since then, every one of these issues has grown bigger, more pervasive, and more dangerous.

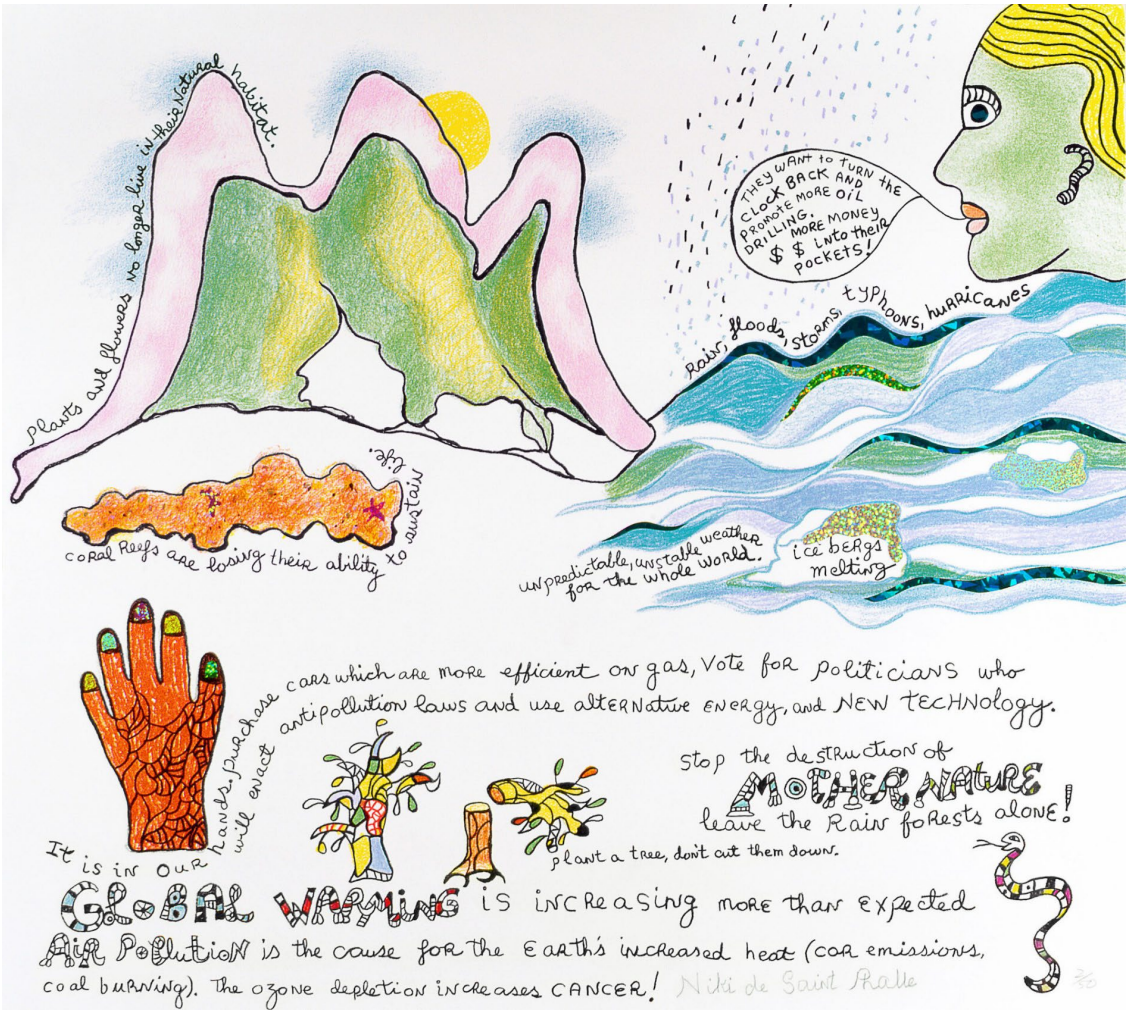

Figure 10.2: Drawing by the Franco-American artist Niki de Saint Phalle (1930–2002). She was an internationally renowned sculptor, painter, and filmmaker of the 20th century. Photo source: *Global Warming*, 2001 © Niki Charitable Art Foundation. All rights reserved.

Appendix A

The Young-Frankel SOR method

The Young-Frankel successive overrelaxation method was derived independently by *David M. Young* (Young, 1950) and *Stanley P. Frankel* (Frankel, 1950). This method may be viewed as a generalized Gauss-Seidel method (5.19). Nowadays it represents the standard SOR method and is described in detail in many textbooks, for example in Varga (2009) or Schwarz and Köckler (2011).

We start our brief description of this method by writing down again the iterative methods of Jacobi and Gauss-Seidel which we have already noted in (5.18) and (5.19):

$$\textit{Jacobi method} \qquad \mathbf{D}\, x^{n+1} = -\left(\mathbf{L} + \mathbf{R}\right) x^n + b\,, \tag{A.1}$$

$$\textit{Gauss-Seidel method} \qquad \left(\mathbf{D} + \mathbf{L}\right) x^{n+1} = -\mathbf{R}\, x^n + b\,. \tag{A.2}$$

We subtract $\mathbf{L}\, x^{n+1}$ from both sides of (A.2):

$$\mathbf{D}\, x^{n+1} = -\mathbf{L}\, x^{n+1} - \mathbf{R}\, x^n + b\,. \tag{A.3}$$

This representation of the Gauss-Seidel method elucidates the fact, that this method, while advancing from the first component $k = 1$ successively to the next components $k = 2,\, 3,\, \ldots,\, J$, uses always the most recent of the already calculated values (as mentioned on page 94), in contrast to the Jacobi method (A.1): The kth component of the vector x^{n+1}, i.e. the component x_k^{n+1}, results from the components x_1^{n+1}, …, x_{k-1}^{n+1} just calculated during the actual iteration step and from the components x_{k+1}^n, …, x_N^n already calculated before, during the foregoing iteration step (equation (5.15) is an example). Now we subtract $\mathbf{D}\, x^n$ from both sides of equation (A.3) and left multiply both sides by $\mathbf{D}^{-1}$:

$$\begin{aligned} x^{n+1} &= x^n - \mathbf{D}^{-1}\left(\mathbf{L}\, x^{n+1} + \left(\mathbf{D} + \mathbf{R}\right) x^n - b\right) \\ &= x^n + \Delta x^{n+1}\,. \end{aligned}$$

The quantity $\Delta x^{n+1} = x^{n+1} - x^n = -\mathbf{D}^{-1}\left(\mathbf{L}\, x^{n+1} + \left(\mathbf{D} + \mathbf{R}\right) x^n - b\right)$ signifies the correction demanded from the Gauss-Seidel method at iteration step $n + 1$ (where $n = 0,\, 1,\, 2,\, \ldots$).

The Young-Frankel successive overrelaxation method scales the Gauss-Seidel correction Δx^{n+1} by a relaxation factor $\omega > 1$,

$$\begin{aligned} x^{n+1} &= x^n + \omega\, \Delta x^{n+1} \\ &= x^n - \omega\, \mathbf{D}^{-1}\left(\mathbf{L}\, x^{n+1} + \left(\mathbf{D} + \mathbf{R}\right) x^n - b\right)\,, \end{aligned} \tag{A.4}$$

i.e.

$$(\mathbf{D} + \omega\,\mathbf{L})\,x^{n+1} = \mathbf{D}\,x^n - \omega\,\Big((\mathbf{D} + \mathbf{R})\,x^n - b\Big)$$

or

$$x^{n+1} = (\mathbf{D} + \omega\,\mathbf{L})^{-1}\,\Big((1-\omega)\,\mathbf{D} - \omega\,\mathbf{R}\Big)x^n + \omega\,(\mathbf{D} + \omega\,\mathbf{L})^{-1}\,b\,. \tag{A.5}$$

It includes the Gauss-Seidel method (5.15) with $\omega = 1$. Clearly, (A.5) is a linear non-homogeneous recurrence relation,

$$x^{n+1} = \mathbf{T}\,x^n + c\,, \tag{A.6}$$

where both the so-called iteration matrix $\mathbf{T}$ and the vector c (the non-homogeneous part of the recurrence relation) are functions of the relaxation factor ω:

$$\begin{aligned} \mathbf{T} &= (\mathbf{D} + \omega\,\mathbf{L})^{-1}\,\Big((1-\omega)\,\mathbf{D} - \omega\,\mathbf{R}\Big)\,, \\ c &= \omega\,(\mathbf{D} + \omega\,\mathbf{L})^{-1}\,b\,. \end{aligned} \tag{A.7}$$

The following aspects are fundamental for the further discussion:

1. Starting with any initial approximation x^0 and using any relaxation factor ω, the recurrence relation (A.6) determines a unique sequence of approximations

$$\{x^n\} = x^0,\, x^1,\, x^2,\, \ldots\,. \tag{A.8}$$

2. The sequence (A.8) might be divergent or convergent. If it is convergent then it must converge to the unique solution x of equation (5.16) implying $x^{n+1} = x^n = x$ for $n \to \infty$ and therefore the solution x to be a fixed point of the recurrence relation (A.6):

$$x = \mathbf{T}\,x + c\,. \tag{A.9}$$

To ensure convergence of the sequence (A.8), the iteration matrix $\mathbf{T}$ must fulfil a particular requirement. This requirement follows from the fact that, in case of convergence, the sequence of errors $\{\epsilon^n\}$, where

$$\begin{aligned} \epsilon^n &:= x^n - x \\ &\overset{(A.9)}{=} \mathbf{T}\,x^{n-1} + c - (\mathbf{T}\,x + c) \\ &= \mathbf{T}\,\Big(x^{n-1} - x\Big) \\ &= \mathbf{T}\,\epsilon^{n-1} \\ &= \mathbf{T}^2\,\epsilon^{n-2} \\ &= \quad\vdots \\ &= \mathbf{T}^n\,\epsilon^0\,, \end{aligned} \tag{A.10}$$

has to converge to the null vector. It is clear that this happens for each initial approximation x^0, i.e. for each initial error $\epsilon^0 = x^0 - x$, if, and only if, the matrix $\mathbf{T}$ is a convergent matrix, i.e. a matrix whose sequence of powers $\{\mathbf{T}^n\}$ converges to the null matrix. And this is the case precisely if all the eigenvalues $\lambda_1,\, \lambda_2,\, \ldots,\, \lambda_J$

of $\mathbf{T}$ (which may be complex numbers) have absolute values[1] smaller than one, i.e. precisely if the largest of the J values $|\lambda_1|$, $|\lambda_2|$, ..., $|\lambda_J|$, the so-called spectral radius[2] of the iterative matrix $\mathbf{T}$,

$$\rho(\mathbf{T}) = \max_{k=1,\ldots,J} (|\lambda_k|) \ , \tag{A.11}$$

is smaller than one, $\rho(\mathbf{T}) < 1$. This is a general rule and easy to justify in the special case of a diagonalizable matrix $\mathbf{T}$: We know from linear algebra that for such a matrix there is a regular matrix $\mathbf{P}$ causing the matrix $\mathbf{P}^{-1}\,\mathbf{T}\,\mathbf{P}$ to be a diagonal matrix

$$\mathbf{\Lambda} = \mathbf{P}^{-1}\,\mathbf{T}\,\mathbf{P} = \begin{pmatrix} \lambda_1 & & & \\ & \lambda_2 & & \\ & & \ddots & \\ & & & \lambda_J \end{pmatrix} ,$$

where the diagonal elements of $\mathbf{\Lambda}$ are the eigenvalues of $\mathbf{T}$ (and the columns of $\mathbf{P}$ are the eigenvectors of $\mathbf{T}$). It follows

$$\mathbf{T} = \mathbf{P}\,\mathbf{\Lambda}\,\mathbf{P}^{-1} \tag{A.12}$$

and further $\mathbf{T}^2 = \mathbf{P}\,\mathbf{\Lambda}\,\mathbf{P}^{-1}\,\mathbf{P}\,\mathbf{\Lambda}\,\mathbf{P}^{-1} = \mathbf{P}\,\mathbf{\Lambda}^2\,\mathbf{P}^{-1}$ and consequently, for any $n \in \mathbb{N}$,

$$\mathbf{T}^n = \mathbf{P}\,\mathbf{\Lambda}^n\,\mathbf{P}^{-1} = \mathbf{P} \begin{pmatrix} \lambda_1 & & & \\ & \lambda_2 & & \\ & & \ddots & \\ & & & \lambda_J \end{pmatrix}^n \mathbf{P}^{-1} = \mathbf{P} \begin{pmatrix} \lambda_1^n & & & \\ & \lambda_2^n & & \\ & & \ddots & \\ & & & \lambda_J^n \end{pmatrix} \mathbf{P}^{-1} \ .$$

This confirms that $\mathbf{T}^n \to \mathbf{0}$ for $n \to \infty$ is equivalent to $\rho(\mathbf{T}) = \max(|\lambda_k|) < 1$. The smaller the spectral radius $\rho(\mathbf{T})$, the faster the convergence. After conducting m successive iteration steps, the error has changed approximately by a factor of $\rho(\mathbf{T})^m$; to change the error by a factor of 10^{-p} it needs approximately $m \approx -p \ln 10 / \ln \rho(\mathbf{T}) = -p / \log_{10} \rho(\mathbf{T})$ iteration steps.

The spectral radius $\rho(\mathbf{T})$ of any SOR iteration matrix $\mathbf{T} = \mathbf{T}(\omega)$ depends on the relaxation factor ω. Figure A.1 shows an example. Usually, the function $\rho(\omega)$ has a unique minimum. If this minimum is less than one, then the corresponding relaxation factor $\omega = \omega_{\text{opt}}$ is optimal concerning speed of convergence. This optimal relaxation factor is generally difficult to determine exactly. What is certain is that it must be in the value range between 0 and 2, together with the other relaxation factors ensuring convergence. This follows easily by taking the determinant of the iteration matrix $\mathbf{T}$ given in (A.7):[3]

$$\begin{aligned} \det(\mathbf{T}) = \lambda_1\,\lambda_2\,\ldots\lambda_J &= \det\Big((\mathbf{D} + \omega\,\mathbf{L})^{-1} \Big((1-\omega)\,\mathbf{D} - \omega\,\mathbf{R} \Big) \Big) \\ &= \det(\mathbf{D} + \omega\,\mathbf{L})^{-1} \cdot \det\Big((1-\omega)\,\mathbf{D} - \omega\,\mathbf{R} \Big) \end{aligned}$$

[1] The absolute value of a complex value $z = x + \mathrm{i}\,y$ is the real, positive value $|z| = \sqrt{x^2 + y^2}$.

[2] The eigenvalues λ_1, λ_2, ..., λ_J of a complex $N \times N$ matrix $\mathbf{M}$ constitute the *spectrum* of this matrix. The radius of the smallest circle in the complex plane with center at the origin which incloses all eigenvalues is the *spectral radius* $\rho(\mathbf{M})$.

[3] Some properties of the determinant function are used in the reasoning (matrices $\mathbf{X}$ and $\mathbf{Y}$ should

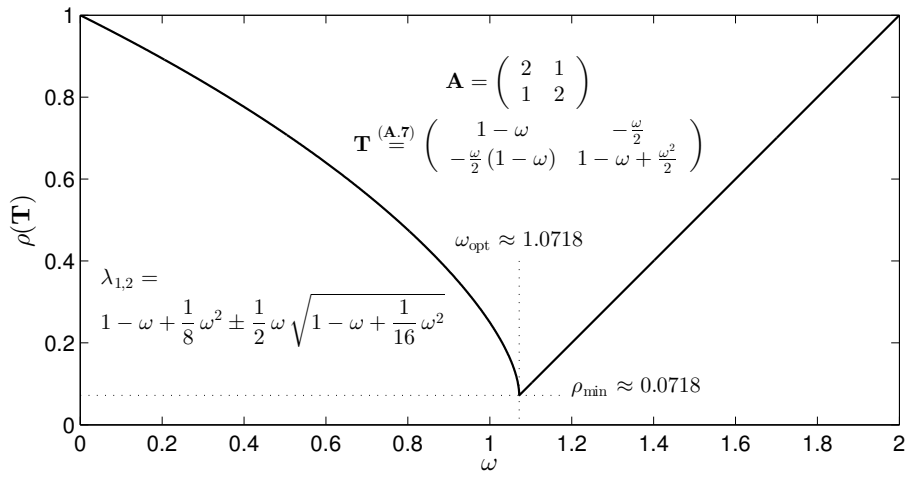

Figure A.1: Spectral radius $\rho(\omega) = \rho(\mathbf{T}(\omega))$ of the iteration matrix (A.7) derived from the matrix $\mathbf{A} = \left(\begin{smallmatrix} 2 & 1 \\ 1 & 2 \end{smallmatrix}\right)$. The spectral radius results with $\rho(\omega) = \max\left(|\lambda_1(\omega)|, |\lambda_2(\omega)|\right)$, where $\lambda_1(\omega)$ and $\lambda_2(\omega)$ are the eigenvalues of $\mathbf{T}$.

$$
\begin{aligned}
&= \frac{1}{\det(\mathbf{D})} \cdot (1-\omega)^J \cdot \det(\mathbf{D}) \\
&= (1-\omega)^J \ .
\end{aligned}
$$

From this it results $|\lambda_1\,\lambda_2\,\ldots\lambda_J| = \left|(1-\omega)^J\right| = |1-\omega|^J$ and from (A.11) also $|\lambda_1\,\lambda_2\,\ldots\lambda_J| \le \rho(\mathbf{T})^J$. It is therefore $|1-\omega|^J \le \rho(\mathbf{T})^J$ and simply $|1-\omega| \le \rho(\mathbf{T})$. A convergent matrix $\mathbf{T}(\omega)$ requires $\rho(\mathbf{T}) < 1$ and thus $|1-\omega| < 1$, i.e.

$$0 < \omega < 2 \tag{A.13}$$

(a necessary but not sufficient condition for convergence of the sequence (A.8)). The iteration procedures (A.5) using relaxation factors $\omega < 1$ are accordingly called successive underrelaxation methods (SUR). They can be used in cases where the iteration matrix $\mathbf{T}(\omega)$ is divergent for relaxation factors $\omega > 1$ and convergent for some $\omega < 1$.

---

be $J \times J$ matrices, α a constant value):

$$
\begin{aligned}
&\det(\mathbf{X}\,\mathbf{Y}) = \det(\mathbf{X}) \cdot \det(\mathbf{Y}) \ , \\
&\det\left(\mathbf{X}^{-1}\right) = \frac{1}{\det(\mathbf{X})} \ , \\
&\det(\alpha\,\mathbf{X}) = \alpha^J \det(\mathbf{X}) \ .
\end{aligned}
$$

If $\mathbf{X}$ has eigenvalues $\lambda_1, \lambda_2, \ldots, \lambda_J$ (which do not have to differ from each other) then

$$\det(\mathbf{X}) = \lambda_1\,\lambda_2\,\ldots\lambda_J \ .$$

If $\mathbf{X}$ is a triangular matrix, either a left triangular matrix with $x_{ij} = 0$ for $i < j$ or a right triangular matrix with $x_{ij} = 0$ for $i > j$ then the determinant of $\mathbf{X}$ is the product of the diagonal elements of $\mathbf{X}$:

$$\det(\mathbf{X}) = x_{11}\,x_{22}\,\ldots x_{JJ} \ .$$

Appendix B

Problem Sets

Problem 1: Warm-up

Calculate the sum

$$S(N) = \sum_{n=1}^{N} n$$

for $N = 100$ and for $N = 10,000$, first by summing all the numbers from 1 to N and then by using Gauss' formula

$$S(N) = \frac{N\,(N+1)}{2}\ .$$

a) Compare the two approaches using the speed to calculate them.

b) Plot a graph of S as a function of N.

Problem 2: More warm-up

Prime numbers between 2 and M can be found using Erathostenes' Sieve which goes as follows: In the vector of numbers from 1 to M, all multiples of the smallest prime still in the vector are cancelled, with the exception of the prime itself. Start with 2.

Problem 3: Hydrostatic pressure in the ocean

Calculate the hydrostatic pressure $p(z)$ of sea water as a function of depth z, by integrating the hydrostatic equilibrium

$$\frac{\mathrm{d}p}{\mathrm{d}z} = -g\,\rho(z)\ , \tag{B.1}$$

where ρ is sea water's density and $g = 9.81\ \mathrm{m\,s^{-2}}$ the gravitational acceleration. Density depends, in a simplified form, on temperature T and salinity S according to

$$\rho(T,S) = \rho_0\Big(1 - \alpha\,(T - T_0) + \beta\,(S - S_0)\Big)\ ,$$

where $\rho_0 = 1028\ \mathrm{kg/m^3}$, $T_0 = 0°\mathrm{C}$, and $S_0 = 35$, and the thermal and haline expansion coefficients are given by $\alpha = 5.4 \cdot 10^{-5}\ \mathrm{K^{-1}}$, and $\beta = 7.6 \cdot 10^{-4}$. Temperature at a depth of $z = 1000$ m is $T = -1°\mathrm{C}$ and increases linearly to $T = 10°\mathrm{C}$ at the

surface ($z = 0$) typical of high latitudes. Surface air pressure is $p = 1.013 \cdot 10^5$ Pa. Assume $S = 37$.

a) The first derivative in (B.1) should be discretized using the Euler forward scheme. Calculate the pressure profile and plot it against z. Hint: Use $\Delta z = 100$ m to discretize the derivative.

b) Calculate pressure by integrating (B.1). The integral can be directly calculated in python. Alternatively, calculate it numerically by approximating the integral by the area of a trapezoid:

$$\int_a^b f(x)\,\mathrm{d}x \approx (b-a)\,\frac{f(a)+f(b)}{2}\ .$$

Show the difference between a) and b).

c) A better approximation is obtained if the interval (a, b) is divided in many small sub-intervals in which the trapezoidal rule is applied.

d) In lower latitudes ocean temperatures vary approximately exponentially from the surface at $T = 20°\mathrm{C}$ to $T = 5°\mathrm{C}$ at 1000 m depth with a scale depth of $d = 150$ m. Again repeat a) but with the exponential temperature profile and plot $\rho(z)$ and $p(z)$.

Problem 4: Energy balance model I

The energy balance model of the atmosphere was introduced in Section 2.2. The balance equation (2.1) reads:

$$h\,\rho\,c\,\frac{\mathrm{d}T}{\mathrm{d}t} = (1-\alpha)\,\frac{S_0}{4} - \varepsilon\,\sigma\,T^4\ . \tag{B.2}$$

Determine the equilibrium temperature for the parameter values given on page 35.

The ice-albedo feedback should be simulated by using the following approximation of the temperature-dependence of the planetary albedo:

$$\alpha = \begin{cases} 0.42 & \text{for } T > -10°\mathrm{C} \\ 0.62 & \text{for } T \le -10°\mathrm{C} \end{cases}\ .$$

In order to solve the differential equation (B.2) you use

a) the Euler forward,

b) the Runge-Kutta scheme of 4^{th} order.

The initial value is $T = 290$ K. Terminate the iteration, if the change of temperature in an iteration step is smaller than 10^{-3} K, or more than 1000 iterations are used. Plot the temperature time series for both schemes and explore the effect of changing the time step.

Problem 5: Energy balance model II (time dependence)

We now extend Problem 4 by including a simple description of the ocean surface layer. We also want to investigate the consequence of a varying solar constant, typical for a solar cycle. Consider the energy balance,

$$(h\,\rho\,c + h_{\mathrm{oc}}\,\rho_{\mathrm{oc}}\,c_{\mathrm{oc}})\,\frac{\mathrm{d}T}{\mathrm{d}t} = (1-\alpha)\,\frac{S(t)}{4} - \varepsilon\,\sigma\,T^4\,, \tag{B.3}$$

where we use $\rho_{\mathrm{oc}} = 1028\ \mathrm{kg\,m^{-3}}$, $c_{\mathrm{oc}} = 3900\ \mathrm{J\,kg^{-1}\,K^{-1}}$ as typical ocean values. In equation (B.3) we have assumed that the atmosphere is in instantaneous equilibrium with the ocean. For albedo use the constant $\alpha = 0.42$, and assume that the solar energy flux $S(t)$ varies sinusoidally with an amplitude of 2‰ and a period of 11 yearsm around the solrar constant of S_0.

Consider different depths of the surface ocean layer, h_{oc}: 50 m, 100 m, 500 m, and 1000 m.

In order to solve the differential equation (B.3) you use

a) the Euler forward,

b) the Runge-Kutta scheme of 4^{th} order.

Try increasing time steps from 1 month, 1 year, 3 years, 5 years to 7 years. Integrate (B.3) over several solar cycles, and produce a graph in which you show T as a function of time. Note how the temporal behaviour depends on ocean depth (phase lag).

Problem 6: One-dimensional tracer advection I

A tracer is released continuously into an aquifer in which water is flowing at a speed of $u = 1$ m/day. We assume that this tracer is salt, whose concentration is measured in grams per kilogram water. The concentration of the tracer at the location of release at $x = 0$ raises from 0 for $t < 0$ abruptly to $C_0 = 100$ g/kg at time $t = 0$ and is held constant thereafter, $t > 0$. Determine the time, when the tracer concentration exceeds 0.1 g/kg at a distance of 500 m from the location of release.

The problem is described by the one-dimensional advection equation:

$$\frac{\partial C}{\partial t} + u\,\frac{\partial C}{\partial x} = 0\,.$$

Solve this equation using

a) central differences,

b) upstream scheme,

c) using a diffusive correction described in Section 3.8.

d) What is the exact time?

Plot the numerical solutions at different subsequent times. Try different time steps.

Problem 7: One-dimensional tracer advection II (radioactive decay)

Assume now that the tracer considered in Problem 6 is tritium, the unstable isotope of hydrogen (^{3}H). Tritium decays radioactively (β-decay) with a half life of 12.3 years. The initial activity is 120 Bq/liter.

Determine the time, when the tracer activity first exceeds 2 Bq/liter at a distance of 500 m from the location of release.

The problem is now described by

$$\frac{\partial C}{\partial t} + u\,\frac{\partial C}{\partial x} + \lambda\, C = 0\ .$$

Plot the numerical solutions at different subsequent times.

Problem 8: One-dimensional tracer advection III (implicit scheme)

Solve Problem 7 now with an implicit scheme as described in Section 3.6.3. Use Euler forward in time and central differences in space. The discretized problem can be written in matrix form.

Problem 9: Energy balance model III (time and latitude dependence)

Consider the one-dimensional energy balance model which was presented in (4.9). The energy balance now reads:

$$h\,\rho\,c\,\frac{\partial T}{\partial t} = (1-\alpha)\,\frac{S}{4} - \varepsilon\,\sigma\,T^4 + \frac{h\,\rho\,c}{R^2\,\cos\varphi}\,\frac{\partial}{\partial\,\varphi}\left(K\,\cos\varphi\,\frac{\partial T}{\partial\varphi}\right)\ , \tag{B.4}$$

where the latitudinally dependent eddy diffusivity K (in $\mathrm{m^2\,s^{-1}}$), the albedo α and the incoming solar radiation S are given by

$$\begin{aligned} K = K(\varphi) &\approx (1.5 + 2.5\,\cos\varphi)\,10^6\ \mathrm{m^2\,s^{-1}} \\ \alpha = \alpha(\varphi) &\approx 0.6 - 0.4\,\cos\varphi \\ S = S(\varphi) &\approx S_0\left(0.5294 + 0.706\,\cos^2\varphi\right)\ . \end{aligned}$$

$S_0 = 1361\ \mathrm{W/m^2}$ is the solar constant. The values of the other parameters are given in Section 2.2.

Define a grid where the temperatures are given at the centres of the grid boxes, and the first derivatives $\partial T/\partial\varphi$ are given at the box edges, as in the figure below.

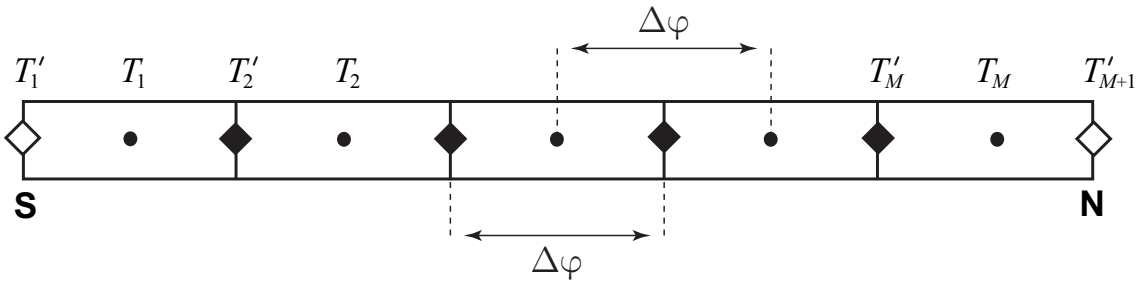

The temperatures are evaluated at the points, the derivatives at the diamonds. The boundary conditions are imposed at the open diamonds. The discretized first derivative is given by

$$T_i' = \frac{T_i - T_{i-1}}{\Delta\varphi} \ ,$$

the second derivative is evaluated at the points, and given by

$$T_i'' = \frac{T_{i+1}' - T_i'}{\Delta\varphi} \ .$$

a) Calculate the steady-state temperature as a function of latitude. Choose 1° as the meridional resolution, and Euler forward for the time discretization with $\Delta t = 20$ min. Note that you need at least 10,000 iterations for convergence.

b) Compare the temperature with that obtained for $K = 0$ (no meridional heat flux).

c) Compare the result with the surface air temperature data set (data will be provided during the lecture).

Problem 10: Wind-driven circulation (two-dimensional PDE)

The first model of the wind driven large-scale circulation in a closed basin was proposed by Henry Stommel as introduced in Section 6.7.

The stream function Ψ satisfies the partial differential equation (PDE) (6.52),

$$\beta \frac{\partial \Psi}{\partial x} = \frac{\partial \tau_{yz}}{\partial x} - \frac{\partial \tau_{xz}}{\partial y} - R \left(\frac{\partial^2 \Psi}{\partial x^2} + \frac{\partial^2 \Psi}{\partial y^2} \right) \ ,$$

and $\Psi = 0$ on the boundary. The PDE should be solved in a rectangular domain of zonal extent of $L = 7000$ km, and $B = 5000$ km meridional extent. The circulation is driven by a zonal wind stress for which we assume the simple profile (6.54):

$$\tau_{xz} = -\tau_0 \cos\left(\frac{\pi}{B}\, y\right) \ , \qquad \tau_{yz} = 0 \ ,$$

with $\tau_0 = 0.1\ \mathrm{N\,m^{-2}}$. We select $\beta = 2 \cdot 10^{-11}\ \mathrm{m^{-1}\,s^{-1}}$, and $R = 1/(6\ \mathrm{days})$.

a) Discretize the PDE using central differences. Use the Method of Successive Overrelaxation (SOR) to calculate the stream function. The iteration can be terminated when the maximum relative error is smaller than 10^{-6}, i.e., $\max\left(\xi_{i,j} / \left(e_{i,j}\, \Psi_{i,j}\right)\right) < 10^{-6}$ (see Section 5.3.2).

b) Determine the optimum relaxation parameter ω by plotting the number of iterations as a function of ω.

c) Make a contour plot of the stream function.

d) Plot the stream function $\Psi(x, y = B/2)$ for three values of the friction: $R = 1/(2 \text{ days})$, $1/(6 \text{ days})$, $1/(20 \text{ days})$. Note that your discretisation might not be appropriate to represent a very narrow western boundary current whose width scales as R/β.

Problem 11: Lorenz-Saltzman model I

The Lorenz-Saltzman model is a simple but powerful model for flow in the atmosphere. It is the starting point of Chaos Theory, first described by Ed Lorenz in his landmark paper entitled *Deterministic non-periodic flow* (Lorenz, 1963). The equations (7.26) of this famous model read:

$$\frac{\mathrm{d}X}{\mathrm{d}t} = -\sigma\, X + \sigma\, Y \ ,$$

$$\frac{\mathrm{d}Y}{\mathrm{d}t} = -X\, Z + r\, X - Y \ ,$$

$$\frac{\mathrm{d}Z}{\mathrm{d}t} = X\, Y - b\, Z \ .$$

All quantities are dimensionless. These equations describe the small-scale thermal convection of an incompressible fluid in a box. The physical meaning of X, Y, and Z, and the derivation are given in Section 7.2.

Calculate the solution of the Lorenz-Saltzman model using the 4^{th} order Runge-Kutta scheme (see Section 2.3) with a time step of $\Delta t = 12/2000$. Use the following parameters: $r = 28$, $\sigma = 10$, and $b = 8/3$. Calculate the solution for two slightly different initial conditions:

$$\begin{array}{lll} 1. & X_1(0) = 1, & Y_1(0) = 2, \quad Z_1(0) = 11.01 \\ 2. & X_2(0) = 1, & Y_2(0) = 2, \quad Z_2(0) = 11.02 \ . \end{array}$$

a) Plot the first 10,000 time steps in the Y-Z-plane.

b) Plot the distance between the solutions starting from the two initial conditions as a function of time. The distance is defined as

$$d(t) = \sqrt{(X_1 - X_2)^2 + (Y_1 - Y_2)^2 + (Z_1 - Z_2)^2} \ .$$

Problem 12: Lorenz-Saltzman model II

The predictability of atmospheric flow depends on the current state of the atmosphere. Predictability can be determined by integrating an ensemble of initial con-

ditions that are within certain predefined bounds.

We now use the Lorenz-Saltzman model to calculate ensembles from initial conditions at $t = 0$ which are located in circles of radius 0.5 in the Y-Z-plane, centered at the three locations:

$$(X_1, Y_1, Z_1) = (1, 2, 42) \; ;$$
$$(X_2, Y_2, Z_2) = (1, 2, 9) \; ;$$
$$(X_3, Y_3, Z_3) = (1, -1, 11) \; .$$

Follow how the circles deform as time progresses. Consider the time interval from $t = 0$ to $t = 0.5$.

Problem 13: Equatorial waves I

This and the last problem take you on a *tour d'horizon* revisiting many concepts presented in this course. Consequently, these are quite demanding.

An important element to predict the El Niño-Southern Oscillation phenomenon is to simulate the propagation of ocean waves along the equator. Here, we numerically solve the shallow water equations (8.24). The dynamics are described by the perturbations h to the thermocline layer of thickness H, extending from west to east in the equatorial Pacific. Thickness anomalies drive a flow (u, v) which, through its divergence, feeds back on the perturbation h. We consider an equatorial β-plane and assume $\tilde{\tau}_x = 0$.

The following values for the constants are selected: $\beta = 2.283 \cdot 10^{-11}\,\mathrm{m^{-1}s^{-1}}$, $g' = 5.6 \cdot 10^{-2}\,\mathrm{m\,s^{-2}}$ is the reduced gravity, $r^{-1} = 2.5\,\mathrm{yr}$ is a damping timescale, and $H = 150\,\mathrm{m}$ is the thickness of the unperturbed thermocline. The domain is a rectangular basin of zonal and meridional extent of $L = W = 10,000\,\mathrm{km}$, centered at the equator.

For the discretization we choose a C-grid (see Section 6.5) with $N = M = 200$ grid points and use formulations for the derivatives similar to (6.37), with first-order spatial differences and central differences in time. Note that for stability reasons, the friction terms in (8.24) need to be averaged over two preceding time steps, e.g. $u_{i,j}^{n+1} = u_{i,j}^{n-1} + 2 \cdot \Delta t \cdot f^n - \Delta t \cdot r \cdot (u_{i,j}^n + u_{i,j}^{n-1})$, where f^n contains all other terms at time step n; see subsection 2.3.3.

The boundary conditions are $u(\pm L/2, y) = 0$, $v(x, \pm W/2) = 0$, i.e., no flow across the basin boundaries. Other boundary values need not be specified. The domain is made large enough in the y-direction so that boundary effects are not relevant during the selected integration time.

As an intial perturbation at $t = 0$ we set $h(x, y) = h_0\, \mathrm{e}^{-0.5((x/(a_x L_E))^2 + (y/(a_y L_E))^2)}$, with $h_0 = 50\,\mathrm{m}$, L_E is the equatorial Rossby radius, and a_x, a_y are scaling factors determining the zonal and meridional extent of the perturbation. We set $u(x, y) = v(x, y) = 0$ at $t = 0$.

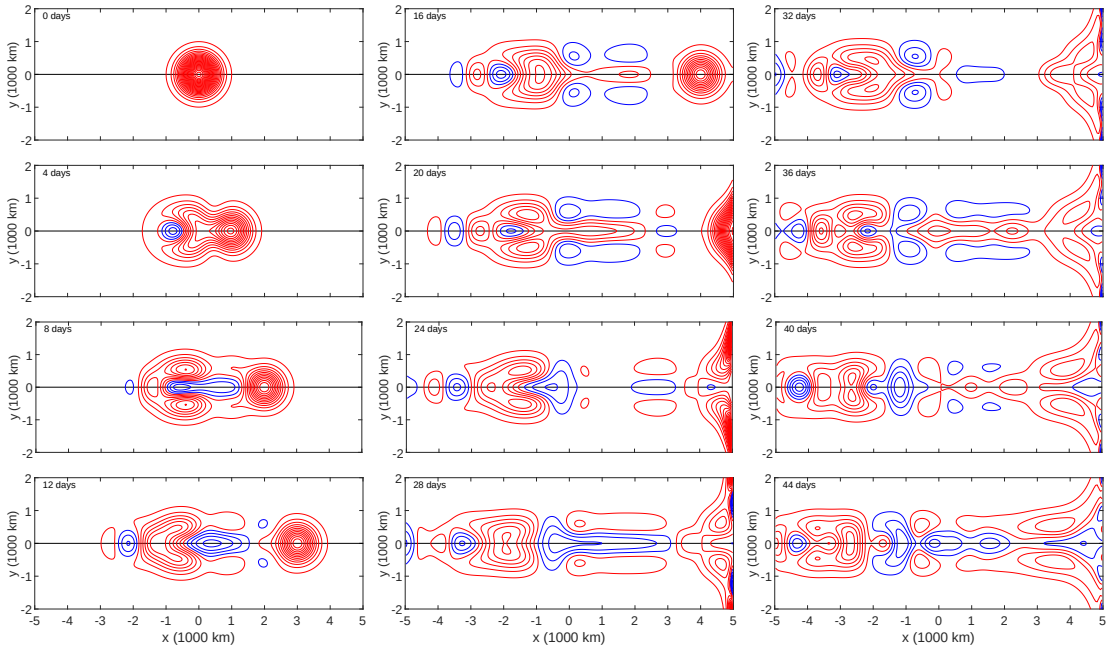

Figure B.1: Evolution of $h(x, y, t)$ starting from a Gaussian perturbation with $a_x = a_y = 1$. A time step of 0.02 days was used; positive thermocline thickness anomalies (warm anomaly) are plotted in red contours. Various types of equatorial waves travel along the equator with characteristic phase speeds, and Kelvin waves escape polewards along the eastern boundary of the domain. Once they reach the northern and southern boundaries (not shown), they travel westwards, unless suppressed during the time stepping.

a) Write the discretized schemes for the equation system (8.24) assuming a C-grid. Note that the first time step is Euler forward.

b) Formulate the numerical boundary conditions for the four boundaries of the rectangular domain. Take into account that you use the C-grid and select carefully which subgrid lies on the respective physical boundaries.

c) Estimate the time step that you need for stability by first assuming the phase speed of the equatorial Kelvin wave to be important. Also, estimate the equatorial Rossby radius L_E for the given parameter values.

   It turns out that a time step about 5 times shorter than this first estimate is needed for stability. Discuss the reason for this by considering the dispersion relation shown in Fig. B.2 and make a quantitative argument.

d) Simulate the propagation of the equatorial waves by showing contour plots of $h(x, y, t)$ at $t = i \cdot (4\,\text{days}), i = 0, ...11$, see Fig. B.1. For the initial perturbation we choose $a_x = a_y = 1$. As contour levels $[-49 : 2 : 49]$ are suggested, and for clarity we display the domain limited by $-L/2 \leq x \leq +L/2, -W/5 \leq y \leq +W/5$.

e) As in d) but now with $a_y = 0.3$.

f) Discuss the evolution of the wave fields for both values of a on the basis of the dispersion relation for equatorial waves shown in Fig. B.2.

g) Integrate out to $t = 200\,\text{days}$ and observe the westward propagation of Kelvin waves along the northern and southern boundaries. Repeat the integration

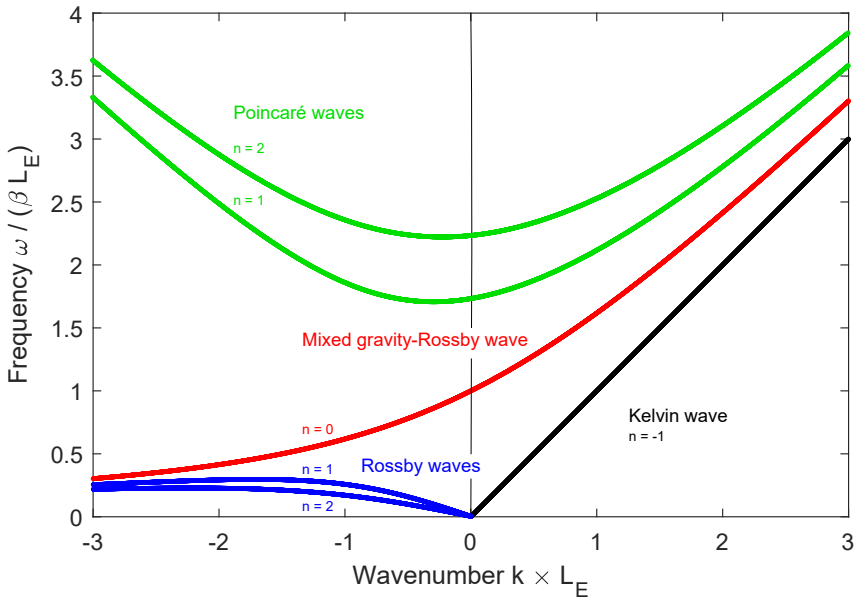

Figure B.2: Dispersion relation of equatorial waves (see page 194 how to derive it). There are four types of equatorial waves: $n \geq 1$ modes of each high-frequency gravity waves (Poincaré waves) and low-frequency Rossby waves, and one mode ($n = 0$) of a mixed gravity-Rossby wave (Yanai wave) and a Kelvin wave ($n = -1$). Note that for the Kelvin wave the phase speed $c_{ph} = \omega/k$ is only positive, i.e. the phase propagates eastwards), whereas it is strictly negative for the Rossby waves whose phase propagates westward. However, wave energy is transported at the group velocity $c_{gr} = \partial\omega/\partial k$. Therefore, Rossby and Poincaré waves transport energy in both zonal directions.

and suppress these Kelvin waves by setting $h(x, y, t) = 0$ in the vicinity of these boundaries at every time step.

Problem 14: Equatorial waves II

Extending Problem 13, we further explore the simulated equatorial waves employing two approaches. The first is the so-called *Hovmøller diagram* which displays the time evolution of a variable $f(x, t)$ in one space dimension. The Hovmøller diagram is obtained by contouring the field $f(x, t)$ with the time dimension along the y-axis. This permits the visualisation of wave propagation and a straightforward determination of the phase velocities.

The second approach is the 2-dimensional *Fourier spectrum* of a variable $f(x, t)$ from which the dispersion relation of the simulated waves can be determined. This is achieved by contouring the field $\hat{f}(k, \omega) = \iint f(x, t)\mathrm{e}^{i(kx-\omega t)}dxdt$ in the (k, ω)-plane.

We employ the simulation obtained in Problem 13g and store the thermocline depth field at the equator $h_{\mathrm{eq}}(x, t) = h(x, y = 0, t)$ at every time step for later analysis. We set $f(x, t) = h_{\mathrm{eq}}(x, t)$.

a) Plot the Hovmøller diagram for $h_{\mathrm{eq}}(x, t)$ and observe the propagation of the phases of the different wave types. Note the time when a standing wave pattern has developed in the basin.

b) To determine the dispersion relation of the simulated waves, calculate the Fourier spectrum of $h_{\mathrm{eq}}(x,t)$ and contour $\hat{h}(k,\omega)$ in the (k,ω)-plane.

c) Repeat the simulation with an initial Gaussian perturbation of much smaller spatial extent by choosing $a_x = a_y = 0.1$. This excites gravity wave modes of higher order that will be emerge in the dispersion relation.

d) Repeat the simulation with an Gaussian perturbation of second order in the y-direction. Use as initial condition $\partial h(x,y)/\partial y$ with $a_x = a_y = 1$, where $h(x,y)$ is the initial condition from Problem 13. In addition to the second-order Poincaré waves, this excites the Yanai wave, the mixed gravity-Rossby wave, which will appear in the dispersion relation.

Hints to obtain the exact dispersion relation for equatorial waves:

Analogous to the procedure decribed in subsection 6.4.5, we first bring all terms of (8.24) to the left-hand side and eliminate u and h by calculating

$$\begin{aligned}\partial^2/\partial t^2(8.24\mathrm{b}) &- g'\partial^2/\partial t\partial y(8.24\mathrm{c})\\ &- g'H\partial/\partial x(\partial/\partial x(8.24\mathrm{b}) - \partial/\partial y(8.24\mathrm{a}))\\ &- \beta y(\partial/\partial t(8.24\mathrm{a}) - g'\partial/\partial x(8.24\mathrm{c}))\ .\end{aligned}$$

Then, assume $v(x,y,t) = \tilde{v}(y)\,\mathrm{e}^{\mathrm{i}(kx-\omega t)}$ to obtain an ordinary differential equation in $\tilde{v}(y)$. This differential equation is also solved in Quantum Mechanics when considering the harmonic oscillator: Solutions are Hermite polynomials. They are finite only if

$$\omega^2 - k^2 - k/\omega = 2n+1\,,\ (n = 0,1,2,...)\,, \tag{B.5}$$

and decay as $\mathrm{e}^{-1/2(y/L_E)^2}$, where $L_E = (\sqrt{g'H}/\beta)^{1/2}$ is the equatorial Rossby radius. Equation (B.5) is the non-dimensional dispersion relation for successive modes n of equatorial waves. It is a polynomial of order 3 in ω. In addition, there is the equatorial Kelvin wave for $n = -1$, however, it does not result from the derivation above because $v = 0$. The dispersion relation of the equatorial Kelvin wave is simply $\omega = \beta L_E^2\, k$. This is the only equatorial wave that is non-dispersive, i.e., all wavelengths travel at the same phase speed $c_{ph} = \beta L_E^2$.

References

Alley, R.B., J. Marotzke, W.D. Nordhaus, J.T. Overpeck, D.M. Peteet, R.A. Pielke Jr., R.T. Pierrehumbert, P.B. Rhines, T.F. Stocker, L.D. Talley, and J.M. Wallace (2003): Abrupt climate change. *Science*, **299**, 2005–2010.

Barker, S., P. Diz, M.J. Vautravers, J. Pike, G. Knorr, I.R. Hall, and W.S. Broecker (2009): Interhemispheric Atlantic seesaw response during the last deglaciation. *Nature*, **457**, 1097–1102.

Bjerknes, J. (1969): Atmospheric teleconnections from the equtorial pacific. *Monthly Weather Review*, **97**, 163–172.

Blunier, T. and E.J. Brook (2001): Timing of millennial-scale climate change in Antarctica and Greenland during the last glacial period. *Science*, **291**, 109–112.

Blunier, T., J. Chappellaz, J. Schwander, A. Dällenbach, B. Stauffer, T.F. Stocker, D. Raynaud, J. Jouzel, H.B. Clausen, C.U. Hammer, and S.J. Johnsen (1998): Asynchrony of Antarctic and Greenland climate change during the last glacial period. *Nature*, **394**, 739–743.

Boutle, I., R.H.S. Taylor, and R.A. Römer (2007): El Niño and the delayed action oscillator. *American Journal of Physics*, **75**, 15–24.

Broecker, W.S. (1987): The biggest chill. *Natural History Magazine*, **96**, 74–82.

Broecker, W.S. (1997): Thermohaline circulation, the Achilles heel of our climate system: will man-made CO_2 upset the current balance? *Science*, **278**, 1582–1588.

Broecker, W.S. (1998): Paleocean circulation during the last deglaciation: a bipolar seesaw? *Paleoceanography*, **13**, 119–121.

Broecker, W.S. and G.H. Denton (1989): The role of ocean-atmosphere reorganizations in glacial cycles. *Geochimica et Cosmochimica Acta*, **53**, 2465–2501.

Broecker, W.S., D.M. Peteet, and D. Rind (1985): Does the ocean-atmosphere system have more than one stable mode of operation? *Nature*, **315**, 21–26.

Bryan, F. (1986): High-latitude salinity effects and interhemispheric thermohaline circulations. *Nature*, **323**, 301–304.

Bryan, F. (1987): Parameter sensitivity of primitive equation ocean general circulation models. *Journal of Physical Oceanography*, **17**, 970–985.

Bryan, K. (1969): A numerical method for the study of the circulation of the World Ocean. *Journal of Computational Physics*, **4**, 347–376.

Bryan, K. and M.D. Cox (1967): A numerical investigation of the oceanic general circulation. *Tellus*, **19**, 54–80.

Budyko, M.I. (1969): The effect of solar radiation variations on the climate of the earth. *Tellus*, **21**, 611–619.

Cayan, D.R. (1992): Latent and sensible heat flux anomalies over the northern oceans: The connection to monthly atmospheric circulation. *Journal of Climate*, **5**, 354–370.

Clark, P.U., N.G. Pisias, T.F. Stocker, and A.J. Weaver (2002): The role of the thermohaline circulation in abrupt climate change. *Nature*, **415**, 863–869.

Courant, R., K. Friedrichs, and H. Lewy (1928): Über die partiellen Differenzengleichungen der mathematischen Physik. *Math. Ann.*, **100**, 32–74.

Dansgaard, W., S.J. Johnsen, H.B. Clausen, D. Dahl-Jensen, N. Gundestrup, C.U. Hammer, and H. Oeschger (1984): North Atlantic climatic oscillations revealed by deep Greenland ice cores. *In:* J.E. Hansen (Editor), *Climate Processes and Climate Sensitivity (Geophysical Monograph)*, pp. 288–298. American Geophysical Union.

Dansgaard, W., S.J. Johnsen, H.B. Clausen, D. Dahl-Jensen, N.S. Gundestrup, C.U. Hammer, C.S. Hvidberg, J.P. Steffensen, A.E. Sveinbjörnsdottir, J. Jouzel, and G. Bond (1993): Evidence for general instability of past climate from a 250-kyr ice-core record. *Nature*, **364**, 218–220.

Domingues, C.M., J.A. Church, N.J. White, P.J. Gleckler, S.E. Wijffels, P.M. Barker, and J.R. Dunn (2008): Improved estimates of upper-ocean warming and multi-decadal sea-level rise. *Nature*, **453**, 1090–1093.

Egger, J. (1997): Flux correction: Tests with a simple ocean-atmosphere model. *Climate Dynamics*, **13**, 285–292.

EPICA Community Members (2006): One-to-one coupling of glacial climate variability in Greenland and Antarctica. *Nature*, **444**, 195–198.

Ferreira, D., J. Marshall, T. Ito, and D. McGee (2018): Linking glacial-interglacial states to multiple equilibria of climate. *Geophysical Research Letters*, **45**, 9160–9170.

Ferreira, D., J. Marshall, and B. Rose (2011): Climate determinism revisited: Multiple equilibria in a complex climate model. *Journal of Climate*, **24**, 992–1012.

Frankel, S.P. (1950): Convergence rates of iterative treatments of partial differential equations. *Mathematical Tables and Other Aids to Computation*, **4**, 65–75.

Ganachaud, A. and C. Wunsch (2000): Improved estimates of global ocean circulation, heat transport and mixing from hydrographic data. *Nature*, **408**, 453–457.

Gill, A.E. (1982): *Atmosphere-Ocean Dynamics.* Academic Press, 662 pp.

Griffies, S.M. (2005): *Fundamentals in Ocean Climate Models.* Princeton, 528 pp.

Haltiner, G.J. and R.T. Williams (1980): *Numerical Prediction and Dynamic Meteorology.* Wiley, 2 ed., 496 pp.

Haney, R.L. (1971): Surface thermal boundary condition for ocean circulation models. *Journal of Physical Oceanography*, **1**, 241–248.

Hartmann, D.L. (2016): *Global Physical Climatology, 2nd Edition.* Elsevier, 498 pp.

Hasselmann, K. (1976): Stochastic climate models. part i: Theory. *Tellus*, **28**, 473–485.

Hasselmann, K. (1982): An ocean model for climate variability studies. *Progress in Oceanography*, **11**, 69–92.

Hegerl, G. C., K. Hasselmann, U. Cubasch, J. F. B. Mitchell, E. Roeckner, R. Voss, and J. Waszkewitz (1997): Multi-fingerprint detection and attribution analysis of greenhouse gas, greenhouse gas-plus-aerosol and solar forced climate change. *Climate Dynamics*, **13**, 613–634.

Hirst, A. C. (1986): Unstable and damped equatorial modes in simple coupled ocean-atmosphere models. *Journal of the Atmospheric Sciences*, **43**, 606–630.

Hoffman, P. F., D. S. Abbot, Y. Ashkenazy, D. I. Benn, J. J. Brocks, P. A. Cohen, G. M. Cox, J. R. Creveling, Y. Donnadieu, D. H. Erwin, I. J. Fairchild, D. Ferreira, J. C. Goodman, G. P. Halverson, M. F. Jansen, G. Le Hir, G. D. Love, F. A. Macdonald, A. C. Maloof, C. A. Partin, G. Ramstein, B. E. J. Rose, C. V. Rose, P. M. Sadler, E. Tziperman, A. Voigt, and S. G. Warren (2017): Snowball Earth climate dynamics and Cryogenian geology-geobiology. *Science Advances*, **3**, e1600983.

Holton, J. R. and G. J. Hakim (2013): *An Introduction to Dynamic Meteorology, 5th Edition*. Academic Press, 552 pp.

Houghton, J. (2001): *The Physics of Atmospheres*. Cambridge University Press, 3 ed., 336 pp.

Houghton, J. (2009): *Global Warming: The Complete Briefing*. Cambridge University Press, 4 ed., 456 pp.

Hu, A., G. A. Meehl, W. Han, J. Lu, and W. G. Strand (2013): Energy balance in a warm world without the ocean conveyor belt and sea ice. *Geophysical Research Letters*, **40**, 6242–6246.

Huber, C., M. Leuenberger, R. Spahni, J. Flückiger, J. Schwander, T.F. Stocker, S. Johnsen, A. Landais, and J. Jouzel (2006): Isotope calibrated Greenland temperature record over Marine Isotope Stage 3 and its relation to CH_4. *Earth and Planetary Science Letters*, **243**, 504–519.

IPCC (2001): *Climate Change 2001 - The Scientific Basis: Contribution of Working Group I to the Third Assessment Report of the Intergovernmental Panel on Climate Change* [Houghton, J.T. et al. (eds.)]. Cambridge University Press, 892 pp.

IPCC (2007): *Climate Change 2007 - The Physical Science Basis: Contribution of Working Group I to the Fourth Assessment Report of the Intergovernmental Panel on Climate Change* [Solomon, S. et al. (eds.)]. Cambridge University Press, 1009 pp.

IPCC (2013): *Climate Change 2013 - The Physical Science Basis: Contribution of Working Group I to the Fifth Assessment Report of the Intergovernmental Panel on Climate Change* [Stocker, T.F. et al. (eds.)]. Cambridge University Press, 1535 pp. www.climatechange2013.org.

IPCC (2021): *Climate Change 2021 - The Physical Science Basis: Contribution of Working Group I to the Sixth Assessment Report of the Intergovernmental Panel on Climate Change* [Masson-Delmotte, V. et al. (eds.)]. Cambridge University Press. www.ipcc.ch/report/ar6/wg1.

Jayne, S.R. and J. Marotzke (2002): The oceanic eddy heat transport. *Journal of Physical Oceanography*, **32**, 3328–3345.

Joos, F., G.K. Plattner, T.F. Stocker, O. Marchal, and A. Schmittner (1999): Global warming and marine carbon cycle feedbacks on future atmospheric CO_2. *Science*, **284**, 464–467.

Joos, F., R. Roth, J. S. Fuglestvedt, G. P. Peters, I. G. Enting, W. von Bloh, V. Brovkin, E. J. Burke, M. Eby, N. R. Edwards, T. Friedrich, T. L. Froelicher, P. R. Halloran, P. B. Holden, C. Jones, T. Kleinen, F. T. Mackenzie, K. Matsumoto, M. Meinshausen, G. K. Plattner, A. Reisinger, J. Segschneider, G. Shaffer, M. Steinacher, K. Strassmann, K. Tanaka, A. Timmermann, and A. J. Weaver (2013): Carbon dioxide and climate impulse response functions for the computation of greenhouse gas metrics: a multi-model analysis. *Atmospheric Chemistry and Physics*, **13**, 2793–2825.

Jouzel, J., V. Masson-Delmotte, O. Cattani, G. Dreyfus, S. Falourd, G. Hoffmann, B. Minster, J. Nouet, J.-M. Barnola, J. Chappellaz, H. Fischer, J.C. Gallet, S. Johnsen, M. Leuenberger, L. Loulergue, D. Lüthi, H. Oerter, F. Parrenin, G. Raisbeck, D. Raynaud, A. Schilt, J. Schwander, E. Selmo, R. Souchez, R. Spahni, B. Stauffer, J.P. Steffensen, B. Stenni, T.F. Stocker, J.L. Tison, M. Werner, and E.W. Wolff (2007): Orbital and millennial Antarctic climate variability over the past 800,000 years. *Science*, **317**, 793–796.

Kilic, C., F. Lunkeit, C. C. Raible, and T. F. Stocker (2018): Stable equatorial ice belts at high obliquity in a coupled atmosphere-ocean model. *Astrophysical Journal*, **864**.

Kilic, C., C. C. Raible, and T. F. Stocker (2017): Multiple climate states of habitable exoplanets: The role of obliquity and irradiance. *Astrophysical Journal*, **844**.

Knutti, R., T.F. Stocker, F. Joos, and G.-K. Plattner (2002): Constraints on radiative forcing and future climate change from observations and climate model ensembles. *Nature*, **416**, 719–723.

Knutti, R., T.F. Stocker, F. Joos, and G.K. Plattner (2003): Probabilistic climate change projections using neural networks. *Climate Dynamics*, **21**, 257–272.

Kraus, E.B. and J.A. Businger (1994): *Atmosphere-Ocean Interaction*. Oxford University Press, 362 pp.

Krishnamurti, T.N. and L. Bounoua (1996): *An Introduction to Numerical Weather Prediction Techniques*. CRC Press, 1 ed., 293 pp.

Lenton, T.M. (2011): Early warning of climate tipping points. *Nature Climate Change*, **1**, 201–209.

Lorenz, E.N. (1963): Deterministic nonperiodic flow. *Journal of the Atmospheric Sciences*, **20**, 130–141.

Lorenz, E.N. (1979): Forced and free variations of weather and climate. *Journal of the Atmospheric Sciences*, **36**, 1367–1376.

Lorenz, E.N. (1984): Irregularity: A fundamental property of the atmosphere. *Tellus*, **36**, 98–110.

Lorenz, E.N. (1996): *The Essence of Chaos*. University of Washington Press, 227 pp.

Lozier, M.S. (2010): Deconstructing the conveyor belt. *Science*, **328**, 1507–1511.

Lüthi, D., M. Le Floch, B. Bereiter, T. Blunier, J.-M. Barnola, U. Siegenthaler, D. Raynaud, J. Jouzel, H. Fischer, K. Kawamura, and T.F. Stocker (2008): High-resolution carbon dioxide concentration record 650,000–800,000 years before present. *Nature*, **453**, 379–382.

Maier-Reimer, E. and K. Hasselmann (1987): Transport and storage of CO_2 in the ocean – an inorganic ocean-circulation carbon cycle model. *Climate Dynamic*, **2**, 63–90.

Manabe, S. and K. Bryan (1969): Climate calculations with a combined ocean-atmosphere model. *Journal of the Atmospheric Sciences*, **26**, 786–789.

Manabe, S. and R.J. Stouffer (1988): Two stable equilibria of a coupled ocean-atmosphere model. *Journal of Climate*, **1**, 841–866.

Manabe, S. and R.J. Stouffer (1994): Multiple-century response of a coupled ocean-atmosphere model to an increase of atmospheric carbon dioxide. *Journal of Climate*, **7**, 5–23.

Manabe, S. and R. T. Wetherald (1967): Thermal equilibrium of the atmosphere with a given distribution of relative humidity. *Journal of the Atmospheric Sciences*, **50**, 241–259.

Marchal, O., T.F. Stocker, F. Joos, A. Indermühle, T. Blunier, and J. Tschumi (1999): Modelling the concentration of atmospheric CO_2 during the Younger Dryas climate event. *Climate Dynamics*, **15**, 341–354.

Marotzke, J. (2000): Abrupt climate change and thermohaline circulation: Mechanisms and predictability. *Proceedings of the National Academy of Science of the USA*, **97**, 1347–1350.

McGuffie, K. and A. Henderson-Sellers (2005): *A Climate Modelling Primer*. Wiley, 3 ed., 296 pp.

McPhaden, M.J., A.J. Busalacchi, R. Cheney, J.R. Donguy, K.S. Gage, D. Halpern, M. Ji, P. Julian, G. Meyers, G.T. Mitchum, P.P. Niiler, J. Picaut, R.W. Reynolds, N. Smith, and K. Takeuchi (1998): The tropical ocean global atmosphere observing system: A decade of progress. *Journal of Geophysical Reseach–Oceans*, **103**, 14169–14240.

Mikolajewicz, U., M. Gröger, E. Maier-Reimer, G. Schurgers, M. Vizcaíno, and A.M.E. Winguth (2007): Long-term effects of anthropogenic CO_2 emissions simulated with a complex earth system model. *Climate Dynamics*, **28**, 599–633.

Müller, S.A., F. Joos, N.R. Edwards, and T.F. Stocker (2006): Water mass distribution and ventilation time scales in a cost-efficient, three-dimensional ocean model. *Journal of Climate*, **19**, 5479–5499.

Moss, R.H., J.A. Edmonds, K.A. Hibbard, M.R. Manning, S.K. Rose, D.P. van Vuuren, T.R. Carter, S. Emori, M. Kainuma, T. Kram, et al. (2010): The next generation of scenarios for climate change research and assessment. *Nature*, **463**, 747–756.

Mouginot, J., E. Rignot, A. A. Bjork, M. van den Broeke, R. Millan, M. Morlighem, B. Noel, B. Scheuchl, and M. Wood (2019): Forty-six years of Greenland Ice Sheet mass balance from 1972 to 2018. *Proceedings of the National Academy of Science of the USA*, **116**, 9239–9244.

Myhre, G., E.J. Highwood, K.P. Shine, and F. Stordal (1998): New estimates of radiative forcing due to well mixed greenhouse gases. *Geophysical Research Letters*, **25**, 2715–2718.

NAS (2021): *Reflecting Sunlight: Recommendations for Solar Geoengineering Research and Research Governance*. National Academies of Sciences, Engineering, and Medicine, 328 pp.

Nehrbass-Ahles, C., J. Shin, J. Schmitt, B. Bereiter, F. Joos, A. Schilt, L. Schmidely, L. Silva, G. Teste, R. Grilli, J. Chappellaz, D. Hodell, H. Fischer, and T. F. Stocker (2020): Abrupt CO_2 release to the atmosphere under glacial and early interglacial climate conditions. *Science*, **369**, 1000+.

North, G.R., D.A. Short, and J.G. Mengel (1983): Simple energy balance model resolving the seasons and the continents - Application to the astronomical theory of the ice ages. *Journal of Geophysical Research*, **88**, 6576–6586.

Oeschger, H., J. Beer, U. Siegenthaler, B. Stauffer, W. Dansgaard, and C.C. Langway (1984): Late glacial climate history from ice cores. *In:* J. E. Hansen and T. Takahashi (Editors), *Climate Processes and Climate Sensitivity*, vol. 29 of *Geophysical Monograph Series*, pp. 299–306. American Geophysical Union.

Otto, F. E. L. (2017): Attribution of weather and climate events. *Annual Reviews of Environment and Resources*, **42**, 627—646.

Paillard, D. (1998): The timing of Pleistocene glaciations from a simple multiple-state climate model. *Nature*, **391**, 378–381.

Pedro, J.B., M. Jochum, C. Buizert, F. He, S. Barker, and S.O. Rasmussen (2018): Beyond the bipolar seesaw: Toward a process understanding of interhemispheric coupling. *Quaternary Science Reviews*, **192**, 27–46.

Peixoto, J.P. and A.H. Oort (1992): *Physics of Climate*. Springer, 520 pp.

Petit, J.R., J. Jouzel, D. Raynaud, N.I. Barkov, J.-M. Barnola, I. Basile, M. Bender, J. Chappellaz, M. Davis, G. Delaygue, M. Delmotte, V.M. Kotlyakov, M. Legrand, V.Y. Lipenkov, C. Lorius, L. Pépin, C. Ritz, E. Saltzman, and M. Stievenard (1999): Climate and atmospheric history of the past 420,000 years from the Vostok ice core, Antarctica. *Nature*, **399**, 429–436.

Phillips, N.A. (1956): The general circulation of the atmosphere: a numerical experiment. *Quarterly Journal of the Royal Meteorological Society*, **82**, 123–164.

Plattner, G.K., R. Knutti, F. Joos, T.F. Stocker, W. von Bloh, V. Brovkin, D. Cameron, E. Driesschaert, S. Dutkiewicz, M. Eby, N.R. Edwards, T. Fichefet, J.C. Hargreaves, C.D. Jones, M.F. Loutre, H.D. Matthews, A. Mouchet, S.A. Müller, S. Nawrath, A. Price, A. Sokolov, K.M. Strassmann, and A.J. Weaver (2008): Long-term climate commitments projected with climate-carbon cycle models. *Journal of Climate*, **21**, 2721–2751.

Pöppelmeier, F., D. J. Janssen, S. L. Jaccard, and T. F. Stocker (2021): Modeling the marine chromium cycle: new constraints on global-scale processes. *Biogeosciences*, **18**, 5447–5463.

Pöppelmeier, F., F. Joos, and T. F. Stocker (2023): The coupled ice sheet-Earth System model Bern3D v3.0. *Journal of Climate*, **36**, 7563–7582.

Press, W.H., B.P. Flannery, S.A. Teukolsky, and W.T. Vetterling (1992): *Numerical Recipes in FORTRAN 77: The Art of Scientific Computing*, vol. 1. Cambridge University Press, 2 ed., 992 pp.

Press, W.H., S.A. Teukolsky, W.T. Vetterling, and B.P. Flannery (1996): *Numerical Recipes in Fortran 90: The Art of Scientific Computing*, vol. 2. Cambridge University Press, 2 ed., 500 pp.

Press, W.H., S.A. Teukolsky, W.T. Vetterling, and B.P. Flannery (2007): *Numerical Recipes 3rd Edition: The Art of Scientific Computing*. Cambridge University Press, 3 ed., 1256 pp.

Probst, P., R. Rizzi, E. Tosi, V. Lucarini, and T. Maestri (2012): Total cloud cover from satellite observations and climate models. *Atmospheric Research*, **107**, 161–170.

Randall, D. A. (1994): Geostrophic adjustment and the finite-difference shallow-water equations. *Monthly Weather Review*, **122**, 1371–1177.

Rempfer, J., T. F. Stocker, F. Joos, J.-C. Dutay, and M. Siddall (2011): Modelling isotopes of neodymium with a coarse resolution ocean circulation model: Sensitivities to model parameters and source/sink distributions. *Geochimica Cosmochimica Acta*, **75**, 5927–5950.

Renssen, H., H. Goosse, T. Fichefet, V. Brovkin, E. Driesschaert, and F. Wolk (2005): Simulating the Holocene climate evolution at northern high latitudes using a coupled atmosphere-sea ice-ocean-vegetation model. *Climate Dynamics*, **24**, 23–43.

Richardson, L.F. (2007): *Weather Prediction by Numerical Process (Cambridge Mathematical Library)*. Cambridge University Press, 2 ed., 250 pp. Reprint of original 1922.

Rignot, E., J. Mouginot, B. Scheuchl, M. van den Broeke, M. J. van Wessem, and M. Morlighem (2019): Four decades of Antarctic Ice Sheet mass balance from 1979-2017. *Proceedings of the National Academy of Science of the USA*, **116**, 1095–1103.

Ritz, S.P., T.F. Stocker, and F. Joos (2011): A coupled dynamical ocean-energy balance atmosphere model for paleoclimate studies. *Journal of Climate*, **24**, 349–375.

Ritz, S.P., T.F. Stocker, and S.A. Müller (2008): Modeling the effect of abrupt ocean circulation change on marine reservoir age. *Earth and Planetary Science Letters*, **268**, 202–211.

Robock, A. (2008): 20 reasons why geoengineering may be a bad idea. *Bulletin of the Atomic Scientist*, **64**, 14–18.

Robock, A., L. Oman, and G.L. Stenchikov (2008): Regional climate responses to geoengineering with tropical and Arctic SO_2 injections. *Journal of Geophysical Research*, **113**, D16101.

Ruddiman, W.F. (2007): *Earth's Climate: Past and Future*. W.H. Freeman, 2 ed., 388 pp.

Saha, S., S. Nadiga, C. Thiaw, J. Wang, W. Wang, Q. Zhang, H. M. Van den Dool, H.-L. Pan, S. Moorthi, D. Behringer, D. Stokes, M. Peña, S. Lord, G. White, W. Ebisuzaki, P. Peng, and P. Xie (2006): The NCEP climate forecast system. *Journal of Climate*, **19**, 3483–3517.

Saltzman, B. (1962): Finite amplitude free convection as an initial value problem – I. *Journal of the Atmospheric Sciences*, **19**, 329–341.

Saltzman, B. (2001): *Dynamical Paleoclimatology: Generalized Theory of Global Climate Change*. Academic Press, 354 pp.

Saltzman, B. and K. A. Maasch (1991): A first-order global model of late Cenozoic climatic change. II. Further analysis based on a simplification of CO_2 dynamics. *Climate Dynamics*, **5**, 201–210.

Schiller, A., U. Mikolajewicz, and R. Voss (1997): The stability of the North Atlantic thermohaline circulation in a coupled ocean-atmosphere general circulation model. *Climate Dynamics*, **13**, 325–347.

Schär, C., O. Fuhrer, A. Arteaga, N. Ban, C. Charpilloz, S. Di Girolamo, L. Hentgen, T. Hoefler, X. Lapillonne, D. Leutwyler, K. Osterried, D. Panosetti, S. Rüdisühli, L. Schlemmer, T. C. Schulthess, M. Sprenger, S. Ubbiali, and Wernli H. (2020): Kilometer-scale climate models. *Bulletin of the American Meteorological Society*, pp. E567–E587.

Schär, C., P.L. Vidale, D. Lüthi, C. Frei, C. Häberli, M.A. Liniger, and C. Appenzeller (2004): The role of increasing temperature variability in European summer heatwaves. *Nature*, **427**, 332–336.

Schwarz, H.R. and N. Köckler (2011): *Numerische Mathematik*. Springer, 8 ed., 595 pp.

Sellers, W.D. (1969): A global climatic model based on the energy balance of the earth-atmosphere system. *Journal of Applied Meteorology*, **8**, 392–400.

Sherwood, S. C., M. J. Webb, J. D. Annan, K. C. Armour, P. M. Forster, J. C. Hargreaves, G. Hegerl, S. A. Klein, K. D. Marvel, E. J. Rohling, M. Watanabe, T. Andrews, P. Braconnot, C. S. Bretherton, G. L. Foster, Z. Hausfather, A. S. Heydt, R. Knutti, T. Mauritsen, J. R. Norris, C. Proistosescu, M. Rugenstein, G. A. Schmidt, K. B. Tokarska, and M. D. Zelinka (2020): An assessment of Earth's climate sensitivity using multiple lines of evidence. *Reviews of Geophysics*, **58**, e2019RG000678.

Siedler, G., J. Church, and J. Gould (Editors) (2001): *Ocean Circulation and Climate: Observing and Modeling the Global Ocean*, vol. 77 of *International Geophysics Series*. Academic Press, 715 pp.

Siedler, G., S. M. Griffies, J. Gould, and J. A. Church (Editors) (2013): *Ocean Circulation and Climate, 2nd Edition. A 21st Century Perspective*, vol. 103 of *International Geophysics Series*. Academic Press, 904 pp.

Siegenthaler, U. and F. Joos (1992): Use of a simple model for studying oceanic tracer distributions and the global carbon cycle. *Tellus B*, **44**, 186–207.

Siegenthaler, U., T.F. Stocker, E. Monnin, D. Lüthi, J. Schwander, B. Stauffer, D. Raynaud, J.-M. Barnola, H. Fischer, V. Masson-Delmotte, and J. Jouzel (2005): Stable carbon cycle-climate relationship during the late Pleistocene. *Science*, **310**, 1313–1317.

Smolarkiewicz, P.K. (1983): A simple positive definite advection scheme with small implicit diffusion. *Mon. Weather Rev.*, **111**, 479–486.

Soden, B.J., R.T. Wetherald, G.L. Stenchikov, and A. Robock (2002): Global cooling after the eruption of Mount Pinatubo: A test of climate feedback by water vapor. *Science*, **296**, 727–730.

Stocker, T. (2011): *Introduction to Climate Modelling*. Springer, 179 pp.

Stocker, T. F. (2013a): The closing door of climate targets. *Science*, **339**, 280–282.

Stocker, T. F. (2013b): The ocean as a component of the climate system. *In:* G. Siedler, S. M. Griffies, J. Gould, and J. A. Church (Editors), *Ocean Circulation and Climate, 2nd Edition. A 21st Century Perspective*, International Geophysics Series, 103, pp. 3–30. Academic Press.

Stocker, T.F. (1998): The seesaw effect. *Science*, **282**, 61–62.

Stocker, T.F. (2000): Past and future reorganizations in the climate system. *Quaternary Science Reviews*, **19**, 301–319.

Stocker, T.F. (2003): South dials north. *Nature*, **424**, 496–499.

Stocker, T.F. and S.J. Johnsen (2003): A minimum thermodynamic model for the bipolar seesaw. *Paleoceanography*, **18**, 1087.

Stocker, T.F. and O. Marchal (2000): Abrupt climate change in the computer: Is it real? *Proceedings of the National Academy of Science of the USA*, **97**, 1362–1365.

Stocker, T.F. and A. Schmittner (1997): Influence of CO_2 emission rates on the stability of the thermohaline circulation. *Nature*, **388**, 862–865.

Stocker, T.F. and D.G. Wright (1991): A zonally averaged ocean model for the thermohaline circulation. Part II: Interocean circulation in the Pacific-Atlantic basin system. *Journal of Physical Oceanography*, **21**, 1725–1739.

Stocker, T.F., D.G. Wright, and L.A. Mysak (1992): A zonally averaged, coupled ocean-atmosphere model for paleoclimate studies. *Journal of Climate*, **5**, 773–797.

Stommel, H. (1948): The westward intensification of wind-driven ocean currents. *Transactions, American Geophysical Union*, **29**, 202–206.

Stommel, H. (1958): The abyssal circulation. *Deep Sea Research*, **5**, 80–82.

Stommel, H. (1961): Thermohaline convection with two stable regimes of flow. *Tellus*, **13**, 224–230.

Stommel, H. and A.B. Arons (1960): On the abyssal circulation of the world ocean–I. Stationary planetary flow patterns on a sphere. *Deep Sea Research*, **6**, 140–154.

Stroeve, J.C., V. Kattsov, A. Barrett, M. Serreze, T. Pavlova, M. Holland, and W. N. Meier (2012): Trends in arctic sea ice extent from CMIP5, CMIP3 and observations. *Geophysical Research Letters*, **39**, L16502.

Tang, Y., R.-H. Zhang, T. Liu, W. Duan, D. Yang, F. Zheng, H. Ren, T Lian, C. Gao, and M. Mu (2018): Progress in ENSO prediction and predictability study. *National Science Review*, **5**, 826–839.

Tilmes, S., D. G. MacMartin, J. T. M. Lenaerts, L. van Kampenhout, L. Muntjewerf, L. Xia, C. S. Harrison, K. M. Krumhardt, M. J. Mills, B. Kravitz, and A. Robock (2020): Reaching 1.5 and 2.0°C global surface temperature targets using stratospheric aerosol geoengineering. *Earth System Dynamics*, **11**, 579–601.

Timmermann, A., S.-I. An, J.-S. Kug, F.-F. Jin, W. Cai, A. Capotondi, K.M. Cobb, M. Lengaigne, M.J. McPhaden, M.F. Stuecker, K. Stein, A.T. Wittenberg, K.-S. Yun, T. Bayr, H.-C. Chen, Y. Chikamoto, B. Dewitte, D. Dommenget, P. Grothe, E. Guilyardi, Y.-G. Ham, M. Hayashi, S. Ineson, D. Kang, S. Kim, W.M. Kim, J.-Y. Lee, T. Li, J.-J. Luo, S. McGregor, Y. Planton, S. Power, H. Rashid, H.-L. Ren, A. Santoso, K. Takahashi, A. Todd, G. Wang, G. Wang, R. Xie, W.-H. Yang, S.-W. Yeh, J. Yoon, E. Zeller, and X. Zhang (2018): El Niño-Southern Oscillation complexity. *Nature*, **559**, 535–545.

Trenberth, K.E. (Editor) (1992): *Climate System Modeling*. Cambridge University Press, New York, 1 ed., 788 pp.

Trenberth, K.E., J.M. Caron, and D.P. Stepaniak (2001): The atmospheric energy budget and implications for surface fluxes and ocean heat transports. *Climate Dynamics*, **17**, 259–276.

Tziperman, E. and H. Gildor (2003): On the mid-pleistocene transition to 100-kyr glacial cycles and the asymmetry between glaciation and deglaciation times. *Paleoceanography*, p. 1001.

UNFCCC (1992): *United Nations Framework Convention on Climate Change*. United Nations. URL http://unfccc.int.

UNFCCC (2015): *The Paris Agreement*. United Nations. URL https://unfccc.int/sites/default/files/english_paris_agreement.pdf.

Uppala, S.M., P.W. Kållberg, A.J. Simmons, U. Andrae, V.D.C. Bechtold, M. Fiorino, J.K. Gibson, J. Haseler, A. Hernandez, G.A. Kelly, X. Li, K. Onogi, S. Saarinen, N. Sokka, R.P. Allan, E. Andersson, K. Arpe, M.A. Balmaseda, A.C.M. Beljaars, L. Van De Berg, J. Bidlot, N. Bormann, S. Caires, F. Chevallier, A. Dethof, M. Dragosavac, M. Fisher, M. Fuentes, S. Hagemann, E. Hólm, B.J. Hoskins, L. Isaksen, P.A.E.M. Janssen, R. Jenne, A.P. Mcnally, J.-F. Mahfouf, J.-J. Morcrette, N.A. Rayner, R.W. Saunders, P. Simon, A. Sterl, K.E. Trenberth, A. Untch, D. Vasiljevic, P. Viterbo, and J. Woollen (2005): The ERA-40 re-analysis. *Quarterly Journal of the Royal Meteorological Society*, **131**, 2961–3012.

Vallis, G. K. (2017): *Atmospheric and Oceanic Fluid Dynamics, 2nd Edition*. Cambridge, 946 pp.

Varga, R.S. (2009): *Matrix Iterative Analysis*, vol. 27 of *Springer Series in Computational Mathematics*. Springer, 358 pp.

Vogel, M. M., R. Orth, F. Cheruy, S. Hagemann, R. Lorenz, B. J. J. M. van den Hurk, and S. I. Seneviratne (2017): Regional amplification of projected changes in extreme teemperatures strongly controlled by soil moisture-temperature feedbacks. *Geophysical Research Letters*, **44**, 1511–1519.

Vogel, M. M., J. Zscheischler, and S. I. Seneviratne (2018): Varying soil-moisture-atmosphere feedbacks explain divergent temperature extremes and precipitation projections in central Europe. *Earth System Dynamics*, **9**, 1107–1125.

Washington, W.M. and C.L. Parkinson (2005): *Introduction to Three-dimensional Climate Modeling*. University Science Books, 2 ed., 368 pp.

Wedi, N. P., I. Polichtchouk, P. Dueben, V. G. Anantharaj, P. Bauer, S. Boussetta, P. Browne, W. Deconinck, W. Gaudin, I. Hadade, S. Hatfield, O. Iffrig, P. Lopez, P. Maciel, A. Mueller, S. Saarinen, I. Sandu, T. Quintino, and F. Vitart (2020): A baseline for global weather and climate simulations at 1 km resolution. *Journal of Advances in Modeling Earth Systems*, **12**, e2020MS002192.

Wild, M., D. Folini, M.Z. Hakuba, C. Schär, S.I. Seneviratne, S. Kato, D. Rutan, C. Ammann, E.F. Wood, and G. König-Langlo (2015): The energy balance over land and oceans: an assessment based on direct observations and CMIP5 climate models. *Climate Dynamics*, **44**, 3393–3429.

Willebrand, J. (1993): Forcing the ocean by heat and freshwater fluxes. *In:* E. Raschke and D. Jacob (Editors), *Energy and Water Cycles in the Climate System*, pp. 215–233. Springer.

Willeit, M., A. Ganopolski, R. Calov, and V. Brovkin (2019): Mid-pleistocene transition in glacial cycles explained by declining CO_2 and regolith removal. *Science Advances*, **5**, eaav7337.

Woodruff, S.D., R.J. Slutz, R.L. Jenne, and P.M. Steurer (1987): A Comprehensive Ocean-Atmosphere Data Set. *Bulletin of the American Meteorological Society*, **68**, 1239–1250.

Young, D. M. (1950): *Iterative methods for solving partial differential equations of elliptic type*. Ph.D. thesis, Harvard University.

Zaucker, F., T.F. Stocker, and W.S. Broecker (1994): Atmospheric freshwater fluxes and their effect on the global thermohaline circulation. *Journal of Geophysical Research*, **99**, 12443–12457.

Zebiak, S. E. and M. A. Cane (1987): A model El Niño-Southern Oscillation. *Monthly Weather Review*, **115**, 2262–2278.

Acknowledgement

Christoph Raible took care of the problem sets during our joint teaching of this course. Beat Ihly has translated the original manuscript into LaTeX, checked critically all derivations and redrafted many figures. He also significantly expanded sections 3.4, 6.4 and parts of section 6.8 to make them more accessible for the students and authored Appendix A. These contributions are gratefully acknowledged.